Flinders UNIVERSITY
ADELAIDE · SOUTH AUSTRALIA

A STUDY OF CHEMICAL AND PLASMA DEPOSITION OF ORGANOSILANE THIN FILMS

by

Alexander J. Sibley

Thesis

Submitted to Flinders University

for the degree of

Doctor of Philosophy

College of Science and Engineering

13th March 2019

DECLARATION

I certify that this thesis does not incorporate without acknowledgment any material previously submitted for a degree or diploma in any university; and to the best of my knowledge and belief it does not contain any material previously published or written by another person except where due reference is made in the text.

Alexander James Sibley

7/11//2018

SUMMARY

As industry and society in general become more away of the need for increased energy efficiency, strong, lightweight metals such as magnesium are being seriously considered for a range of applications. The high reactivity and thus corrosion rate magnesium in atmospheric conditions necessitates the development of new, environmentally benign materials and technology for corrosion prevention. Organosilanes are one such class of materials, originally pursued as adhesion promoters, but their ability to form highly cross-linked barrier coatings makes them a good candidate for corrosion prevention.

This thesis examines the fundamental interactions between the model organosilane “propyl-trimethoxysilane” (PTMS) and pure magnesium surfaces. Initially, conventional dip coating was examined with the purpose of investigating the uptake kinetics of PTMS onto magnesium. It was found that the chemical deposition of PTMS onto magnesium is oscillatory, in agreement with previously undertaken studies of a similar nature using different pure metallic surfaces. Unlike those studies, it was found here that the high reactivity of magnesium led to its rapid degradation in the acidic conditions necessary to effectively catalyse the film deposition process, making such chemical deposition unsuitable for future investigation.

A different method of film deposition was therefore investigated: plasma enhanced chemical vapour deposition. Plasma-based film deposition allows cleaning, pre-treatment and deposition to all be performed in a clean vacuum environment, without the need for organic solvents. In order to pursue this area of research, a radio frequency inductively coupled plasma (RF-ICP) chamber was constructed, including the design and fabrication of a suitable RF matching network. Through a comprehensive literature review, the deposition of PTMS in such a way has thus far not been reported, so a fundamental study was undertaken into the effects of various experimental plasma parameters on the resultant film composition and structure. Analysis of these films using a combination of X-Ray photoelectron spectroscopy and scanning Auger spectromicroscopy established that silicon containing films were deposited from PTMS, although the composition was significantly different to that of the PTMS molecule itself, with a reduction in carbon and oxygen content due to the decomposition of the molecule in the plasma environment. Additionally, it was found through elemental mapping with scanning Auger spectromicroscopy that the morphology of the magnesium itself had an effect on the uniformity of the deposited films.

To eliminate any such effects, magnesium surfaces were diamond polished to a mirror finish in order to study the effects of PTMS plasma power on the deposited films with the Fourier

Transform Infra-Red spectroscopy (FTIR), in addition to the other aforementioned spectroscopies. No significant compositional change was observed with increasing plasma power however, the use of high energy resolution X-ray Photoelectron Spectroscopy (XPS) identified a change in the chemical bonding environment of silicon, with an increased amount of silicon bonded to four oxygen atoms, as opposed to three as is present in the PTMS molecule. FTIR spectroscopy gave direct evidence of crosslinking between silicon and oxygen species, as well as correlating the reduction in carbon within the film to a reduction in hydrocarbon species.

In addition to fundamental studies into film deposition from pure PTMS vapour, a proof of concept investigation was undertaken into the functionalisation of organosilane films through the mixture of PTMS and other materials within the plasma environment. The addition of carbon (in the form of methane) to the PTMS plasma led to no significant change in composition, however, an increase in silicon to carbon bonding was observed compared to films deposited from PTMS alone. By increasing the oxygen content within the plasma, either in the form of oxygen gas or water vapour, a significant reduction in carbon within the film was observed, with a greater reduction caused by oxygen. High energy resolution XPS analysis of films deposited from these precursors revealed that all silicon present within these films was attached to four oxygen atoms, implying a silicon dioxide like film. Finally, an attempt was made to incorporate nitrogen into the PTMS plasma films in order to provide a method of cost effective amine functionalisation. While initial XPS results were promising, with nitrogen detected spectrally, further efforts to locate nitrogen using Auger electron spectromicroscopy were unsuccessful. Nevertheless, the developed plasma deposition capability, and the fundamental understanding of film deposition from PTMS vapour provides a solid foundation for future studies into organosilane films.

CONTENTS

DECLARATION iii

SUMMARY v

CONTENTS vii

Table of Figures ix

ACKNOWLEDGEMENTS xv

1 Chapter 1: Introduction 1

1.1 Metals, Alloys and Oxides 1

1.2 The Process of Corrosion: 4

1.3 Coatings: A Method for Corrosion Prevention 8

1.4 Plasma Polymerization 15

1.5 Aims of this Research 23

2 Chapter 2: Experimental 25

2.1 Selection of Analytical Techniques 25

2.2 Electron Spectromicroscopy 26

2.3 Other Analysis Techniques 47

2.4 Materials 52

2.5 Chemical Dip Coating Procedures 53

3 Chapter 3: Chemical Dip Coating of PTMS onto Magnesium Oxide 55

3.1 Introduction 55

3.2 Surface Etching and Microstructure 55

3.3 XPS Analysis 56

3.4 Scanning Auger Microscopy 58

3.5 Summary 67

4 Chapter 4: Design, Construction and Testing of a Plasma Chamber for Thin Film Deposition 68

4.1 Plasma Chamber Construction 68

4.2 Preliminary Organosilane Deposition: 75

4.3 Time Dependent Investigation of Plasma Deposited PTMS Films 79

4.4 Plasma Power Dependence on PTMS deposition ... 95

4.5 Stability of plasma deposited PTMS films ... 106

4.6 Summary ... 107

5 Chapter 5: Effect of Experimental Plasma Parameter Variation on PTMS Thin Film Composition and Structure ... 109

5.1 Surface Morphology Analysis by AFM ... 109

5.2 XPS Analysis of PTMS Films ... 112

5.3 Scanning Auger SpectroMicroscopy Studies on PTMS Film Composition and Coverage ... 118

5.4 ATR-FTIR ... 131

5.5 Summary ... 135

6 Chapter 6: Modification of PTMS Plasma Films Through the Addition of Functional Gases ... 137

6.1 Modifying Elemental Composition of Plasma Deposited PTMS Films ... 140

6.2 Nitrogen Functionalised PTMS Plasma Films ... 145

6.3 Summary ... 147

7 Chapter 7: Conclusions and Future Work ... 149

7.1 Conclusions ... 149

7.2 Recommendations for Future Work ... 152

8 References ... 154

TABLE OF FIGURES

Figure 1.1: a) General structure of mono-silanes b) General structure of bis-silanes 10
Figure 1.2 High resolution ToF-SIMS spectrum of aluminium coated with GPS. Peaks are labelled according to best fitting mass fragments. Reproduced from Abel et al. [94] 12
Figure 1.3: a) Illustration of the three species which are present in the model for oscillatory uptake of organosilanes. b) Theoretical uptake curves for each individual species; ($\theta_{1,2,3}$), the sum of all three; θ, and the curve that best fits experimental data; $\theta_1+\theta_3$. c) Experimentally obtained uptake curve of 0.75% pH 3 PTMS solution onto aluminium substrates. Reproduced from Quinton et al. [103] 13
Figure 2.1 Diagram of a) XPS and b) AES emission processes (modified from Kibel [1]).... 27
Figure 2.2: Energy level diagram representation of the photoemission process the relevant energy terms. Modified from Kibel [1]. 28
Figure 2.3 Differences between XPS spectra of a pure magnesium surface obtained with two different X-Ray energies: 1486.6eV corresponding to $Al_{K\alpha}$ X-rays in green, and 1253.6eV corresponding to $Mg_{K\alpha}$ X-rays in blue. 31
Figure 2.4: Cross sectional comparison of Auger electron, secondary electron and characteristic X-Ray emission 32
Figure 2.5 Auger electron and X-ray emission relative probabilities for increasing atomic numbers. Reproduced from Hubin and Terryn [171] 32
Figure 2.6: Energy distribution of electrons emitted after irradiation by an electron beam. Reproduced from Kibel [1] 33
Figure 2.7: a) Example Auger electron spectrum of a magnesium surface. b) The same spectrum plotted as a derivative of electron counts per second vs kinetic energy 34
Figure 2.8: Inelastic Mean free path of an electron vs Kinetic energy. Reproduced from Kibel [1], originally published by Seah and Dench [174].. 37
Figure 2.9 The LHS-10 Located at Flinders University 37
2.10 SPECS Electron and Ion spectroscopy apparatus located at Flinders University 39
Figure 2.11 The PHI-710 Scanning Auger Nanoprobe at Flinders University 40
2.12 Cross sectional geometry of a concentric hemispherical analyser. Modified from Hoffman [165], Originally published by Seah [175]... 42
Figure 2.13: Cross section of a cylindrical mirror analyser. Modified from Kibel [1] 45
Figure 2.14: Sample mounts used for a) LHS-10 XPS b)SPECS XPS and c) PHI-710 Scanning Auger Nanoprobe 46
Figure 2.15 Schematic of an atomic force microscopy in operation 48
Figure 2.16 The Bruker Dimension Fastscan used in this work 49
Figure 2.17 Schematic Diagram of a Michelson interferometer. Reproduced from Stuart [178]

.... 51
Table 2.1 Purities and suppliers of gases used for plasma experiments 53
Figure 3.1: Photograph of visible difference between polished magnesium pre (left) and post (right) pH 3.0 acetic acid pre-treatment 55
Figure 3.2: a) SEM image of pure magnesium abraded with 1200p silicon carbide paper. b) SEM of the same magnesium surface post etching for 30 minutes in pH 3 acetic acid........ 56
Figure 3.3: Surface coverage value "Γ" plotted against time. The dotted line is plotted as a guide to the eye. A significant decrease in coverage can be observed between 40 and 50 seconds. 57
Figure 3.4: a) SEM image of 10 second dip coat of PTMS onto magnesium. b) Scanning Auger elemental maps of silicon (green) and magnesium (red), overlayed onto each other 59
Figure 3.5: a) SEM image of 30 second dip coat of PTMS onto magnesium 3.5b) Overlayed scanning Auger elemental maps of silicon (green), magnesium (red) and carbon (blue)..... 59
Figure 3.6: Large FoV (500μm) SEM image of 50 second dip coated magnesium sample. Areas of PTMS attachment appear as darker regions on SEM image. Highlighted in cyan: area of PTMS film with cracks caused by curing. Highlighted in yellow: circular feature in magnesium surface. Highlighted in green: location chosen for further microscopy seen in Figure 3.7.. 60
Figure 3.7: a) SEM of 50 second PTMS dip coated sample and 7b) Overlayed elemental maps of silicon (green) and magnesium (red) of the same area. Silicon signal is strong in the dark area of the surface seen in the upper right part of the SEM image 61
Figure 3.8: a) Large FoV (500μm) SEM of image showing a region of the magnesium surface coated by PTMS for 50 seconds (top half of image), with the approximate area of figure 3.8b) outlined in green. b) highlighted in green. 3.8b) SEM image of the area outlined within figure 3.8a), where a section of PTMS film has been removed from the magnesium substrate. 3.8c) SEM image of the area highlighted within 3.8b) and 3.8d) overlayed elemental maps of silicon (green) and magnesium (red) of the area shown by 3.8c) 63
Figure 3.9 a) SEM image of 100 second PTMS dip coat of magnesium surface. Previous areas of thick PTMS film have been removed. b) Overlayed elemental maps of silicon (green) and magnesium (red) corresponding to SEM image of 3.9a). 64
Figure 3.10 a) SEM image of 100 second PTMS dip coat of magnesium surface at higher magnification than seen in Figure 3.9. b) Corresponding overlayed elemental map of silicon (green) and magnesium (red) of SEM image seen in 3.10 a). 65
Figure 3.11: a) 100μm^2 area of a 200 second PTMS dip coated magnesium surface. Areas of PTMS film can be readily observed, with some thicker areas as signalled by the presence of charging. b) Large FoV (500μm) SEM image of 1000 second PTMS dip coated magnesium surface. Large, cracked, islands of PTMS film are visible on the magnesium

surface. 66
4.1 a) Frontal view of plasma chamber showing (from top to bottom) variable capacitance matching unit with control knobs, copper coil antenna encased in resin and fibreboard, steel chamber containing lit PTMS plasma, Turbomolecular pump and rotary vane pump. b) Side view of the chamber, including Baratron and Micro-ion Plus gauges 69
4.2 Circuit diagram of the matching circuit constructed for the plasma chamber used for this work. 74
Figure 4.3: Images of (left to right) PTMS, water and argon plasma 74
Figure 4.4 Comparison of XPS spectra of a magnesium surface that was exposed to PTMS vapour (blue), and one that was exposed to a PTMS plasma (red). The pressure of both vapour and plasma were identical ($1.0x10^{-3}$torr) as was exposure duration (5 minutes). 75
Figure 4.5: XPS spectra of magnesium surfaces after abrasion with 1200p silicon carbide paper (black) and subsequent oxygen plasma pre-treatment for 5 minutes at 20W applied power (green). Primary photoelectron and Auger peaks are labelled. 76
Figure 4.6: a)SEM image of oxygen plasma treated magnesium surface. The area highlighted in yellow represents the location chosen for the example depth profile seen in Figure 4.7 77
b), c), d): Elemental maps of magnesium, carbon and oxygen respectively, obtained for the same area as the SEM image in a). The analysis field of view (FoV) is 100μm, obtained using 10kV beam with 10nA current. 78
Figure 4.7 a) Auger Electron Spectroscopy (AES) depth profiles of carbon, oxygen and magnesium obtained from the area of an oxygen plasma treated surface as highlighted in Figure 4.6 a). The magnesium profile was deconvoluted into two constituent components; a metal and an oxide. b) Stack plot of differentiated AES spectra showing the evolution of the magnesium peak shape (top to bottom) as the depth profile progresses. The change in peak shape is modelled using Linear Least Squares (LLS) fitting (as described in Chapter 2, Section 2.1.8) to produce the two separate profiles seen in a). 78
Figure 4.8: a) and b) Two example AFM images of pure magneisum substrates after both polishing with 1200p silicon carbide paper and oxygen plasma treatment 79
Figure 4.9 Green: Plot of surface coverage (Γ) vs plasma deposition time. Cyan: Plot of C:Si ratio vs plasma deposition time. Both plots are calculated from XPS data averaged from 3 separate samples. Error bars are calculated from standard deviation. 80
Inset: Deposition times between 0 and 300 seconds 80
Figure 4.10: Theoretical structure of PTMS 81
Figure 4.11: a) SEM image of magnesium surface after exposure to PTMS plasma for 10 seconds. b) Overlayed elemental maps of magnesium (red), silicon (green) and carbon (blue). 82

Figure 4.12: a)SEM image of a magnesium surface after exposure to PTMS plasma for 30 seconds b) Overlayed elemental maps of magnesium (red), silicon (green) and carbon (blue) for the corresponding area. c) and d) false colour elemental maps of magnesium and silicon respectively 84
4.13 a) SEM image of magnesium surface after exposure to PTMS plasma for 60 seconds. b) Overlayed of elemental maps of magnesium (red), silicon (green) and carbon (blue). c) False colour elemental map of magnesium for the corresponding area. 86
Figure 4.14: a) SEM image of magnesium surface exposed to PTMS plasma for 120 seconds. b) Overlayed elemental magnesium (red), silicon (green) and carbon (blue). c) and d) false colour elemental maps of carbon and oxygen respectively. 88
Figure 4.15: a) SEM image of m surface exposed to PTMS plasma for 300 seconds. Highlighted regions indicate areas of further analysis by AES b) Overlayed elemental magnesium (red), silicon (green) and carbon (blue). c) False colour elemental map of magnesium d) AES spectra obtained for the areas indicated in 13a). 90
Figure 4.16 a)SEM image of magnesium surface exposed to PTMS plasma for 1800 seconds. b) Overlayed elemental magnesium (red), silicon (green) and carbon (blue)....... 91
Figure 4.17: a)SEM image of magnesium surface exposed to PTMS plasma for 3600 seconds. b) Overlayed elemental magnesium (red), silicon (green) and carbon (blue)....... 92
Figure 4.18: a) Depth profiles of elements present on magnesium surface after PTMS plasma treatment of 3600 seconds. b) Individual depth profile of silicon KLL Auger transition 93
Figure 4.19: Silicon depth profiles of surface films produced on magnesium by various exposure times to 20W $1x10^{-3}$Torr PTMS plasma treatment. 94
Figure 4.20: Plot of film depth vs duration of exposure to PTMS plasma. Error bars are given as the standard deviation. Two separate lines are plotted in order to guide the eye along two separate coating domains, which meet at a plasma duration of 120s. 94
4.21 Plot of coverage (Γ) vs applied power of PTMS plasma after a 1 minute exposure duration at $1x10^{-3}$Torr. Error bars are given as the standard deviation. 96
Figure 4.22 Plot of C:Si ratio vs Applied PTMS plasma power. 97
4.23 a) SEM image of a magnesium surface exposed to a PTMS plasma at 10W for 60 seconds. b) Overlayed elemental maps of magnesium (red), silicon (green) and carbon (blue), c) false colour elemental map of magnesium d) false colour elemental map of carbon. 99
Figure 4.24 a) SEM image of a magnesium surface exposed to a 30W PTMS plasma for 60 seconds. b) Overlayed elemental maps of magnesium (red), silicon (green) and carbon (blue). c) False colour elemental map of magnesium. 100
Figure 4.25 a) SEM image of a magnesium surface exposed to a PTMS plasma at 30W for

60 seconds. b) Overlayed elemental maps of magnesium (red) and silicon (green) 101
Figure 4.26: a) SEM image of a magnesium surface exposed to a PTMS plasma at 50W for 60 seconds. b) Overlayed elemental maps of magnesium (red), silicon (green) and carbon (blue). c) False colour elemental map of magnesium 102
Figure 4.27 a) SEM image of a magnesium surface exposed to a PTMS plasma at 100W for 60 seconds. b) Overlayed elemental maps of magnesium (red), silicon (green) and carbon (blue) 103
Figure 4.28: a) SEM image of a magnesium surface exposed to a PTMS plasma at 50W for 60 seconds. b) Overlayed elemental maps of magnesium (red) and silicon (green) 104
Figure 4.29: Depth profiles of the silicon KLL Auger transition for samples of magnesium oxide exposed for 60 seconds to PTMS plasma at a range of applied RF powers. 105
Figure 4.30 Plot of film depth vs applied plasma power. Error bars are given as the standard deviation. A natural logarithmic trend line has also been fitted, with an R^2 value of 0.9814. 105
Figure 4.31 XPS spectra of PTMS plasma coated magnesium surfaces sonicated in various solvents for a duration of 5 minutes.. 106
Figure 5.1: AFM images of diamond polished (1μm) magnesium surfaces........................ 110
Figure 5.2: a-f) Representative AFM images of PTMS coated, diamond polished magnesium surfaces 111
Figure 5.3 Variation of elemental composition with applied plasma power of PTMS films on magnesium 113
Figure 5.4: Ratios of elemental composition vs applied plasma power 114
Figure 5.5 a) Structure of the molecule "HMDSO" b) Structure of the molecule "PTMS" ... 115
5.6 Example Deconvolution of the Si2*p* photoelectron peak. This spectrum is obtained from a PTMS film deposited at 10W 116
Figure 5.7 Plot of Si2*p* peak composition vs applied plasma power. 117
Figure 5.8: a-l) SEM images of magnesium surface after PTMS plasma deposition with an applied power of between 10W and 100W, along with accompanying overlayed elemental maps of silicon (green), oxygen (red) and carbon (blue). 120
Figure 5.9: a) SEM Image of a magnesium surface coated by a PTMS plasma with an applied power of 40W. b)-e) Elemental map of carbon overlayed onto SEM image with decreasing transparency. f) Elemental map of silicon. The bar on the right hand side of the image gives an indication of the intensity scale for all presented maps. The "thermal" scale ranges from black at the lowest intenstiy to white at the highest. 121
Figure 5.10: Percentage elemental composition of Plasma deposited PTMS films obtained from AES spectra vs applied plasma power 123
Figure 5.11: Elemental ratios of C:Si, O:Si, and C:O of films deposited from PTMS plasma vs

applied plasma power, obtained from AES spectra. 124
Figure 5.12 a) SEM image of a PTMS film deposited onto polished magnesium with an applied plasma power of 10W. b) AES spectra taken at the areas indicated. 125
Figure 5.13 a) and b) Depth profiles of areas highlighted in Figure 5.12 126
Figure 5.14: Percentage elemental compositions of films deposited from PTMS plasma vs applied plasma power as determined by AES and argon ion depth profiling 127
Figure 5.15: Elemental ratios of C:Si, O:Si and C:O for films deposited from PTMS plasma vs applied plasma power as determined by AES and argon ion depth profile.................... 127
Figure 5.16 Depth profiles from multiple magnesium surfaces coated with PTMS plasma with an applied power of a) 10W, b) 50W and c) 100W 129
Figure 5.17 Average values for PTMS film depth with increasing applied plasma power... 130
Figure 5.18: FTIR spectrum between $4000cm^{-1}$ and $600cm^{-1}$ of a) Pure liquid PTMS and b) A film deposited from PTMS plasma.. 132
Figure 5.19: Overlayed FTIR spectra obtained for films deposited onto magnesium surfaces from PTMS plasma at applied powers of 10W, 50W and 100W. 134
Figure 6.1 Comparison between silicon bonding environment present in PTMS films deposited at two separate pressures: $1x10^{-3}$Torr and $2x10^{-3}$Torr at a) 20W, and b) 100W 139
Figure 6.2: Comparison between silicon bonding environment present in films deposited from pure PTMS and a mixture of PTMS and CH_4 at a) 20W, and b) 100W 141
Figure 6.3 Comparison of Si2*p* photoelectron peak deposited at 20W from pure PTMS vapour and a mixture of PTMS and oxygen 144
Figure 6.4 Comparison between silicon bonding environment present in films deposited from pure PTMS and a mixture of PTMS and N_2 at a) 20W, and b) 100W................................. 146

ACKNOWLEDGEMENTS

I imagine that with any document of this size, there are many people that require thanking. This one is certainly no exception. Out the myriad people that I would like to acknowledge, the first is my supervisor, Jamie Quinton. I thank you for all the support and opportunities you've provided me – from simple discussions, to the installation of world class scientific equipment and employment opportunities. I am certain that without your influence, from the first weeks of my undergraduate studies to now I wouldn't be able to call myself a scientist, let alone a physicist. Thanks also to my co-supervisor, Gunther Andersson. Although our interactions have reduced during the later parts of my research, I am thankful for the advice and you provided me early on and the opportunities to work on some amazing equipment.

I would like to give a special thanks at this point to Science and Engineering workshop staff past and present. In particular, Andrew Dunn, Chris Price, Bill Drury, and Bob Northeast. Your knowledge and assistance made much of my project possible. I'm sure that you could have done without many of the problems that we brought to you, but there was never a moment's pause in your efforts to keep our laboratories running.

I have been fortunate in my time at Flinders to have been involved in a number of different research groups, all containing excellent scientists to serve as role models and to share in the excitement and disappointments of everyday research life. Specifically, the "Smart Surface Structures", or now the "Super" group at Flinders University, which is one of the most inclusive and friendly groups of people I've had the pleasure to be a part of. Out of these group members there are a few that I would like to thank individually for their particular help and advice. Firstly Dr Anders Barlow – you finished just as I was starting not only showing me that a PhD is possible, but also provided a colossal amount of experience and instruction in how to keep a surface science laboratory running smoothly in a short amount of time. I hope that I have been a worthy successor. Thanks also to Dr Christopher Gibson for both providing me with training and employment within the AMMRF, and sharing advice, as well as the joys and frustrations that go along with managing a research lab. To my office mates, (Dr) Natalya Schmerl and (Dr) Benjamin Chambers, thanks for all the times, good and not so good, shared in the office. You helped make it a home away from home (though not one that I'd want to live in), and I will be forever grateful for your support over the years.

To the friends and family members that have supported me throughout my PhD, I sincerely thank you, especially my parent for providing me with not only accommodation, but also for recognising my enjoyment of science and guiding me towards it, even if I hadn't realized it at the time. Finally, to Bonnie for all the love, support and (most especially) patience you've given me, especially over the past few months, which I know have been difficult for us both. I could never have done any of this without you.

Finally, I would like to acknowledge that this PhD was supported by an Australian Government Research Training Program Scholarship, in addition to a Flinders University Research Scholarship and Faculty of Science and Engineering Research Award.

1 CHAPTER 1: INTRODUCTION

1.1 Metals, Alloys and Oxides

From simple tools and weapons, to electronic circuits and spacefaring vehicles, metals have played a vitally important part in human history. For a significant majority of this time, iron and its alloys have been the primary amongst industrial metals [2]. With the rapid advancement of modern mining and metallurgical procedure, lightweight materials have seen increased use in the 20th and 21st centuries, especially in the automotive, construction and aeronautical industries, where high strength to weight ratio and ease of processing are of paramount importance. Aluminium is the most commonly used non-ferrous metal, and even more abundant (it is the third most common element present in the earth's crust) [3]. Another strong, lightweight metal, the use of which has rapidly accelerated in the past decades is magnesium. As the 8th most common metal, it is not as abundant in the earth's crust as either aluminium or iron, it is however, the third most abundant element dissolved in salt water [4]. Thus, magnesium is unique among structural metals in that it can be extracted from both terrestrial deposits and the ocean [4]. Magnesium is the lightest of the structural elements, with the lowest density of all metallic construction materials [5], being less than a quarter of iron, and two thirds that of aluminium. This gives magnesium a favourable strength to weigh ratio [6-14]. This makes magnesium very well suited as an alternative to aluminium in applications where weight saving without a loss of structural integrity is important [15, 16] especially for the automotive and aerospace industries [4, 17] where reducing greenhouse gas emissions is necessary [16, 18-20]. Other valuable properties of magnesium include excellent castability [4, 5, 12, 14, 17], weldability[5, 21], machinability[17], electromagnetic shielding [4] and vibrational damping[12, 13, 22]. These give it many further applications in electronic goods, handheld tools and other household equipment [7, 22]. As a metal, magnesium is inherently more recyclable than polymers that could serve the same purposes [5, 12, 23].

In addition to the benefits of superior physical properties such as strength and density, magnesium is an inherently biocompatible material with low toxicity [24-26]. Indeed, the Mg^{2+} ion is an essential mineral [27, 28], and is present in large quantities in the human body [29]. This, coupled with the well suited mechanical properties make magnesium an excellent candidate for an implant material [24, 25, 28, 30-32], reducing physical irritation and inflammatory responses [30] as well as more severe complications such as the formation of blood clots (thrombosis) and the narrowing of veins (restenosis) [30]. The use of magnesium as an implant has increased since the mid-20th century [33] however, issues with rapid

corrosion have led to their replacement with titanium since it has become more abundant and cost effective. That magnesium corrodes into a biocompatible by-product does however, lead to the potential for magnesium to be used as a biodegradable implant. Biodegradable implants are at the forefront of biomaterials research [31]. As opposed to conventional metallic or polymer implants, they are able to be dissolved, absorbed, consumed or excreted by the human body [34] negating the need for secondary surgeries to remove implants[35]. Current biodegradable implants made from polymers [36] do not have the required mechanical strength for many applications [31].

1.1.1 Limitations of metals: Corrosion

There are several properties that make metals, desirable for use in a range industries, especially as previously mentioned, magnesium. However, they all suffer a significant drawback in the form of corrosion. Corrosion is a process undergone when a metal (or a constituent of a metal alloy) combines with environmental elements (usually oxygen and water), causing a chemical reaction that results in the deterioration of the metal [37]. The corrosion of metals poses a vast problem for a large number of industries and should not be understated. It has been estimated that the cost of corrosion around the world exceeds $1.8 Trillion USD [38] spread over a range of industries. Corrosion could also present a hazard to human life, from something as major as a bridge collapse, to something as subtle as water pipes leaching metal ions into drinking water.

There are several different mechanisms for corrosion but the most common types are uniform corrosion and localised corrosion. Uniform corrosion is the most common and described as a regular removal of metal from the surface, occurring when a corrosive environment (most commonly the atmosphere) has access to the entire surface. Localised corrosion occurs when either a corrosive agent is in direct contact with a small area of a metal, or there is a defect (or interface between metals in an alloy) in the metal surface which, owing to its higher surface energy and hence reactivity, is intrinsically more prone to corrosion.

While corrosion poses a problem for all metals, magnesium and its alloys possess a higher reactivity than transition, or other higher group metals which leads to poorer corrosion resistance. This has been the primary barrier preventing their widespread industrial uptake over aluminium. Pure magnesium is also highly flammable, especially when cut into thin strips or powdered. This means care must be taken during the manufacturing process, especially as sources of ignition could be present and magnesium does not require air to burn [22]. This has limited the widespread use of magnesium and its alloys in many industries, especially those which take place in environments prone to high levels of humidity

[39] where corrosion is more likely to occur, such as the naval or aviation industries.

1.1.2 Metal oxides:

If a bare metal surface is exposed to an oxygen rich environment (like air), a metal oxide surface film is formed. As industrial processes are most commonly undertaken in atmosphere, the formation of this surface oxide is unavoidable. As such, the resistance of a metal to corrosion is more closely related to the properties of the oxide than the metal itself [40]. The properties of metal oxides are as varied as the metals themselves but for the most part, surface oxides are more resistant to corrosion than the underlying metals, aluminium being a stand-out example where its natural oxide significantly enhances the pure metals corrosion resistance.

Because of their importance related to the corrosion of underlying metals, many studies have been undertaken into understanding metal oxides and their growth over the years [17, 39-47] but also how surface oxides can be grown for specific purposes [22]. The study of metal oxides is not a recent endeavour. Metal oxides have been studied in a myriad of ways throughout human history with a range of techniques. Technological advancements over the past century have allowed for the study and understanding of such materials at the atomic level. Of these modern advancements, surface sensitive ultra-high vacuum (UHV) techniques, in particular X-ray photoelectron spectroscopy (XPS) is one of the most useful, due to its aforementioned surface sensitivity and ability to determine elemental concentrations and oxidation states.

An early example of this was reported by Fuggle et al. [41], where X-Ray photoelectron spectroscopy was used to observe the reaction of a range of metals (including aluminium and magnesium) with oxygen and water vapour and study the resulting surface oxides. Although the XPS technique was relatively new at that stage, Fuggle was able to show that the XPS peaks associated with each metal could be deconvoluted into component peaks that were associated with various oxidation states. This was advanced further by Strohmeier, who developed a method of determining the thickness of an oxide layer by measuring the intensity ratios of the oxide to metallic components of the spectral peaks [48].

Studies of aluminium and magnesium have seen a significant amount of attention in this area. One study by Fournier et al. involved using a range of oxygen containing gases (O_2, CO_2 and H_2O) to oxidise high purity magnesium at a range of temperatures and measuring the extent of oxidation with XPS [17]. Through the deconvolution of photoelectron peaks, it was found that irrespective of the temperature or gas used for oxidation (with one exception), a significant component of the magnesium 2*p* photoelectron peak was from the

metallic state of magnesium, implying a very thin or incomplete oxidation layer. This oxide was primarily composed of magnesium oxide (MgO), with magnesium hydroxide ($Mg(OH)_2$) and magnesium carbonate ($MgCO_3$) as secondary and tertiary components, depending on the method of oxidation, which was supported through the deconvolution of their “partner” elemental peaks, oxygen and carbon. The exception was for magnesium which was oxidised by polishing in water, which possessed a much thicker oxide, primarily composed of magnesium hydroxide.

The formation of oxides on magnesium upon immersion into aqueous solutions had previously been studied in more detail by Yao et al. [44]. In that study, surfaces formed by exposure to distilled water, a 3% sodium chloride solution and air were compared via XPS analysis. Oxide growth was found to be far more rapid on those surfaces immersed in liquid, with thicker layers formed (as determined using XPS and Strohmeier’s method). The composition of the oxides formed on immersion was found to be primarily $Mg(OH)_2$, with MgO and $MgCO_3$ also present, compared to a thin, primarily MgO film on the magnesium exposed to air. The hydroxide was found, through the use of argon ion depth profiling, to be present in stronger concentrations at the surface of the oxide layer, gradually converting to MgO nearer to the oxide/metal boundary.

It is noteworthy that oxides formed on metal surfaces are reactive and will change composition depending on the environments in which they are placed. This was demonstrated by Kuroda et al. [49] and later Chen et al. [42] who showed that in moist air or exposure to water vapour, magnesium oxide (MgO) becomes progressively more hydrated until the oxide is primarily comprised of $Mg(OH)_2$.

A group of studies by Do and Splinter et al. [40, 47] have investigated the growth of oxides on alloys as well as pure magnesium and aluminium. Water vapour and humid air was used to grow an oxide film and the techniques XPS and Auger Electron Spectroscopy (AES) were used to analyse the surfaces over a large range of exposures. Results from these studies have shown that the oxidation occurs in three definable steps: firstly an initial adsorption (chemisorption) of water molecules on the surface followed by oxide nucleation and island growth of the oxide. The third step is a (relatively) slow thickening of the film, agreeing with the model for oxide growth detailed by Cabrera and Mott in their “*Theory of oxidation of metals*" [50].

1.2 **The Process of Corrosion:**

The formation of oxides on metal surfaces is inevitable in ambient atmospheric conditions,

and could be considered a form of corrosion, as pure metal is lost to form the oxide. As it is the metal oxide that is exposed to the environment, it are those properties which primarily determine a metals resistance to further corrosion. The oxides of aluminium (Al_2O_3) for instance, are particularly resistant to corrosion as they are inert over a large range of pH values and possess very high hardness and barrier passivation properties [51]. Indeed, the crystalline form of aluminium oxide, corundum (ruby and sapphire are forms of corundum containing different trace elements), has a “Mohs hardness” value of 9, making it one of the hardest known materials.

The oxides of magnesium, however, are far less resistant. The MgO oxide film which grows on magnesium surfaces provides adequate protection to magnesium in dry atmospheric conditions[52], however, as has been stated previously, this oxide reacts readily with water in humid or aqueous conditions to form $Mg(OH)_2$ and H_2 [42, 49, 53]. $Mg(OH)_2$. Magnesium hydroxide is soluble in water at pH values below 12 [17, 54-56], leading to a high rate of dissolution in aqueous environments [32, 56-58], making it far less stable than the oxide films formed on aluminium or stainless steel [56, 59].

In addition, carbon dioxide either gaseous or present in solution can also react with magnesium to form hydrated magnesium-carbonate [60]. In aqueous conditions, especially those containing chloride ions [52, 54, 61], these oxides break down. The consequence of this is that untreated magnesium surfaces will corrode readily in almost all outdoor environments, especially marine ones. The rate of corrosion is problematic when considering the use of magnesium as an implant material. As a biodegradable implant material, dissolution of magnesium in vitro is a beneficial property. However, in aqueous saline environments such as that found in the human body, the rate of magnesium degradation is rapid [62, 63]. This leads to the subcutaneous release of hydrogen gas [64] and the potential for alkalization [29, 31, 65], making magnesium unsuitable as an implant material without modification [7, 35].

Despite the common nature of magnesium, there is still ongoing discussion and debate concerning the exact details of the corrosion mechanisms [32, 57, 66]. This has led to detailed investigations into the corrosion reaction of pure magnesium metal into the soluble Mg^{2+} ion by a number of groups [54, 56-58, 67, 68].

The overall reaction of magnesium with water into the product film (Equation 1.1) can be expressed at in the form of three partial reactions, Equations 1.2, and 1.3 are electrochemical, while Equation 1.4 is chemical [57]

$$Mg + 2H_2O \rightarrow Mg(OH)_2 + H_2 \quad (1.1)$$

$$Mg \rightarrow Mg^{2+} + 2e^- \quad (1.2)$$

$$2H_2O + 2e^- \rightarrow H_2 + 2OH^- \quad (1.3)$$

$$Mg^{2+} + 2OH^- \rightarrow Mg(OH)_2 \quad (1.4)$$

There is some controversy in the field surrounding the existence of Mg^+ as another intermediate in this reaction, due to a strange phenomenon termed the "Negative Difference Effect" (NDE) [57] that involves a deviation from the expected amount of hydrogen evolution at the free corrosion potential to what is observed [68]. Song and Atrens, have expanded upon this, proposing a mixed electrochemical/chemical model to explain the negative difference effect, where the anodic partial reaction occurs as:

$$2Mg \rightarrow 2Mg^+ + e^- \quad (1.5)$$

Hydrogen is then again produced through the chemical reaction of Mg^+ with water, producing Mg^{2+}, OH^- and H_2, which then facilitates the reaction of Mg^{2+} and OH^- into $Mg(OH)_2$.

An alternative viewpoint expressed by Thomas et al. [57] is that evidence for the presence of Mg^+ in the reaction system is circumstantial, and propose instead that the NDE is explained through an enhancement of the Cathodic partial reaction.

1.2.1 Corrosion of Magnesium Alloys

One method for reducing corrosion in metals is through alloying. Alloying itself is an ancient process where two or more metals are combined in order to produce a material with more desirable properties than its constituent elements. For example, bronze is an alloy of copper and either tin or arsenic which is far more durable than pure copper, but remains workable [69]. Thus, by alloying magnesium with other, more stable elements is one of the primary methods by which the problem of corrosion can be reduced. Magnesium alloys can be broadly classed into two groups: those containing Aluminium, and those without [65, 70].

Aluminium is the most common alloying element for Magnesium to reduce corrosion [5, 18, 52, 54], with Zinc and Manganese common additives in different quantities depending on the particular properties required. The "AZ" series is the most common due to their low cost, castability, machinability and favourable mechanical properties such as excellent strength: weight ratio [52]. The naming convention of these alloys refers to primary and secondary alloying elements. For example: AZ91, the most commonly used of all magnesium alloys [52] contains 9% aluminium and 1% zinc. The bulk of the alloys consists of a solid solution of

aluminium and zinc in magnesium with the same crystal structure as pure magnesium [71], commonly known as the alpha (α) phase. In addition, a distinct intermetallic compound with a composition of $Mg_{17}Al_{12}$ is formed [56, 65]. This comparatively aluminium rich intermetallic precipitates as a separate and distinct beta (β) phase along grain boundaries of the α phase and acts as a barrier to corrosion [56, 72, 73]. Similar effects have been observed for the alloy AM50 (5% aluminium, >1% manganese), where regions of aluminium enrichment leads to increased corrosion resistance [10]. The mechanism for this reduction was investigated by Danaie et al, who compared areas of high and low corrosion on AM50 surfaces [74]. It was found that in areas with low amounts of corrosion, a thin layer of aluminium rich material was found. While the β phase exhibits good corrosion resistant properties, the ability of it to affect the corrosion resistance of the bulk material depends upon the precise composition and microstructure. If the β phase is non-continuous or not present in sufficient concentration, it could lead to an increase in corrosion through micro-galvanic coupling between the phases [32, 75]. In addition, it has been demonstrated that as the β phase increases, the subsequent depletion of aluminium in the α phase can lead to increased corrosion from the centre of α phase grains [65]. This phenomenon has also been observed after extended aging of magnesium/aluminium alloys [72]. So, while the β phase has positive impact on corrosion resistance, the overall behaviour is highly dependent on its morphology and distribution of phases [18]. Ideally, grains of α phase material should be small, with a large β phase evenly distributed along their boundaries to prevent corrosion spreading between grains. Or, more generally, a finer microstructure leads to more corrosion resistance [19]. This microstructure is controlled primarily by the cooling rate of the alloy [59]; a faster cooling leading to smaller grain sizes and vice versa.

The addition of other elements along with aluminium can also contribute favourable properties. The presence of zinc as either a primary or secondary alloying element has been found to have a positive effect on corrosion performance through the reduction in the negative effects caused by iron, nickel or copper impurities [56]. Manganese shares this useful property by either combining with iron and settling out of the molten alloy during production, or through forming an intermetallic which has no apparent negative effect to corrosion [19]. This makes it another common alloying element [76]. Titanium has also been used as a beneficial alloying element, increasing the resistance of magnesium alloys by modifying the microstructure [77].

The second main group of alloys are those that contain small amounts of zirconium instead of aluminium [65, 70]. Zirconium has been found to be an effective purifier [78] of magnesium, as well as refining the grain size of magnesium, leading to significant

improvements in the corrosion behaviour [65]. Similar to manganese, zirconium reacts with iron impurities in molten magnesium which then settle out due to their increased density, leading to a purer, more corrosion resistant material.

In either kind of magnesium alloy, corrosion resistance is highly dependent on the concentration of impurities, namely: iron, copper, nickel, and cobalt [32, 52, 54, 57]. Of these impurities iron is the most common. The activity of magnesium leads to galvanic coupling between the bulk magnesium and iron particles dramatically reduces the corrosion resistance of both magnesium and its alloys [32, 79]. In alloys containing aluminium, the presence of iron can lead to the formation of the intermetallic $FeAl_3$ at grain boundaries, which also acts as a cathode relative to the bulk magnesium, having an even more pronounced effect on corrosion [19].

A review by Cao et al. found that when the corrosion rates of a range of magnesium alloys were compared from previous literature, none possessed a significant reduction in corrosion compared to high purity magnesium [80]. Alloying is also potentially problematic when considering magnesium as a material for implants. While alloying could reduce the corrosion rate, there are concerns with the biocompatibility of alloying elements or their corrosion products [29].

1.3 **Coatings: A Method for Corrosion Prevention**

The preceding literature has made it clear that the surface oxides of magnesium are unsuitable for the prevention of corrosion. In addition, while alloys have been developed that can reduce corrosion, there is no alloying material that causes a drastic increase corrosion performance, as chromium does for iron in stainless steels [68]. Barrier coatings therefore play a key role in the corrosion protection of magnesium (and indeed all metal surfaces susceptible to corrosion).

Coatings can protect the underlying substrate from corrosion in two ways: by providing a physical barrier between the metal and corrosive substances, or by chemically inhibiting corrosion. A barrier coating must fulfil a number of requirements to provide adequate protection. Firstly, the coating must adhere strongly to the metal surface. Secondly, it should fully cover the entire surface and be free of holes or defects. It is also valuable for films to have a "self-healing" mechanism, especially for applications where physical damage to the coating may occur. Without these features, any protective coating will be ineffective and be easily undermined or removed by corrosive substances.

During the production of metal sheets and foils they are covered with lubricating and

protecting oils. These oils and other contaminants must be removed, lest they decrease adhesion of the coatings to the metal surface in order to fulfil the first condition outlined above. Mechanical and wet chemical methods (often involving organic solvents) are the most common, although modern technology in the form of vacuum based plasma processes is becoming more accessible [81].

Paint is probably the most common coating applied to metal surfaces. In addition to modifying the metal's appearance, paint provides a simple physical barrier to the environment. In order to improve performance, other anti-corrosive coatings are used in conjunction with paint, in order to inhibit corrosion chemically or as adhesion promoters between the metal surface and paint layer [51]. Of these anti-corrosive coatings, those based on chromates are historically the most common [2].

1.3.1 Chromate conversion coatings

Methods for producing chromate films on aluminium alloys were developed in the early 20th century. Since then, chromates (the oxides of chromium) have been used as an effective treatment for the corrosion protection of metals and alloys alike, including those of iron, aluminium, copper, magnesium and zinc. Chromate coatings protect metals in two main ways. Firstly, they provide a physical film, which protects against the environment. Secondly chromium ions present in the films are able to leach to areas that have been damaged, leading to a ‘self-healing’ film [82].

Chromate conversion usually takes the form of a chromic acid ($HCrO_4$) treatment. The chromic acid reacts with and dissolves the metal surface, causing the precipitation of a $Cr(OH)_3$ layer, hence the common term ‘conversion coating’.

Hexavalent chromium ions (Cr^{6+}) ions are dispersed throughout the surface film [83] and are able to migrate and further react with uncoated areas of the metal surface, providing the self-healing properties previously mentioned. This behaviour is limited however, with an investigation by Hughes et al. finding only small concentrations of Cr^{6+} on the external surface of the coating [84].

Unfortunately, the Cr^{6+} ion is geno-toxic and a known carcinogen. Continual exposure has been shown to increase the likelihood of lung cancer in particular [85, 86]. Chromium accumulation in the environment and its long term effects are also of concern [51]. This has led to regulation and increased costs involved with the use of chromates. As a consequence, research into a safer and more environmentally friendly method of corrosion protection has become more common. A wide range of other coatings have been investigated. A review by

Gray and Luan lists many examples including: electrochemical plating, other chemical conversion processes, anodizing, gas phase depositions and organic coatings [7]. Each of these types of coatings possess both advantages and disadvantages, and are a broad field of research in and of themselves.

1.3.2 Organosilane Coatings:

One of the most promising alternatives to chromates is the group of silicon-based compounds known as organosilanes [87]. Silanes often have enhanced properties such as thermal endurance, moisture and chemical resistance, mechanical strength or electrical performance when compared to purely organic materials [82].

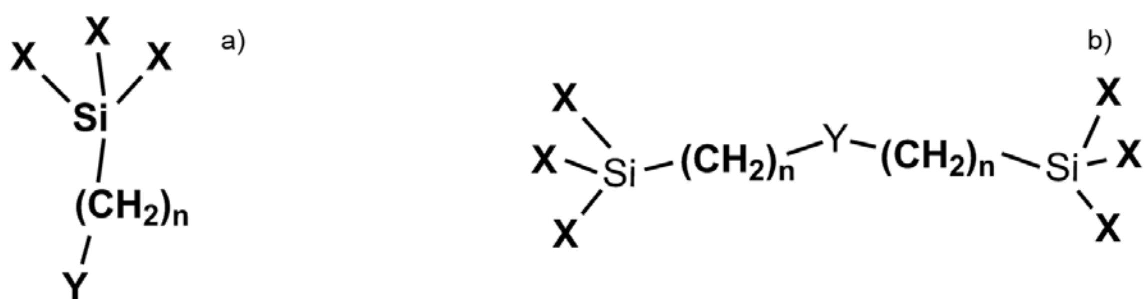

Figure 1.1: a) General structure of mono-silanes b) General structure of bis-silanes

Silane molecules of the form $X_3Si(CH_2)_nY$ (Figure 1.1 a)) are known as "monosilanes". This class of chemicals was first explored by Plueddemann as coupling agents for reinforcing glass fibres in 1962. Since then, they have gained acceptance and use in industry as both adhesion promoters between dissimilar materials and as surface treatments for passivation of metals [88]. Another form of organosilane that are becoming more commonly studied are "bis-silanes" of the form: $X_3Si(CH_2)_nYSi(CH_2)nX_3$ as shown in Figure 1.1 b).

Both varieties of organosilane share a similar structure. The group designated “X” represents a hydrolysable group. This usually takes the form of either a methoxy- or ethoxy- group. Their presence limits cross linking between organosilane molecules in solution, providing stability of the chemical in the liquid state. The “Y” group in the example structures represents a functional group. Organosilanes can possess a wide range of functionality which can be tailored to suit particular applications. Groups such as: epoxy, vinyl, halide or amines are especially common. It should be noted that functionality is not a requirement of organosilane molecules, and organosilanes that possess a simple hydrocarbon chain are not uncommon.

As adhesion to metal surfaces is of paramount importance to providing an effective barrier to

corrosion, the mechanisms by which organosilanes bond to metal surfaces must be well understood. A potential bonding mechanism was postulated by Plueddemann in his text: *Silane Coupling Agents* [88]. For a chemical bond to be formed between a typical organosilane molecule and a metal surface, both the organosilane must be hydrolysed, and the surface must possess hydroxyl groups. Either acidic or basic conditions may be used to catalyse the hydrolysis of organosilanes, with neutral pH conditions undergoing the slowest rate of hydrolyzation with a change of pH by one in either direction providing 10 times the hydrolysis rate [89]. A condensation reaction may then take place between the hydroxyl groups of the organosilane and the surface. This reaction is also pH dependant, with a pH of approximately 4 providing the slowest rate of condensation. Thus in a basic organosilane solution, the rates of both hydrolysis and condensation will be rapid, promoting gelation of the organosilane solution. If a low pH is chosen, the hydrolysis rate will remain rapid, but with a low rate of condensation, providing a more stable solution [90]. In an acid catalysed environment, hydrogen bonds are formed as an intermediary step prior to condensation. Over time, a highly cross-linked siloxane (Si-O-Si) network should be formed on the surface, which is thermally stable and strongly bound to the metal surface, with properties dependant on any functional group possessed by the original organosilane [91].

Since the proposal of this bonding mechanism a large amount of research has been dedicated to confirm it experimentally. Due to the thin nature of deposited organosilane films, surface sensitive analysis techniques have been heavily utilized. Methods such as X-ray photoelectron spectroscopy (XPS) [92, 93] and Secondary Ion Mass Spectrometry (SIMS) [93, 94] are able to provide unique information about the structure and composition of deposited organosilane coatings, allowing previously theoretical bonding information to be investigated experimentally.

Studies such as one by Fang et al. [93] investigated organosilane coatings on aluminium using both XPS and SIMS in an attempt to find evidence of metal-siloxane bonding. A fragment of mass 71(AMU) was identified as Al-O-Si. In 2000 however, Abel et al. [94] put these results into question, as there are several fragments of a similar mass to that previously identified as Al-O-Si that could have led to an erroneous assignment. In their study, Abel et al. performed SIMS using a time of flight analyser which possesses much higher mass resolution to that of the quadrupole analyser used in previous studies. From their results, it was found that the SIMS peak at 71AMU, seen in Figure 1.2, is actually a peak comprised of several different components. One of these components was attributable to an Al-O-Si structure, providing strong evidence for a bond between the silane molecules and the metal surface occurring. Furthermore, a slightly larger mass fragment with a mass of

85AMU was found and assigned to Al-O-Si=CH2, making it far less likely that the peak observed at 71AMU is due to either contamination or fragments of the organosilane molecule itself [95, 96].

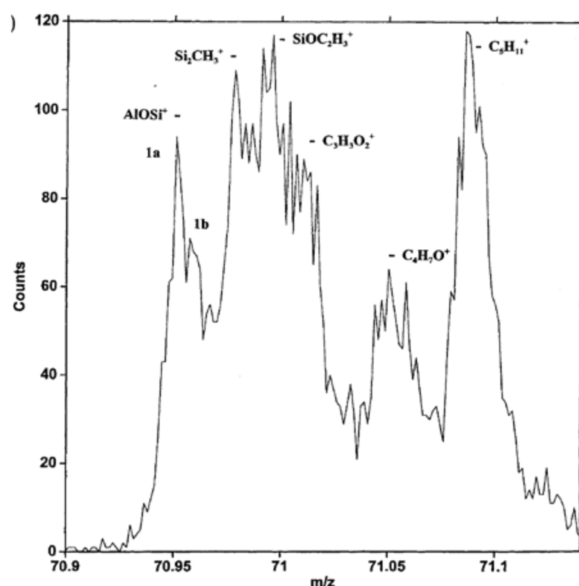

Figure 1.2 High resolution ToF-SIMS spectrum of aluminium coated with GPS. Peaks are labelled according to best fitting mass fragments. Reproduced from Abel et al. [94]

While experimental confirmation of the existence of a metal-siloxane linkage is valuable, the exact mechanism of the bond formation is equally important. During one such study in 1997, Quinton et al. aimed to investigate the initial adsorption kinetics of a model organosilane (Propyltrimethoxysilane (PTMS)) onto aluminium and iron oxide surfaces using XPS [97]. It was found that on aluminium oxide surfaces, after an initial increase in surface organosilane concentration, there was significant sharp decrease in concentration followed by another smooth increase to an equilibrium coverage. This oscillation in the adsorption isotherm implied a far more complicated bonding system than previously expected. It was initially hypothesised that this oscillation was caused by the presence of secondary surface species, leading to a series of in depth investigations [98-101]. A SIMS study comparing the surface structure at different points on the adsorption isotherm supported the existence of two distinct surface species involved with the adsorption of PTMS [99]. Oscillations were also observed on a range of different (industrial) metals: iron, zinc and chromium. The rate at which the PTMS layer reached its initial ‘maximum’ coverage was found to be a function of several variables, including solution pH, concentration and each metal oxides’ iso-electric point. Metals with a higher IEP (aluminium and zinc) were found to have a slower initial uptake compared to those with a lower IEP (chromium and iron) [101].

A mathematical model of this behaviour was constructed in order to describe the physical

phenomenon occurring during film growth [102, 103]. This model, seen diagrammatically in Figure 1.3, consists of a three component system including: individual hydrolysed PTMS molecules (squares, θ_1), water molecules (triangles, θ_2) and larger PTMS oligomers (hexagons, θ_3). Initially, PTMS molecules adsorb and bond to the metal surface as through the condensation reaction described by Plueddemann. As other PTMS molecules bond either to adjacent areas of the surface or to one of the other available silanol groups on the molecule, water is produced. As the condensation reaction that produces the initial metal-siloxane linkage is reversible, this can result in the removal of PTMS from the surface, causing the observed oscillation. Finally, larger oligomeric PTMS species bond to the surface permanently (or with increased stability). This behaviour is represented by the sum of the theoretical uptake curves of θ_1 and θ_3, which agrees well with experimental data.

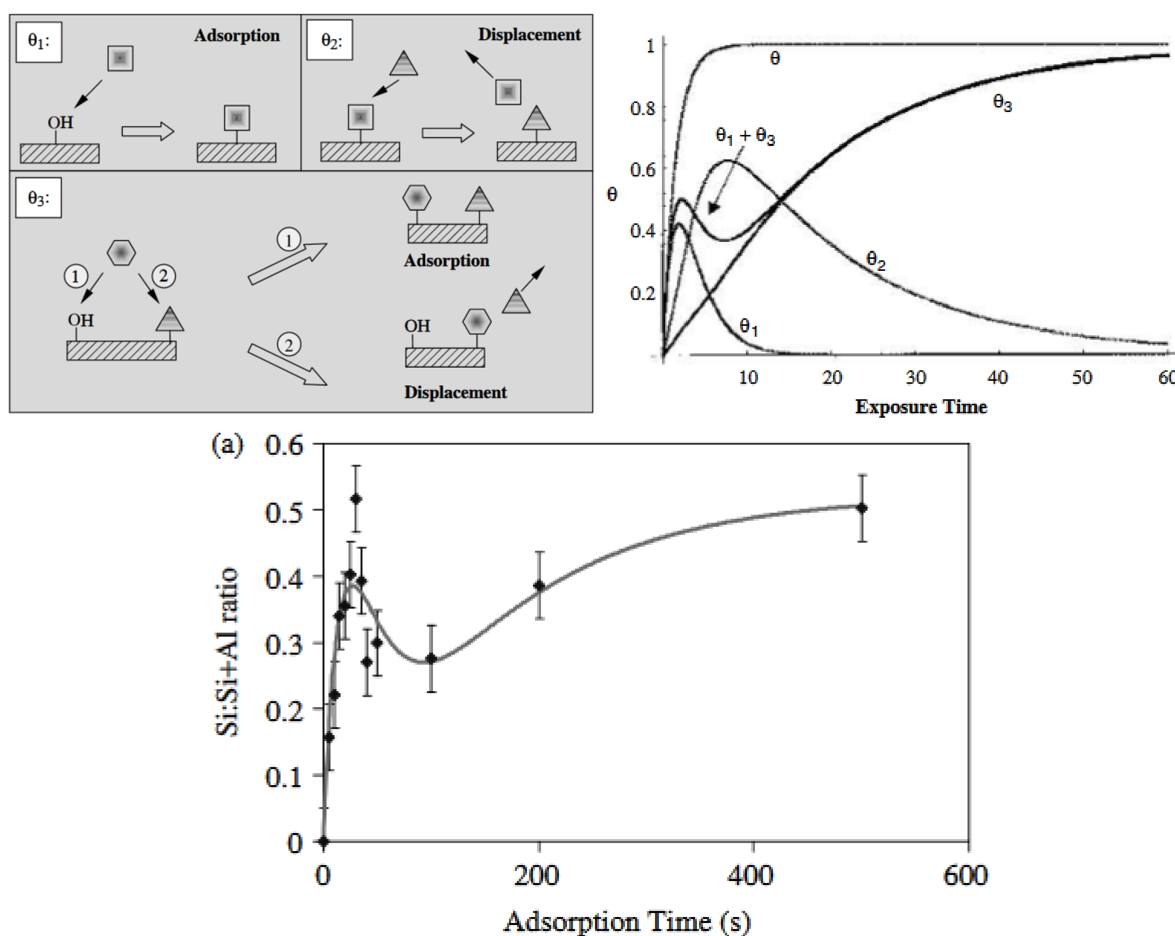

Figure 1.3: a) Illustration of the three species which are present in the model for oscillatory uptake of organosilanes. b) Theoretical uptake curves for each individual species; ($\theta_{1,2,3}$), the sum of all three; θ, and the curve that best fits experimental data; θ_1+θ_3. c) Experimentally obtained uptake curve of 0.75% pH 3 PTMS solution onto aluminium substrates. Reproduced from Quinton et al. [103]

The oscillatory uptake phenomenon has subsequently been observed for a range of different organosilanes including: aminopropyl-triethoxysilane (APS) [104-106], glycidoxypropyl-

trimethoxysilane (GSP) [107], octyl-trichlorosilane (OS) [108] and octadecyl-trimethoxysilane (ODTMS) [109].

APS has also been found to demonstrate additional anomalous behaviour when attached to metal surfaces. Rather than bonding purely through siloxane linkages, the molecule attaches to the surface through a protonation of the amine functional group, leading to weaker attachment to the metal surface. Bonding through protonation of the amine group has been demonstrated on a range of surfaces including: tin [110], aluminium [111], steel [112] and glass [113]. This effect was observed, along with oscillatory uptake by Quinton et al. [104], where it was also demonstrated that the orientation of the APS molecule on aluminium surfaces varied along with the oscillation in uptake

In 1984, it was established by Boerio and Dillingham that the pH of the APS solution had a pronounced effect on the properties of the resultant films. In addition, this effect was different for iron and titanium [114]. This led to a comprehensive investigation by Horner et al. in 1992 that compared the attachment of APS to a wide range of substrates [115]. It was found that attachment of APS through a protonated amine group occurred readily on silicon, aluminium and titanium, moderately in iron chromium and nickel, and to a lesser extent on magnesium, which correlates well to the isoelectric points of their oxides.

Increased protonation of amine groups has been linked to decreased corrosion protection performance. A study by Subramanian et al. in 1998 [116] examined the effect of this protonation by comparing APS films with the non-functional bis-silane “bis-triethoxysilyl-ethane” (BTSE) on iron. It was shown that BTSE films alone performed much better as an anticorrosive than APS. This difference in performance was postulated to be due to a higher concentration of Fe-O-Si bonds formed by BTSE films than APS, measured through the use of XPS and Infra-Red spectroscopy.

Susac et al. performed another study comparing the attachment of APS and BTSE on aluminium alloy surfaces. In that investigation it was found that on freshly polished surfaces the film formed by BTSE was irregular compared to APS films, which were complete and of even thickness. The discrepancy between the two was thought to be caused by the lack of available attachment sites for siloxane bonds to form. Hence, the ability for APS to bind to the surface via protonation of the amine allows a film to be formed, irrespective of the available siloxane attachment sites. When metal samples were allowed to oxidise in air before coating, BTSE formed a more complete film [117]. A range of other investigations have demonstrated the advantage of pre-treatments in order to produce a surface which encourages the formation of metal-siloxane bonding [118-121]. Additionally, organosilanes can be deposited in a multi-step process, as performed in a study by Song and Van Ooij

[122], where films of BTSE and APS were investigated as an anticorrosive film. In their study, BTSE was used as a dense, hydrophobic layer that was well adhered to the surface through metal siloxane bonds, and APS was deposited as an outer coating that was able to bind to multiple kinds of paints without the detrimental effects on adhesion that occur when APS binds to the surface via protonation of the amine group. Thus this coating regime was able to provide corrosion protection equivalent to chromate conversion coatings. This method of coating was also adopted by Liu et al.[123] for the purpose of corrosion protection of magnesium alloy implants. BTSE was used as an undercoat to provide a stable foundation for the deposition of an APS film. APS was chosen here, for its ability to bind to other molecules, in this case the anti-coagulant “heparin”. The addition of heparin led to a decrease in the attachment of blood platelet cells to the implant which have previously been shown to cause thrombus formation and consequent failure of implants [124]. These studies show that for a given application, it is important to select an organosilane with the appropriate functionality.

How films are treated post deposition is equally as important for film stability. In order for organosilane films to be the most effective, it has been found that curing of the films at an elevated temperature is important. Curing of the films by heating for an extended period allows free silanol (Si-O-H) groups to condense into Si-O-Si linkages, resulting in a denser, more highly cross-linked, and therefore more effective barrier film [125]. However, the condensation reaction that produces these siloxane bonds is reversible [82, 88]. An additional benefit of curing then, is that it expedites the removal of water in the film, leading to increased long term stability [126]. A review conducted by Van Ooij et al. has shown that a range of temperatures and curing times for several different organosilanes have been investigated [82]. Some organosilanes, such as BTSE, have been found to require a higher temperature for complete curing [126] compared to APS [127].

1.4 **Plasma Polymerization**

While wet chemical methods are by far the most common and well-studied for the deposition of organosilane films, there are associated drawbacks. Many organosilanes are insoluble in water and require the use of organic solvents, an undesirable property on the industrial scale [128]. There are water based organosilanes that have been shown to have promising properties for corrosion protection. Unfortunately, they are also unstable in solution, and hydrolyse rapidly to form large oligomers in solution, reducing the amount of available sites for binding to the surface and therefore adhesion [82, 129].

There are, however, a range of alternative methods of deposition. Vacuum based methods

such as physical vapour deposition and chemical vapour deposition (PVD and CVD respectively) have been used since the mid-20th century [130]. Both methods have associated challenges. PVD techniques, which involve the deposition of a film from a vaporised solid precursor (such as sputter deposition, thermal evaporation and electron beam deposition) usually have relatively low deposition rates and require high quality precursor material. CVD processes use a volatile precursor, which reacts or decomposes from the gas phase onto a substrate. The energy for reaction comes from either heating the entire system or through having a heated substrate. The high temperature requirements are the main disadvantage to this process; thus Plasma Enhanced Chemical Vapour Deposition (PECVD) was developed. The same volatile precursors are used, but are first excited into a reactive plasma state, reducing the requirements for high temperatures. The act of creating plasma is not trivial, and requires a thorough understanding of the physical phenomenon involved.

1.4.1 Plasma

The term plasma was originally coined by Langmuir in 1928 [131], in describing the oscillations within ionized gases. More generally, plasma is often referred to as the fourth state of matter, although one not commonly understood or thought of. On a cosmic scale, plasma is the commonest of all states of matter, comprising almost the entirety of the known universe, in forms ranging from dense stellar material present in every star, to low density plasma found in luminous nebulae and interstellar clouds. Terrestrially, our interactions with plasma are less obvious, although not as rare as might be imagined, with examples seen in both the natural world as well as the synthetic. Natural examples of plasma include lightning strikes, and the polar aurora, while human fabricated plasma are used in fluorescent lighting and the aptly named “plasma” screen display.

A layman definition of plasma, commonly used to explaining the concept is that a plasma is a partially or fully ionised gas. This definition, while overly simplistic, is a good place to begin an explanation of what a plasma truly is. Any gas in thermal equilibrium, will contain a distribution of ionised and neutral species depending upon the temperature and the ionisation potentials of the species present. This degree of ionisation is given by the Saha equation [132] (Equation 1.6), where n_n and n_i are the density (number per m^3) of ionized and neutral atoms respectively; U_i is the ionization potential of gas (the energy required to remove the outermost electron of a molecule of the gas), and T is the temperature of the gas.

$$\frac{n_i}{n_n} \approx 2.4x10^{21} \frac{T^{3/2}}{n_i} e^{-U_i/k_B T} \qquad (1.6)$$

To put this in physical terms, the atoms of an ideal gas possess a distribution of energies given by the Maxwell-Boltzmann distribution. An atom in such a state (ignoring external electromagnetic influence) can only be ionised when it has a collision with enough thermal energy to result in the removal of an electron. For a 'cold' gas, such as air at room temperature, this occurrence is very rare with the result from the Saha equation giving a ratio of ionised to neutral atoms as approximately 1×10^{-122}. As the temperature is increased, the amount of ionization remains very low, due to the dependence on the exponential of the ratio of ionization potential to the gas temperature. When these two quantities are of a similar order of magnitude, the density ratio rises rapidly, putting the gas into a plasma state (until fully ionized). It should also be noted that as the amount of ionization increases, so does the probability of an ion encountering an electron and thus neutralizing.

Despite the incredibly small number for the ionization ratio at room temperature, it is non zero, implying some small degree of ionization in all gases at room temperature. As not all gases are plasma, taking ionisation as the sole definition is inadequate, and a more explicit definition is needed. In his original description of the phenomenon, Langmuir wrote: “The ionized gas contains ions and electrons in about equal numbers so that the resultant space charge is very small. The name plasma is used to describe this region containing balanced charges of ions and electrons”. In his textbook *Introduction to Plasma Physics and Controlled Fusion*, Chen simplifies where he describes plasma as “A quasineutral gas of charged and neutral particles which exhibits collective behaviour.” [132]. The term ‘quasineutral’ is not one often encountered, but useful as a way of describing plasma as a whole. On a large (relative to the size of the plasma) scale, the plasma appears neutral (all positive and negative charges cancel out). If, however, you view the plasma on smaller scales, then behaviour associated with the coulomb potential of individual charge carriers (ions and electrons) are observable and the plasma is no longer considered neutral. The length that this transition occurs over is known as the Debye length, and is mathematically defined as:

$$\lambda_D = \left[\frac{k_B T_e}{4\pi e^2 n_e}\right]^{1/2} \qquad (1.7\ )[133]$$

Where T_e is ‘equivalent’ electron temperature, 'e' is elementary charge, and n_e is electron density.

An alternative perspective on the physical interpretation of the Debye length is to think if it as an effective "shielding distance". As electrons are more mobile than the larger positive ions (which are at least the size of a proton), they are more able to respond to fluctuations in

positive charge concentrations, and effectively screen them from observation. If the scale of a plasma system is shorter than the Debye length, then the electrons are not able to move far enough and any surplus charges are detectable. This leads to a condition for a plasma to be considered as such: the density of charged species must be sufficient so that the Debye length is less than the dimensions of the plasma as a whole [133].

The fact that the majority of species in a plasma are charged gives rise to the 'collective behaviour' described in Chen's definition. In a gas, each molecule has no net electrostatic charge and thus in the absence of external stimuli, experiences no net force (ignoring the minuscule effect of gravity) other than those involved in any collisions it experiences. These collisions are thus what dominates its motion. Recalling that individual particles within a plasma are charged, through their motion they generate electromagnetic fields, thus exerting influence over the movement of other particles without necessarily colliding in the Newtonian sense. The sum of these fields, and thus the plasma as an entity, will determine the behaviour of any particle within the plasma in addition to external stimuli.

There are a range of ways to satisfy these conditions and produce a plasma. While it is possible to increase the temperature of a gas until enough ionised species exist, the temperature needed is impractical in a lab-based setting. Other, more common, methods for producing useful laboratory-based plasma usually involve the use of strong electric fields and high vacuum, usually in a steel chamber with conductive, earthed walls. Applying a strong electromagnetic field to such a system results in any free electrons being accelerated to a high enough velocity to produce further ionisation, eventually resulting in a sustained plasma (as long as energy is continually applied). By varying the magnitude of the energy supplied, the amount of ionisation can also be varied. In such a system, the total amount of ionisation is usually below 1%, and considered a 'cold' plasma [134]. The use of the term cold arises from the fact that the ion temperature is usually quite close to room temperature, however, the electron velocity and temperature (several thousand degrees Kelvin [135]) is much greater due to the mass difference between ions and electrons [136].

To produce such a plasma, there is a choice between using a "DC" or "AC" voltage. DC plasma is often used for the purpose of sputter coating and in glow discharge tubes. Two electrodes are used, and a high voltage on the order of kV applied, often with the sample stage as one of the electrodes. The static electric field means that the plasma is highly directional, with ions attracted to the cathode, and electrons to the anode. This is precisely why this method of plasma production is used in sputter coaters – positive noble gas ions are attracted to an cathodic target. As sputtering is usually a result regardless of the application, then contamination from sputtered material is a significant drawback to DC

plasma.

Using AC electric fields results in a non-directional plasma (though directionality can be imparted through the use of a bias voltage or magnetrons). The frequency of oscillation used can vary wildly, but the most common is probably 13.56MHz, in a short wave radio (RF) band assigned to scientific purposes. The antennae used to produce the RF signal can be constructed in a range of geometries and can be either internal or external. Internal antenna are in direct contact with the plasma source gas, and therefore require less input power to produce a plasma. However, interactions between plasma species and the antenna are possible, so in circumstances where this may be problematic external antenna are used. External antenna are usually isolated from the plasma by a quartz or glass dielectric window, and because of this the energy required to sustain the plasma is usually higher.

An advantage of RF plasma generation over DC, is the decoupling of the plasma source from sample. As the sample stage in an RF chamber is not intrinsically linked to the plasma generation (as in most DC chambers), a positive or negative electrical bias can be applied. This gives a measure of control over the species that are able to interact with the sample without necessarily influencing the species in the plasma itself.

1.4.2 Plasma Polymerized Organosilanes

Despite being far less common as a coating mechanism plasma polymerisation (distinct from conventional polymerization) has been studied in various fields, including corrosion protection, for many years. The comparative rarity of plasma techniques is likely due to the use of expensive and hard to maintain vacuum equipment. While other methods for producing plasma are available, the most common method of plasma deposition requires a vacuum chamber capable of pressures less than 0.1Pa [137], along with an associated way of introducing an organic vapour and igniting it into a plasma. The technical aspects and difficulties associated with such a setup will be discussed in Section 4.1

Early studies of the technique by one of its pioneers: Yasuda et al. [138, 139], used a simple glow discharge plasma to investigate the reactive nature of species in the plasma state compared to the feed gas when forming plasma polymerised films. In 1984, Yasuda found that plasma polymers can be formed on a surface in an ultrathin layer which is strongly bonded to a wide range of substrates and possess characteristics more like inorganic materials than purely polymeric ones, making them good protective coatings [140]. The inorganic nature of the plasma films grown in this way seems to depend on the ratio: $\frac{W}{FM}$ where W is the plasma discharge power, F is the flow rate of the monomer and M is its

molecular weight.

There is a wide range of precursor molecules that can be used to produce thin films via plasma depositions. To produce silicon containing films, the gas silane (SiH_4) can be used as a plasma precursor. By mixing silane with oxidisers such as oxygen and NO_2 silica films can be created. Silane is a highly flammable gas (it may auto ignite at temperatures below 54°C), as well as toxic [141, 142], so is not often used. Trimethylsilane (TMS) is a safer precursor, used by Yasuda in a collaboration with Van Ooij to deposit organosilane films onto steel for the purposes of corrosion protection [143-146]. In these investigations, the composition of the plasma mixture was varied by the addition of oxygen, argon and hydrogen. Overall, the plasma deposited films were found to have a positive impact on corrosion protection, when compared to uncoated metal. Plasma composition was, however, found to have a pronounced effect on performance. Most notably, films deposited from a mixture of oxygen and were much thinner (15-25nm compared to 60-100nm), more inorganic, and exhibited poorer corrosion protection compared to the other films. These results initially appear contradictory to those presented previously for chemically deposited organosilane anti-corrosion films, where a well formed oxide layer was advantageous from the perspective of film attachment. However, there is a significant difference between the two deposition mechanisms. In the previous case, oxygen was used to produce a surface that would facilitate bonding to chemical solutions whereas, in the plasma investigations, the oxygen is mixed with the TMS precursor to react with carbon present in that molecule. This is due to the fact that TMS is a very different material to the organosilanes seen in those studies. Instead of an oxidised silicon ‘core’, it consists of only Si-C bonds, and thus creates a film that is ‘alkoxysilane’ in nature, rather than ‘siloxane’ [145, 146].

Plasma films deposited from oxygen containing organosilanes have also been investigated. Some of the earliest films of this nature are produced from the organosilane hexamethyldisiloxane (HMDSO), which features an oxygen linkage between two silicon atoms, making it one of the simplest examples of a bis-organosilane. HMDSO films are commonly used in industry, and have applications in several fields, such as barrier films on food and pharmaceuticals, as well as a component in “spray on bandages” [147]. They have also been investigated for the purposes of corrosion protection, including on magnesium as a potential biological implant material [35]. Angelini et al. [8, 148] have deposited HMDSO films onto both steel and magnesium alloy surfaces, with oxygen used as both a pre-treatment and in the deposition mixture. Oxygen pre-treatments were (in contrast to previous studies on TMS) found to have an advantageous effect on film adherence, while films formed from a mixture of HSDMSO and oxygen were inorganic in nature and increased the

corrosion resistance of coated substrates.

The structure of films deposited from mixtures of HMDSO and other gases have been further investigated by several groups. Ko et al. [35] deposited HMDSO films through a low temperature RF discharge plasma onto pure magnesium for the explicit purpose of corrosion protection of implant materials. XPS was used to determine the composition of these films and how they were affected by applied plasma power. The oxygen/carbon/silicon ratios were observed not to vary significantly for plasma powers between 30W and 100W however, the thickness of the deposited films increased with power. This directly translated to performance in corrosion tests in a 'physiological saline solution' with powers above 50W performing the best, with a significant reduction in magnesium corrosion. Further in-depth investigations of HMDSO films by XPS have also been performed by Alexander et al. [149, 150], who measured how both the film composition and chemical bonding environment of silicon changed with the addition of oxygen to the plasma mixture. In general, it was found that plasma created from a pure HMDSO monomer resulted in a film that is chemically similar to the monomer, while by increasing the amount of O_2 within the plasma mixture, the properties of the film are converted to something more silica-like, likely due to the ability of oxygen to react with carbon present in the monomer to a gaseous species which is able to be pumped from the reaction vessel. Through analysis of the Si2*p* photoelectron peak, with high resolution XPS, the bonding environment of silicon could be determined and related to known compounds. Films deposited from pure HMDSO vapour were rich in $Si(-O)_2$ (silicon bonded to two oxygen atoms, such as in PDMS), compared to films deposited from the gas mixture containing the highest proportion of oxygen which had 51% of silicon atoms bonded to four oxygen ($Si(-O)_4$), and a further 36% attached to three ($Si(-O)_3$).

Thus far, all of the organosilicon films deposited using plasma have been created from relatively simple monomers. It is possible however, to use more complex organosilane molecules to form films from plasma deposition. A series of studies by Batan et al. [151, 152] compared organosilane films of BTSE deposited by wet chemistry and two separate plasma methods. The primary difference between the two plasma chambers compared were their operating pressures. One creates plasma at (or near) atmospheric pressure and the other operates at vacuum. XPS analysis supported by infra-red spectroscopy showed that the films deposited from atmospheric plasma were primarily inorganic in nature, with increased concentrations of silicon and oxygen. This is in comparison to the films deposited through other methods, which were more organic in character. Secondary Ion Mass Spectrometry (SIMS) was also used to examine the interface between the aluminium substrates and the plasma deposited films. Both were found to attach to the surface through an interfacial layer

of metal-siloxane bonds, similar to those found in films deposited by wet chemical methods. The adherence of the films was investigated through exposure to an ultrasonic water bath and while there was a decrease in silicon concentration, for the most part, the films were strongly attached to the metal surfaces.

Knowing that it is possible to plasma deposit films from a complex bis-organosilane, it follows that functionalized organosilanes can also be deposited in this way. In practice, this is not trivial. The plasma environment is reactive, with many competing processes, including the fragmentation of the monomer and etching of the surface by charged high energy species [153]. Despite these challenges, several groups have successfully used plasma methods to deposit amine containing organosilane films from an APS precursor and retained functionalisation. [154, 155]. Similarly, Cech et al. have deposited films from vinyltriethoxysliane, with IR spectroscopy used to confirm that the vinyl group was present and undamaged by the plasma treatment [156].

1.4.3 Challenges associated with plasma deposition

Compared to chemical deposition, there are some significant advantages to plasma deposition of thin films: solvents are not needed, and cleaning, pre-treatment and deposition can take place in the same clean, vacuum environment. However, the process of creating plasma is complex, which leads to a wide range of variables that must be considered. Some variables, such as plasma frequency, applied power, precursor gas pressure and duration of exposure are easy to manipulate experimentally. Others are inherent to the chamber used and are less immediately obvious. Plasma deposition is known to be highly system dependant, which can lead to discrepancies between films deposited from different chambers at seemingly similar conditions [157, 158]. The method of plasma generation [143, 144], and geometry of the chamber itself (including the location of the power source) will have an effect on the species present. Consequently, the location of the sample surface within the chamber is vitally important as the film formed will be dependent on the density and composition of the plasma at the sample surface [156-158].

While it is often reported that plasma processes are substrate independent, it is known that there are interactions between gas phase species and the surface of the substrate [137, 157, 159]. Indeed, if there were no interaction, then any chemical bonding between plasma species and the surface would be difficult. Recent investigations into the influence of the substrate chemistry and morphology have demonstrated that the initial growth of the film is highly substrate dependent [160-162].

1.5 **Aims of this Research**

Thus far, this chapter has established the need for corrosion protection of metal surfaces, particularly magnesium due to its high reactivity. Organosilanes coating have been identified as having the potential to replace chromate conversion as an environmentally benign anti-corrosive treatment. A significant proportion of the prior research conducted into the use of organosilanes has been conducted using aluminium or steel substrates. Magnesium however, has seen comparatively little, and the majority of that which does exist is performed on alloys. In order to develop effective anti-corrosion treatments for magnesium, it is necessary to understand how it interacts with organosilanes on a fundamental level.

The investigations presented here, therefore use pure magnesium, rather than an alloy, as a substrate. Similarly, the organosilane selected is "propyltrimethoxysilane" (PTMS), which possesses only an inert propyl- functional group, making it a good model for other industrially relevant organosilanes such as APS. However, as it does not possess the same functionality, it is not appropriate to examine the effectiveness of PTMS for any applications that other, functional, organosilanes may have such as corrosion protection.

Plasma-based deposition methods are an exciting, modern alternative to traditional wet chemical processes. Plasma enhanced chemical vapour deposition has several advantages, notably that film formation takes place in a clean, vacuum environment, without the need for solvents (including water). This is an important consideration, as water is able to reverse the siloxane bond, so performing deposition in a dry vacuum negates the necessity for any post deposition curing step. Thus far, to our knowledge, the investigation of PTMS as a precursor for such methods of film deposition has not been reported, so it is unknown what composition or structure any resultant films will have.

The purpose of this dissertation is to therefore increase understanding of the process of PTMS film formation on magnesium, with the following primary research aims:

I. *To determine if the organosilane PTMS undergoes oscillatory uptake onto pure magnesium, conforming to the model created by Quinton et al. [98-101]?*
II. *Can plasma-based methods be used to deposit organosilane films onto magnesium from PTMS, and how do these films compare to those deposited chemically?*
III. *To investigate the effects of experimental plasma parameters on the composition and structure of plasma polymerized PTMS films.*
IV. *To investigate the possibility of functionalising plasma polymerized PTMS films in-situ through the addition of other gases to the plasma environment.*

In all aspects of this work, surface sensitive analysis techniques will be used in order to determine the composition and structure of deposited organosilane films. Primary amongst these techniques are two forms of electron spectroscopy: X-Ray Photoelectron Spectroscopy (XPS) and Scanning Auger Spectromicroscopy. Scanning Auger Spectromicroscopy is complimentary to this, in that it can determine surface elemental composition with high spatial resolution.

2 CHAPTER 2: EXPERIMENTAL

2.1 Selection of Analytical Techniques

In answering the research aims, the appropriate selection of analytical techniques to be used is of great importance, with consideration given to the nature of the information required and equipment availability. The most important information to be obtained for this research is both the elemental composition of the deposited films, and their morphology (how that composition is distributed across the surface), however topological and chemical bonding information can also provide vital information about the structure of deposited films.

X-ray photoelectron spectroscopy (XPS) is one of the most useful surface analysis techniques, and is commonly used for thin film analysis (as evidenced in the preceding literature review). XPS is able to accurately determine average surface composition in addition to providing valuable information about the bonding environments of surface species present. However, a limitation of XPS is that it does not give any information about the morphology of the surface. Therefore, complementary electron spectroscopy and microscopy techniques are also utilized.

Of these, Secondary Electron Microscopy (SEM) is possibly the most common. SEM is able to produce high resolution images by scanning a focussed electron beam across surfaces and hence information about its microstructure. However, this provides only limited compositional information and as such it is coupled here, with Scanning Auger Spectromicroscopy, a fusion of Auger Electron Spectroscopy and Scanning Auger Microscopy that is able to provide information about not only the elemental composition, but also morphology of deposited films.

These techniques will constitute the bulk of the analysis to be performed and are surface sensitive - an important consideration when the deposited films are likely to be on the order of nanometres in thickness. In addition, they are supported by the use of Atomic Force Microscopy (AFM) and Fourier Transform Infra-Red (FTIR) spectroscopy. AFM is a microscopic technique which uses a sharp tip to scan across a surface in order to accurately determine the topography of a surface, while FTIR spectroscopy is able to provide information about the chemical bonds present.

The subsequent chapter will provide a fundamental introduction to these techniques, the technical details of measurements performed and the interpretation of the data acquired from each.

2.2 Electron Spectromicroscopy

In general, electron spectroscopy is a method for determining the electronic structure of a surface by measuring the kinetic energy of electrons emitted upon exposure to radiation. Electron microscopy is the method of determining the physical structure of objects using electrons as a source of radiation (in contrast to conventional microscopy which uses light). Both of these sets of techniques are invaluable to the field of surface science and characterization. The primary analysis techniques used throughout this work are forms of electron spectroscopy and microscopy. In particular, X-ray photoelectron (XPS) and Auger Electron (AES) Spectroscopies; and Secondary Electron (SEM) and Scanning Auger Microscopies (SAM). The physical processes involved in these techniques are very similar, and in the case of AES and SAM, the two techniques are performed within a single vacuum system. For simplicity, the term 'spectromicroscopy' will be used to refer to the collective application of the techniques where appropriate.

2.2.1 History of XPS and AES

The two main spectroscopic techniques used in this work are X-ray Photoelectron Spectroscopy and Auger Electron Spectroscopy. These two techniques were developed independently of each other in the 20th century and provide complementary information about surface composition and electronic structure. The basis of XPS is the photoelectric effect, which is the process by which electrons are emitted from a surface upon exposure to light of sufficient energy. This phenomenon was discovered in 1887 by Heinrich Hertz and the attempts to describe the observed behaviour culminated in 1905, with an explanation by Albert Einstein, using the description of light as discrete particles which he called 'quanta', but became later known as photons. For this, he was awarded the 1921 Nobel Prize in Physics. The development of the phenomenon into an experimental technique for surface elemental analysis was first accomplished by Kai Siegbahn and his group at Uppsala University in 1954. Due to the importance of this work, he was awarded the Nobel Prize in Physics in 1981. He named the technique Electron Spectroscopy for Chemical Analysis (ESCA), a term that was and may be used interchangeably with XPS, although as more surface analysis techniques were developed, XPS has become the dominant name.

The Auger effect was discovered independently by both Lise Meitner in 1922 [163] and Pierre Auger in 1923 (as the central part of his PhD [164]) after whom the process was named. The possibility of using the Auger effect to perform surface analysis was first mentioned by Lander in 1953, after observing Auger peaks in the secondary electron emission spectrum of material irradiated by an electron beam [165], albeit with too low an intensity to be practical. However, it was not until 1965, that Harris [166, 167] showed that

electronically differentiated spectra greatly enhanced the signal to noise ratio (SNR) of the Auger peaks. Shortly after, Weber and Peria [168] used the same techniques on previously existing (and far more common at that time) Low Energy Electron Diffraction (LEED) optics. This lead directly to the commercial development of AES as an analytical technique, the first commercial instruments being available in 1969 [169].

2.2.2 Theory of XPS and AES

There are many similarities between XPS and AES. Both are highly surface-sensitive analysis techniques with a requirement of high vacuum and have spectral features that are characteristic of specific elements. Key differences between the two emission processes however, mean that they do not provide strictly identical information, but are complimentary to each other. Due to these differences, each technique will be discussed separately.

2.2.2.1 The photoelectric effect

Figure 2.1 shows the processes for both photoelectron and Auger emission. In 2.1 a), a photon with energy hν is absorbed by a core level electron with binding energy E_b. As X-rays with a photon energy of several thousand electron volts (KeV) are used (much greater than E_b), the irradiated electron is emitted from the surface is known as a photoelectron and possesses a non-zero kinetic energy.

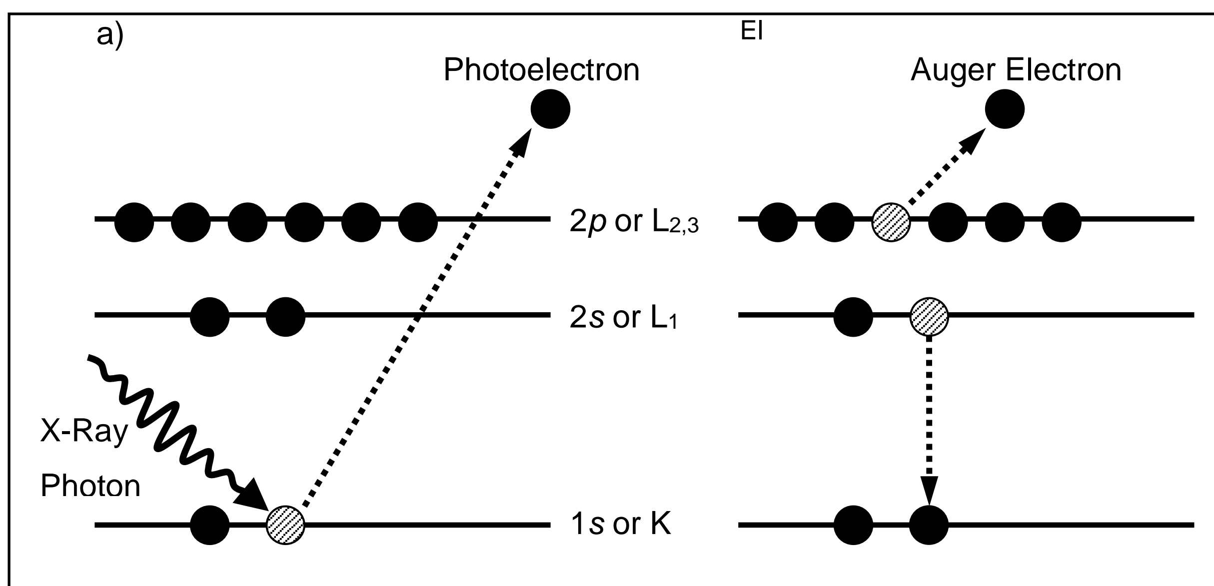

Figure 2.1 Diagram of a) XPS and b) AES emission processes (modified from Kibel [1])

As seen from the energy level diagram in Figure 2.2, the kinetic energy (E_k) of the ejected photoelectron will be equal to the initial photon energy, minus the energy needed to

overcome both the binding energy (E_b) and the sample work function (Φ_s), as described by Equation 2.1.

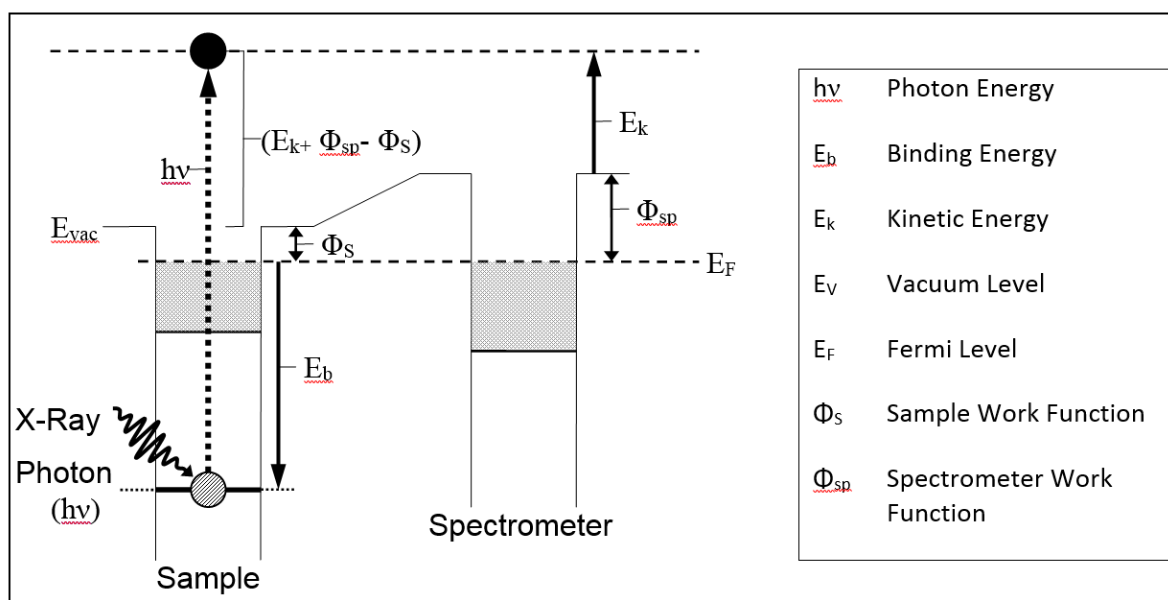

Figure 2.2: Energy level diagram representation of the photoemission process the relevant energy terms. Modified from Kibel [1].

$$E_k = h\nu - E_b - \Phi_S \quad (2.1)$$

However, as the sample and spectrometer are electrically connected, their Fermi levels shift into alignment with each other. Therefore, the kinetic energy as measured by the spectrometer in regard to the Fermi energy is reduced by the difference in the spectrometer work function and sample work function (Equation 2.2).

$$E_k = h\nu - E_b - \Phi_S - (\Phi_{sp} - \Phi_S) \quad (2.2)$$

The term for the sample work function can clearly be cancelled out, leaving just the spectrometer work function

$$E_k = h\nu - E_b - \Phi_{sp} \quad (2.3)$$

This is an important distinction for practical XPS analysis, as Φ_{sp} is a constant that can be determined experimentally on a per-instrument basis, we are left with:

$$E_k = h\nu - E_b \quad (2.4)$$

The photon energy: $h\nu$ is a known quantity, by measuring the kinetic energy of emitted electrons, their binding energies can be determined. By measuring the amount of electrons

emitted by a surface, and plotting against the energy they are detected at, a spectrum of elemental binding energies can be constructed. As binding energy is an intrinsic quantity to individual elements, peaks on this spectrum will correspond to the core electron energy levels of the elements present within the surface. All elements from lithium and above can be detected in this manner. Hydrogen and helium do not have 'core' level electrons, or rather, their core level electrons are also valence electrons. As the photoionization cross section of these levels is very small, they are not detected in XPS.

Because the value of E_b is dependent on the energy levels of elements in the surface, if the spectrum is plotted as it is produced i.e. on the kinetic energy scale, then the 'locations' of these peaks will shift based on the photon energy. As different XPS instrumentation can use a range of different X-ray sources, then it is common to construct XPS spectra on a binding energy scale, easily achievable by rearranging Equation 2.5 such that:

$$E_b = h\nu - E_k \quad (2.5)$$

The X-ray photon sources used for lab based XPS instruments such as the ones used in this project produce X-rays by accelerating electrons that are thermionically emitted from a (cathodic) filament into a metallic anode. This leads to the production of X-rays of an energy particular to the metal used, known as characteristic X-rays. The choice of anode is important: the energy of the X-rays produced must be sufficiently high to produce photoelectrons, and the energy distribution of the emitted X-rays (or line width) should be small, as the resolution of the technique depends greatly on this. The most common X-ray anodes used in XPS are those made of aluminium and magnesium. The energies of the $Al_{K\alpha}$ and $Mg_{K\alpha}$ transitions are sufficiently high (1486.6eV and 1253.6eV, respectively) to produce photoelectrons, and the line width of both is narrow enough for good resolution (0.85eV and 0.7eV, respectively).

2.2.2.2 The Auger Effect

After the ionization of a core electron, such as by the emission of a photoelectron as occurs in XPS, the atom is left in an excited state. This unfavourable situation is rapidly remedied by an electron from a higher energy level filling the core hole. The excess energy from the difference in binding states is then shed by the atom by one of two competing processes. One is the emission of a characteristic X-ray, and the other is the ejection of an electron from a higher energy level, leaving a doubly ionized atom (as depicted in Figure 2.1 b)). The latter process is known as the Auger effect, and the resulting emitted electron is known as an 'Auger' electron.

The kinetic of the emitted Auger electrons is given by Equation 2.6:

$$E_{kA} = E_K - E_{L1} - E_{L2,3} - U_{eff} \quad (2.6)$$

Where E_K E_{L1} and $E_{L2,3}$ are the electron energy levels involved, and the term "U_{eff}" represents the extra energy needed to remove an electron from the doubly ionised atom [170] Auger electrons are labelled according to these levels, using a different form of nomenclature, (which is also used for X-ray generation), where energy levels are labelled as K, L M etc. This is in comparison to XPS, where the 1*s*, 2*s*, 2*p* etc. nomenclature is used. For the example transition shown in Figure 2.1, the Auger electron is designated a KLL Auger electron – the initial ionization is from the K shell, and the two valence electrons are in L shells. As atomic number increases, the yield of KLL Auger electrons decreases, corresponding to an increase in the yield of characteristic X-rays. As there are more populated electron shells and thus transitions for higher atomic numbers, Auger electrons are able to still be detected for these elements, although it is the LMM and MNN transitions that are seen in spectra. The only elements not detectable with AES are hydrogen and helium, which cannot undergo the Auger process as at least two electron shells are necessary.

As with XPS, these quantities are well known, and the kinetic energy of emitted Auger electrons is identical for transitions between the same energy levels within the same atom. Thus, as with XPS, by producing a spectrum of electron counts vs energy, peaks associated with elementally specific Auger transitions can be identified. Of note here is that the kinetic energy of the released Auger electron is independent of the energy of the original ionizing species, an important distinction between Auger and photoelectron processes, where in the latter, E_K is directly dependent on the incident photon energy. Therefore, while Auger peaks will be detectable in XPS, any method of core level ionization can be used in order to produce Auger electrons and therefore a spectrum by which a surface can be elementally characterized.

The most common method for producing electrons in a stand-alone AES system is through the use of a high energy electron source. This is due to the relative ease by which high energy electrons can be produced with large currents, in addition to the ability to focus them to a small spot size, this gives AES as a technique greater spatial resolution than XPS, where the sample is 'flooded' with X-rays and the sampling area is determined by the geometry and optics of the analyser.

2.2.3 Practical considerations in XPS and AES

Both XPS and AES spectra involve the measurement of electrons according to their kinetic energy. Due to the ionisation of core level electrons by X-rays, Auger electron peaks will be

present in XPS spectra. The energy of Auger electrons produced in either XPS or AES remains constant regardless of the excitation energy used (whether that be an electron beam or photon source) and as such, in AES, it is convention to plot results on a kinetic energy scale. Conversely, in XPS results are plotted on a binding energy scale, as the kinetic energy of photoelectrons is explicitly dependent on the energy of the X-rays used. This conversion has been discussed previously, however there are some consequences due to this change in scale. Because the kinetic energy of Auger electrons does not change with photon energy, performing a conversion to the binding energy scale causes the apparent binding energy (although the term binding energy does not strictly apply to Auger electrons) of Auger peaks to shift, along with the photon energy used. These shifts are well accounted for, however, and handbooks of spectra for pure materials exist for the most common X-ray energies, making identification simpler. The property of Auger electron peaks 'shifting' in XPS spectra can actually be beneficial. There are some cases, (one of which is pertinent to this investigation) where Auger electron peaks overlap with relevant photoelectron peaks. Figure 2.3 shows two XPS spectra produced with different X-ray energies, with photoelectron and Auger peaks labelled. In the spectrum produced using a magnesium X-ray anode, the Auger peaks are present in a region of the spectrum which also contains the Mg2*p* photoelectron peak, while in the spectrum produced using an aluminium X-ray anode, the Auger peaks are present between the C1*s* and O1*s* peaks and do not interfere with any other photoelectron peaks which are likely to be observed throughout this work. Due to the interference in the Mg-kα case, only Al-kα X-rays were used for this project.

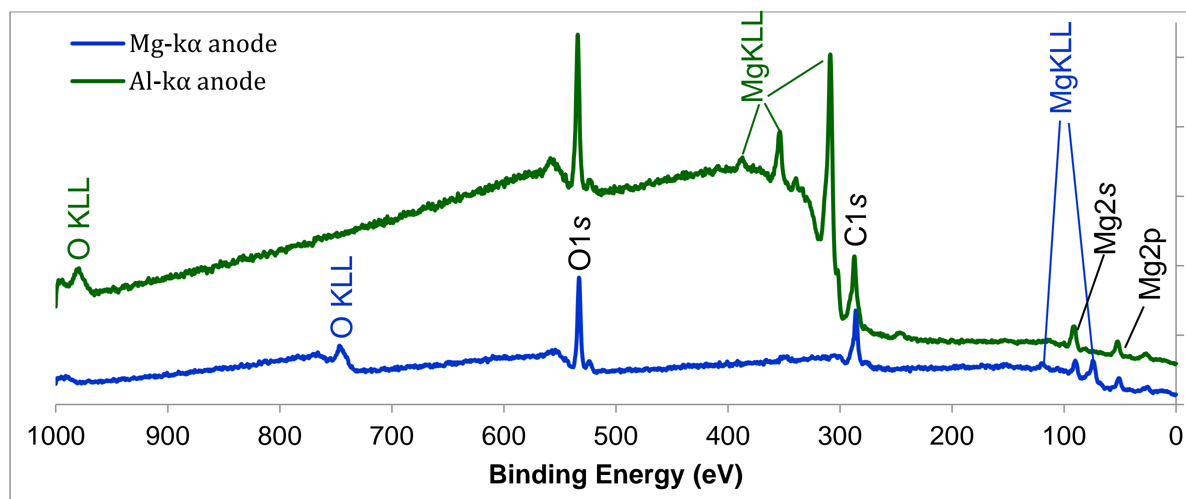

Figure 2.3 Differences between XPS spectra of a pure magnesium surface obtained with two different X-Ray energies: 1486.6eV corresponding to $Al_{K\alpha}$ X-rays in green, and 1253.6eV corresponding to $Mg_{K\alpha}$ X-rays in blue.

As Auger electrons can be produced without the need for X-rays, in AES such interferences can be avoided entirely by using alternative methods of Auger electron generation As

previously mentioned the most commonly used method in AES is using a high energy electron beam. When an electron beam is incident on a surface, there are a range of complex interactions that take place. The processes of particular concern in this case are the emission of both Auger electrons and characteristic X-rays, as depicted in Figure 2.4. The primary electron beam penetrates several micrometres into the sample, depending on the energy of the beam. A more energetic beam will penetrate further into the surface with scattering of this beam as it travels further into the surface causing the 'teardrop' shape to become more pronounced with increasing beam energy. This primary electron beam will cause ionization events throughout this volume, leading to the production of both characteristic X-rays and Auger electrons as the ionized species relax.

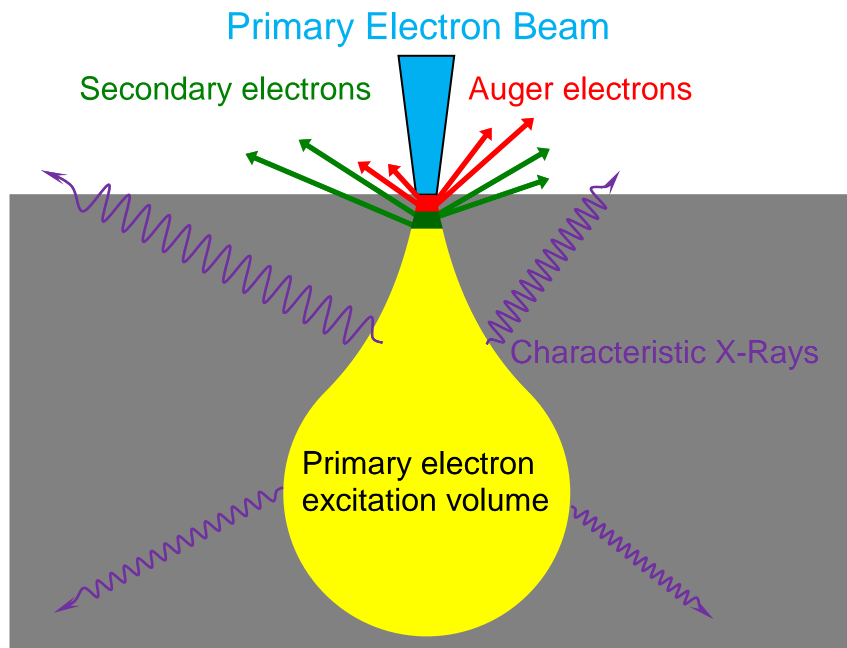

Figure 2.4: Cross sectional comparison of Auger electron, secondary electron and characteristic X-Ray emission

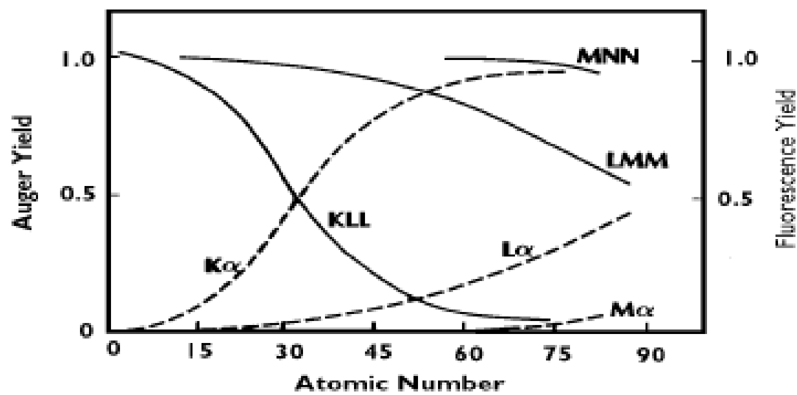

Figure 2.5 Auger electron and X-ray emission relative probabilities for increasing atomic numbers. Reproduced from Hubin and Terryn [171]

As previously mentioned, these two processes are competitive. Figure 2.5 depicts the probabilities of each transition. Generally, as atomic number increases, and thus the occupancy of electron levels, the probability of X-ray fluorescence increases. Therefore, Auger KLL emission is the most favourable process for lightweight elements until Kα X-ray emission becomes more prevalent (at approximately element 33 - arsenic). However, as atomic number increases, higher electron levels become available, allowing additional Auger transitions to occur, along with characteristic X-ray emission.

Unlike the choice of photon energy in XPS, the energy of the primary electron beam used for AES does not directly affect the energy of Auger electrons. However, the choice of beam energy is important, in a practical setting. Figure 2.6 shows a theoretical distribution of electrons emitted by a surface irradiated by an electron beam. At low energy, a large asymmetrical peak can be seen, associated with secondary electrons with a broad distribution of energies. Superimposed over this 'tail' is the peak associated with Auger electrons. This is also a slightly asymmetrical peak, caused by Auger electrons which have come from slightly further in the surface. At high energies, the primary electron peak can be seen, created from electrons that have elastically scattered from the surface, also known as 'backscattered' electrons. There are a series of 'loss peaks' corresponding to primary electrons that have suffered discrete plasmon losses in energy. If the beam energy used is too low, then the elastic peak and associated plasmon loss peaks will interfere with the Auger peak. To avoid such interference, beam energies of at least 3keV are used to create AES spectra.

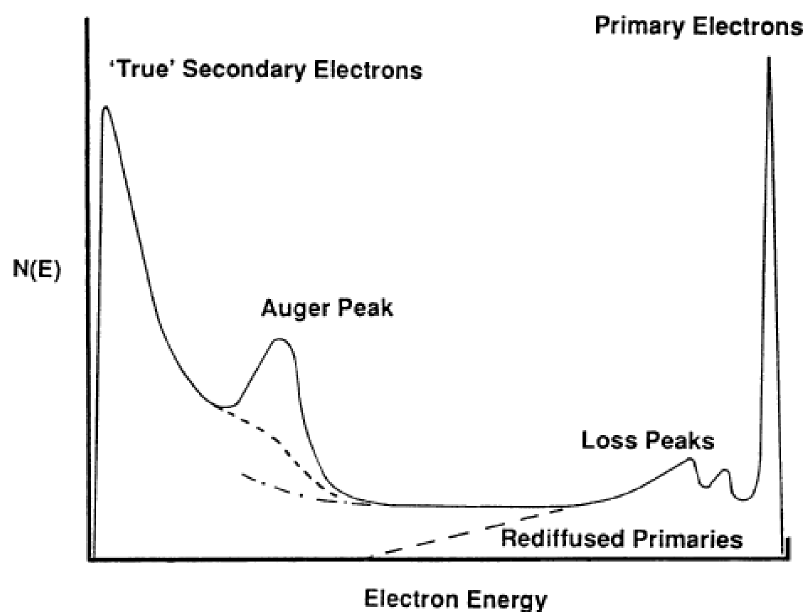

Figure 2.6: Energy distribution of electrons emitted after irradiation by an electron beam. Reproduced from Kibel [1]

An example AES spectrum of a magnesium surface is shown in Figure 2.7 a). The peaks are labelled according to the element and different transitions are numbered, rather than with their individual transitions for simplicity. It should be noted that the spectrum is plotted on a kinetic energy scale here, compared to binding energy which is used for XPS spectra. Also of note is the large background that increases with energy. This can be suppressed by plotting a derivative spectrum, as in Figure 2.7 b), which increases the sensitivity of small peaks in areas of large background, such as the Silicon KLL peak, at approximately 1621eV, which will be of key importance in this work.

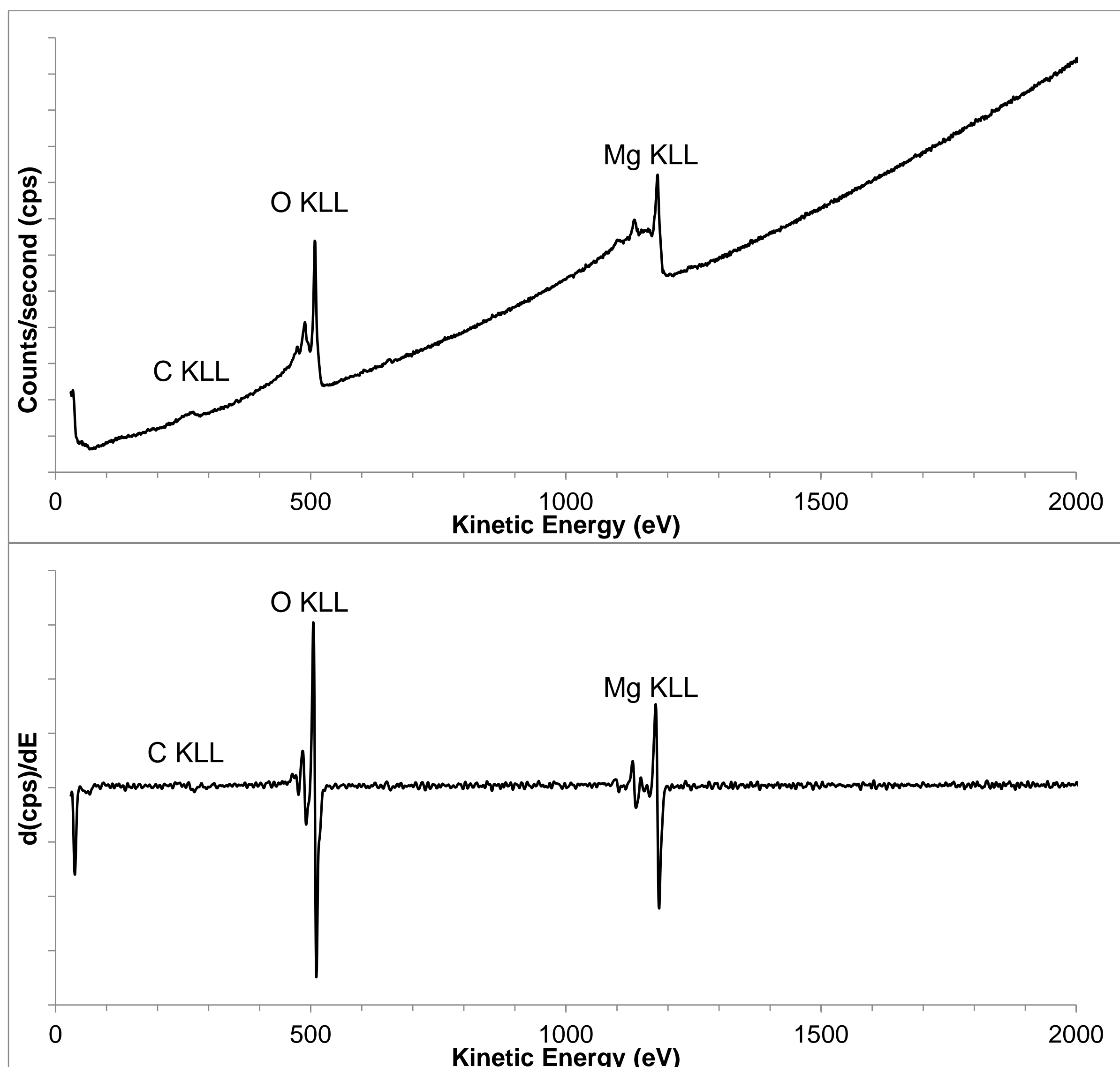

Figure 2.7: a) Example Auger electron spectrum of a magnesium surface. b) The same spectrum plotted as a derivative of electron counts per second vs kinetic energy

2.2.4 Electron Microscopy

Conventional light microscopy is limited by the wavelength of the light used [172]. In

response to the particle theories of light at the time, Louis de Broglie proposed in his 1924 PhD thesis the concept that matter may behave like a wave, with the ‘wavelength’ of the particle (with non-zero mass) given by:

$$\lambda = \frac{h}{p} \tag{2.7}$$

The so called ‘de Broglie wavelength’ of an electron, even at a low energy is orders of magnitude shorter than that of visible light. Therefore, using electrons as a source of ‘illumination’ should allow the imaging of materials far smaller than optical microscopy allows. This is the basis of electron microscopy.

Unlike light, a beam of electrons cannot be magnified using glass lenses. However, in 1926, Hans Busch demonstrated that electron beams can be controlled through the use of electromagnetic fields, allowing them to be focussed, defocused and deflected. By thus using these electron lenses, it is possible to raster the electron beam across the surface. In 1935, Max Knoll became the first person to scan a surface with an electron beam to form an image. He did this without the use of lenses, and as such his system had a poor resolution of 100μm. In 1938, Manfred Von Ardenne developed the first true electron microscope, by adding scanning coils to a transmission electron microscope. Research and development of the technique continued until the first commercial instrument was developed by Cambridge Scientific instruments in 1965. Since then, scanning electron microscopy has been a staple technique for surface analysis [173].

Different kinds of electron microscopy exist to examine different species generated by the irradiation of surfaces with electrons. Perhaps the two most common forms of electron microscopy are Scanning Electron Microscopy (SEM) and Transmission electron Microscopy (TEM). In TEM, images are produced from primary electrons that pass through the sample and are detected on the opposite side to the sample. This form of microscopy has very high resolution and magnification, but also requires very careful sample preparation to create a thin enough sample to image successfully. Scanning Electron Microscopy relies on detecting the secondary electrons that are emitted from a sample to create an image. Secondary electrons are those that are created through inelastic scattering processes of the primary beam, and are of much lower energy - generally less than 50eV. The topography of the surface has a major impact in the generation of secondary electrons - electrons emitted from a surface that does not face the detector, or is blocked by the topography of the surface will appear darker, so SEM images are a very good representation of the physical surface, akin to a black and white optical photograph.

Electron beams of the energies used for these kinds of electron microscopy will also generate Auger electrons. The two techniques are thus often paired, with SEM imaging allowing the identification of areas for selective AES analysis. It is also possible to perform microscopy using Auger electrons. Similarly to SEM, the electron beam is rastered across the surface, with Auger electrons of the desired elements detected at each point on the surface. In such a way, a two-dimensional image of the intensity of each chosen element can be constructed. This technique is called Scanning Auger Microscopy (SAM), and the images that are created are commonly referred to as elemental maps. Elemental maps produced using SAM have a resolution similar to that of SEM, and are able to image the same elements as AES (with atomic number ≥ 3). Due to the relatively lower intensity of Auger emission over secondary electrons, the time spent at each point on the elemental map to obtain sufficient signal: noise ratios is considerably longer.

For comparison, another contemporary elementally sensitive mapping technique known as Energy-Dispersive X-Ray analysis (EDX), is used to detect characteristic X-rays emitted from surfaces. These X-rays, are able to escape the surface from within the entire electron beam irradiation area, typically 5-10μm deep into the sample (see Figure 2.4). In contrast, Auger electrons can only escape from the outer 5-10nm of the surface without losing any energy and therefore, EDX does not have the surface sensitivity achievable with SAM.

2.2.5 Surface Sensitivity

One of the most important aspects of the techniques discussed thus far is that they are all surface sensitive. Both X-rays and high energy electrons are capable of penetrating micrometres into the sample, with photoelectrons, Auger electrons and secondary electrons generated throughout these depths. All of these species possess far less kinetic energy when compared to the primary electron source and consequently, they generally travel much shorter distances before experiencing non-specific energy loss events of unquantifiable magnitude. If the energy loss is minor, then the electron is still able to be emitted. Instead of appearing on a spectrum as a defined peak, they will instead contribute to the background. Alternatively, if the energy loss is on the order of the kinetic energy of the electron then it will be re-absorbed within the material. The average distance that species are able to travel without such loss events is known as the Inelastic Mean Free Path (IMFP or λ). A plot of IMFP and kinetic energy is shown in Figure 2.8. From this it can be seen that the escape depth of both Auger electrons and photoelectrons (with a kinetic energy range of approximately 10eV to 2000eV) is approximately 1-10nm. This makes both AES and XPS very surface sensitive techniques, and ideal methods to be used in a project involving thin films.

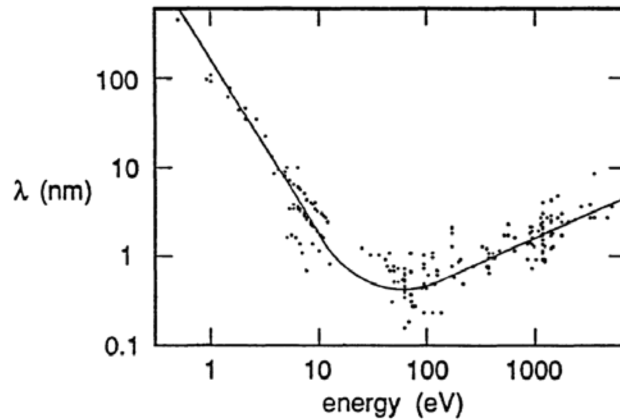

Figure 2.8: Inelastic Mean free path of an electron vs Kinetic energy. Reproduced from Kibel [1], originally published by Seah and Dench [174]

Secondary electrons are of much lower energy (from near 0eV to 20eV [1]), so while it could be intuitive that their escape depths to be correspondingly shorter, from Figure 2.8, it is clear that as kinetic energy decreases, the IMFP rises. This can be explained by a reduction in the cross-section of inelastic scattering events (below some threshold energy) that is; the probability of energy loss events decreases along with electron kinetic energy. Secondary electrons that possess enough energy to reach the detector will therefore be generated from approximately the top 50nm of the surface.

2.2.6 XPS experimental setup

Two XPS apparatus were used throughout the investigations presented here, a Leybold Heraeus LHS-10, and a custom SPECS system.

2.2.6.1 LHS-10

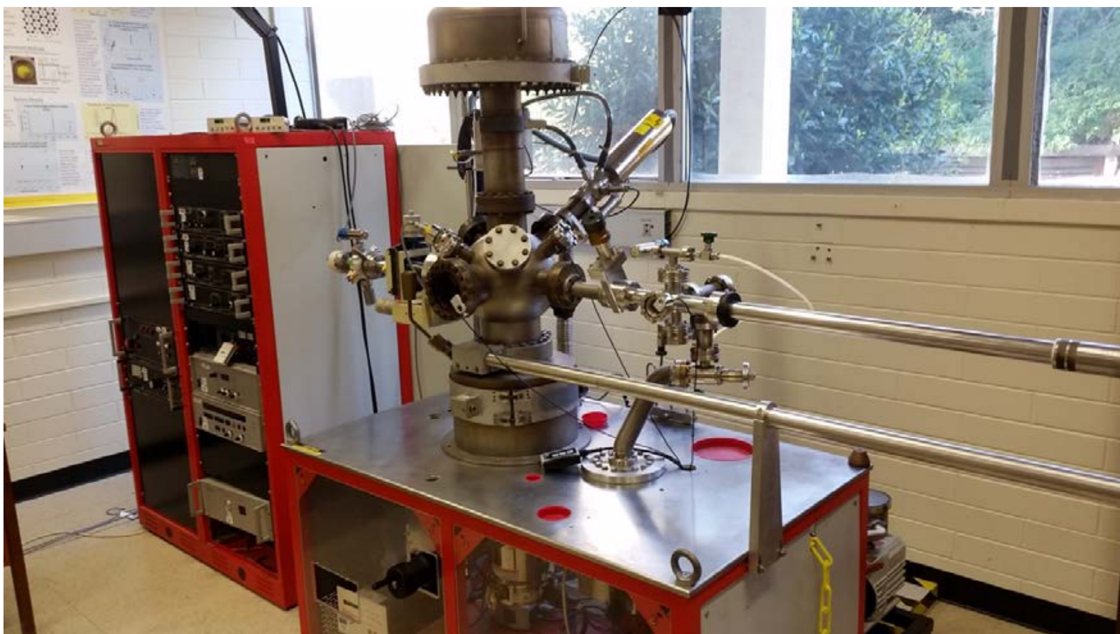

Figure 2.9 The LHS-10 Located at Flinders University

The Leybold Heraeus LHS 10 at Flinders University is an older system, commissioned early in the 1980's, originally with the capabilities of performing XPS, AES and Ion Scattering Spectroscopy. In this work, the LHS-10 (Figure 2.9) was set up only to perform XPS measurements. The vacuum system itself consists of two separate vacuum chambers: a large, spherical analysis chamber and a small load lock (or introductory) chamber used for sample introduction and to allow rapid transfer of samples from atmosphere to the analysis chamber. Attached to the analysis chamber are the original EA-10/100 Concentric Hemispherical Analyser (CHA) spectrometer with the multi-channel plate detector upgraded to a channeltron, and modern SPECS XR-50 dual anode X-ray source, which replaced the original X-ray source in 2008. Ultra-high vacuum is a necessity for XPS analysis, to allow photoelectrons that are emitted from the sample to be detected in the CHA without losses due to collisions with gaseous species. The main chamber is pumped by an Edwards STP-451 magnetically levitated turbomolecular pump, while the load lock chamber is pumped by a Pfeiffer TC-600 turbomolecular pump. Both turbo pumps are backed by Pfeiffer Duoline rotary vane pumps (Duo 10M and 5M respectively). This allows the LHS-10 to reach an absolute base pressure of ~$7x10^{-10}$ Torr, with the pressure during analysis better than $5x10^{-8}$Torr. The SPECS X-ray source is mounted at 56° degrees to the analyser, while the analyser itself is mounted normal to the surface. The source itself possesses both a magnesium and aluminium anode and is thus capable of generating both $Mg_{K\alpha}$ and $Al_{K\alpha}$ X-rays discussed in Section 2.1.2.1. Due to the aforementioned interference of magnesium Auger peaks with the Mg2*p* and Mg2*s* photoelectron lines when using the $Mg_{K\alpha}$ source (See Figure 2.3), only $Al\text{-}_{K\alpha}$ X-rays were used for this investigation. For X-ray generation, the source was operated with an accelerating voltage of 12.5kV and emission current of 20mA, for a total X-ray power of 250W. Data is recorded through a custom made program “X-spect” written for LabVIEW.

2.2.6.2 SPECS XPS

The second XPS instrument used in this work is actually a single apparatus attached to a larger instrument, custom built by SPECS GmbH. This instrument, capable of performing low energy electron and ion spectroscopies, along with XPS. The instrument is considerably newer, commissioned in 2010 and consists of a central vacuum chamber, with several load chambers for introduction of both solid and liquid samples. A base vacuum pressure of $1x10^{-10}$ mbar is achieved by differential pumping by several Pfeiffer turbomolecular pumps of varying sizes. Pressure during analysis is approximately $1x10^{-9}$ mbar. XPS is carried out through a retractable SPECS XR-50 dual anode X-ray source and a "Phoibos HSA 100" Concentric Hemispherical analyser. This analyser is modern compared to the one used in the LHS 10, with kinetic energy determination achieved through 5 separate electron

detecting channeltrons. This results in a far greater SNR and much faster data collection, especially at higher energy resolution. The X-ray source is identical to the one used in the LHS-10 instrument, also mounted at 56° to the analyser. As the analyser is more sensitive, the source is operated at a lower power setting of 200W (10kV and 20mA emission current). Data was acquired on this instrument using the "SPECSLAB" software package.

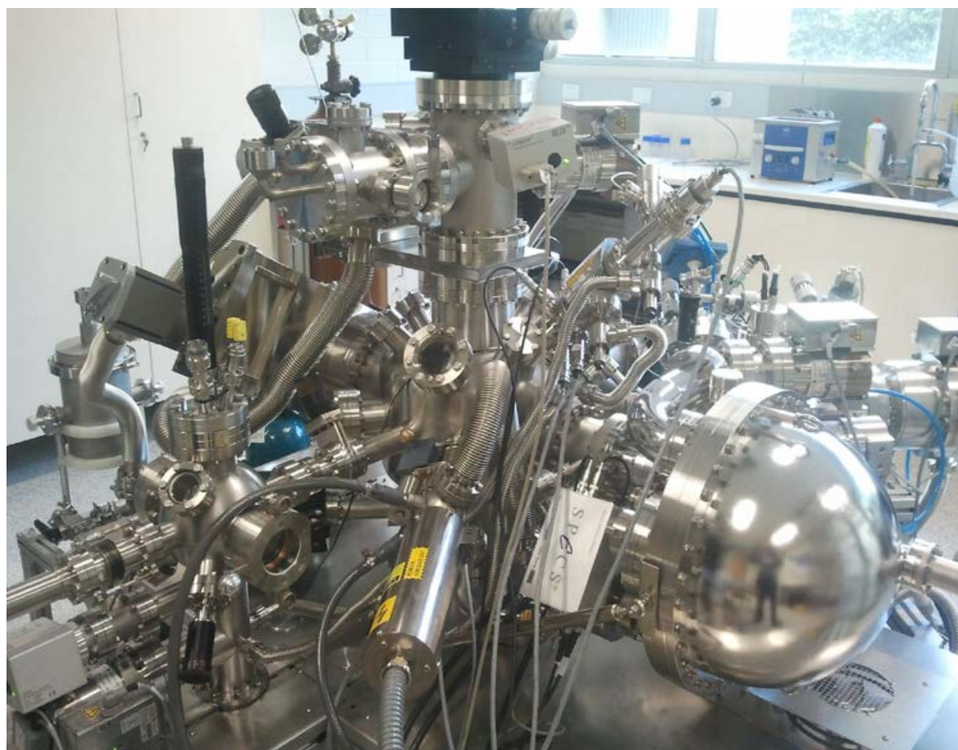

2.10 SPECS Electron and Ion spectroscopy apparatus located at Flinders University

2.2.7 Data Processing

Data obtained from both XPS instruments was analysed using CASA XPS software. Spectra were charge corrected to the adventitious component of the carbon 1*s* photoelectron peak, located at 284.8eV to remove the effects of any surface charging that occurred. Background removal was performed within the software using a 'Shirley' function, with the areas of each of the main photoelectron peak intensity corrected for photoemission cross-section with each elemental core-level peak's known relative sensitivity factor. For high resolution studies, photoelectron peaks were fitted with Gaussian-Lorentzian functions in order to achieve the best fit for the data, within physical limitations.

2.2.8 Scanning Auger SpectroMicroscopy Experimental Setup

All three of Auger Electron Spectroscopy, Scanning Auger Microscopy and Scanning Electron Microscopy were performed on a PHI710 Scanning Auger Nanoprobe (Figure 2.11). This instrument was installed at Flinders University in 2014.

Figure 2.11 The PHI-710 Scanning Auger Nanoprobe at Flinders University

The electron source used is a Schottky thermal field emission electron source, able to deliver a high flux of electrons of energies between 1 and 25kV. This is coaxially mounted with a cylindrical mirror analyser, as described in the following Section 2.18. The key advantage to this analyser geometry is that it allows Auger electrons to be collected in a 360° ring around the electron source, meaning that 'shadowing' from surface topology is greatly reduced.

A 'scintillation' secondary electron detector is also mounted adjacent to the electron source, allowing SEM to be performed in conjunction with AES measurements. This allows areas of interest to be identified for further analysis with Auger spectromicroscopy.

Also mounted is a "06-350" floating column argon ion gun. From this, argon ions are accelerated towards the sample at a range of energies (between 10V and 5kV). At higher energies (above 500V), this bombardment leads to the removal of material from the surface. By taking AES spectra stepwise with bombardment, depth profiling is able to be performed. The rate of sputtering is calibrated to silicon dioxide, where the time taken to remove a SiO_2 film of known thickness from a wafer of pure silicon is measured. As theoretical relative sputter rates are known, this allows the accurate determination of surface sputter depth.

The instrument itself consists of 3 separate vacuum chambers. As with both XPS instruments, a small load lock chamber is used for preliminary sample pumping and

outgassing, and is evacuated by a turbomolecular pump, backed by a Pfeiffer Duoline M10 rotary vane pump. The other two chambers are the main analysis chamber and the chamber containing the electron source; both are kept at ultra high vacuum with a base pressure of $1x10^{-10}$Torr. This is accomplished through the use of a differential ion pump in each chamber, combined with a titanium sublimation pump. Notably, these pumps are vibration free, which is necessary when imaging surfaces at very high magnification. To further reduce the effects of mechanical vibration from both internal and external sources, the entire apparatus is kept on a 'floating' air table inside an acoustic enclosure, and low noise electronics used.

The software used to operate the PHI-710 is "SmartSoft-AES" (version 5.2.0.8), while data analysis is performed on “Multipak" software (version 9.8.0.19) both designed by Ulvac-Phi Inc. A key feature of the "SmartSoft” program is that it allows for ‘image registration’: the use of SEM imaging to periodically monitor analysis locations while performing AES, SAM and depth profiling measurements. This counteracts any variations caused by charging of the surface, thermal variation, or vibrations that could cause the beam to drift. In addition, the software is able to perform a Linear Least Squares (LLS) fitting, a common form of linear regression. This is a process by which a curve is fitted to a set of data through the reduction of the residuals (or offsets) of each point from the curve. For the data collected throughout this research project, the LLS fitting in Multipak was used in order to deconvolute depth profiles in order to obtain information about the oxidisation of the magnesium substrate. This was performed as an iterative process with 60 iterations performed.

Analysis performed during this project used a beam energy ranging between 1kV to 20kV. A 1kV beam voltage was used for two purposes: for wide field of view (FoV) SEM imaging of surfaces up to $2mm^2$, and to align the focal point of the analyser with the surface. The latter of these was accomplished by measuring a spectrum containing the elastic electron peak, and adjusting the height of the stage to maximise the intensity of this peak. The primary beam energy used for both AES and SAM measurements was a 10kV, 10nA beam. This beam was found to provide a good balance between spatial resolution and SNR for the features that were being examined. Occasionally, a 20kV 10nA beam was used in order to image smaller features with increased spatial resolution. SEM images were taken with a resolution of 1024x1024 pixels, while the resolution of SAM elemental maps was varied between 128x128 and 512x512 pixel resolution. This pixel resolution is much lower than the instrument is capable of, but was found to be sufficient for the features being examined here.

2.2.9 Electron Energy Analysers

The two kinds of electron energy analysers used for XPS and AES in this research are the

"Concentric Hemispherical Analyser" (CHA) and the "Cylindrical Mirror Analyser" (CMA), so named for their respective geometries which can be seen in Figures (2.12 and 2.13). The two XPS instruments used in this work utilize CHA type analysers, while the Scanning Auger Nanoprobe is equipped with a CMA. While fundamentally, the data obtained using both types of analysers in the same, both have benefits in different circumstances.

2.2.9.1 The Concentric Hemispherical Analyser

In a CHA, electrons emitted from the surface are focussed by an electrostatic lens onto a slit at the entrance to a void between two concentric hemispheres. The two hemispheres are both charged, with a potential difference between the two, such that V2 is negative with respect to V1. Thus, an electric field exists between the two hemispheres such that an electron entering the analyser will be deflected in a curve towards an electron detector. The kinetic energy of the electron will change the radius of the path that it takes causing them to travel in a curve such that if it is too low, or too high, then the electron will be accelerated towards the inner or outer hemisphere instead of the electron detector. Some electrons will have a kinetic energy such that they will enter the analyser and follow a path with a radius Ro. This energy is known as the pass energy E_o, and can be changed by sweeping the voltages V1 and V2, thus allowing electrons of a different kinetic energy to the detector.

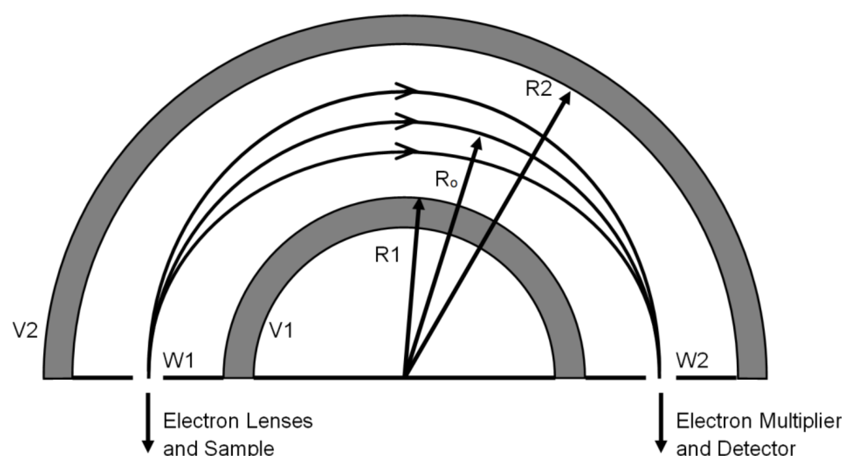

2.12 Cross sectional geometry of a concentric hemispherical analyser. Modified from Hoffman [165], Originally published by Seah [175]

In practice, this is not how analysis is performed, due to the relationship between the analyser resolution and the pass energy. Energy resolution is defined in two ways: absolute resolution (ΔE), and relative resolution. Absolute resolution of an analyser can be measured through the "full width at half maximum" (FWHM) of a spectral peak, while relative resolution is the ratio of the absolute resolution to the total electron kinetic energy. There are several factors which can influence the absolute resolution. The energy spread imposed by the

natural line width of the X-rays used will impose a limit to resolution, as will the thermal broadening of peaks. The analyser geometry itself also has an effect on the absolute resolution as defined by Equation 2.8 [176].

$$\Delta E = E_o\left(\frac{W_1+W_2}{2R_o}\right) \quad (2.8)$$

Where W_1 and W_2 are the entrance and exit slit widths to the analyser, and R_o is the mean radius of the analyser. Resolution can therefore be experimentally controlled in several ways: decreasing the slit width, increasing the analyser radius, and reducing the pass energy. Modern analysers like the SPECS "Phoibos HSA 100", have variable entrance and exit slit widths, while other instruments such as the EA-10/100 on the LHS 10 do not. Even if slits are of variable width it is usually by discrete, fixed amounts. The analyser radius is a fixed quantity for each apparatus, and while increasing the radius would improve the resolution, keeping the equipment practical for a laboratory setting is important.

By decreasing the pass energy then, it is possible to improve the resolution. If, in a CHA, a spectrum was created by changing the voltages between the hemispheres, then the pass energy would inherently change as electrons with different kinetic energies are detected (E_o=E_k in this case). Instead, the initial electrostatic lensing system is used to reduce the energy of incoming electrons by a controlled amount and thus select the pass energy. This is accomplished in two ways: Fixed Analyser Transmission (FAT) mode, and Fixed Retarding Ratio (FRR) mode. These modes are also known by the names "Constant Analyser Energy" and "Constant Retarding Ratio" respectively. For simplicity, only the terms FAT and FRR will be used.

In FAT mode, the voltages V_1 and V_2 on the hemispheres are set to a specific values, (with the difference between these called the pass potential V_o) and will thus only allow electrons of a single pass energy (E_o) to the detector (within some energy variance ΔE). A spectrum is generated by applying and varying a retarding voltage to the incoming electrons within the lens system, reducing their kinetic energy to a chosen pass energy for each point on the spectrum. For example, for a pass energy of 20eV an incoming electron with E_k of 200eV must be slowed by 180eV, whereas a 500eV electron must be slowed 480eV. As seen in Equation 2.8, the pass energy has a direct influence on the energy resolution obtainable. Therefore, in FAT mode, as the pass energy remains constant, so too does the resolution of the analyser. By increasing the retarding voltage and thus decreasing the pass energy, resolution may be increased. There is a trade-off in that by increasing the retardation factor, fewer electrons will enter the analyser thus reducing the signal to noise ratio.

In the second mode of operation, Fixed Retarding Ratio (FRR) mode, the analyser voltages and the lens system are used in conjunction to slow incoming electrons by a fixed ratio (such that E_k/E_o =constant). For example if a ratio of 10 is used, then the case of the 200eV electron described previously would be slowed to 20eV with an identical pass energy of 20eV. However a 500eV electron would be slowed to 50eV, likewise with a pass energy of 50eV. Consequently, the resolution of the analyser changes throughout the spectrum, with lower resolution at high kinetic energies. The count rate (and therefore SNR) however, will be increased for electrons with higher kinetic energies, when compared to the same detection in FAT mode.

Relating these concepts to the apparatus, in the LHS 10, in order to obtain a good SNR, FRR mode, with a Retardation factor of 10 and a pass energy of 20eV was used in wide energy survey scans for qualitative analysis, while FAT mode, also with a pass energy of 20eV was used for high resolution spectroscopy of select energy ranges containing relevant photoelectron peaks.

2.2.9.2 The Cylindrical Mirror Analyser

The fundamental operating principle of a cylindrical mirror analyser (CMA) is the same as a CHA, although with different analyser geometry. In a CMA, two concentric cylinders (as the name suggests) are separated by a vacuum, with a potential between them. The inner cylinder is kept at ground, with the other at a negative voltage [1]. Electrons enter through a ring at the base of the analyser, and are deflected in an arc between the cylinders and detected at the top. As with a CHA, only electrons of a certain kinetic energy will be permitted, based on the arc that they will take as seen in Figure 2.13. In a CMA, the kinetic energy of incoming electrons is selected by ramping the voltage of the outer cylinder, rather than through a voltage applied by a series of electron lenses. The reason for this, is that as the entrance to a CMA is a ring, as opposed to a single slit, there exists a 'focal point' for the analyser. That is, electron energy measurement is best accomplished where the surface is at some distance "F" from the analyser [1]. Due to the length they require, a set of electron lenses would obscure this point. Therefore, FAT mode is not possible in a CMA, as the selection of electrons must depend on their kinetic energies. As such, CMAs operate in a mode akin to FRR mode, with energy resolution reducing with increased electron kinetic energy. It is therefore common for the resolution of CMAs to be quoted in terms of percentage relative resolution, rather than absolute resolution for each value of kinetic energy.

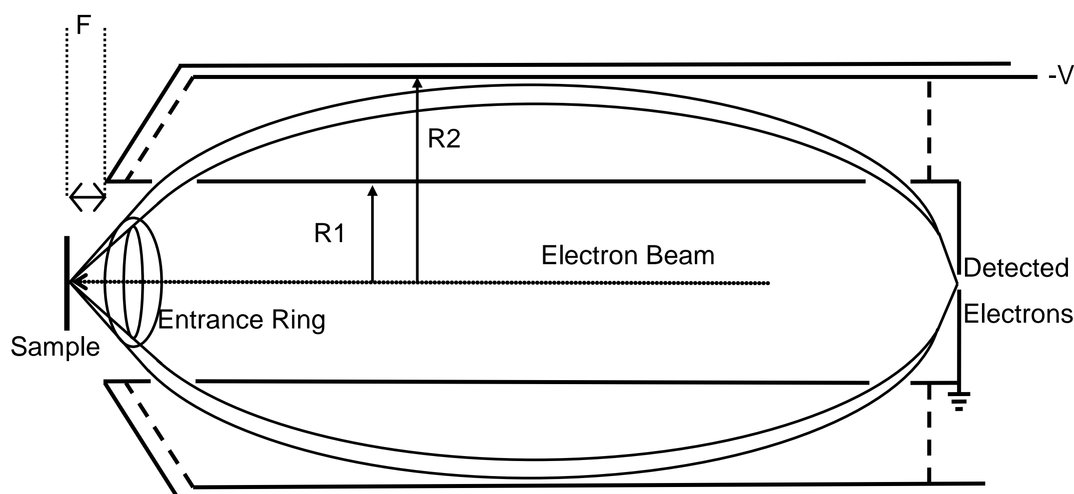

Figure 2.13: Cross section of a cylindrical mirror analyser. Modified from Kibel [1]

While this lack of consistent resolution would seem to make the CHA a more favourable choice, the use of a CMA is still common among AES apparatus. The natural line widths for Auger transitions are often in the order of 1-3eV, so the requirements for ultra-high energy resolution from the analyser are relaxed, with CMAs able to provide sufficient energy resolution for AES analysis. The geometry of the analyser also provides several advantages. As mentioned in Section 2.1.2.2, AES is most commonly performed using a focussed, high energy electron source. By mounting the electron gun within the centre of the analyser, the shadowing effects of surface topology are reduced, allowing accurate elemental mapping of surfaces. Using a small, focussed beam of electrons means that there is comparatively less signal being generated than for an X-ray source, which has a wide irradiation area. The entrance ring of a CMA has a higher acceptance angle than the slit of a CHA, giving it consequently higher signal to noise ratios [175]. As many other species are generated by the electron beam, then there will also be a large background of secondary electrons and inelastically scattered primary electrons that the Auger peaks are superimposed onto. Historically, in order to counteract this background, an 'AC modulation' was applied to the analyser, so that an 'analogue derivative' spectrum is obtained, suppressing the large linear background and allowing the Auger peaks to be more easily identified. With modern detection systems, including the use of multiple channeltrons, the signal:noise ratio is much improved, so data is obtained as a plot of detected electrons vs. energy and then differentiated numerically.

2.2.10 High Vacuum Sample Requirements

The way that samples are introduced to each of the vacuum chambers is through specially designed sample mounts, seen in Figure 2.14 a) for the LHS-10 and Figure 2.14 b) for the

SPECS instrument. This introduces a size limitation to the samples of approximately 10x10mm to allow the introduction and removal of samples without damage to them or the apparatus. Samples are attached to the sample mounts using either copper tape, with a conductive adhesive, or mechanical attachment with metal screws and molybdenum masks. Conductivity to the sample is of paramount importance, as with the ejection of photo- and Auger electrons, a positive charge can build up on the surface, if no way of replenishing electrons is available. Charging of the surface leads to columbic interactions with ejected photoelectrons, changing their kinetic energy and thus the resulting spectrum. As magnesium is a conductive metal, charging was not a significant issue, however, there is no guarantee that any deposited film is also conductive. To counter any charging, an electron flood gun is present in both systems, which supplies an excess of low energy (>10eV) electrons, though this was found to be unnecessary.

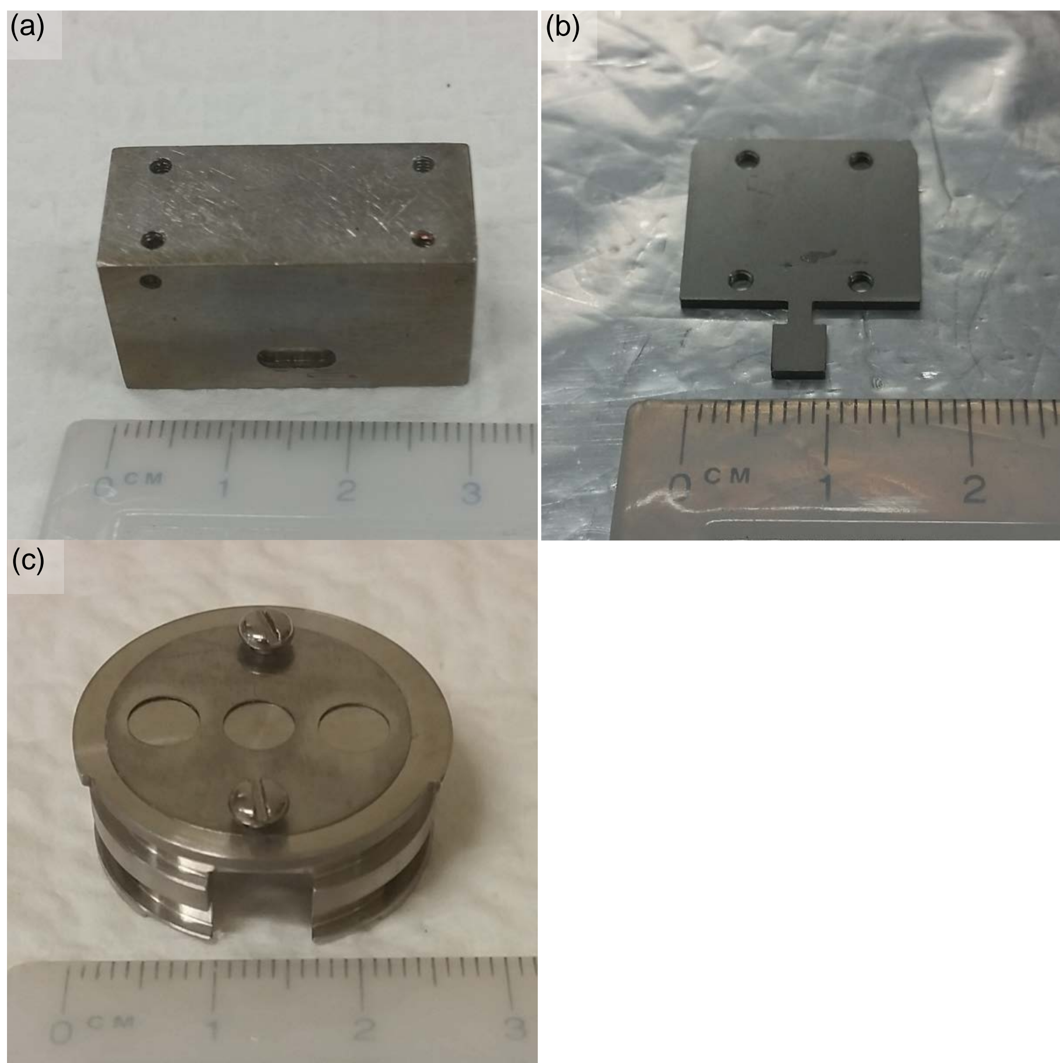

Figure 2.14: Sample mounts used for a) LHS-10 XPS b)SPECS XPS and c) PHI-710 Scanning Auger Nanoprobe

The sample mounts used for the PHI-710 are pictured in Figure 2.14 c). The sample stage in the PHI instrument is capable of 5 axis control so much larger, or multiple samples are able to be introduced at once. Samples are attached to the mounts mechanically using screws and molybdenum masks, to reduce sample charging to the surface.

The only other sample requirement is that of vacuum compatibility. Ultra high vacuum is a necessity for XPS and AES. As such samples must not only be able to survive in such an environment, but also preserve the vacuum. All samples exposed to air have a layer of adsorbed atmospheric gases and water vapour, which when exposed to the low pressure environment will ‘outgas’ and increase the prevailing pressure in the analysis chamber, meaning that more pumping time is required before analysis can be performed. Any particulate matter present within the sample could also become dislodged if present, potentially contributing as a contaminant in further experiments. More problematic are materials which have a high vapour pressure such as sulphur, which could potentially coat or react with surfaces inside the chamber, causing permanent damage.

2.3 Other Analysis Techniques

2.3.1 Atomic Force Microscopy

While electron microscopy is able to create high magnification images of surfaces, the images it generates are 2-dimensional. They possess a ‘pseudo 3-dimensional’ quality, but any height information provided is strictly qualitative and subject to misinterpretation as contrast is due to local changes in the liberation of secondary electrons. A different form of microscopy is therefore required if quantitative information about surface topography is required.

Atomic Force Microscopy (AFM) is a form of Scanning Probe Microscopy which is a family of analysis techniques based on the concept of measurement via interactions that take place between a sharp tip and a surface that is scanned across it. In AFM, the tip is located at the end of a flexible cantilever, with a surface that is mounted onto a three-dimensional scanner. As the surface is brought close to the tip, attractive and repulsive forces between the atoms of the surface and the tip cause the cantilever to deflect. A laser is focussed onto the back of the cantilever, with a position sensitive photodetector used to collect the reflected light (see Figure 2.15). This detector can thus measure the deflection of the tip, which is used to adjust the scanner position to maintain interaction between the tip and surface as constant in a feedback loop. By plotting the change in “z” height of the scanner as the tip traverses the surface, a three-dimensional image of the surface is generated. In practice the AFM can be operated in one of several distinct modes based on what kind of interaction between the tip

and surface is kept constant: contact mode, tapping mode and PeakForce tapping mode.

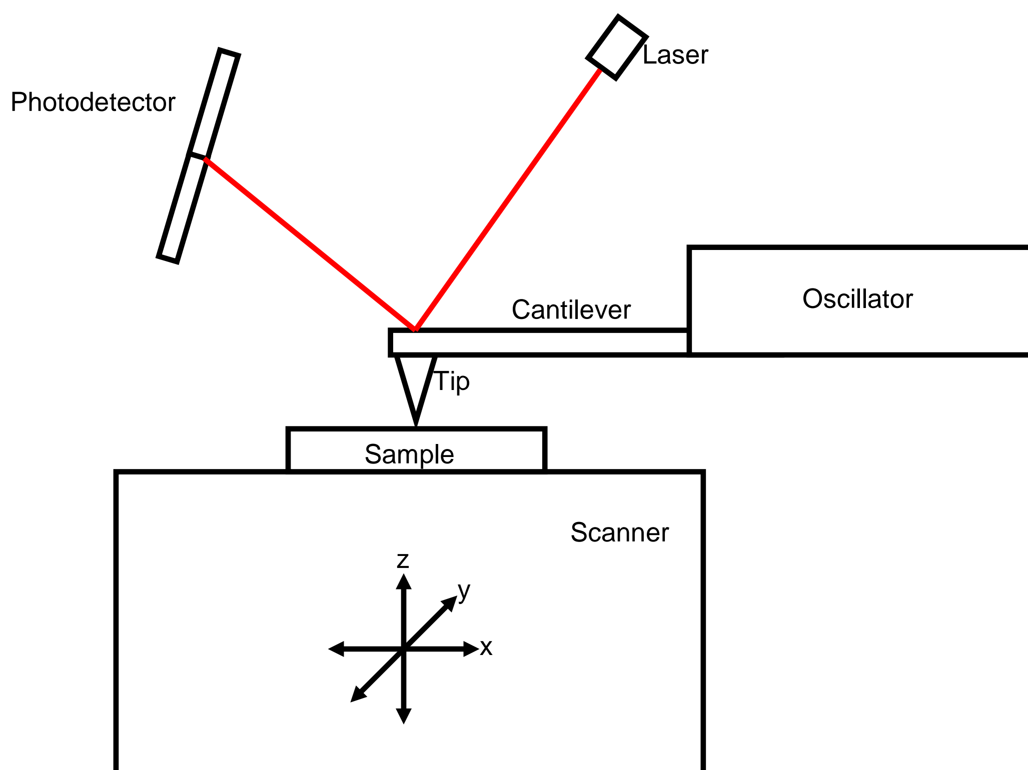

Figure 2.15 Schematic of an atomic force microscopy in operation

In contact mode, the tip is suspended several Angstroms (Å) away from the surface, and as the tip scans across the surface, the feedback system keeps the force between the tip and surface constant.

The mode used to collect all AFM data in this work however was PeakForce tapping mode, a variant of tapping mode. Conventional tapping mode (also known as intermittent contact, vibrating or AC mode) was developed in order to overcome a problem in contact mode wherein the tip may damage (or become damaged by) rough surfaces. In tapping mode, the cantilever is driven to vibrate rapidly (near the resonant frequency of the cantilever; between 45 and 95 kHz for the tips used in this work), with the tip coming into contact with the surface at the nadir of each oscillation. It is the amplitude of the cantilever's oscillation that is kept constant by the feedback system, which (as in contact mode) moves the sample stage in order to produce a topographic image of the surface.

PeakForce tapping is a relatively new mode of AFM operation which, similar to conventional tapping mode, uses a vibrating cantilever. The frequency of this oscillation is fixed at a value much lower than the cantilever's resonant frequency. In contrast to tapping mode, it is not the amplitude of the oscillation that is monitored, but rather the deflection of the cantilever. For each oscillation of the cantilever, a "Force-Distance" curve is obtained; measuring both

the attractive and repulsive forces that act on the tip as it approaches and withdraws from the surface. The maximum or "peak" force experienced by the cantilever for each oscillation is kept constant via an electronic feedback mechanism. The increased level of control over this force allows high resolution AFM images to be obtained with far less potential damage to the tip, soft surfaces, or both.

Figure 2.16 The Bruker Dimension Fastscan used in this work

All AFM imaging performed throughout this project was acquired using a Bruker Dimension Fastscan system utilizing a Nanoscope V controller (Figure 2.16). AFM images were acquired in PeakForce tapping mode, with imaging parameters including set-point, scan rate and feedback gains adjusted to optimize image quality and minimize imaging force. Nanoscope Analysis software version 8.1 was used to perform 1st order flattening and obtain roughness measurements. The AFM scanner itself was calibrated in x, y and z directions using silicon calibration grids (Bruker model numbers PG: 1µm pitch, 110nm depth and VGRP: 10µm pitch, 180nm depth). The AFM probes utilized were Bruker ScanAsyst air probes with nominal resonant frequency of 70kHz, nominal spring constant of 4N/m and nominal tip diameter of 4nm. Images were collected with an X-Y size of 10µm x 10 µm,. While it is possible to produce smaller images with AFM, in order to accurately compare AFM with SEM and Auger microscopy, the chosen scale was found to be a good compromise.

2.3.2 Fourier Transform Infra-Red Spectroscopy

Fourier Transform Infra-Red Spectroscopy (FTIR) is a spectroscopic technique used to

obtain information about functional groups and bonds present in a material. When exposed to infrared radiation, bonds in molecules will absorb energy of particular wavelengths, depending on the vibrational energy transitions that occur. These vibrational energy transitions will occur in molecules where the dipole moment is able to change in a molecule as it vibrates or rotates [177]. The dipole moment varies between molecular species and therefore each has a different natural vibration frequency. If the frequency of an incident IR wave is equal to this natural vibration frequency, then the bond will absorb this energy. In general, an infrared spectrum is acquired by passing IR radiation through a sample and determining how much radiation is either absorbed or transmitted across a band of frequencies. In such a spectrum, the absorbance of IR radiation will cause peaks to appear at frequencies characteristic of individual functional groups, allowing information about bonding structures present to be determined. If the sample analysed is a single chemical, then the collective functional groups present in the IR spectrum will form an effective 'fingerprint' of the molecule. In such a way, IR spectroscopy may be used to investigate not only unknown samples, but also to monitor changes to the functional groups present in a known molecular species.

The infrared range of the electromagnetic spectrum spans from 700nm to 1mm in wavelength (which corresponds to an energy range of 1.24meV to 1.7eV). It is impractical to obtain spectra across this entire region, so it is commonly divided into three regions: Near IR, Mid IR and Far IR. The most common analysis region for FTIR spectroscopy is the mid infrared range, between wavenumbers of 400 and 4000cm^{-1}, due to the presence in this region of the vibrational and rotational absorptions of a range of important organic compounds.

Infrared spectroscopy was originally performed using dispersive components (commonly NaCl crystals) and a monochromator in order to select for particular wavelengths. While serviceable, the necessity for the monochromators to limit the admitted light to a single frequency means that a long time is taken to acquire data with a sufficient signal to noise ratio. Modern IR instruments utilise a broad band light source Michelson interferometer (Figure 2.17), with light passing through the interferometer and sample to the detector. The detector records the signal as an interferogram, which is then converted computationally using a Fourier Transform into a spectrum of either absorbance or transmittance (as required) vs. photon energy (in wavenumbers (cm^{-1})).

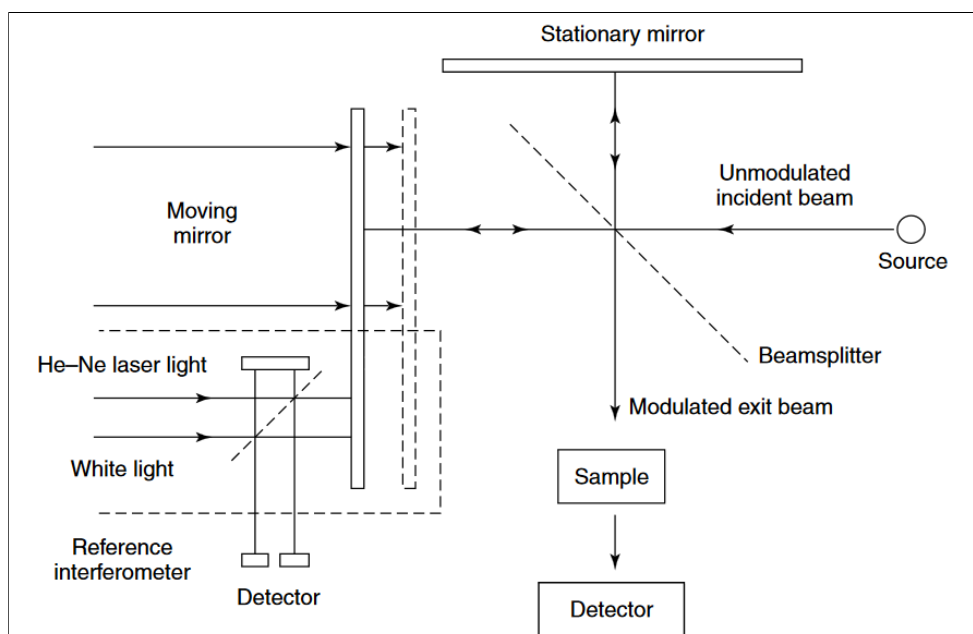

Figure 2.17 Schematic Diagram of a Michelson interferometer. Reproduced from Stuart [178]

The simplest way to acquire FTIR data is for the radiation to pass through the sample and measure the intensity of absorbed or transmitted light. Unfortunately, this method of acquisition is only possible for either liquids or thin, transparent solids. The materials examined in this work are solid, metallic and non-transparent, so analysing the thin films deposited on them with FTIR requires an alternative method of data acquisition. In this case, a variant of FTIR is used known as Attenuated Total Reflectance spectroscopy (ATR). In ATR, the IR light source is directed into a crystal with the sample placed upon it. The angle of incidence of this light is chosen such that it is reflected internally within the crystal. When the light reflects from the crystal surface in contact with the sample, there is a small interaction with the sample itself, in the form of an evanescent wave, some of which is absorbed by the sample, as it would for a transparent sample in conventional FTIR. This interaction area is limited to material in direct contact with the crystal (the wave decays exponentially) Therefore, to increase absorbance, pressure is applied to solid samples in order to maximise this contact area, although not so much as to damage the crystal itself. Due to this, softer materials are able to conform to the surface better than harder ones. To increase the signal obtained for hard samples (such as magnesium), surfaces must be as flat as possible to maximise contact area. With regard to the surface sensitivity of ATR-FTIR, the penetration depth (d_p) of the wave into the sample (and therefore the sampling depth) is given by equation 2.9 [177]:

$$d_p = \frac{\lambda / n_1}{2\pi\sqrt{\sin\theta - \left(n_1 / n_2\right)^2}} \tag{2.9}$$

Where λ is the wavelength of the incident light, θ is the incident angle on the sample, n_1 is the refractive index of the sample and n_2 is the refractive index of the ATR crystal. Without knowing the refractive index of the organosilane films produced, the exact penetration depth of the evanescent wave into the sample surface is unable to be determined accurately. However, an estimate can be made by using the refractive index of other organosilane films. In a study by Franquet et al., the refractive index of thin, chemically deposited BTSE films was experimentally determined to be approximately 1.66. The refractive index of the ZnSe ATR crystal is known to be 2.4, and the angle of incidence used for the experiments here was 45 degrees. Therefore, by substituting these values into Equation 2.9, the penetration depth can been calculated across the range of a typical mid IR spectrum: from $400cm^{-1}$ to $4000cm^{-1}$ (which is $2.5x10^{-5}m$ to $2.5x10^{-6}m$ when converted to wavelength). This calculation results in values for d_p of between approximately 5μm and 500nm, values significantly higher than any of the previously discussed spectroscopic techniques. Consequently, ATR-FTIR spectroscopy is far less surface sensitive.

Franquet https://onlinelibrary.wiley.com/doi/pdf/10.1002/sia.1245

The FTIR spectrometer used for all FTIR spectra obtained throughout this work is a PerkinElmer Frontier, with a "Universal ATR" attachment utilizing a three reflection Diamond/ZnSe crystal. Spectra were collected using air as a background and plotted on an absorbance vs. wavenumber scale.

2.4 **Materials**

2.4.1 Substrates

Polycrystalline magnesium substrates of 99.9% purity were obtained from Goodfellow Materials Cambridge LTD as 100x100mm sheets. These were then sheared using a guillotine shear, into 10x10mm samples for use in both dip coating and plasma experiments. Pure magnesium was chosen, as opposed to an alloy, as this study was foremost a fundamental study of the interactions between magnesium and organosilanes. The presence of alloying elements would make studying these interactions much more difficult, even if their presence leads to improved corrosion resistance. Polycrystalline magnesium was used, as opposed to a single crystal, as it does provide a degree of 'realism'.

2.4.2 Organosilane selection

Propyltrimethoxysilane (97%) was obtained from Sigma Aldrich LTD. PTMS is one of the

simplest alkoxy silanes, which makes it a good choice for fundamental studies. It is also a good representation of other, more complex organosilanes. Compared to the functionality that other silanes possess, the propyl group is relatively inert. It has already been established in literature that bonding can occur between the amine group of APS and metal surfaces for instance. The propyl chain is also the basis of APS, and a range of other organosilanes, which makes it a good model for those materials in a study such as this. The three methoxy groups that are present are used to prevent the silane condensing during storage or transport. They must therefore be removed through a hydrolysis step. Methoxy groups have been shown to hydrolyse faster than longer chain alkoxy groups [90]. When attempting to produce a film, a rapid rate of hydrolysis in comparison to the rate of condensation is preferable (see Section 1.3.2).

2.4.3 Solvents

2.4.3.1 Water

All organosilane solutions, and any cleaning involving rinsing with water is performed with pure water which has been de-ionised and filtered to milli-q standards.

2.4.3.2 Acetic Acid:

Acetic acid used as a catalyst for organosilane hydrolysis was sourced from sigma Aldrich ltd. as glacial acetic acid, and diluted to the required concentration.

2.4.3.3 Gases

A range of gases are used for cleaning and pre-treating using plasma. The gases used are listed, along with purity's and sources in Table 2.1 below:

Table 2.1 Purities and suppliers of gases used for plasma experiments

Gas	Purity (%)	Source
Oxygen	99.9	BOC
Argon	99.997	BOC
Nitrogen	99.99	BOC

2.5 Chemical Dip Coating Procedures

2.5.1 Pre Treatment for Dip Coating

In order to ensure that an effective and comparable study is done, the magnesium surfaces

must be both cleaned and pre-treated. The resulting surfaces must then be identical and suitable for further reaction with organosilane species. The process used to accomplish this here is as follows:

As received magnesium samples were briefly abraded with 1200p grade silicon-carbide paper to provide a uniform initial surface finish, and to remove any large particulate contaminants. Samples were then cleaned in an ultrasonic bath of ethanol for 10 minutes, then dried under a dry nitrogen flow to remove any finer particulate matter, or residue from the abrasion treatment.

Samples were pre-treated in a solution of acetic acid with a pH of 3. This pre-treatment has been used previously in literature for comparable studies on other metals [101]. This pre-treatment is chosen, as not only does it etch the metal surface to a native oxide, removing any remaining carbonaceous material, but it is also the major constituent in the organosilane solution used. The etching is again done ultrasonically, for 30 minutes, after which, samples are rinsed with deionised water and dried under a nitrogen flow.

A 0.75% PTMS solution is used in order to study any oscillatory behaviour. As found by Quinton et al. These oscillations are a product of both the iso-electric point of the material, but also the concentration [100, 101]. A lower concentration solution is used here in order to more easily observe any oscillations. This solution is prepared by adding the necessary quantity of organosilane to a continuously stirred solution of pH 3 acetic acid. This organosilane solution is stirred for 1 hour in order to ensure complete hydrolysis of the PTMS molecule. A pH of 3 is chosen in order to decrease the hydrolysis time, while the condensation time is increased, as found by Osterholtz and Pohl [89]. The hydrolysis of the organosilane can be observed to be completed when the PTMS is completely dissolved and miscible with the acetic acid solution.

2.5.2 Dip Coating Procedure:

Magnesium samples were immersed in the prepared PTMS solution for the desired time. Each sample was given a dedicated vessel which contained an equal amount of solution. Samples were added to the solution as a collective group at approximately the same time. They were then removed after the desired dip time had elapsed. Samples were then cured in an oven at 80°C, in order to remove any excess water still present in the film, completing any unfinished condensation reactions.

3 CHAPTER 3: CHEMICAL DIP COATING OF PTMS ONTO MAGNESIUM OXIDE

3.1 Introduction

Organosilane coatings are a more environmentally benign solution and have been the focus of much study for this purpose. One such mechanism of organosilane film growth is the oscillatory adsorption effect, reported by Quinton et al. in a series of papers [97-103]. In these studies, the adsorption uptake of the model organosilane propyl-trimethoxysilane (PTMS) was investigated on a range of metal substrates including aluminium, zinc, iron and chromium. It was found that the uptake of silane onto these surfaces did not follow kinetics resembling Langmuir or any other form of monotonically increasing growth as might be expected, but instead exhibited an oscillatory growth mechanism due to the complex inter-molecular and molecular-surface interactions which occur. Magnesium however, was not investigated and thus it is unknown whether PTMS follows the oscillatory behaviour on the surface of magnesium.

3.2 Surface Etching and Microstructure

It was immediately apparent that the pre-treatment and dip coating caused significant etching and discolouration of the magnesium surface, as shown in Figure 3.1. It has been previously reported that this particular pre-treatment does not affect other metals in such a dramatic way [101], but clearly the increased reactivity of magnesium when compared to aluminium or iron leads to significantly more etching.

Figure 3.1: Photograph of visible difference between polished magnesium pre (left) and post (right) pH 3.0 acetic acid pre-treatment

The apparent microstructure of the magnesium surface was also observed to become vastly

altered by the acetic acid pre-treatment. Figure 3.2 shows SEM images of the magnesium surface immediately after abrasion and also after the ultrasonic acetic acid treatment, clearly illustrating changes in the morphology of surface features. On the initial abraded sample, the grooves formed by the polishing process are relatively large and easily visible, and the surface is mostly comprised of magnesium and oxygen, with some trace carbon contamination. The surface of the sample after pre-treatment is significantly different. As well as an obvious visible discolouration, the SEM image shows a rough looking surface with several raised features that may indicate grain boundaries where a preferential chemical etching process has occurred.

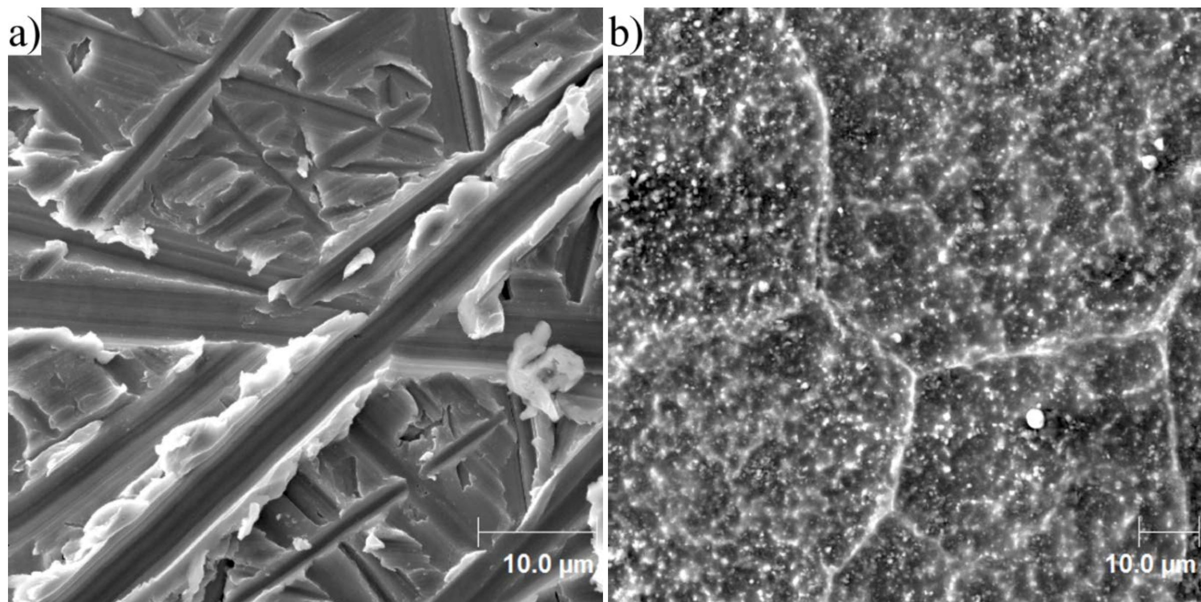

Figure 3.2: a) SEM image of pure magnesium abraded with 1200p silicon carbide paper. b) SEM of the same magnesium surface post etching for 30 minutes in pH 3 acetic acid.

3.3 XPS Analysis

In order to measure film growth, then a way of experimentally determining surface coverage must be utilized. This was achieved through the use of XPS, where the elemental concentrations of silicon and magnesium are found, and then converted into a value for coverage, Γ, defined by Equation 3.1:

$$\Gamma = \frac{\%Si}{\%Si + \%Mg} \tag{3.1}$$

Where %Si and %Mg are the percentage elemental concentrations of silicon and magnesium, as measured by XPS, with each acting as elemental markers for the film and substrate respectively. This ratio is ideal for observing slight variations in small values for coverage, and is therefore useful to observe the initial growth of films; as the coating grows

on the surface and signal from the substrate decreases, the value of Γ approaches 1. This is in comparison to using the ratio of silicon to magnesium directly, where the ratio approaches infinity as magnesium coverage approaches zero. It should be noted here, that while oxygen and carbon are detected in XPS, they are present on both the substrate and within the PTMS molecule, are therefore unsuitable as exclusive elemental markers. As discussed in Chapter 1, the use of the term "Γ" was first reported by Quinton et al.[97], in order to investigate PTMS uptake onto aluminium. Subsequent investigations were then performed on iron, chromium and zinc surfaces (as described previously in Chapter 1, Section 1.3.2, with oscillatory uptake observed for all substrates [101, 102].

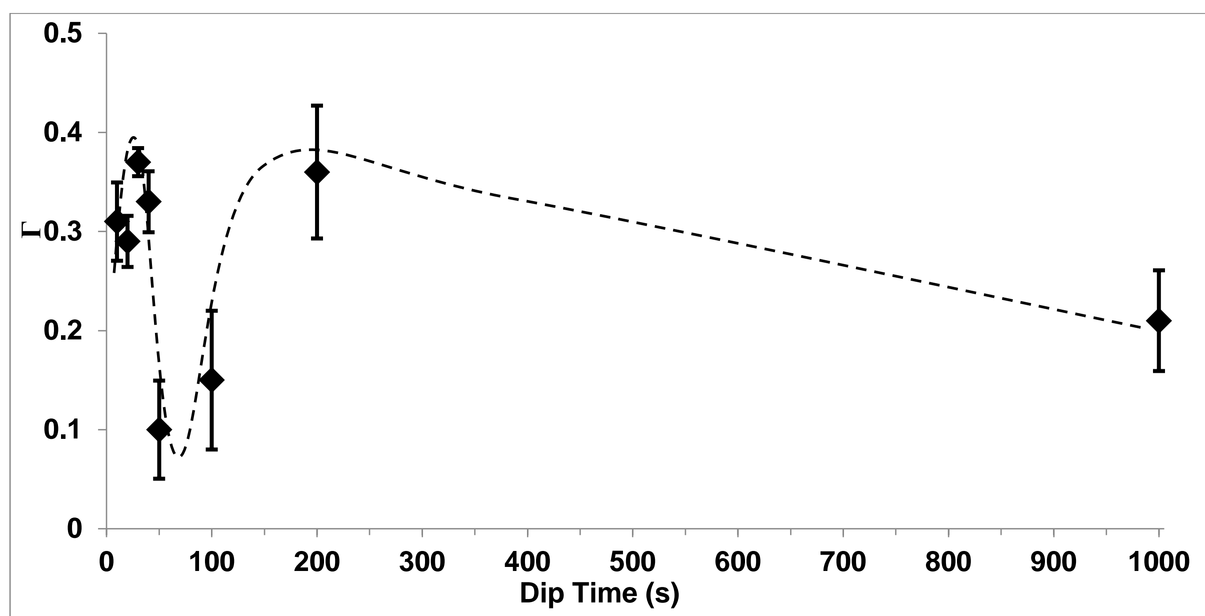

Figure 3.3: Surface coverage value "Γ" plotted against time. The dotted line is plotted as a guide to the eye. A significant decrease in coverage can be observed between 40 and 50 seconds.

Figure 3.3 indicates the measured surface coverage, Γ, as a function of exposure time to provide the film uptake curve for magnesium samples dip-coated in PTMS solution. Each data point on the curve in Figure 3.3 is the mean value for coverage from three individual samples, with an error bar obtained from the standard deviation in coverage. Similar to previous studies of this type, the uptake of PTMS appears to occur in an oscillatory fashion, rather than following a conventional model for adsorption, which has not been observed or reported previously for magnesium surfaces. However, there are several differences between this result and previous studies of this nature using other metal surfaces.

Firstly, the overall coverage of PTMS on magnesium is lower than that of aluminium, iron and chromium, which at the peak of their oscillations, possessed a value for Γ of

approximately 0.5, 0.95 and 0.6 respectively [101, 102]. Zinc oxide surfaces however, have the oscillation peak at a Γ value of approximately 0.3, slightly lower than what is seen here. The next observable difference, is that while the deviation of Γ between the first three samples is quite low, after dip time of 40 seconds there is significant variation between samples at each time point. Additionally, instead of reaching an equilibrium or complete coverage, there is a decrease (in coverage) between PTMS dip times of 200 and 1000 seconds, rather than the uptake curve increasing to an asymptote. The root cause of these differences is thought to be due to the continual etching of the magnesium surface by the acetic acid used as both the pre-treatment and catalyst in the silane solution. This etching provides a competitive process to adsorption and molecular self-assembly at the surface. Unless the deposition of PTMS progresses into a complete film that can act as a protective coating, then etching will continue until the magnesium surface is completely dissolved into the organosilane solution, which is indeed what occurs. Even if a larger or thicker magnesium token was used, as the deposition time increases, the overall amount of free silanol groups present in solution would decrease through inter-molecular cross-linking reactions, decreasing the rate of condensation reactions involved in attachment and cross-linking, and making the growth of a complete film even less likely.

3.4 **Scanning Auger Microscopy**

As a technique capable of two dimensional elemental mapping, scanning Auger spectromicroscopy was used to further investigate the morphology and structure of the deposited surface films. Indeed, a limitation of XPS is that it cannot determine between a thin film of PTMS spread across the entire surface, and a thick, incomplete one. The first notable observation from Auger spectromicroscopy results, is that the deposited films appear to be inhomogeneous, with a variety of different morphological features present across samples at different points on the uptake curve.

At short dip times, such as the 10 second exposure sample presented in Figures 3.4 a) and b), film-like structures appear to be forming, with silicon spectroscopically present (in green) correlating well with these features. Though these structures are small in size (less than 50μm in diameter, compared to the analysis area of XPS, which is on the order of mm^2), they are good evidence for the early stages of island-like growth.

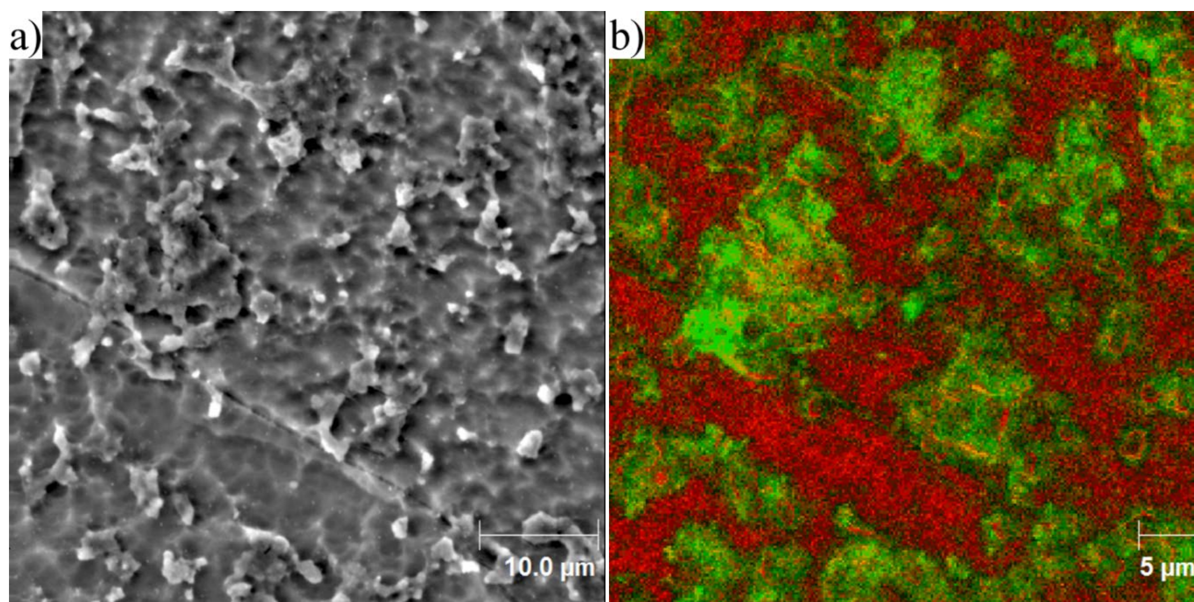

Figure 3.4: a) SEM image of 10 second dip coat of PTMS onto magnesium. b) Scanning Auger elemental maps of silicon (green) and magnesium (red), overlayed onto each other

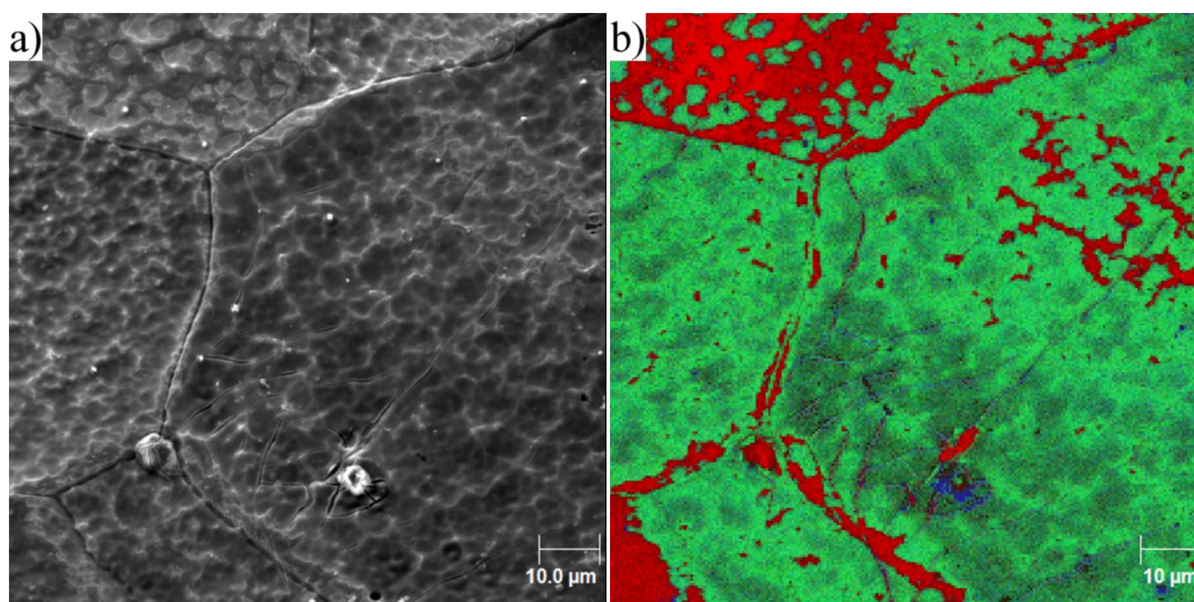

Figure 3.5: a) SEM image of 30 second dip coat of PTMS onto magnesium 3.5b) Overlayed scanning Auger elemental maps of silicon (green), magnesium (red) and carbon (blue)

Figure 3.5 b) shows the surface created after a 30 second PTMS deposition time. The island-like features seen previously for a 10 second exposure appear to have coalesced into a complete film which covers greater areas of the surface. However, the film still appears to be incomplete, with uncoated regions of magnesium observable between film domains. These are attributable to features present in the SEM image; most notably as darker areas present near the top, left-hand side of Figure 3.5. An interesting observation to make here is

that the features on the magnesium surface, previously attributed to grain boundaries, are able to be clearly identified in Figure 3.5 b) as areas that are not coated by PTMS. By looking closely at both the SEM image and elemental maps, it can be seen that there is silicon present within these features while the edges remain, for the most part, uncoated. There are several potential explanations for this behaviour. It may simply be that the rate of adsorption at the grain boundaries is slower, so the film grows up to these edges relatively quickly. As the boundaries are too large to be bridged by individual PTMS molecules or smaller oligomers, the film growth across these regions occurs comparatively slowly. Alternatively, as discussed briefly, etching of the magnesium by the acetic acid catalyst is still occurring on areas of uncoated magnesium oxide which is likely preferential at these grain boundaries. In addition to the features attributed to grain boundaries, there are also cracks present in more complete areas of film. These are very different in appearance and are attributed to the curing process. As the film is cured, condensation reactions are forced to completion, causing a contraction of the film, which leads to splitting. This could also contribute to a withdrawal of the film from the grain boundaries.

From the XPS data presented in Section 3.3, it is known that as dip time increases there is a reduction in surface coverage. Figure 3.6 is an SEM image of a magnesium surface coated for 50 seconds, which places it at the low point of the oscillation.

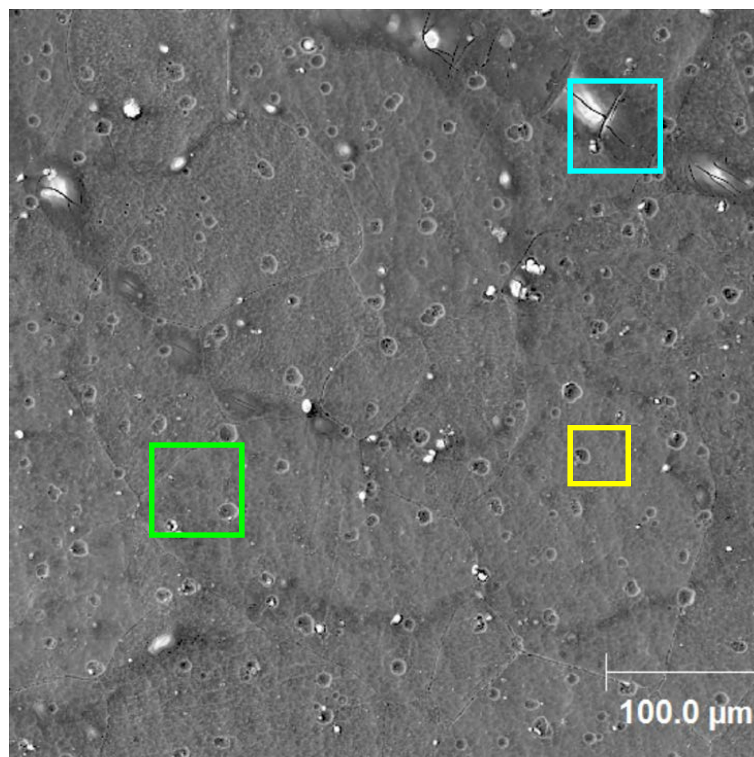

Figure 3.6: Large FoV (500µm) SEM image of 50 second dip coated magnesium sample. Areas of PTMS attachment appear as darker regions on SEM image. Highlighted in cyan: area of

PTMS film with cracks caused by curing. Highlighted in yellow: circular feature in magnesium surface. Highlighted in green: location chosen for further microscopy seen in Figure 3.7.

The grain boundaries caused through the etching of the magnesium surface by acetic acid are still visible, although they appear finer than what has been shown previously due to the larger scale of the image. Unlike in Figure 3.5, a PTMS film does not cover the majority of the surface. Instead, areas of PTMS are sparsely present across the surface in 'island chains' with many displaying cracks as highlighted by the cyan box in Figure 3.6. These cracks are thought to be caused by increased tension within the film as the curing process causes it to contract.

A large amount of vaguely circular features are also present on the surface (with an example highlighted in yellow in Figure 3.6), which were not detected on any previous samples. Both an area of film and one of these features is highlighted in green in Figure 3.6, and examined with increased magnification in Figure 3.7. The circular features are identifiable on samples of this exposure time and longer, with the one in Figure 3.7a) appearing at the intersection of the grain boundaries. While a distinct feature in the SEM image, spectroscopically in 3.7b), this feature does not appear to show any significant differences in composition to the surrounding material, and appears to be a feature of the magnesium surface. The control sample (Figure 3.2b), has no such structures visible on the surface, so it is unlikely that they are caused by the etching of magnesium by acetic acid alone.

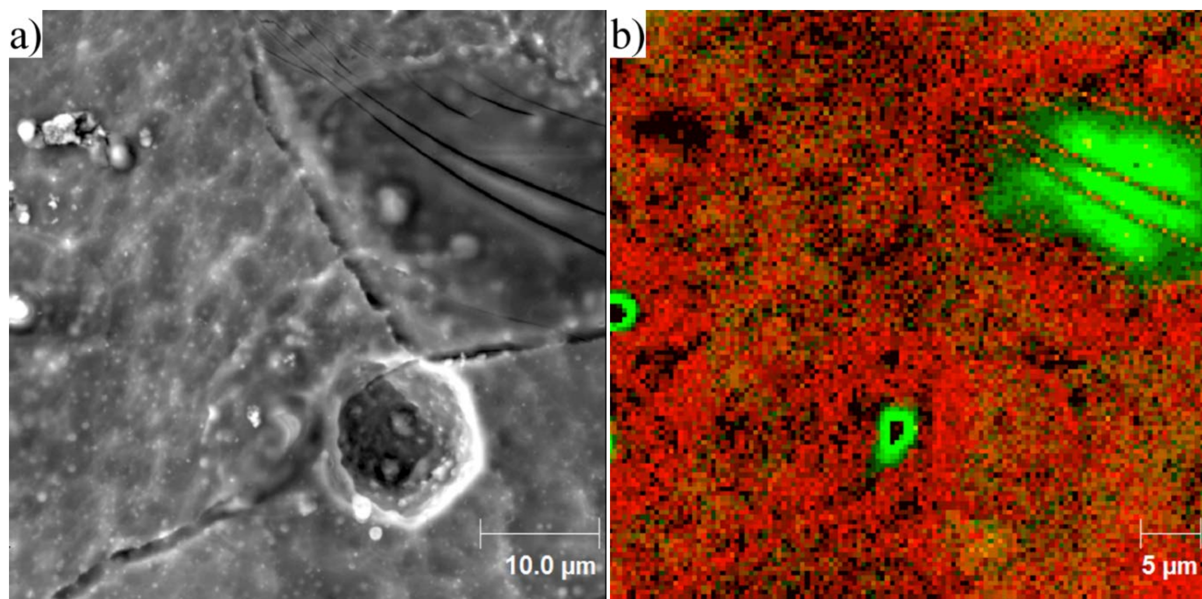

Figure 3.7: a) SEM of 50 second PTMS dip coated sample and 7b) Overlayed elemental maps of silicon (green) and magnesium (red) of the same area. Silicon signal is strong in the dark area of the surface seen in the upper right part of the SEM image

The dark feature seen in the upper right area of the SEM image in 3.7a), is an area of PTMS film, clearly correlated with the strong silicon signal present in the elemental map in figure 3.7b), including several of the cracks associated with film curing. Less obvious from the SEM image, are several smaller areas of strong silicon signal that are also present. These appear as green 'rings' in 3.7b), which is attributed to charging of these areas of the surface under electron beam irradiation, causing the spectral location of the silicon Auger electron peak to shift such that it is no longer appears within the software's analysis region defined for the silicon peak. This implies that these areas of silicon are sufficiently non-conductive to prevent either the replenishment of electrons lost to the Auger effect, or the dissipation of electrons from the primary beam. Features such as these were not seen on any previous samples, and the exact process of their formation is unknown. There are two likely explanations: they are either strongly attached remnants of the earlier PTMS film that has continued to grow, rather than detaching with the majority of the film or alternatively, larger particles of PTMS that have condensed in solution, then been deposited onto the surface. In addition to these 'thicker' areas of film, there is a faint silicon signal detected across some remaining areas of the surface in either a very thin and uniformly distributed layer, or a sparse one. It is unknown whether this silicon is a remainder of the film that is present at the peak of the adsorption oscillation, or newly attached.

Further examination of 50 second exposure samples led to the discovery of, seemingly, very different areas of the surface. Figure 3.8a) shows one such area, where large deposits of PTMS film, hundreds of micrometres squared in area, can be seen. Some of these areas are thick enough that the insulative nature of the organosilane film produces charging effects within the SEM image. This is observed as a 'lightening' of the surface where the film becomes thicker, in comparison to Figure 3.7, where areas of increased silicon coverage appear darker in the SEM image. Charging of the surface, either positive or negative, adds or subtracts kinetic energy to electrons emitted from the surface. SEM imaging relies on the quantity of secondary electrons emitted, rather than the energy of individual electrons. Auger electron spectromicroscopy however, is explicitly dependent on the energies of electrons. Therefore, where charging occurs and these energies are shifted significantly, and with changing intensity as the surface is under continual irradiation by the electron beam, Auger electron spectra become difficult and unreliable to acquire.

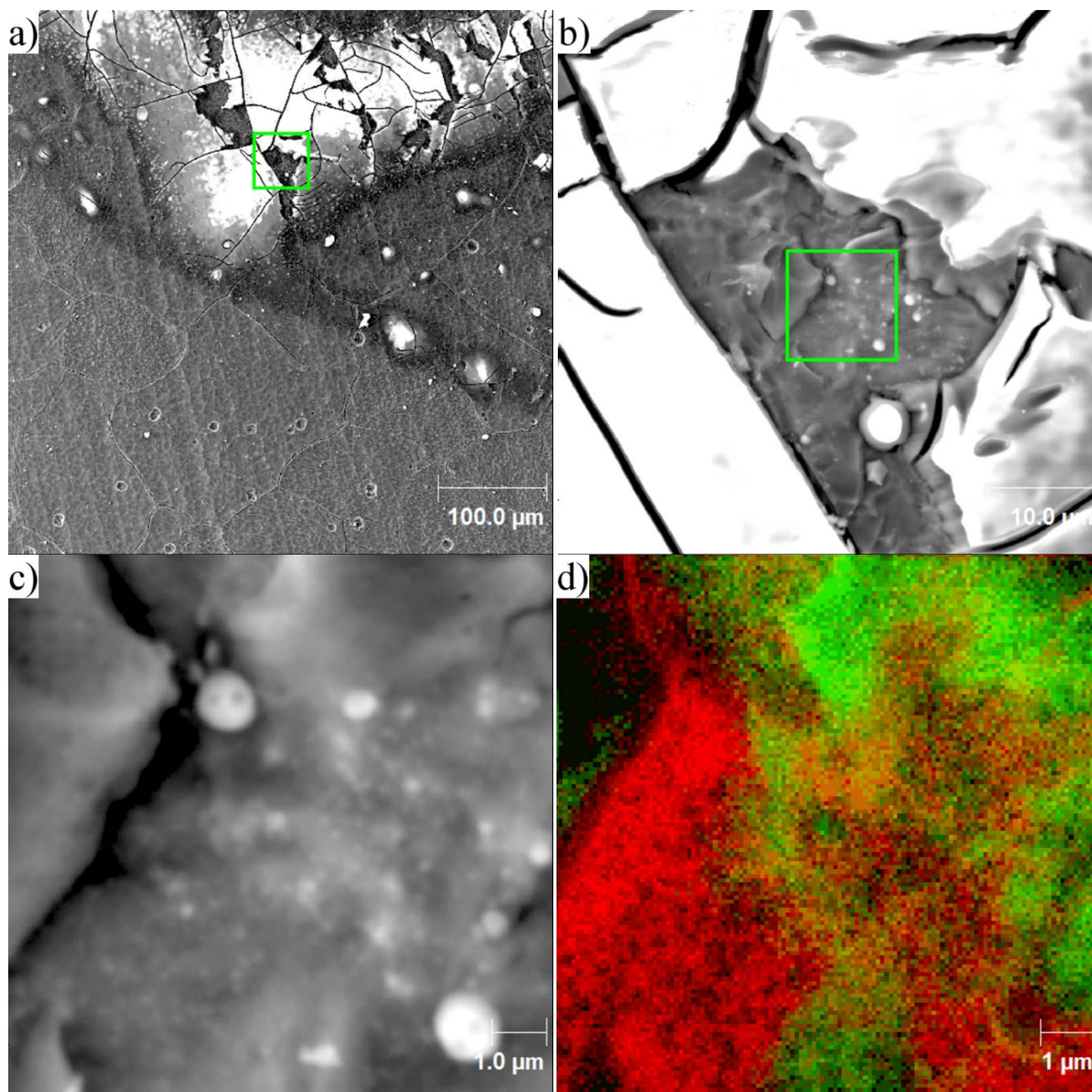

Figure 3.8: a) Large FoV (500μm) SEM of image showing a region of the magnesium surface coated by PTMS for 50 seconds (top half of image), with the approximate area of figure 3.8b) outlined in green. b) highlighted in green. 3.8b) SEM image of the area outlined within figure 3.8a), where a section of PTMS film has been removed from the magnesium substrate. 3.8c) SEM image of the area highlighted within 3.8b) and 3.8d) overlayed elemental maps of silicon (green) and magnesium (red) of the area shown by 3.8c)

By successively zooming in to the areas highlighted in Figures 3.8 a) and b), areas of increased charging may be avoided, allowing further information to be obtained through elemental mapping. In this region of the surface, seen in Figure 3.8 c), it appears that despite the apparent thickness of the film, several cracks have formed, resulting in the removal of material where they intersect. The elemental maps of silicon and magnesium in Figure 3.8 d) show that there is silicon present in this area where the film was seemingly

removed. Either this silicon could be residual material from a larger piece that was removed after the curing step or, alternatively, the PTMS is being removed from the surface in solution, either leaving a remnant of the previously attached film, or a bare magnesium oxide surface. If the latter is the case, then the silicon present here could be from newly attached PTMS molecules.

Evidence for these large areas of film being removed in solution is given by the lack of any such features on later samples. Figure 3.9 shows a region representative of the 100 second dip samples, with a similar value for coverage as Figure 3.8 from XPS data, yet a surface dissimilar in appearance. The lack of thick areas of film across any of the 100 second dip samples means that even these seemingly strongly attached films must have been removed in solution.

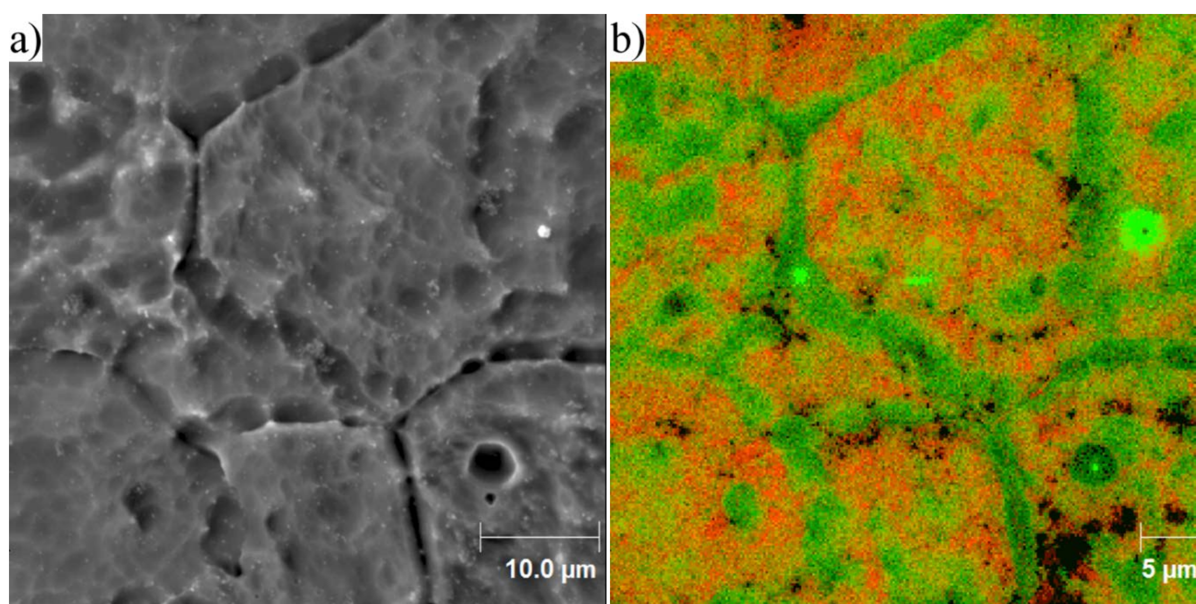

Figure 3.9 a) SEM image of 100 second PTMS dip coat of magnesium surface. Previous areas of thick PTMS film have been removed. b) Overlayed elemental maps of silicon (green) and magnesium (red) corresponding to SEM image of 3.9a).

That is not to say that there is no silicon present at all. The overlayed magnesium and silicon maps in Figure 3.9b) clearly shows islands of silicon present across large sections of the magnesium surface. The presence of the silicon on the SEM image is far more subtle but still visible, as observed previously, as a darkening of the magnesium surface. In contrast to earlier samples, the silicon is spread across the plateaus of the magnesium surface, as well as concentrated near the grain boundaries associated with the etching of magnesium. If these grain boundaries are areas with a reduced deposition rate as was previously presumed for the explanation of the adsorption behaviour seen in Figure 3.5, then it is

curious as to why the same effect is not observed here. By comparing the structure of the grain boundaries in the SEM images of both samples, it becomes clear that there is a difference in the appearance of these edges.

Figure 3.10 shows one of these boundaries at higher magnification, with areas of deposited PTMS seen with increased definition. A dark line associated with the 'grain boundary' is identifiable on the SEM image, despite the apparent coating of silicon, implying a thin film. It is also apparent in the overlayed elemental maps in Figure 3.10 b) that there are many smaller islands of silicon that were not able to be resolved at lower magnification. This gives some evidence for a cycle of continued film growth, despite the low coverage value observed from XPS data.

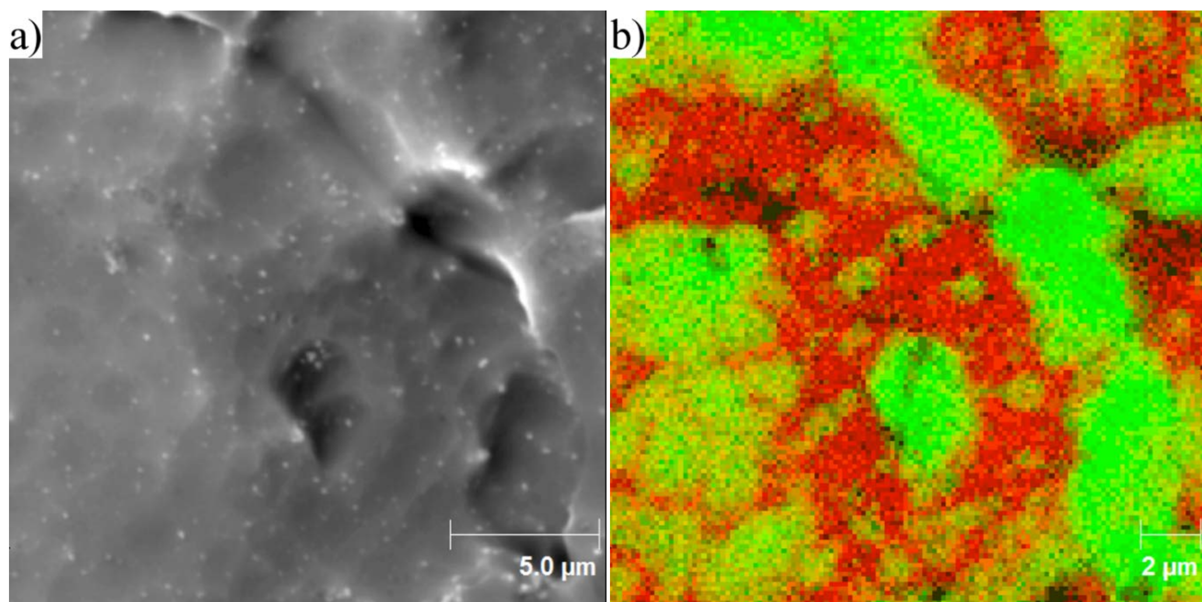

Figure 3.10 a) SEM image of 100 second PTMS dip coat of magnesium surface at higher magnification than seen in Figure 3.9. b) Corresponding overlayed elemental map of silicon (green) and magnesium (red) of SEM image seen in 3.10 a).

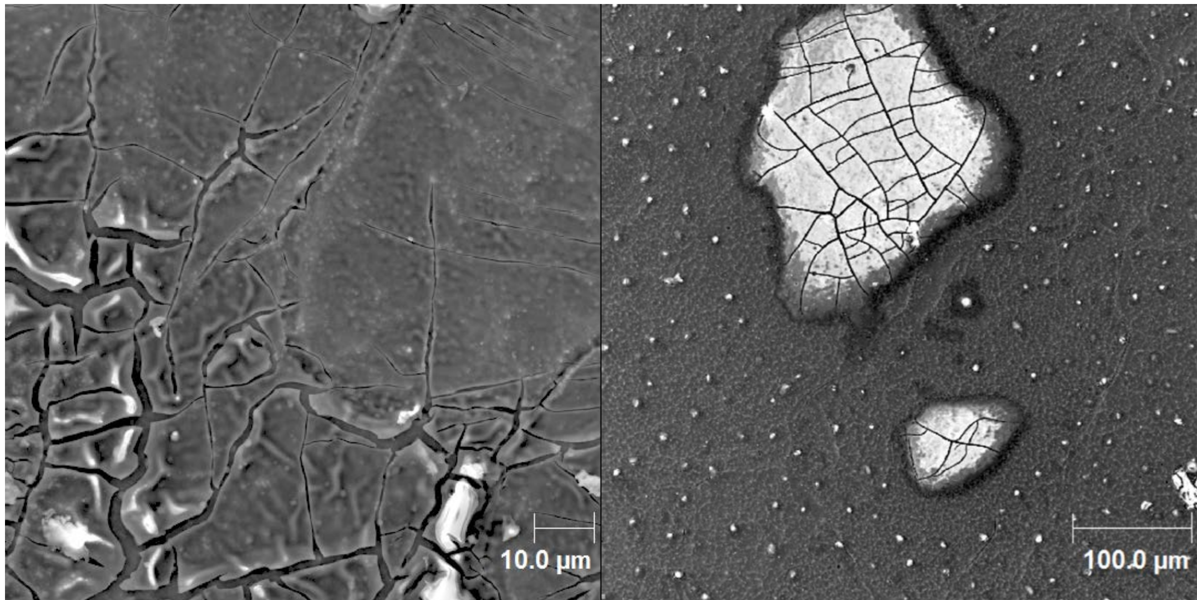

Figure 3.11: a) 100µm^2 area of a 200 second PTMS dip coated magnesium surface. Areas of PTMS film can be readily observed, with some thicker areas as signalled by the presence of charging. b) Large FoV (500µm) SEM image of 1000 second PTMS dip coated magnesium surface. Large, cracked, islands of PTMS film are visible on the magnesium surface.

Further evidence for continued oscillatory behaviour can be seen in the SEM images of samples dipped for 200 and 1000 seconds in Figures 3.11 a) and 3.11 b) respectively. After 200 seconds, the magnesium surface again seems to be coated in a thicker film, though one with a significant amount of the cracking seen on earlier samples. The value for coverage from XPS data for this sample is approximately the same as the 30 second dip coat sample in Figure 3.4 but it is clear that the structure of the surface film in both cases is quite different. The film structure in 3.11 a) appears to be much thicker, with charging seen in some areas of the SEM image. If the film is in fact much thicker and the cracking is caused by the curing of the film, then the observed structures should provide an effective barrier coating. If this were the case, then barring further oscillations in the uptake of PTMS onto the magnesium surface, the value for coverage should increase as dip time increases from this point. Clearly, this is not occurring, as evidenced in both the XPS data Figure 3.3 and the SEM image of an area of a magnesium surface dip coated for 1000 seconds in Figure 3.11 b). There are striking similarities between Figure 3.11 b) and the surfaces dip coated for 50 seconds (seen previously in Figure 3.8 a), which correspond to the low point of the oscillation observed in XPS data). On both surfaces, silicon is confined to large island-like structures, which implies at least a second cycle of film removal, although it is possible that further cycles of film adsorption/removal could occur between the dip times examined.

Longer exposure times were unable to be investigated, as the etching of the magnesium

surface continued until it completely dissolved in the PTMS solution, rather than reaching an equilibrium. Throughout the range of deposition times, competing processes appear to occur. Firstly, the oscillatory uptake of the PTMS onto the magnesium surface, as evidenced by XPS data, and the initial island-like growth of the PTMS film, followed by a thickening and then desorption of said film. Secondly, the etching of the magnesium surface by the acetic acid used as a catalyst, as seen in SEM images which show the continued presence of a surface structure (with potential grain boundaries) similar to the control sample. This etching appears to undermine the film and contribute to the removal of even larger, thicker areas of PTMS film which should, theoretically, be well attached to the surface through multiple metal-siloxane bonds. The continued removal of both magnesium substrate and attached organosilane prevents a complete film from forming to provide a barrier to such etching. Inter-molecular condensation reactions between PTMS molecules means that over time, the amount of sites available to produce metal-siloxane bonds decreases and therefore so does the rate of deposition.

3.5 **Summary**

The uptake of PTMS onto pure magnesium surfaces was investigated through the use of two forms of electron spectroscopy: XPS and AES, as well as electron microscopy. XPS analysis and comparison of the silicon 2*p* and magnesium 2*p* photoelectron peaks has demonstrated that the uptake of PTMS onto pure magnesium appears oscillatory, with an initial growth of the film, followed by a reduction in silicon containing species and a subsequent secondary growth stage. Scanning Auger spectromicroscopy was used to further investigate the growth and structure of the deposited films. It was found that for the short dip times, small islands of PTMS form and grow to a near-complete film across the magnesium surface. For the films investigated with dip time of 50 seconds, a significant decrease in silicon was observed on the surface, supporting XPS results that PTMS is desorbing from the surface. This was followed by further film growth, suggesting that the uptake is oscillatory in nature.

Throughout these experiments, etching of the magnesium substrate by the acetic acid used as a catalyst for PTMS hydrolysis meant that the organosilane film was continually undermined and never reached an equilibrium in coverage. This high rate of magnesium removal meant that samples were completely dissolved after approximately one hour.

4 CHAPTER 4: DESIGN, CONSTRUCTION AND TESTING OF A PLASMA CHAMBER FOR THIN FILM DEPOSITION

The results from the previous chapter have illustrated that it is possible to produce an organosilane film on pure magnesium surfaces using liquid chemical deposition methods. However the typical approach of using acid-catalysed conditions to control the solution and surface chemistry of film formation have proven to be quite problematic for PTMS films on magnesium, as the high reactivity and subsequent solubility of the substrate under these conditions makes the method non-ideal for the deposition of a thick, complete film to passivate the surface.

An alternate technique was therefore investigated, in the form of plasma enhanced chemical vapour deposition. This necessitated the creation of an apparatus capable of both igniting a plasma from a liquid precursor, and using it for the production of organosilane films.

4.1 Plasma Chamber Construction

4.1.1 Vacuum Chamber

The reactor used to perform plasma deposition is pictured in Figure 4.1. It was constructed at Flinders University in 1996, and was originally used for studying crystalline dust particles within plasma environments to simulate processes that occur in space [179, 180]. The chamber had been disused for several years however, and was not operational at the time it was requisitioned for this project. Of the previous experimental setup, only the steel chamber and antenna were salvageable for the purposes of restoration. The bulk of the construction is stainless steel, with the central reaction volume consisting of a cylinder with an internal diameter of 19.5cm and internal height of 19.5cm. Evenly spaced around this cylinder are four rectangular ports, each 50x100mm, two of which are viewports of 10mm thick glass. Another of these leads to a Granville-Phillips Micro-Ion Plus Two-Sensor Combination Vacuum Gauge, and an AX-600 Residual Gas Analyser (RGA), which are separated from the main reaction area by a 150mm steel tube. Below the chamber two pumps: a Pfeiffer HiPace 80 turbomolecular pump, backed by a Pfeiffer Duoline rotary vane pump, are used to evacuate the chamber to an observed base pressure of 1.0×10^{-7} Torr. Access to the chamber is through the top port, where a removable quartz plate (of thickness 13mm) is sealed via a nitrile gasket and secured by an aluminium ring, which is bolted to the main chamber.

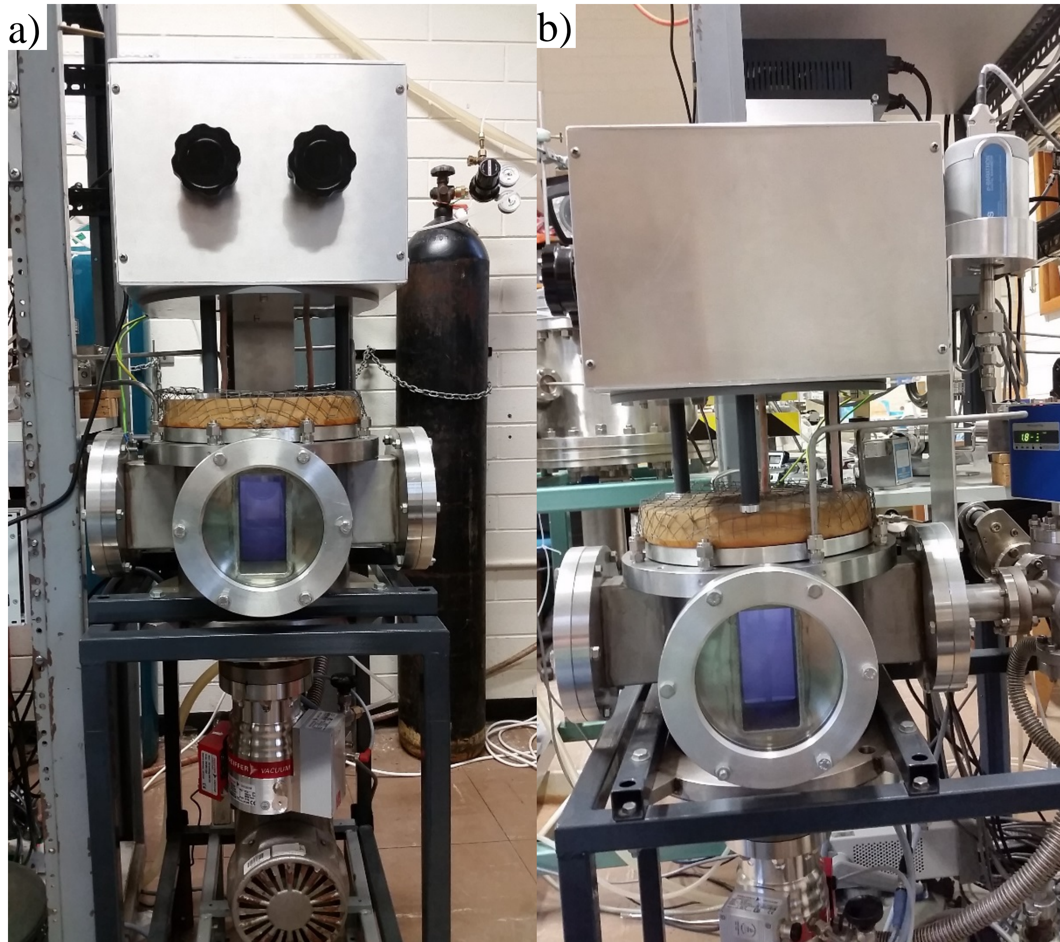

4.1 a) Frontal view of plasma chamber showing (from top to bottom) variable capacitance matching unit with control knobs, copper coil antenna encased in resin and fibreboard, steel chamber containing lit PTMS plasma, Turbomolecular pump and rotary vane pump. b) Side view of the chamber, including Baratron and Micro-ion Plus gauges

The antenna sits atop the quartz window, and consists of a planar coil antenna made up of eight turns of copper tubing contained in an epoxy resin (Araldite). Gas, both pressurised and from vaporised liquid precursor material is supplied to the chamber through eight 9/16" (14.2875mm) Swagelok fittings, which can be independently operated through 1/4" stainless steel tubing. One of these is connected to an MKS E27C Capacitance Manometer (or baratron) for measurement of pressure when the plasma environment is present. The baratron is an important part of the system, due to the physical nature of its operation (it measures capacitance between a movable diaphragm and an electrode) it is gas independent and thus not affected by charged species within the plasma environment. It is therefore also possible to accurately measure the pressure of plasma comprised of a mixture of feed gases, a feature that will become important in Chapter 6.

4.1.2 RF Matching Unit Theory, Design and Construction

During construction and assembly, the lack of an RF matching circuit for the antenna was of concern. Power transfer in RF circuits works quite differently than in conventional DC applications, so simply connecting to a RF power supply is not an effective option as the impedances are likely to be significantly different. For effective and optimal power transfer to occur, the impedance of the source electronics must be matched to that of the plasma. An AC circuit's impedance (Z) is represented by a complex number phasor, consisting of ('real') resistance (R) and ('imaginary') reactance (X) to describe the overall phase shift between voltage and current. Resistance is a well-understood value: the opposition to a flow of current, with the relation between it, the voltage applied to the circuit, and the current delivered given in a DC circuit by Ohms law (V=IR). To fully understand the importance of reactance in regard to plasma chamber operation, the background theory of AC circuits must be given.

In an AC circuit, the current and voltage oscillate sinusoidally, as given by the time dependent equations:

$$V = V_o \sin(\omega t + \theta) \quad (4.1)$$

$$I = I_o \sin(\omega t) \quad (4.2)$$

Where V_o and I_o are peak voltage and current, ωt is the phase (where ω is the angular frequency, given as $\omega = 2\pi f$ and θ is the phase difference between voltage and current. In a purely resistive circuit, there is no phase shift between voltage and current, so Ohms law still applies for all time points, as: $V_o = I_o Z$, or more generally, using the root mean squared current and voltage: $V_{RMS} = I_{RMS} Z$

Impedance is used, rather than resistance as the circuit used to produce an RF plasma is not purely resistive. The antenna used to couple the source electronics to the gas to be ignited into plasma is an inductor, and any plasma sheaths created around surfaces in the chamber during operation possess capacitive components. In AC circuits, both of these components give non-zero values for 'reactance', making the system more challenging to work with. The term reactance is used to describe the measure of opposition to *change* in both current and voltage. Inductors and capacitors affect reactance in different ways, so it makes sense to break it down into two separate components, the capacitive reactance: X_C and the inductive reactance: X_L.

4.1.2.1 Capacitive reactance:

In a DC circuit, opposite charges build up on each parallel plate and once fully charged,

current ceases to flow. The voltage is related to the capacitance by the amount of charge stored on each plate (Q), such that $= \frac{Q}{C}$. This identity still applies for capacitance in AC circuits at any given moment. In an AC circuit voltage is a continually changing quantity and a capacitor in such a circuit will likewise constantly charge and discharge, and therefore not block the flow of current. The current that flows is equal to the rate at which charge is stored on the plates, therefore the charge on the capacitor is equal to the integral of current flowing onto the plate with respect to time such that:

$$Q = \int I.dt \quad (4.3)$$

So,

$V_C = \frac{1}{C}\int I.dt$ (where V_C signifies the voltage across the capacitance) (4.4)

Substituting Equation 4.2 into Equation 4 4 above leads to:

$$V_C = \frac{1}{C}\int I_0 \sin(\omega t).dt \quad (4.5)$$

$$V_C = -\frac{I_0}{\omega C}\cos(\omega t) \quad (4.6)$$

Using the identity: $cos(\theta) = -sin\left(\theta - \frac{\pi}{2}\right)$, it becomes

$$V_C = \frac{I_0}{\omega C}\sin\left(\omega t - \frac{\pi}{2}\right) \quad (4.7)$$

The value $\frac{1}{\omega C}$ is the capacitive reactance, X_C, defined as the ratio of peak voltage to peak current: $V_o = I_o X_C$

So:

$$V_C = V_o \sin\left(\omega t - \frac{\pi}{2}\right) \quad (4.8)$$

By comparing this to the original Equation 4.2 for Current: $I = I_o \sin(\omega t)$, it is clear that there is a phase shift of $-\frac{\pi}{2}$ radians in phase between the voltage and the current, where the voltage reaches its peak (for an ideal circuit that is purely capacitive) $\frac{\pi}{2}$ behind the current. This comes from the slight delay between current beginning to flow and charge actually building up on the plates. As the current and voltage are not in phase, $V_o = I_o X_C$ is valid, but $V = IX_C$ at any instant is not.

4.1.2.2 Inductive reactance:

In an inductor, the current flowing through the coil creates a magnetic field (as per Faraday's law of induction). The flux of this magnetic field φ_B is proportional to the current flowing. The inductance produced by an inductor is therefore defined as:

$$\varphi_B = L.I \tag{4.9}$$

Faraday's law (for a single loop) gives the emf, E_L (in this case in an inductor) as:

$$E_L = -d\frac{\varphi_B}{dt} \tag{4.10}$$

The sum of the voltage drop across the inductor, V_L, and the emf generated by the inductor must be equal to zero, (from Kirchhoff's rule (the sum of changes in potential around any closed path of a circuit must be zero).

$$V_L = -E_L \tag{4.11}$$

$$V_L = d\frac{\varphi_B}{dt} = \mathrm{L}\frac{\mathrm{dI}}{dt} \tag{4.12}$$

$$V_L = \mathrm{L}\frac{\mathrm{d}I_0\sin(\omega t)}{dt} \tag{4.13}$$

$$V_L = \omega \mathrm{L} I_0 \cos(\omega t) \tag{4.14}$$

By applying the trigonometric identity $cos(\theta) = sin\left(\theta + \frac{\pi}{2}\right)$

$$V_L = \omega \mathrm{L} I_0 \sin(\omega t + \frac{\pi}{2}) = V_0 \sin(\omega t + \frac{\pi}{2}) \tag{4.15}$$

Again, comparing the functions for current and voltage, there is again a phase shift of $\frac{\pi}{2}$ with the voltage 'leading' the current, or alternately, the current reaches its peak after the voltage. The physical cause of this is the existing emf from the previous voltage cycle impedes the flow of current when the potential is switched, leading to a slight delay in current.

The value ωL is termed the inductive reactance, X_L, and can also be defined as the ratio of peak voltage to peak current such that $V_o = I_o X_L$.

It should be noted, that both X_C and X_L are frequency dependent terms ($\omega = 2\pi f$), so that when f→0, as in a DC circuit, the reactance in a capacitor approaches infinity (and no current is passed), while in an inductor it becomes 0 (there is no back emf produced, and therefore no impedance to the flow of charge), as would be expected if a constant voltage

were supplied to such components and a steady state was reached.

These definitions are for ideal capacitors and inductors. In a real world device, the overall reactance is a combination of inductive and capacitive reactance from all individual components ($X_T=X_C+X_L$). Real world devices also have non-zero resistances, so the quantity termed “Impedance” is used. Impedance is defined as the complex number $Z=R+iX_T$ (commonly expressed as $Z=R+jX$ to avoid confusion with the symbol for electrical current, “I”). As each component will affect the phase of the circuit in a different way, the overall value for impedance for the circuit depends on the impedance for each component.

In an RF plasma system, the impedances of the power source and plasma itself must be well matched for power to be effectively transferred. Most plasma systems are unique, with resistive, capacitive and inductive components based on the antenna used, the geometry of the chamber and stray emf from their location in a laboratory, and that is before any gas is introduced to the chamber, or power supplied. When a plasma reaction is initiated, it also creates its own complex impedances. As such, a variable matching circuit is needed to connect the source to the ‘load’ for a variety of conditions. Importantly, there is a significant difference between the impedance of a particular volume of gas, and that same volume in the plasma state, and each plasma that is lit must be tuned for a variety of experimental plasma parameters such as applied RF power, the plasma gas pressure and composition

There is a range of typical matching circuits used, where inductors and capacitors are placed in particular geometries in order to change the value of the source circuit to better match the load. The circuit designed and constructed for the chamber used in this work used a “Pi” design, so called due to the geometry made by the inductor and two variable capacitors used, as can be seen in Figure 4.2. The inductor has an inductance of ~3.7μH (I1), while the two variable capacitors have capacitances of 32 – 950pF (C1) and 33 – 500pF (C2). Once constructed it was housed in a stainless steel box, to eliminate interference from stray RF sources.

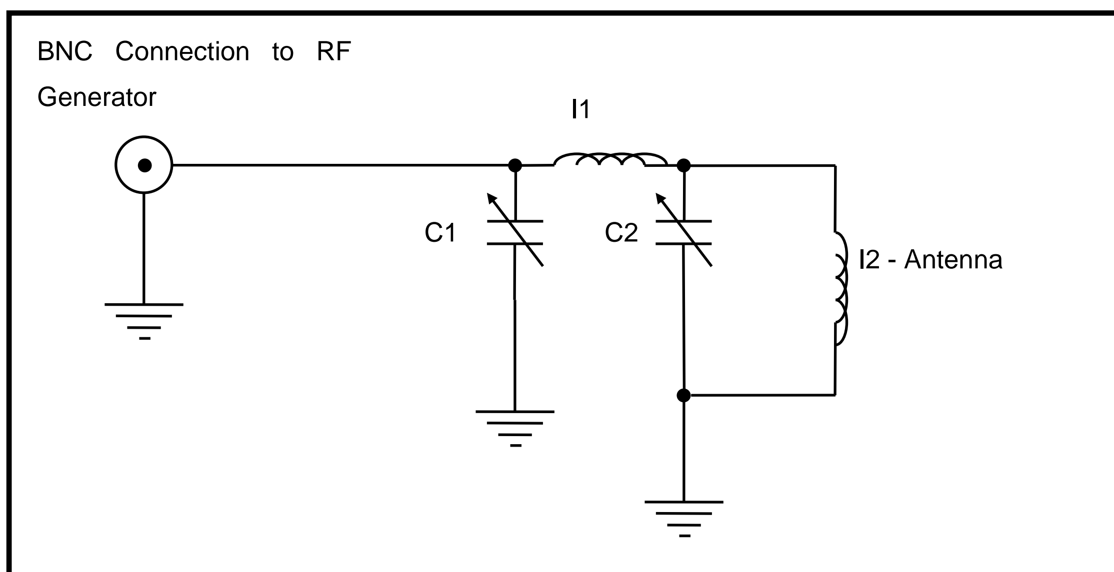

4.2 Circuit diagram of the matching circuit constructed for the plasma chamber used for this work.

Initial plasma operations were carried out with a range of gases including oxygen, argon, nitrogen and water, examples of which can be seen in Figure 4.3. The colours visible for the water and argon plasma were consistent with those seen in another operational plasma chamber in the laboratory. An attempt was also made to use a Quadrupole Mass Spectrometer (QMS) in order to determine the constituents within the plasma. However, the operational pressure range of the QMS lies below that of the prevailing supply gas pressures used for generating plasma, and was therefore unable to be used.

Figure 4.3: Images of (left to right) PTMS, water and argon plasma

4.2 **Preliminary Organosilane Deposition:**

With the plasma chamber operational, simple deposition experiments were undertaken. A liquid source, separate to the other gas lines, was attached and pure vapour from liquid PTMS was ignited into a plasma. The XPS results seen in Figure 4.4 show the difference between a control magnesium sample that was exposed to PTMS vapour and one exposed to PTMS plasma. Notably, the magnesium 2*s*, 2*p* and Auger peaks visible in the blue spectrum are replaced with silicon 2*s* and 2*p* peaks after plasma treatment, while carbon and oxygen 1s peaks are detectable in both. This makes it clear that the plasma results in film deposition, where the vapour by itself does not. As a proof of concept, these results were promising, but further investigation of the films produced is required.

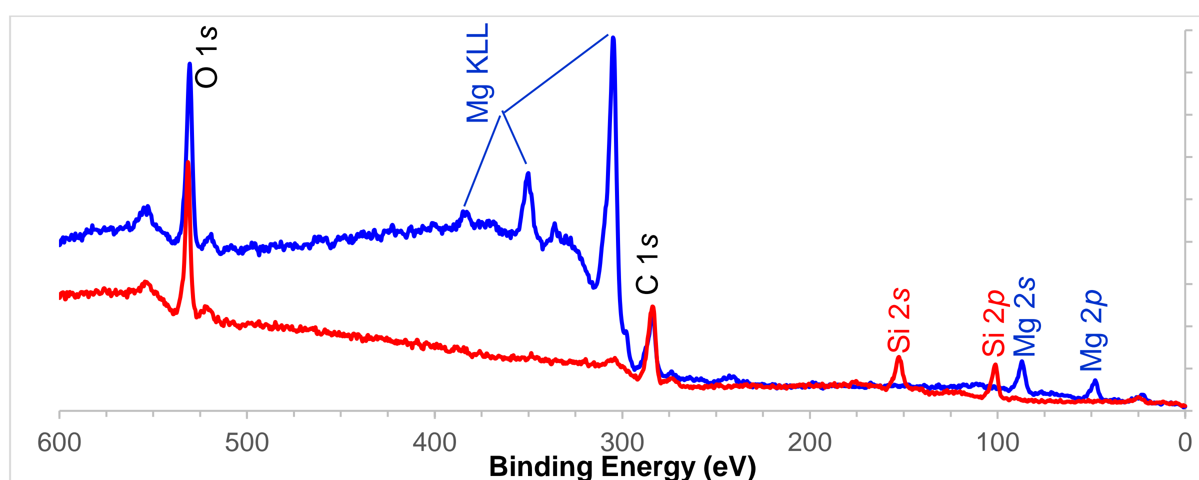

Figure 4.4 Comparison of XPS spectra of a magnesium surface that was exposed to PTMS vapour (blue), and one that was exposed to a PTMS plasma (red). The pressure of both vapour and plasma were identical (1.0×10^{-3}torr) as was exposure duration (5 minutes).

As previously established in Chapter 1 (Section 1.4.3), plasma reactions are incredibly complex and influenced heavily by chamber design and geometry. Thus power, duration and pressure values used in previous literature will not directly translate to the chamber used here, even when compared with those that utilise similar methods of plasma generation. Consequently, basic testing of the chamber and the influence of various experimental plasma parameters needed to be undertaken.

For these experiments, different plasma environments were used for pre-treatment and film deposition experiments. Oxygen plasma was utilized for pre-treatment purposes. The method by which plasma is able to clean the surface is a combination of physical and, for the chosen gas, chemical methods. Physically, high-energy atoms and molecules in the plasma will bombard the surface and potentially remove any weakly bound species. Chemically, oxygen ions and radicals are very reactive, especially with carbon, and so are able to react

with contamination present on the surface, while leaving the native oxide intact. Indeed, oxygen may also react with the magnesium surface to produce a more uniform oxide layer, which is favourable for PTMS attachment.

Shown in Figure 4.5 are the XPS spectra resulting from samples of pure magnesium abraded by 1200p silicon carbide paper, one of which was subsequently exposed to an oxygen plasma of 20W for 5 minutes. The key photoelectron peaks detectable are the oxygen 1*s*, carbon 1*s* and magnesium 2*p* levels. The purpose of the oxygen plasma treatment was twofold. Firstly, to produce a uniform oxide layer on the magnesium for further attachment of organosilane molecules and secondly, as a cleaning step to remove surface contaminants. The presence then, of carbon in both spectra in Figure 4.5, implies that the cleaning procedure was insufficient to remove all surface carbon. Alternatively, as the sample was exposed to atmosphere between plasma treatment and analysis, it is possible that the carbon present in the spectrum here is adventitious carbon, which has attached to the surface during this transfer procedure, and the oxygen plasma treatment was able to completely remove carbon from the surface.

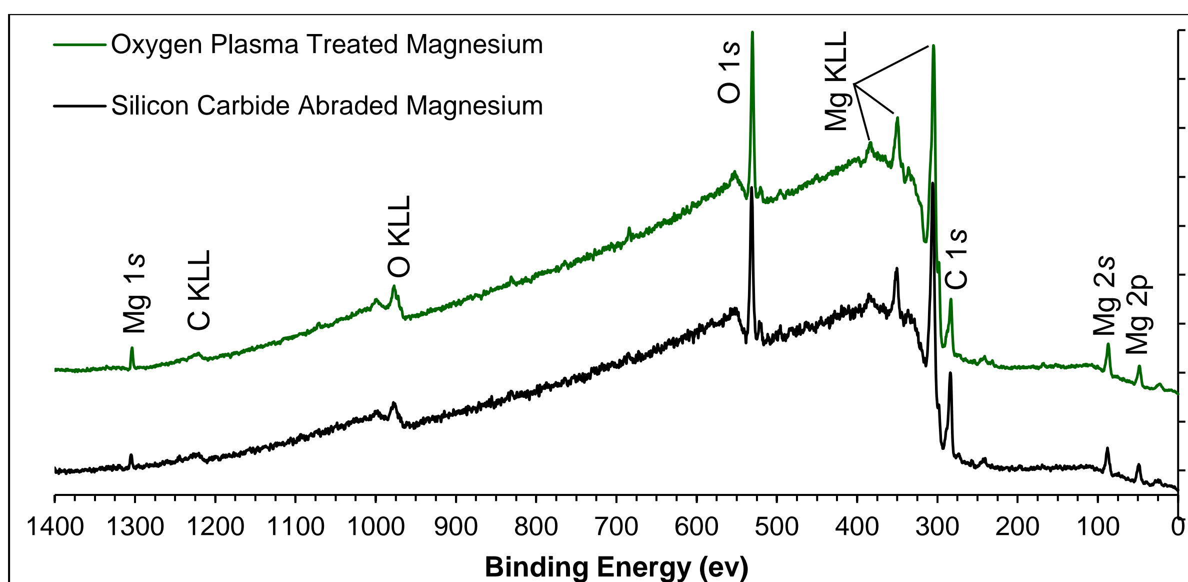

Figure 4.5: XPS spectra of magnesium surfaces after abrasion with 1200p silicon carbide paper (black) and subsequent oxygen plasma pre-treatment for 5 minutes at 20W applied power (green). Primary photoelectron and Auger peaks are labelled.

In order to further investigate the carbon presence, scanning Auger spectromicroscopy was adopted. Figure 4.6 consists of elemental maps of magnesium, carbon and oxygen, along with an SEM image of the analysis area. The carbon map in Figure 4.6 b) shows that the presence carbon on the surface is by no means uniform. Of interest is that there seems to be a correlation between rougher areas of the surface and the intensity of the carbon and

oxygen elemental maps. In areas of the surface with greater roughness, there appears to be a corresponding increase in carbon content. It is likely then, that materiel present in recessed areas of the sample is more difficult to remove. However, if the roughness of the surface affects the plasma interactions, this could have implications for any deposition performed on these surfaces.

Depth profiling of the pre-treated surface as seen in Figure 4.7 shows that the carbon is present only in a very thin surface layer (<5nm), while the oxide layer on the magnesium is approximately 20nm thick. The thickness of the oxide layer was determined by examining each individual spectrum that comprises the depth profile and noting the sputtering depth at which oxygen is removed from the surface.

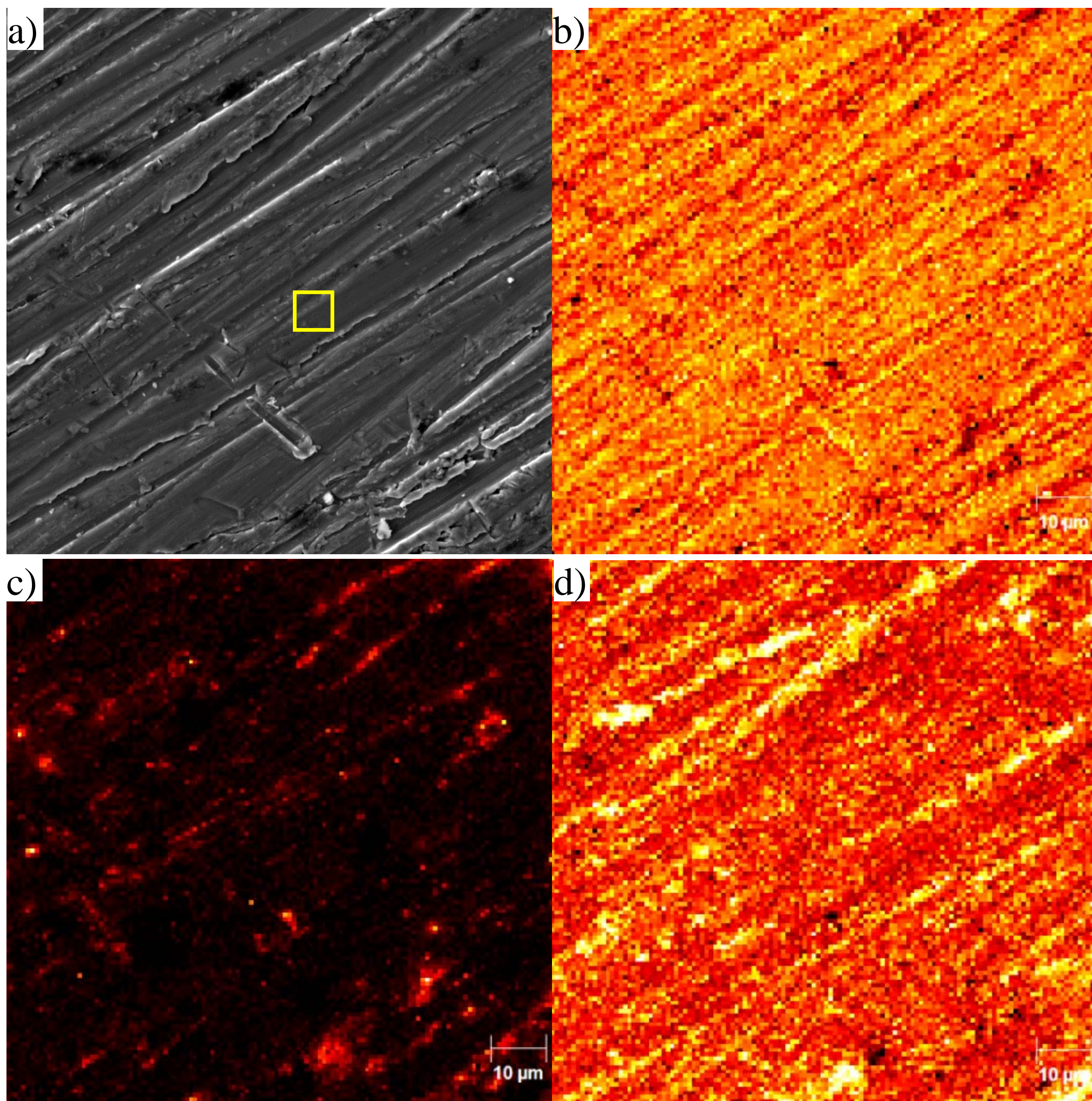

Figure 4.6: a)SEM image of oxygen plasma treated magnesium surface. The area highlighted in

yellow represents the location chosen for the example depth profile seen in Figure 4.7.

b), c), d): Elemental maps of magnesium, carbon and oxygen respectively, obtained for the same area as the SEM image in a). The analysis field of view (FoV) is 100μm, obtained using 10kV beam with 10nA current.

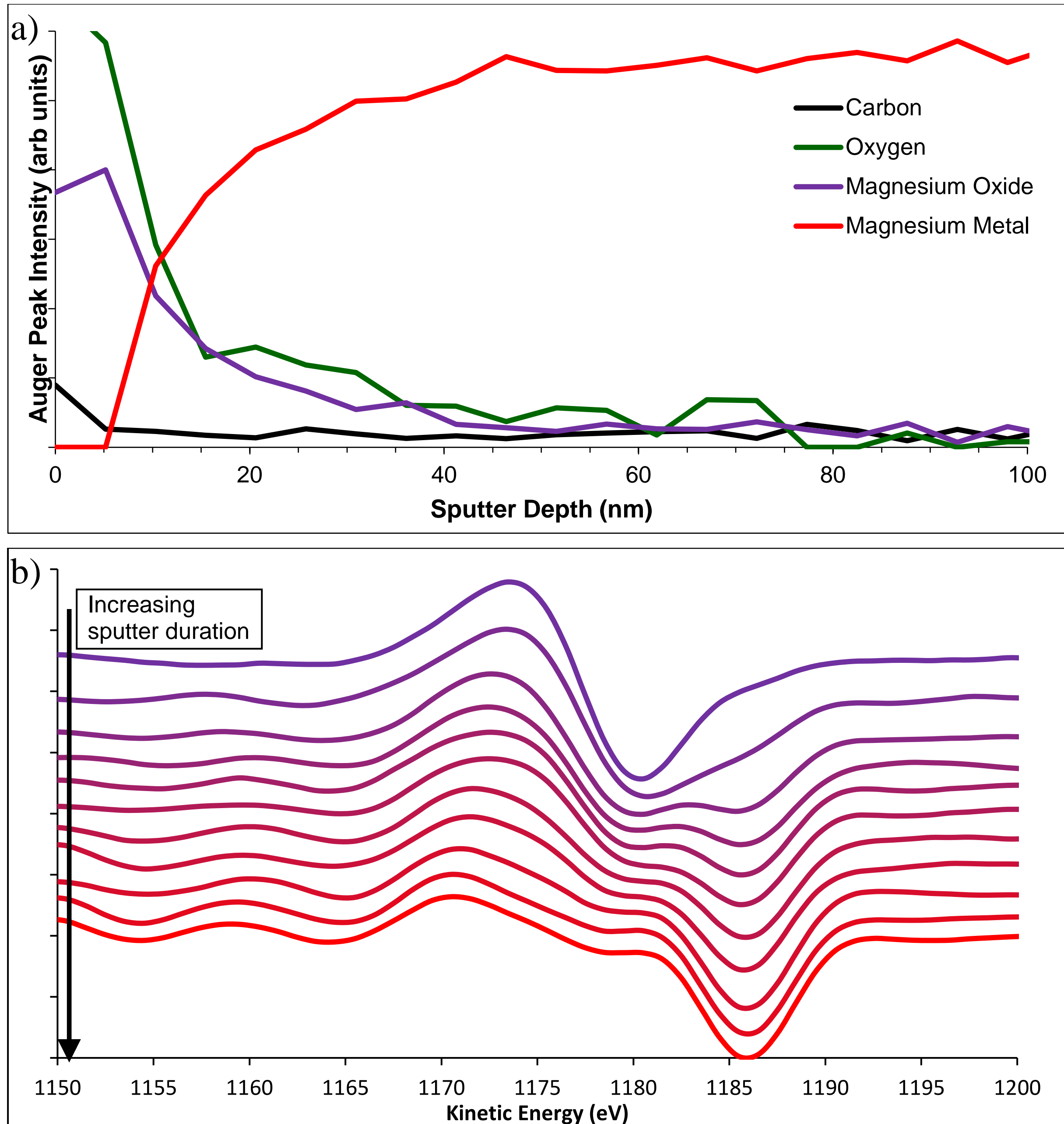

Figure 4.7 a) Auger Electron Spectroscopy (AES) depth profiles of carbon, oxygen and magnesium obtained from the area of an oxygen plasma treated surface as highlighted in Figure 4.6 a). The magnesium profile was deconvoluted into two constituent components; a metal and an oxide. b) Stack plot of differentiated AES spectra showing the evolution of the magnesium peak shape (top to bottom) as the depth profile progresses. The change in peak shape is modelled using Linear Least Squares (LLS) fitting (as described in Chapter 2, Section 2.1.8) to produce the two separate profiles seen in a).

4.2.1 Morphology of the Magnesium Surface

AFM was used to quantify surface roughness. Figure 4.8 shows two example AFM images of the kind used to calculate average roughness across three separate samples, with five such images obtained per sample. The average value of R_q, or RMS, roughness obtained for these samples was found to be 92.8±59.4nm. This significant roughness and uncertainty is a product of the surface finish provided by abrasion with 1200p silicon carbide paper, which leaves height features on the order of 5-10% the size of the spatial areas examined.

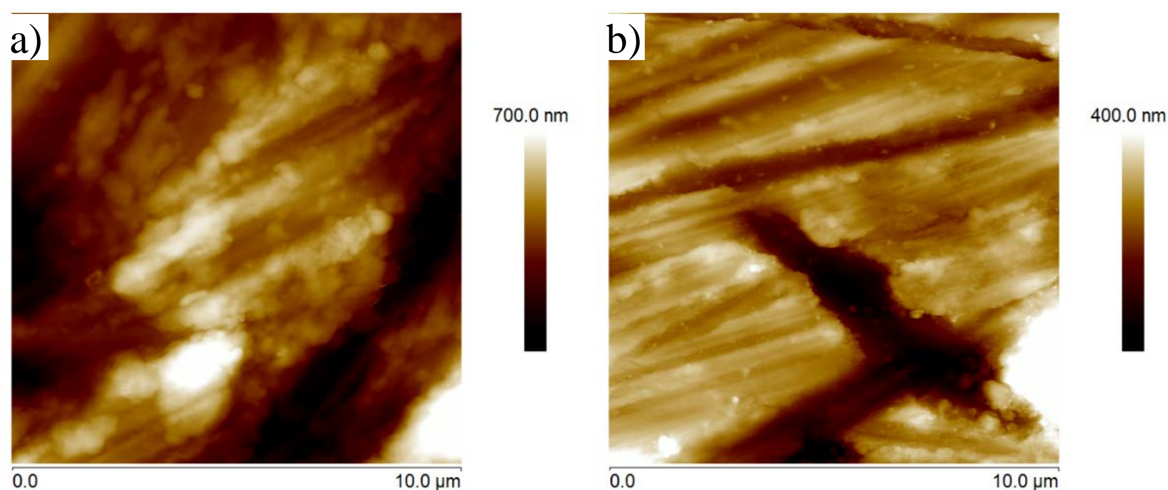

Figure 4.8: a) and b) Two example AFM images of pure magneisum substrates after both polishing with 1200p silicon carbide paper and oxygen plasma treatment

4.3 Time Dependent Investigation of Plasma Deposited PTMS Films

4.3.1 XPS Results

While the oxygen plasma treatment does not remove all carbon, there is a significant reduction compared to the control magnesium surfaces. Most importantly however, is that the surface produced by the oxygen plasma treatment is far more consistent, which allows for accurate comparison between deposited films. A systematic series of experiments were undertaken to examine the influence of both exposure time and applied plasma power on the growth and composition of PTMS films deposited from a pure monomer vapour. The pressure of this vapour was kept constant at 1.0×10^{-3} Torr throughout these experiments, and each variation of time or applied power was examined through three separate plasma treatments, with the magnesium substrate placed in the same location within the chamber for each treatment.

XPS analysis of the samples was used to determine both the coverage of the films, as well as the composition. The former is calculated in the same way as it was for the chemically

deposited films: $\left(\Gamma = \frac{Si}{Si+Mg}\right)$, where silicon and magnesium act as elemental markers for the PTMS film and substrate respectively. As it is known that both oxygen and carbon are present on the substrate as well as a constituent of PTMS, a value for gamma at or near 1 is necessary for the composition of the film to be accurately determined from XPS, implying that none of the underlying magnesium substrate can be detected spectrally.

The first of the XPS results seen in Figure 4.9, are from a series of experiments designed to determine the influence of plasma exposure time on the deposited film. For the films deposited up to 300 seconds in exposure time (which can be more clearly seen in the inset) Langmuir-like growth is observed as the film grows on the surface. Between 120 and 300 seconds, the surface becomes completely covered, after which no further magnesium signal is detectable, implying that over the analysis region of XPS, the surface is covered by a complete film of at least 10-20nm thickness on average.

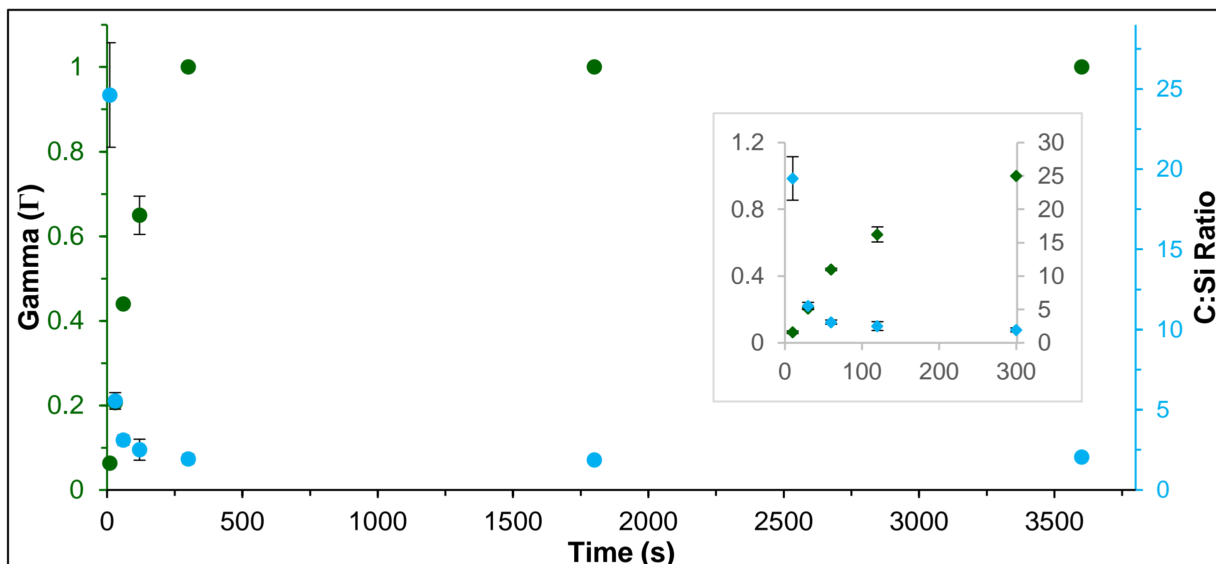

Figure 4.9 Green: Plot of surface coverage (Γ) vs plasma deposition time. Cyan: Plot of C:Si ratio vs plasma deposition time. Both plots are calculated from XPS data averaged from 3 separate samples. Error bars are calculated from standard deviation.
Inset: Deposition times between 0 and 300 seconds

Also plotted in Figure 4.9 is the ratio of C:Si over time, to gain insight into the structure of the film present. What is observed appears to vary inversely with the measured coverage. For the shortest plasma durations, there is much more carbon on the surface at a much higher ratio than that found in the PTMS molecule. This implies that despite the pre-treatment and cleaning procedures, carbonaceous material is not completely removed from the magnesium surface. This material does not seem to inhibit the growth of the organosilane film to any great extent though, as evidenced by the continued growth of the film and disappearance of

the magnesium signal at long exposure times. The rate at which Γ increases is not as great as the rate at which the C:Si ratio falls, which is unexpected. If carbonaceous contamination is present as a separate film on top of the magnesium surface, then the magnesium signal would decrease first (due to the shallow escape depth of photoelectrons) as the PTMS film grows. A likely explanation for the observed behaviour is that some etching of the surface by the PTMS plasma occurs. This rate of etching must be much lower than the rate of film growth however, else the overall coverage would not increase to completion (Γ=1). As the conditions within the plasma chamber during deposition are quite complex, it is likely that such a combination of factors are involved.

Once the magnesium surface is completely coated however, the C:Si ratio remains relatively constant at a value of ~2. As the ratio of C:Si in an un-hydrolysed PTMS molecule is 6:1, and no 'forced' hydrolysis step was undertaken, then this result indicates that on average, the PTMS molecule is fragmented in the plasma environment. By examining the strengths of the bonds present in PTMS, as seen in Figure 4.10 and Table 4.1, the carbon-carbon bonds present in the propyl-chain are the weakest and therefore most likely to dissociate first in an energetic environment. The observed C:Si ratio however, is lower than would occur if just carbon-carbon bonds were broken. The next lowest bond energies are the carbon-oxygen and carbon-silicon bonds which, if broken, would lead to the removal of –methyl groups and any remnants of the propyl chain respectively.

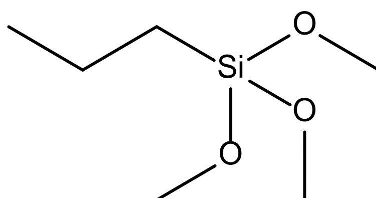

Figure 4.10: Theoretical structure of PTMS

Table 4.1: Average energies of chemical bonds ($kJ.mol^{-1}$)[181]

C-C	347
C-O	358
C-Si	360
Si-O	452

When the O:Si ratio is also examined in a similar manner, the value of this ratio is found to be ~1.3:1. This, as with the C:Si ratio, is lower than 3:1 for PTMS (both hydrolysed and

unhydrolysed), or even 2:1 for a silicon dioxide film. The material that this elemental ratio best resembles, is that of PDMS, which has an elemental composition of C:Si:O equal to 2:1:1.

In a wet chemical system, the reduction in O:Si ratio is not entirely unexpected, where condensation reactions between organosilane molecules or the surface result in the removal of an oxygen atom to water, thereby reducing the overall content of oxygen in the film. However, in a plasma, such elegant reactions are less likely to occur as species are not present in a liquid environment. Instead, the plasma must provide, or create species with enough energy to break one or more of the (strong) silicon-oxygen bonds.

4.3.2 Scanning Auger Spectromicroscopy Results

From the XPS results, it is clear that the elemental composition of the deposited organosilane significantly differs from that of the PTMS precursor molecule. However, due to the lack of complete surface coverage and the large analysis region of XPS, the measured elemental concentrations (especially for those samples with a value of Γ less than one) may not be a true indication of film composition, or distribution. As an example, for films deposited with shorter plasma exposure times (in this case under 300 seconds), it is impossible to determine whether the presence of magnesium in the spectra is a result of an incomplete film, or an evenly distributed one that is thinner than the analysis depth of XPS. Scanning Auger spectromicroscopy was therefore used as a complimentary technique to investigate the surface composition three dimensionally with high lateral spatial resolution.

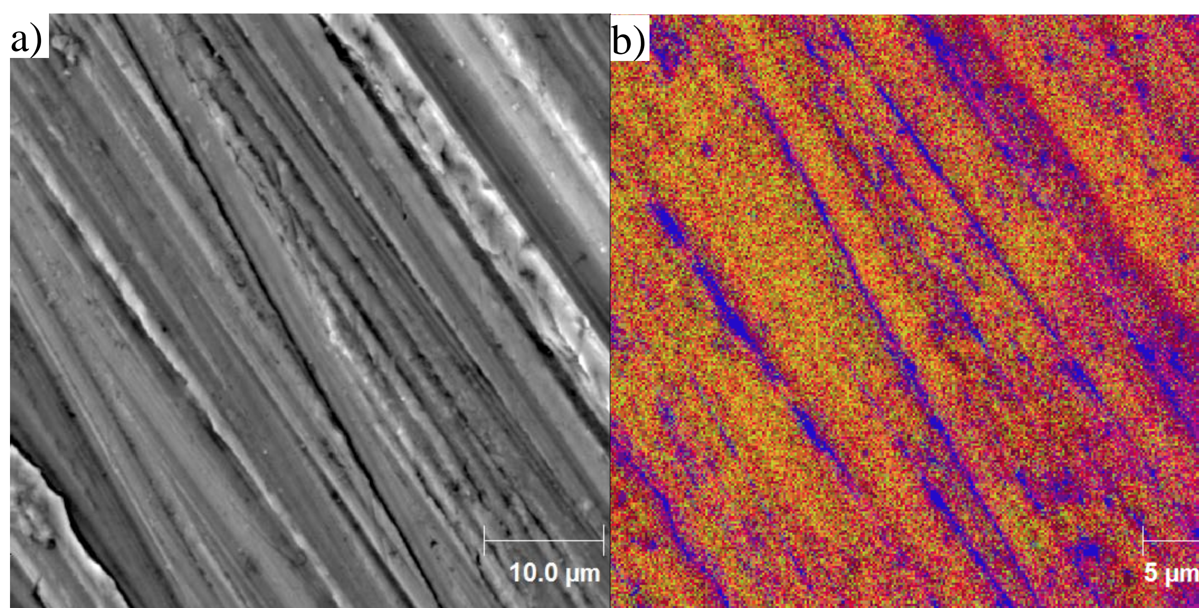

Figure 4.11: a) SEM image of magnesium surface after exposure to PTMS plasma for 10 seconds. b) Overlayed elemental maps of magnesium (red), silicon (green) and carbon (blue).

Beginning with the shortest plasma exposure time of 10 seconds, Figure 4.11 shows both an SEM image (a) and associated elemental maps of a representative area of the magnesium surface (b). In order to efficiently display these maps, each element has been assigned a colour, and then displayed together in a single image. In the maps presented here and for the remainder of this chapter, the elemental maps of magnesium appear in red, silicon is in green and carbon has been assigned blue. Hence they will be referred to from this point as 'RGB overlay' maps. Oxygen maps are not included for this purpose, as this display method is limited to three elements and as oxygen is a constituent part of both the substrate (magnesium oxide) and PTMS, less information about the surface can be obtained by including oxygen.

As could be expected from the elemental maps of the pre-treated sample and the XPS data, carbon is present across the surface, however the distinct 'blue' areas in Figure 4.11 b) show that it is not only as a part of the silane film, but also in the voids and crevasses created by the silicon carbide abrasion procedure. Of particular note is that a significant portion of this carbon is too thick for any magnesium or oxide to be detectable from underneath and is also seemingly uncoated by the silane from the plasma treatment. This implies that the plasma deposition method is not as substrate independent as previously thought – either the species in the PTMS plasma prefer to bond to the areas containing magnesium oxide or the rougher areas of the microstructure of the surface create areas which prevent the species of the plasma attaching here.

Of the silicon itself, while present in a relatively thin layer (magnesium is still detectable everywhere that silicon is), it does cover a significant portion of the surface. That the areas coated by silicon are undetectable on the SEM image is of no particular surprise then, if the deposited layer is so thin.

As plasma deposition time increases, the corresponding increase in silicon coverage from XPS can also be observed microscopically. Figure 4.12 a) shows an SEM image of a representative area of a surface exposed to PTMS plasma for 30 seconds, with the corresponding RGB overlay in Figure 4.12 b). In addition to these maps, individual elemental maps for both magnesium (4.12 c)) and silicon (4.12 d)) are presented.

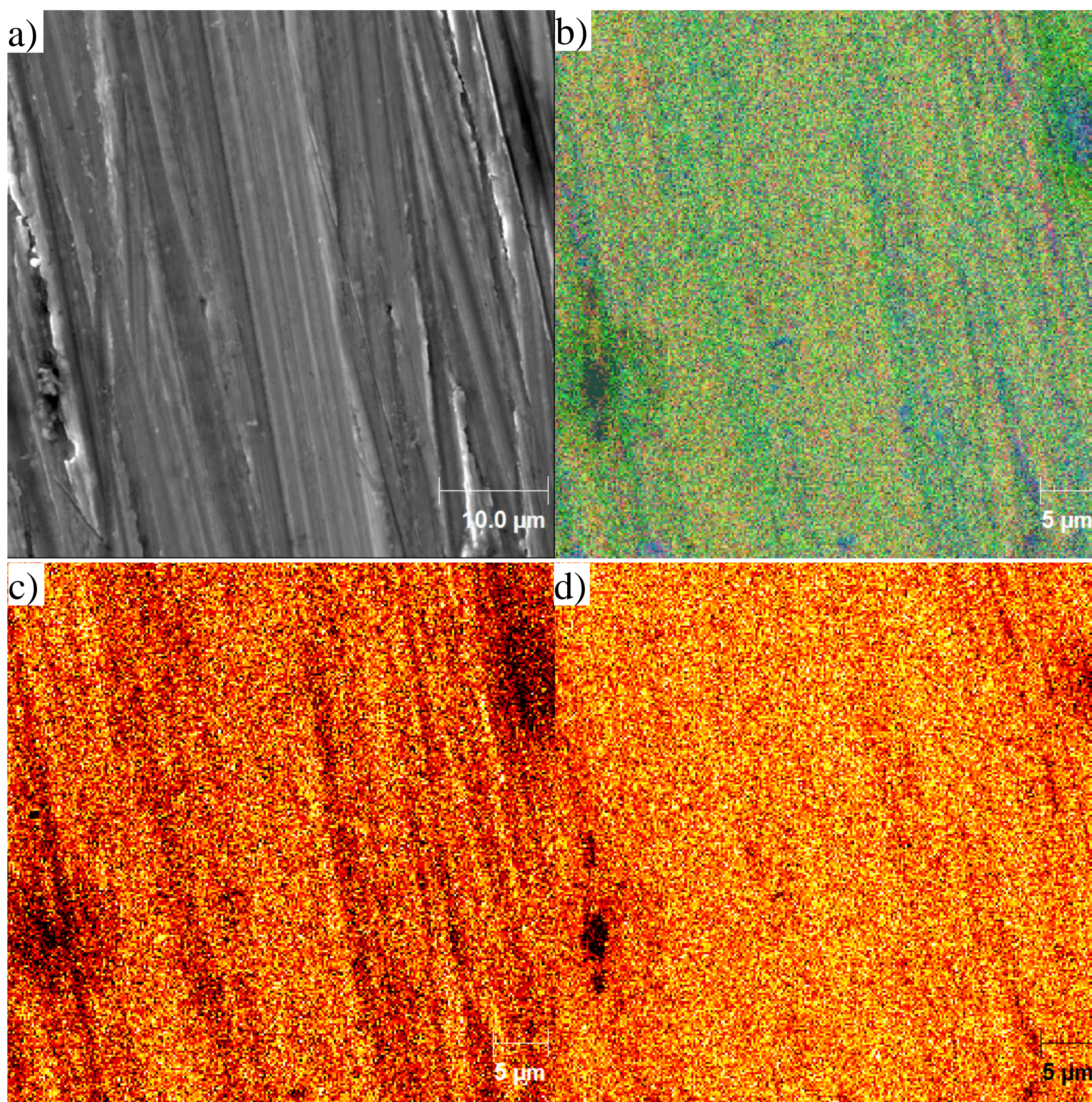

Figure 4.12: a)SEM image of a magnesium surface after exposure to PTMS plasma for 30 seconds b) Overlayed elemental maps of magnesium (red), silicon (green) and carbon (blue) for the corresponding area. c) and d) false colour elemental maps of magnesium and silicon respectively

In Figure 4.12 d), silicon appears to be uniformly distributed across the surface. When comparing this to the magnesium element map however, the fact that magnesium signal is still detectable through the deposited silicon layer implies that this film is thinner than the escape depth of electrons from the magnesium Auger transition. The non-uniformity in the magnesium map also implies that the thickness of the silicon layer is not as uniform as it appears on the silicon map alone: where the deposited layer is thicker, fewer Auger electrons from the magnesium oxide surface layer are able to reach the detector. In Figure 4.11 b), this variation in the intensity of the magnesium signal is signified by 'redder' areas of

the image, which correspond to a stronger magnesium presence and hence a thinner film. The precise cause of this non-uniformity is unknown however, the most likely explanation is that the surface roughness or morphology plays a role in the deposition process. Comparing the SEM image to the RGB overlay, there are physical surface features identifiable by the variation in elemental concentrations there. Some of the features seen in the overlay are areas of increased carbon concentration. When compared with the 10 second plasma exposure time in Figure 4.11 there are fewer areas of strong carbon concentration across the analysis area, despite the continued existence of 'channel-like' features in the magnesium surface. This implies areas of high carbon concentration are being coated, along with the magnesium surface, and preferential binding of the PTMS molecules to the magnesium oxide surface is not a dominant contributing factor to the deposition process.

After 60 seconds of plasma deposition, the elemental maps presented in Figure 4.13 show the silicon signal appearing more intense when compared with shorter deposition times, as could be expected from the XPS data. The elemental map of magnesium in Figure 4.13 c) shows that signal from the substrate remains detectable after this deposition time, implying a thin layer as with shorter deposition times. The intensity of magnesium in this map is also reduced when compared with these shorter times, which does suggest that the deposited layer is thickening as time increases. This can be observed in the RGB overlay, where the elemental map of silicon (in green) is much more intense than seen previously. Despite this, several areas of the RGB overlay show magnesium signal in red with little to no silicon signal detected. These areas correspond to deep scratches in the SEM image (Figure 4.13 a), which suggests that while smoother areas of the surface are more readily coated in silicon by the PTMS plasma, it is either unable or less likely to be deposited in the recessed areas of the surface.

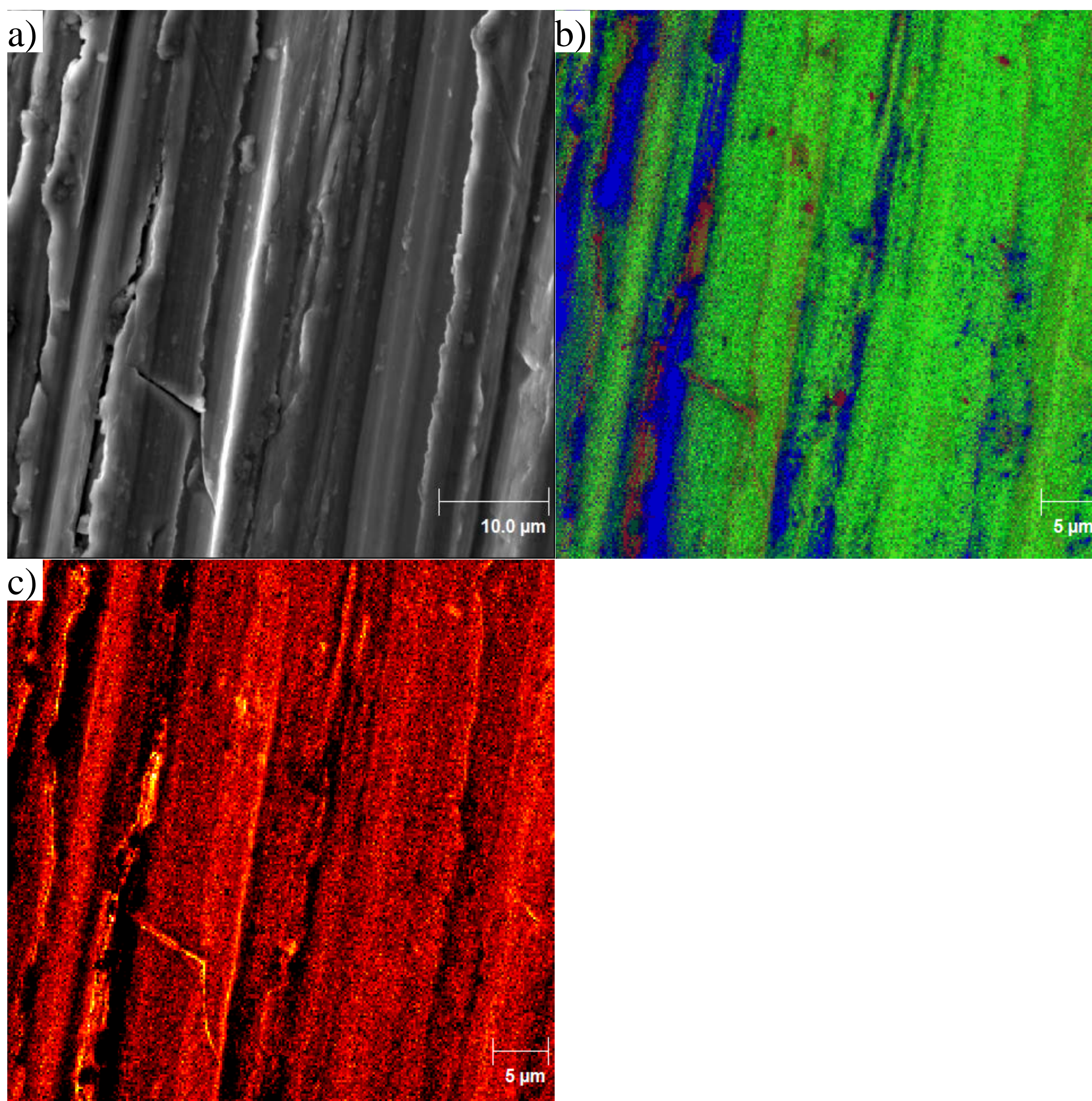

4.13 a) SEM image of magnesium surface after exposure to PTMS plasma for 60 seconds. b) Overlayed of elemental maps of magnesium (red), silicon (green) and carbon (blue). c) False colour elemental map of magnesium for the corresponding area.

Of some concern in Figure 4.13 b) is the presence of carbon on the surface in high concentrations, to the exclusion of both silicon and magnesium. It was previously presumed that such areas of carbon were a remnant of previous contamination that was not removed by the oxygen plasma pre-treatment and would therefore be coated by the PTMS plasma. However, their continued presence despite the coating of other regions of the magnesium substrate necessitates further consideration of the origins of this carbon. There are several other potential causes of these areas of high carbon concentration. It could be that in the process of transferring the samples between the plasma chamber and analytical chambers had led to contamination of the sample. While extreme care was taken to preserve the

surfaces so that any such contamination was minimised, it remains a potential source of contamination. In order to minimize the effects of this form of contamination, several Auger elemental maps were obtained across multiple samples. Areas of carbon contamination were observed in various magnitudes across the surfaces analysed, which implies that if carbon is deposited from an external source, it does so in a non-uniform way. Therefore, it is likely that other mechanisms of carbon deposition are occurring. Another possibility is that carbon is deposited along with any silicon from the PTMS plasma. It was previously pointed out that the overall C:Si ratio is reduced compared to that of the original PTMS molecule. It was assumed that any carbon removed from the molecule during the plasma process would be pumped away in the gas phase, however it is plausible that this carbon could be deposited onto the surface. XPS results come from data taken across a much larger area than that of the elemental maps seen here. If the carbon deposition is localised, then it could have little impact on the overall surface composition seen in XPS.

These areas of carbon seem very similar to those in the 10 second deposition case. In the 30 second case it was observed that there were areas of high carbon concentration that were coated along with the rest of the magnesium surface, so it is unlikely that there is any preferential attachment of carbon over silicon to these regions for a slightly longer deposition. If care is taken when comparing the SEM image to the carbon map, then it can be seen that the areas of high carbon concentration are generally co-localised with the areas where magnesium is detectable in deep scratches. It could be that these recessed areas on the surface allows smaller species to attach to more recessed areas. Unless the PTMS molecule is completely dissociated, then carbon that has been removed from the molecule (especially the methyl groups) would be smaller and thus more able to infiltrate these regions. However, when considering the physical size of the species involved (both the whole PTMS molecule, and any fragments thereof), they are several orders of magnitude smaller than the structures observed on the substrate surface and therefore is not a reasonable explanation of the observed behaviour. Instead, it is likely that these recessed areas of the surface are being 'shadowed' from the plasma deposition process by the surrounding (higher) substrate. Shadowing is (briefly) a reduction in material able to reach these recessed areas of the surface, which therefore experience a reduced rate of film deposition. Only PTMS molecules or molecular fragments with a relatively small angle of incidence are able to interact (and therefore bond) within these areas, as material incident at higher angles will impact on the edges or side walls of grooves in the substrate surface. This phenomenon may also explain the continued presence of carbon on the surface after oxygen plasma cleaning – a similar reduction in incident oxygen within scratches on the surface leads to a reduction in the rate of carbon removal.

As the deposition time increases further, the coating on the surface appears to become complete. Figure 4.14 shows an area of a sample exposed to PTMS plasma for 120 seconds.

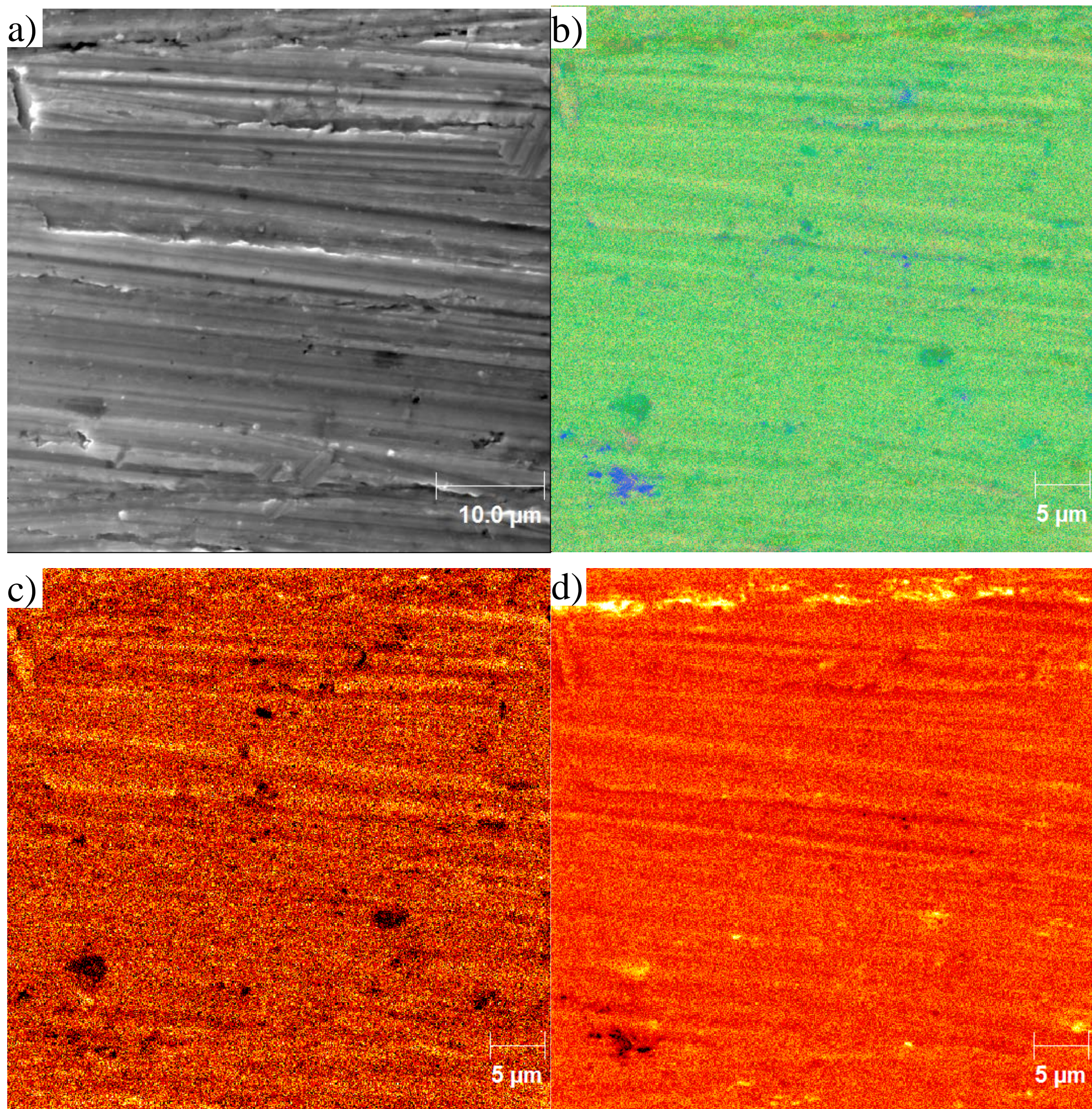

Figure 4.14: a) SEM image of magnesium surface exposed to PTMS plasma for 120 seconds. b) Overlayed elemental magnesium (red), silicon (green) and carbon (blue). c) and d) false colour elemental maps of carbon and oxygen respectively.

The SEM image in 4.14 a) appears the same as previous samples, with scratches present. Unlike the shorter deposition times however, the RGB overlay in Figure 4.14 b) shows that these areas have been coated in silicon. This is promising for any future potential applications, as having a complete, unbroken film is of paramount importance to its effectiveness for corrosion protection. Figure 4.14 c) shows that, in agreement with XPS,

magnesium signal is still detectable across the surface which is also seen in the RGB overlay, showing up as areas with a yellow hue by the combination of silicon and magnesium maps (green and red respectively). Again, the areas of increased magnesium intensity (and thus decreased film thickness) are correlated with those slightly rougher areas of the sample. Figure 4.14 b) also shows areas of carbon on the surface that are present to the exclusion of other elements. This can be seen in 4.14 c), where areas of high carbon concentration correlate to sections of the magnesium map with lower intensity. Compared to earlier time points, the carbon seen here is much more circular in shape, rather than conforming to recesses in the magnesium surface.

In addition to the carbon rich 'blue' regions of the maps, there also appear to be darker areas on the RGB overlay which correlate to dark points on the magnesium map. Initially, it was assumed that these areas were also carbonaceous, but coated by the PTMS plasma. When the oxygen map in Figure 4.14 d) is considered, it is apparent that the darker areas on the RGB overlay strongly correlate with areas of high oxygen intensity on the elemental map. As oxygen is not a part of the RGB overlay, these areas thus appear darker in Figure 4.14 b).

After a plasma exposure duration of 300 seconds, the film produced (as presented in Figure 4.15) is distinctly different to that seen for shorter deposition times. The RGB overlay primarily consists of signal from silicon and carbon, without any significant contribution from magnesium. This is no real surprise when taking into consideration that this is also the first of the samples measured in XPS where no magnesium was detectable. While there is some signal visible in the magnesium map in 4.15 c), it is much decreased compared to those of shorter treatment times. This reduction in signal from the substrate means that the thickness of the deposited film has increased to such an extent that magnesium Auger electrons are no longer detected. The magnesium map itself does appear to show a trace amount of magnesium present across the entire surface, with several distinct features evident. These are primarily associated with a scratch in the surface seen across the bottom of the SEM image in Figure 4.15 a). Due to a low signal to noise ratio, it is possible that the magnesium observed in the elemental map is actually noise. Elemental maps are ideal for examining changes in relative spectral intensity across a two-dimensional image, but in order to acquire such a map in a realistic timeframe, much shorter scan times are used. For elements with large intensities this is not a problem, but can lead to potentially misleading images (like the one in Figure 4.15 c). To more closely investigate this possibility, AES spectra were acquired at locations indicated and the results are displayed in Figure 4.15 d). The spectrum from the location seen in red in 4.15 a) shows that there is small, but non-zero amount of magnesium detectable in these areas. This is in contrast to XPS data in which no magnesium was

detected. As mentioned previously, XPS probes a large area of the magnesium surface. For this reason, small regions of magnesium as seen here may not provide enough signal to be detectable in XPS spectra. As AES probes a much smaller spatial area, in these areas detectable magnesium are resolvable above noise.

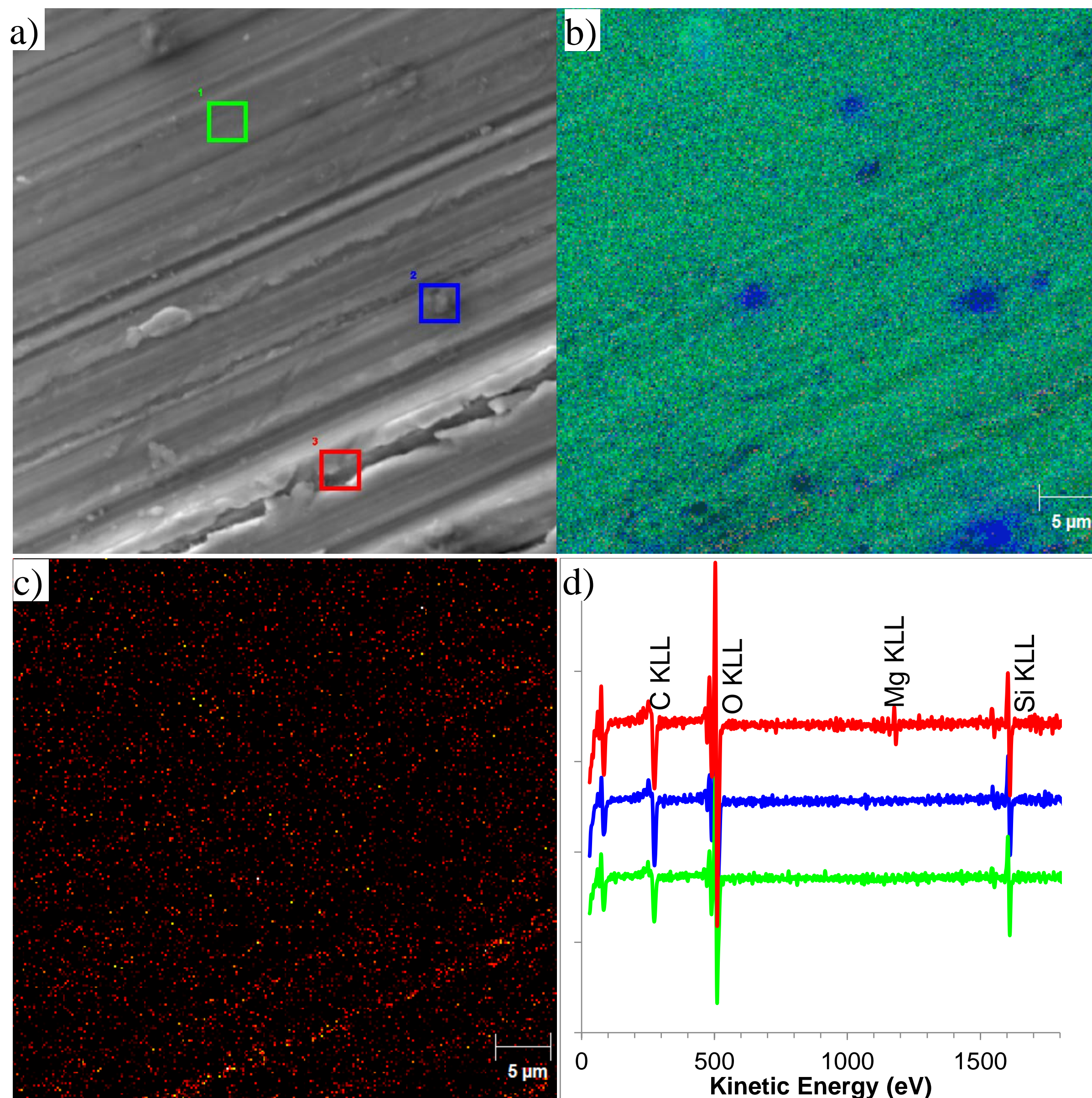

Figure 4.15: a) SEM image of m surface exposed to PTMS plasma for 300 seconds. Highlighted regions indicate areas of further analysis by AES b) Overlayed elemental magnesium (red), silicon (green) and carbon (blue). c) False colour elemental map of magnesium d) AES spectra obtained for the areas indicated in 13a).

The other noteworthy features in Figure 4.15 b) are the areas of relatively high carbon intensity present on the surface, which correlate well to the difference in carbon intensity

observed between the green and blue spectra in Figure 4.15 d). The carbon rich areas of the elemental map are approximately associated with several darker regions seen in the SEM image, Figure 4.15a) and appear similar in shape to the dark features observed in Figure 4.14 b), rather than as streaks seen for earlier deposition times which were generally associated with scratches on the surface. It is therefore unlikely that these areas of carbon are the same as those seen for earlier times (or the pre-treated samples), and the material seen in these maps is a product of the plasma deposition process.

Increasing the time to 1800 seconds, does not result in a significantly different surface coating. The overlayed elemental maps seen in Figure 4.16) show a surface that is similar in composition to the one seen for the 300 second deposition time, although magnesium is not detected spectrally anywhere across this surface. Physical features of the magnesium surface may still be observed in the overlayed elemental maps, primarily through the presence of carbon which is, for the most part, located within troughs produced by the silicon carbide abrasion process. There are however, fewer areas were carbon appears to have been deposited on the surface than what is seen for shorter depositions.

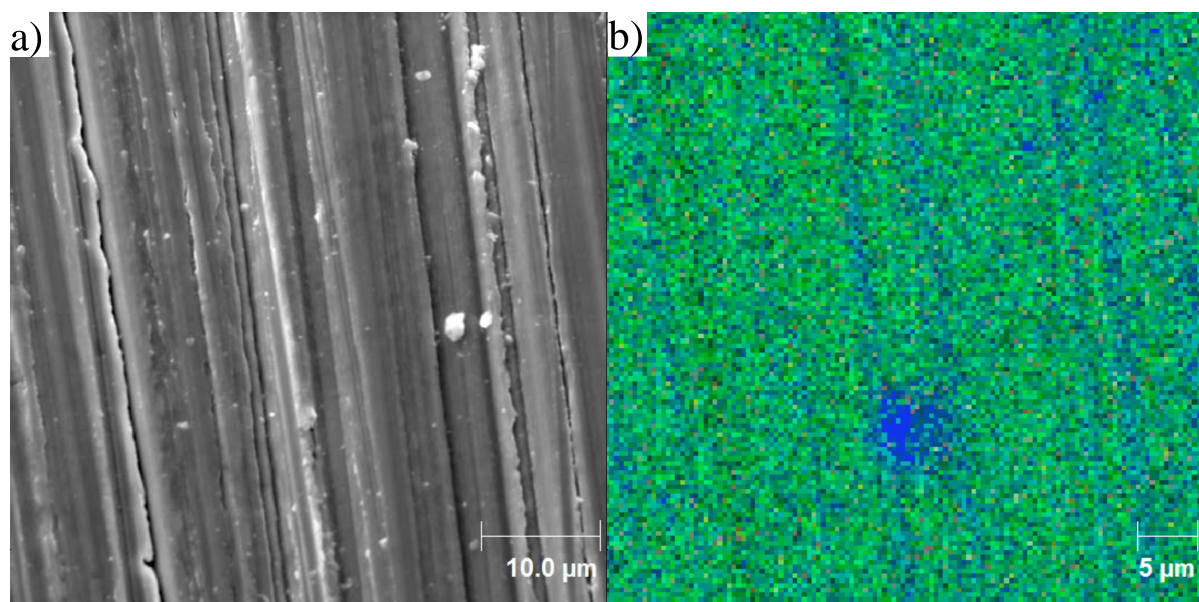

Figure 4.16 a)SEM image of magnesium surface exposed to PTMS plasma for 1800 seconds. b) Overlayed elemental magnesium (red), silicon (green) and carbon (blue)

The longest plasma duration investigated here was one hour, and the associated SEM image and RGB overlay can be seen in Figure 4.17. From XPS, magnesium was unable to be detected spectrally on any of the samples exposed to the PTMS plasma for any duration longer than 300 seconds. However, Auger electron spectromicroscopy was able to be detected magnesium on the 300 second samples. Once exposure time is increased to 1800

seconds however, no more such magnesium signal was detected here, with the surface composition consisting solely of carbon, oxygen and silicon. However, elemental mapping as (depicted in Figures 4.16b) and 4.17b) demonstrates that these elements are not uniformly distributed across the sample and minor variation between the carbon and silicon signal is visible. The roughness of the magnesium substrate is thought to remain the primary cause of this variation, with the scratches from the silicon carbide abrasion process clearly seen in figure 4.17 a) correlating well with the RGB overlay.

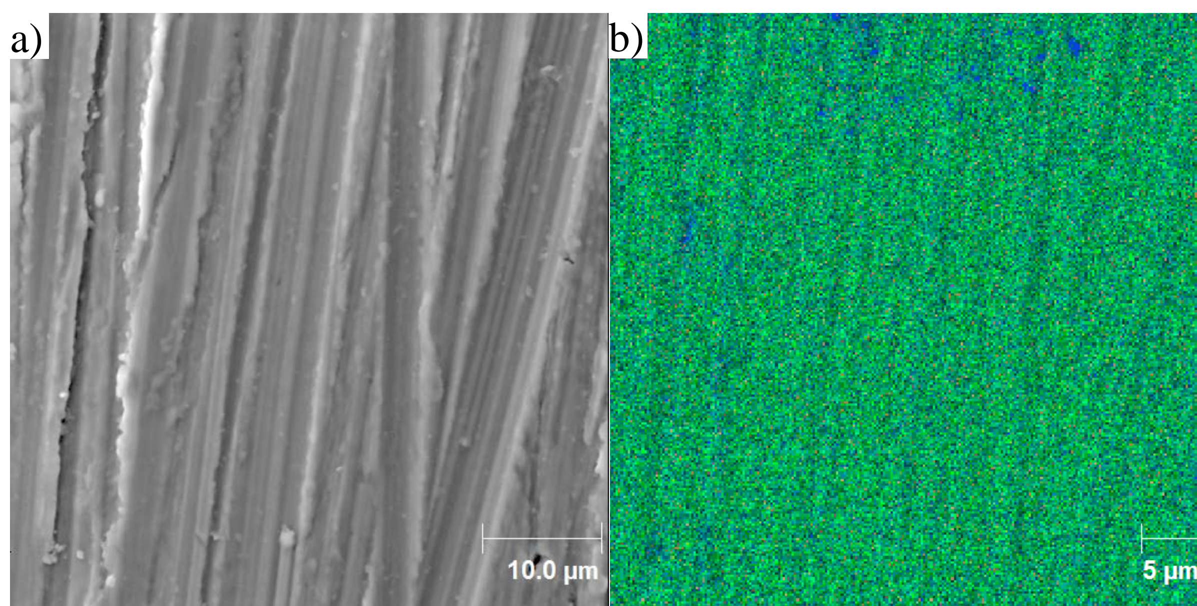

Figure 4.17: a)SEM image of magnesium surface exposed to PTMS plasma for 3600 seconds. b) Overlayed elemental magnesium (red), silicon (green) and carbon (blue)

Areas of high carbon concentration do not seem present to the same extent as on surfaces exposed to the PTMS plasma for shorter durations. This is unusual, as if the carbon seen for short exposure times is deposited on top of the magnesium in the PTMS plasma (as would be expected from the earlier maps – carbon was present to the exclusion of silicon), then it should be a time independent process. One explanation for why such areas are not seen to the same extent for the one hour deposition is that for carbon to chemically attach to the surface during the plasma deposition process, an attachment site is necessary. As the deposition time increases, so does the coverage of the PTMS layer with rougher, carbon containing areas of the surface coated. These rough areas are still observable in SEM images, as the escape depth of the secondary electrons detected in SEM is much greater than Auger electrons, generally the top 50nm of the surface, as opposed to the top 10nm (as given by the plot of inelastic mean free path vs kinetic energy in Figure 2.8, (in Section 2.1.5). In addition, for a film to mask such surface features, then it must be on a similar order of size. From the control AFM measurements conducted previously (Figure 4.8 in Section

4.2.1), it is known that these features are on the order of hundreds of nanometres in size. This means that for the deposited film to obfuscate these features, they must either be at least the same thickness, or preferentially fill these recessed areas akin to a liquid. While there is some variation in the deposition across the surface, recessed areas of the surface appear to be coated by the plasma process to a lesser extent than exposed ones. This behaviour is consistent with the effects of shadowing as described on Page 86, where the rate of deposition in these recessed areas is reduced due to the fact that only material from a small angle of acceptance will not be intercepted by the relatively higher surrounding material.

Through the use of argon ion depth profiling, an estimate of film thickness can be determined. An example depth profile is given in Figure 4.18, showing the change in intensity of selected Auger peaks as material is removed under bombardment by a high energy argon ion beam (of 2kV). Highlighted in Figure 4.18 b) is the silicon depth profile, which is removed after sputtering approximately 100nm into the surface. While this on the order of the average surface roughness determined with AFM imaging, individual surface features several times larger are identifiable

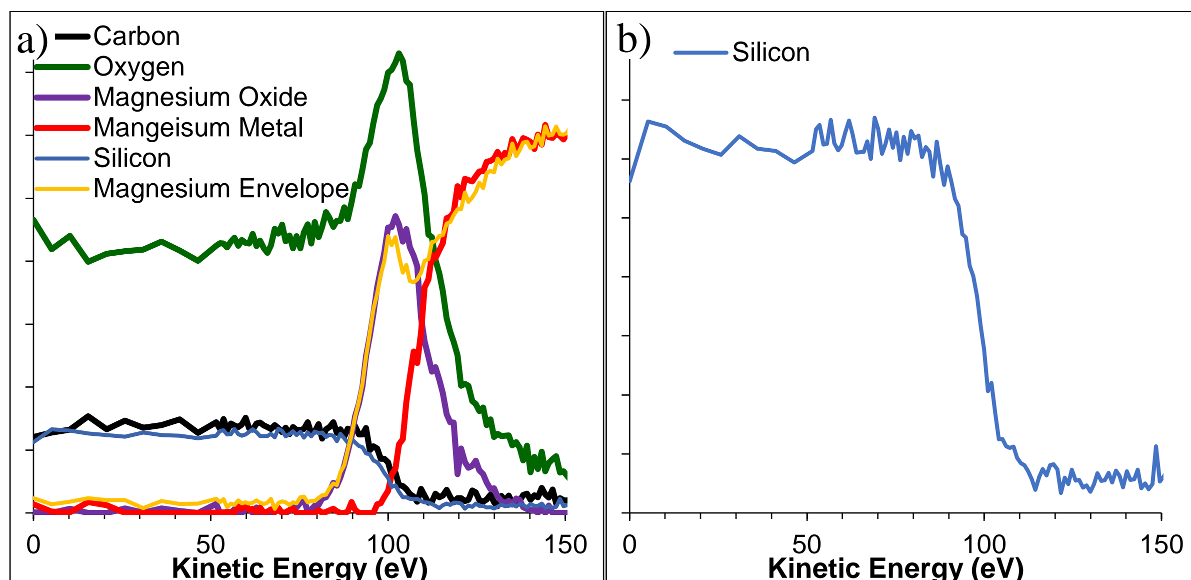

Figure 4.18: a) Depth profiles of elements present on magnesium surface after PTMS plasma treatment of 3600 seconds. b) Individual depth profile of silicon KLL Auger transition

By performing depth profiles on each of the films deposited at a range of PTMS plasma exposure times, an estimate of film growth rate can be obtained. For this process, the same analysis area (50μm^2) was used for all depth profiles, with data displayed here chosen from regions of the surface informed by elemental mapping to be clear of contaminants and thus representative of the average film composition.

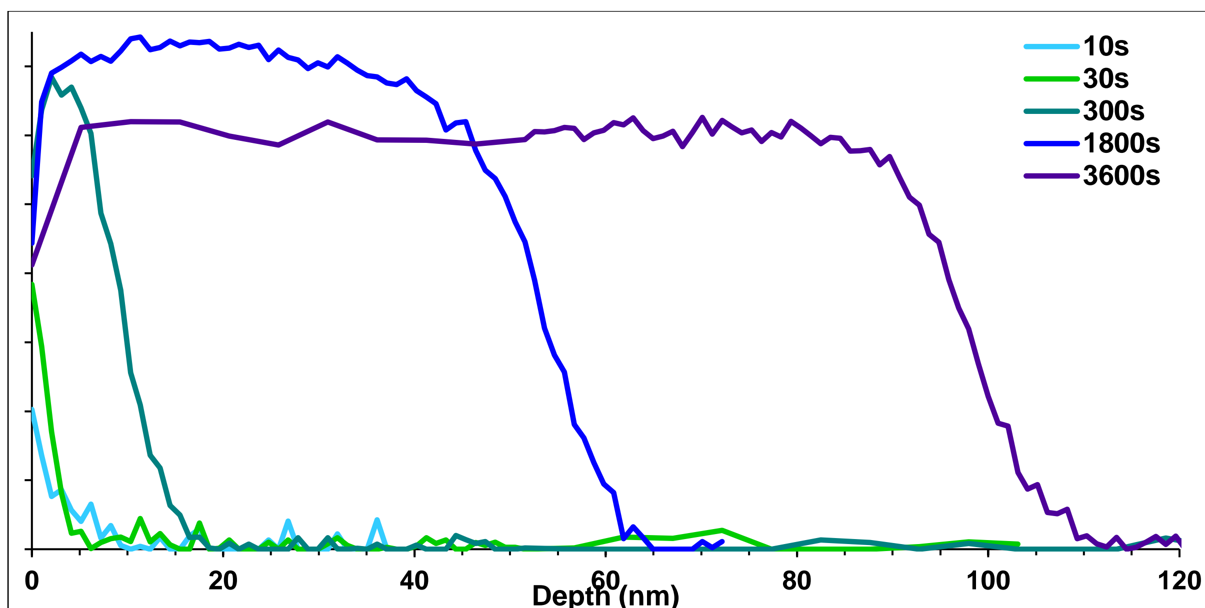

Figure 4.19: Silicon depth profiles of surface films produced on magnesium by various exposure times to 20W 1x10^{-3}Torr PTMS plasma treatment.

Example silicon depth profiles from these areas seen in Figure 4.19 show a clear trend of increasing depth with increasing plasma exposure time. The film is very thin at early time points, which adds uncertainty to the estimates given for depth. Therefore, several locations were 'profiled' across multiple samples for each exposure time. These locations were kept to the same analysis size, and the mean values for film depth are given in Figure 4.20.

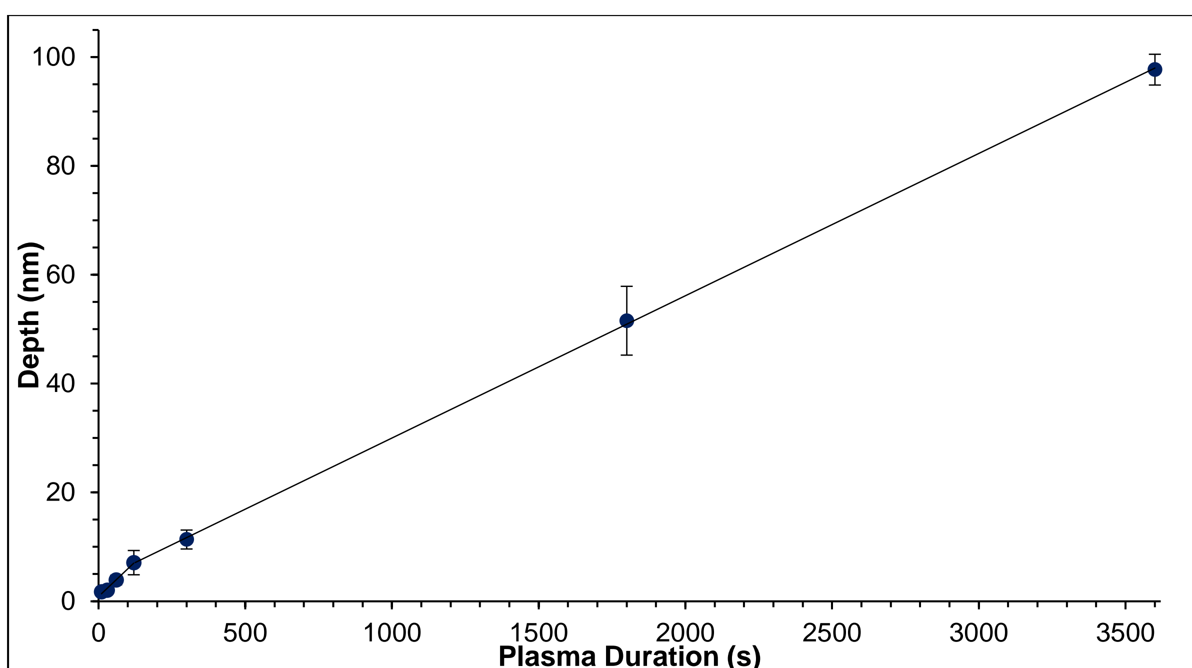

Figure 4.20: Plot of film depth vs duration of exposure to PTMS plasma. Error bars are given as the standard deviation. Two separate lines are plotted in order to guide the eye along two separate coating domains, which meet at a plasma duration of 120s.

The trend seen appears to be approximately linear, with a relatively slow rate of film growth of 100nm per hour. There is some uncertainty present, the total value of which increases with the plasma exposure time and thus thickness. However, as a fraction of the coverage, the relative uncertainties for the earlier time values are much greater, and thus the variation in measurements of film depth reduces along with overall plasma exposure duration. Alternatively rather than a single linear trend, it is likely that the rate of deposition changes as the surface is coated by the silicon containing film. This leads to two distinct domains within the above plot, as demonstrated by the two separate lines plotted in Figure 4.2, which meet at a plasma duration of 120 seconds.

No intrusion of silicon into the surface below the magnesium oxide layer was observed, which was seen as a sharp increase in oxygen intensity compared to the relatively constant concentration for the bulk PTMS film, followed by a decrease to zero as the oxide is removed. The increase in oxygen intensity also corresponded to the emergence of magnesium signal, which increased steadily as first PTMS, and then the oxide were removed. The shape of the magnesium peak also indicates the presence of magnesium oxide and then metal as the sputtering duration increases, as clearly seen in Figure 4.7 b) in Section 4.2, where the oxide is removed, the peak shape changes from a single peak, to one with multiple plasmon resonances associated with metallic magnesium, as well as shifting to a higher kinetic energy. By fitting this peak, an estimate for magnesium oxide thickness can be estimated. The thickness of the oxide layer on the magnesium surface after oxygen plasma pre-treatment was approximately 20nm. The approximate values for oxide thickness seen across the PTMS treated samples vary between 20nm and 60nm. The oxide layer seen in Figure 4.17 a) for instance, is 45nm. Thus, the oxide layer formed by the oxygen plasma treatment does not appear to be affected overmuch by the PTMS plasma.

4.4 **Plasma Power Dependence on PTMS deposition**

4.4.1 XPS Results

By increasing the coupling power of the RF signal applied to the PTMS plasma, further control of the resulting film should be attainable. By changing the power and therefore the energy of the plasma, different species and reactions are able to arise. The following sets of data show the effect of varying power on the surface coverage of the magnesium. To do this, a plasma exposure time of one minute was chosen. In the previous set of measurements this deposition time, along with a fairly low plasma power of 20W, gave a value for coverage of approximately 0.4. Therefore, using this deposition time will allow the effects of power variation on coverage to be investigated.

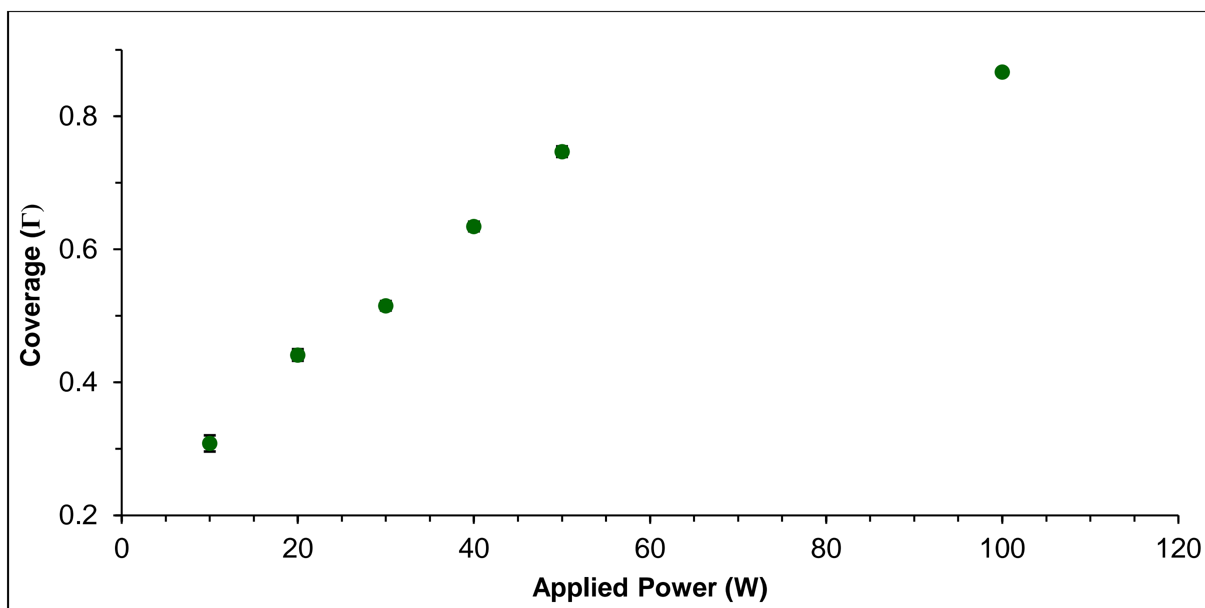

4.21 Plot of coverage (Γ) vs applied power of PTMS plasma after a 1 minute exposure duration at $1x10^{-3}$Torr. Error bars are given as the standard deviation.

The above plot (Figure 4.21) shows the coverage (Γ) against PTMS plasma power. A trend exists that increasing the power of the pure PTMS plasma results in an increase in silicon presence on the surface. The increase in silicon first appears linear with power for lower powers, but the coverage present appears to plateau and reach an asymptote near 0.85 at higher values of applied power. That the value of Γ is prevented from reaching a value of 1, as it did when plasma deposition time was increased past 300 seconds, means that magnesium is still able to be detected spectrally with XPS. As discussed in the previous section, because magnesium is detectable spectrally; the film formed is either incomplete, or evenly distributed and thinner than the escape depth of photoelectrons. The fact that the coverage increases with power is interesting in itself, as it implies that by adding energy to the plasma, more species are created that are able to attach to the magnesium surface, or those already present at lower power are able to attach more readily. That the effect of increasing power is not linear and instead reaches and asymptote implies that there are mechanisms that must be considered. If increasing the power leads to an increase in the fragmentation of the PTMS molecule, then at a constant pressure (and hence monomer flow rate) as is the case for these experiments, at some applied power, the plasma will reach a state where the vast majority of PTMS molecules are fragmented and thus further increasing power will not create more bonding species unless the rate of monomer addition is likewise increased. This concept has been discussed previously in Chapter 1, Section 1.4.2, where the early work into plasma polymerization by Yasuda was reported. In this section, the ratio $\frac{W}{FM}$, where W is the plasma power, F is the monomer flow rate and M is the molecular weight

of the monomer was defined. Conversely, by further increasing the power, the opposite of the intended effect could occur. More energetic species would have a greater ability to etch the surface (including any deposited film) by bombardment of energetic ions, which would lead to an overall decrease in the deposition rate.

As with the analysis performed in Section 4.3.1, further information about the film can be obtained through the use of XPS in addition to the coverage. By examining the C:Si ratio we can obtain useful information about the composition of the deposited film. The chart plotted in Figure 4.22 shows the C:Si ratio against power. By comparing this plot to Figure 4.21, the C:Si ratio follows an approximately inverse trend to that of the coverage, decreasing with power to a value of approximately 2:1. This inverse trend is similar to what was seen for the investigation of exposure time, where carbon present on the magnesium substrate is coated by the PTMS film. When power is increased however, there is the potential for different species to arise. There are two primary consequences of increasing the applied power: firstly, the further dissociation of PTMS molecules and secondly, providing more energy to those species already present to either attach to or etch the substrate.

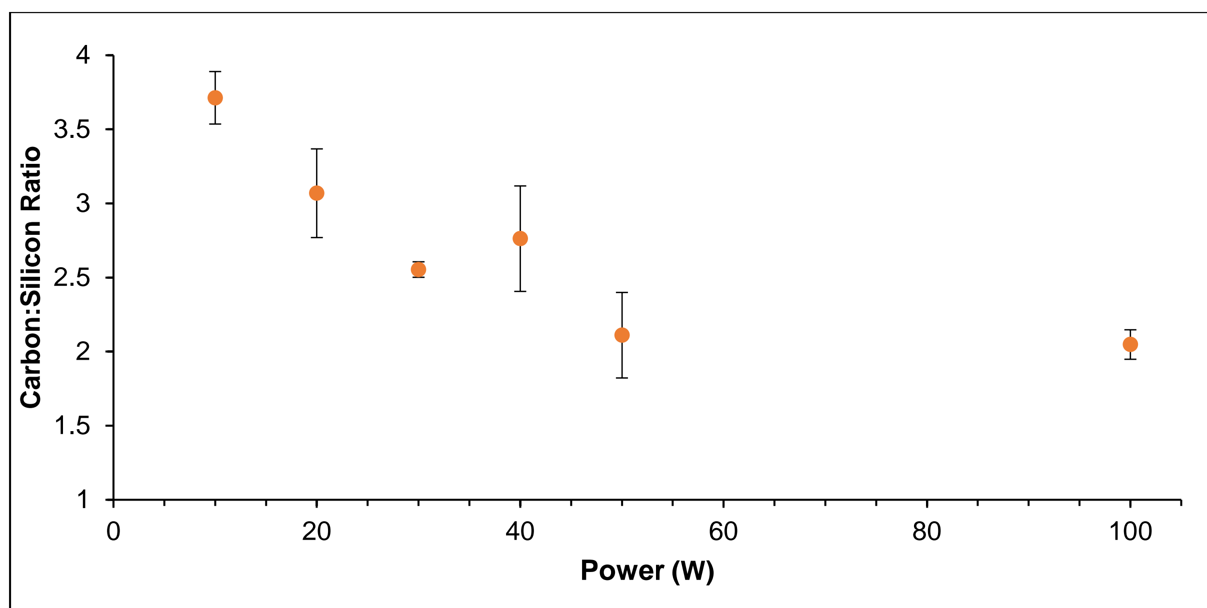

Figure 4.22 Plot of C:Si ratio vs Applied PTMS plasma power.

From the data presented it appears that even the 10W plasma shows a decrease in C:Si ratio (~4:1) compared to the PTMS molecule (6:1). In addition to this, it is known that there is carbon present on the magnesium substrate so it is likely that this ratio is skewed higher, implying that even low power is enough to cause dissociation. There is the possibility that carbon from PTMS is deposited onto the magnesium surface separately however, that carbon concentration decreases as coverage increases implies that this does not play a

significant part in film formation and alkyl- species formed within the plasma are pumped away. Without the ability to directly measure the species present within the plasma, it cannot be stated for certain how increasing power affects the species present within the plasma.

4.4.2 Scanning Auger SpectroMicroscopy Results

Figure 4.23 shows an SEM image (a), RGB overlay (b), magnesium (c) and carbon (d) maps of a magnesium surface exposed to a 10W plasma for 60 seconds. Due to the exposure time chosen, it is appropriate to compare this deposition at 10W to the 60 second sample from Figure 4.12 in Section 4.3.2, which was created from a 20W Plasma. The deposited film in Figure 4.23 b) appears similar in structure to that seen previously, with silicon and carbon both present across much of the analysis area. Magnesium is clearly observed in this overlay, most notably in recessed areas of the sample. The intensity of the silicon signal across the observed area appears slightly lesser to that seen in Figure 4.12, with a corresponding increase in the intensity of the magnesium elemental map in 4.23 c). This implies that by decreasing the applied plasma power, the thickness of the film also decreases. The surface coverage however, does not appear to be significantly lesser than the 20W case. The importance of differentiating between a thin film and an incomplete one has already been established in this work but it may be underlined at this point, where the deposited film is both thin AND incomplete, and only elemental mapping techniques are able to differentiate between the two.

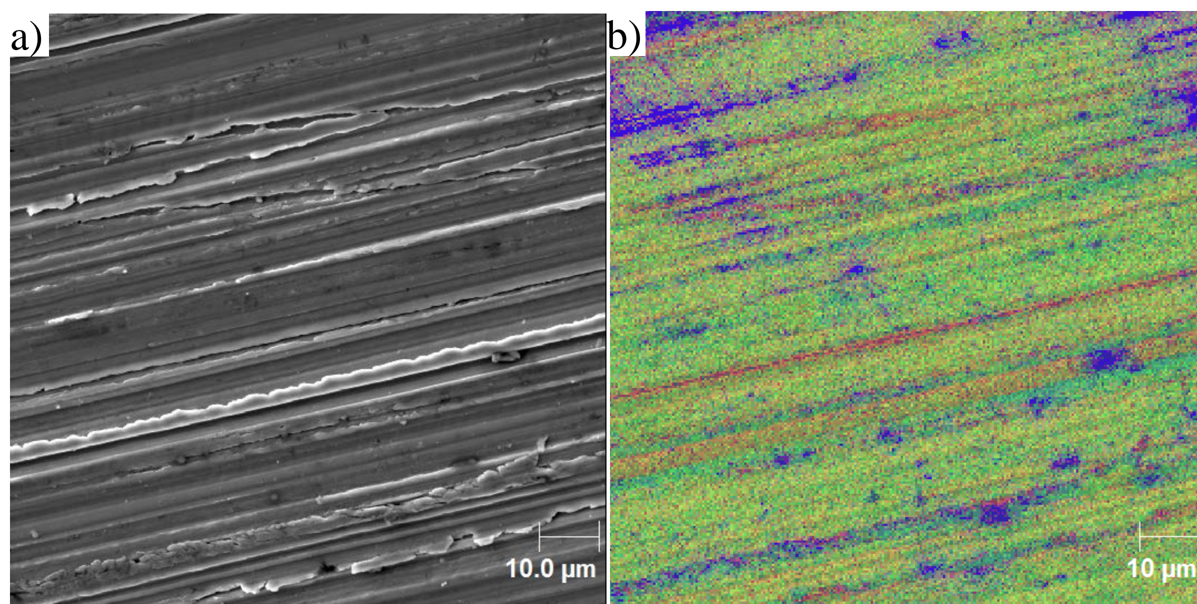

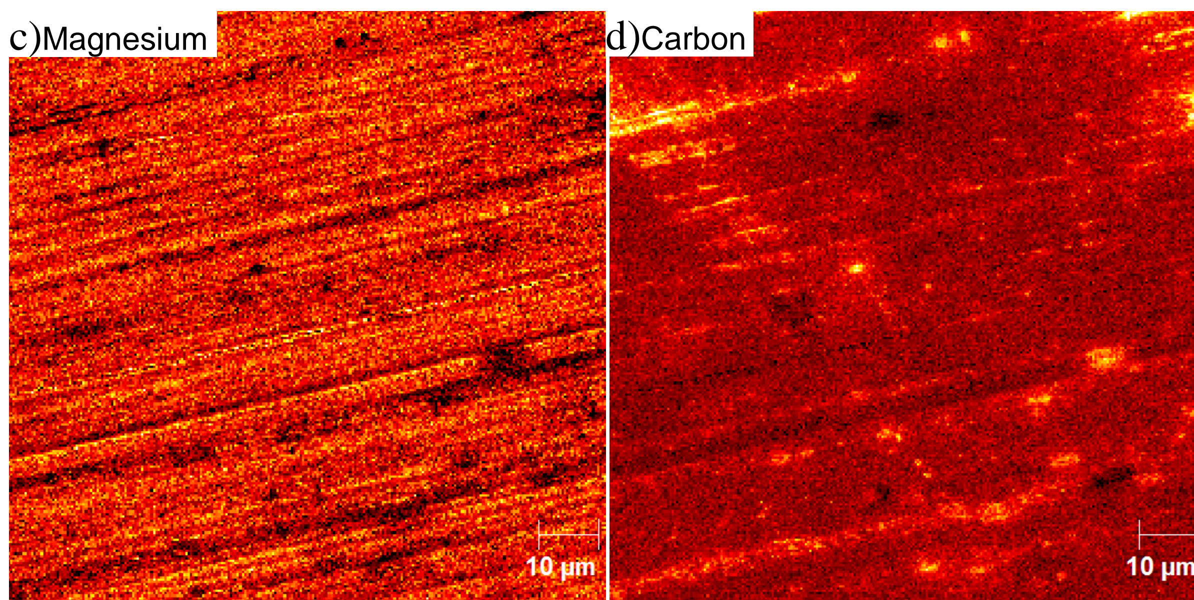

4.23 a) SEM image of a magnesium surface exposed to a PTMS plasma at 10W for 60 seconds. b) Overlayed elemental maps of magnesium (red), silicon (green) and carbon (blue), c) false colour elemental map of magnesium d) false colour elemental map of carbon.

The elemental map of carbon in Figure 4.23d) serves to illustrate that as with previously investigated samples, carbon is not present across the surface in a uniform layer. Instead, there are regions of increased carbon concentration which can be seen in both the overlay and the carbon map itself as being much higher in intensity than the surrounding areas. Most of these areas of increased carbon concentration are associated with physical features of the surface seen in the SEM image in Figure 4.23a), most commonly the channel-like features caused by abrasion with silicon-carbide paper.

When the applied plasma power is increased to 30W, there is not a significant change in the surface that is detected by elemental mapping as shown in Figure 4.24. This is notable when considering that XPS results give an increase in Γ from approximately 0.3 in the 10W case to 0.5 for 30W. By examining the magnesium elemental map in Figure 4.24c), and comparing with the elemental map of magnesium in Figure 4.23 c), there is a slight increase in contrast across the surface. Those areas which correspond to grooves on the surface as seen by SEM imaging continue to show high magnesium signal, whereas 'smoother' areas of the surface show a slight decrease in magnesium concentration. This behaviour is consistent with 'shadowing' of the recessed areas of the magnesium surface, as explained in Section 4.3.2. That less overall magnesium signal is obtained implies that the deposited film is thicker in the 30W case, which explains the increase in Γ observed with XPS.

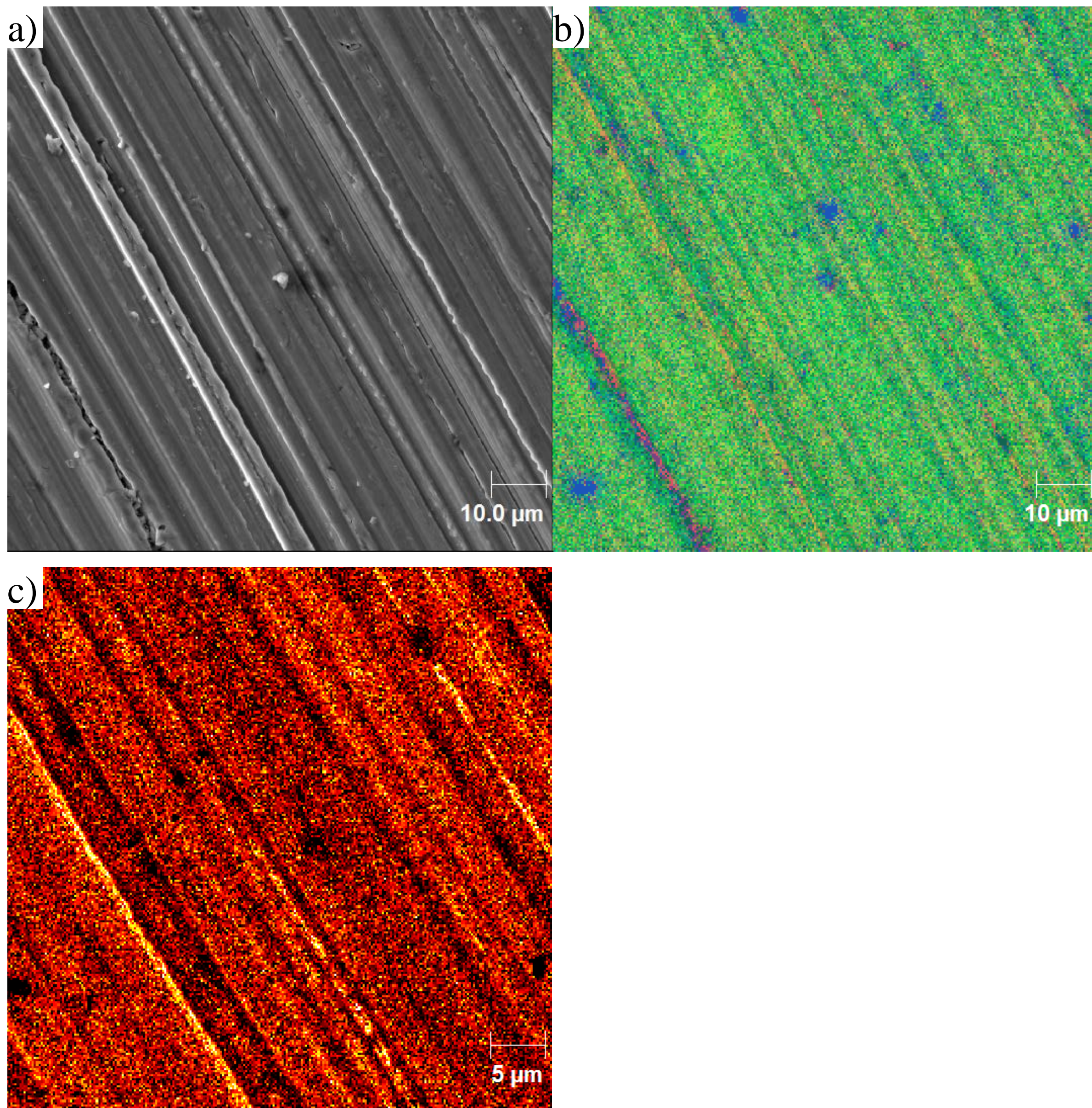

Figure 4.24 a) SEM image of a magnesium surface exposed to a 30W PTMS plasma for 60 seconds. b) Overlayed elemental maps of magnesium (red), silicon (green) and carbon (blue). c) False colour elemental map of magnesium.

The effect of surface morphology on the deposition of the film can be seen even more clearly in Figure 4.25, which shows another area of a surface that has undergone a 30W deposition. The SEM image in 4.25 a) features a smaller field of view, highlighting a scratch in the surface. The associated overlay of silicon and magnesium maps in Figure 4.25 b) shows the variation in magnesium and silicon across this area of the surface. The area of the elemental maps associated with the large trench-like feature on the left hand side of the SEM image shows an increase in magnesium intensity. Silicon is also detected within the region, along with its presence across the rest of the imaged area however, though at a lesser intensity. This is, again, consistent with the concept of 'shadowing', where raised sections of the magnesium substrate reduce the deposition rate of PTMS in adjacent areas.

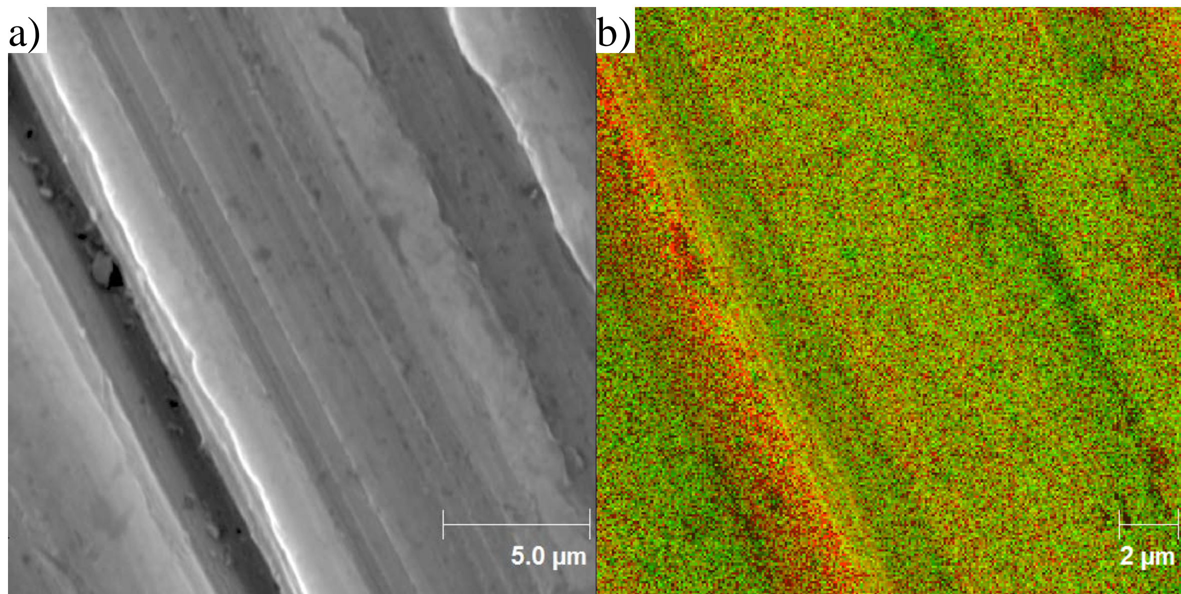

Figure 4.25 a) SEM image of a magnesium surface exposed to a PTMS plasma at 30W for 60 seconds. b) Overlayed elemental maps of magnesium (red) and silicon (green)

With a power of 50W, despite the change in coverage from XPS data being approximately the same as between previous power steps, there is a noticeable shift in the presence of magnesium on the surface. As with the plasma treatments with lower power, the intensity of the magnesium signal in both Figure 4.26b) and the magnesium map itself in 4.26c) is greater in the recessed areas of the sample. The magnesium signal seen across those areas where silicon has coated has however, greatly diminished - to the point where it is almost spectrally undetectable on some areas of the surface. The implication of this is that the film thickness in those areas has increased to approximately the escape depth of the Auger electrons for magnesium. Overall then, it seems that increasing the plasma power has led to an increase in the deposition rate across the majority of the surface. However, shadowing has prevented the recessed areas of the substrate from being coated to the same extent. Whether or not this increase in attachment is simply due to the same species that are present in a lower power environment having more, or that the silicon is converting to a state that is more able to form linkages and thus a thicker layer is unknown from this data.

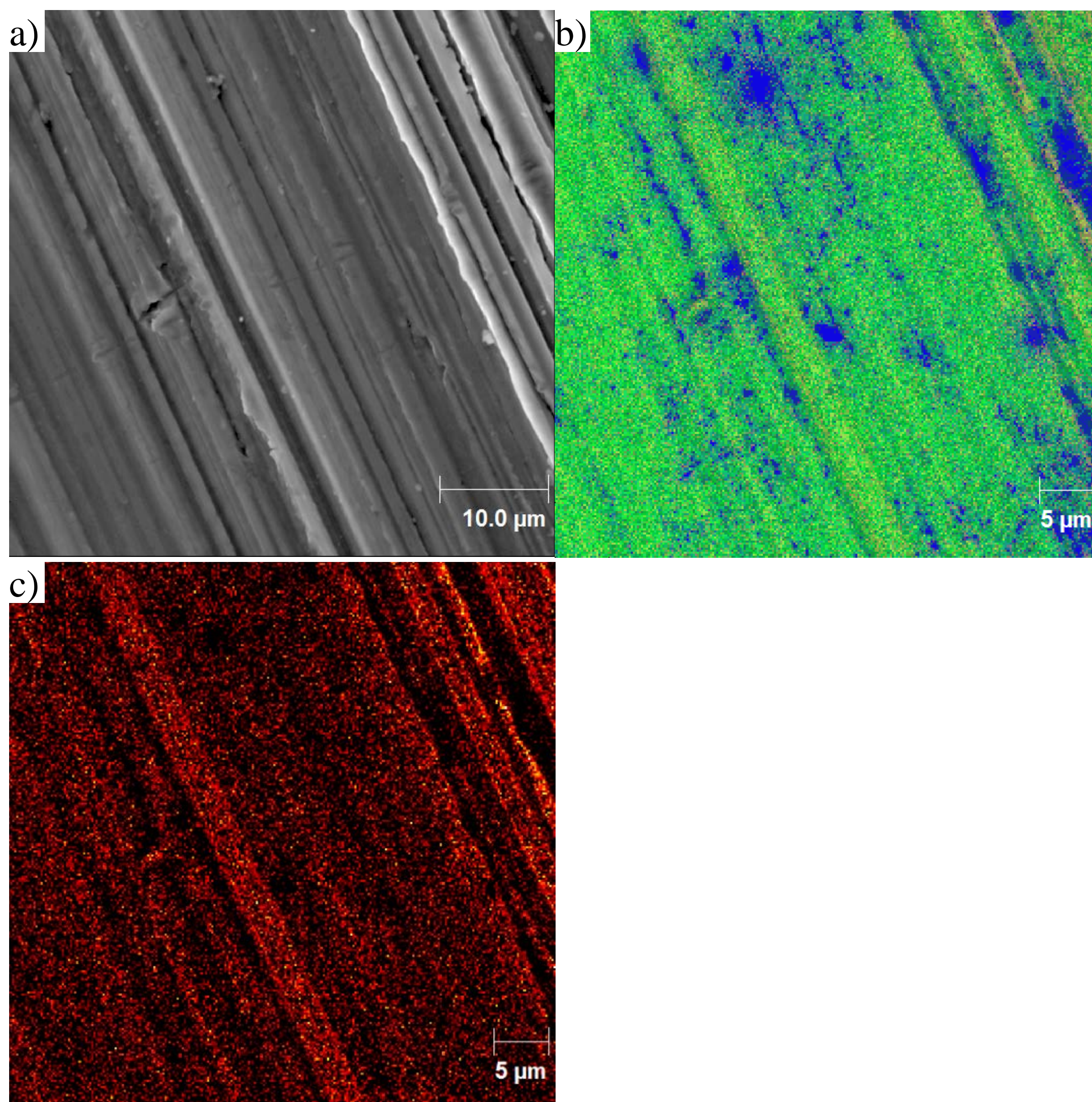

Figure 4.26: a) SEM image of a magnesium surface exposed to a PTMS plasma at 50W for 60 seconds. b) Overlayed elemental maps of magnesium (red), silicon (green) and carbon (blue). c) False colour elemental map of magnesium

The trend continues for films deposited from 100W plasma, an example of which is shown in Figure 4.27. Despite a doubling in the applied plasma power, only a small increase in Γ is observed XPS data, up to approximately 0.85. It is therefore expected that magnesium is present in elemental mapping, and indeed Figure 4.27b) shows that it is, with areas of magnesium clearly visible in red within this image. These are mostly present in recessed areas of the surface, along with areas where carbon dominates, to the exclusion of silicon. The limiting step for complete coverage thus appears to be the duration of the plasma treatment, with 60 seconds not being a long enough duration for rougher areas of the

surface to be completely coated. This is in comparison to the 120 second plasma treatment case, which has a value for coverage of approximately the same. The surface seen there is a very different one. A more complete coating is seen, without areas of uncoated magnesium present, but as the deposited layer is slightly thinner, magnesium signal is still detectable in XPS across that surface, leading to a similar value for Γ. As the rate of deposition is lower for reduced plasma power, the time it takes for the coverage to reach the same value as a higher power is increased. This allows time for species to more evenly distribute across the surface, and hence creates a more uniform film.

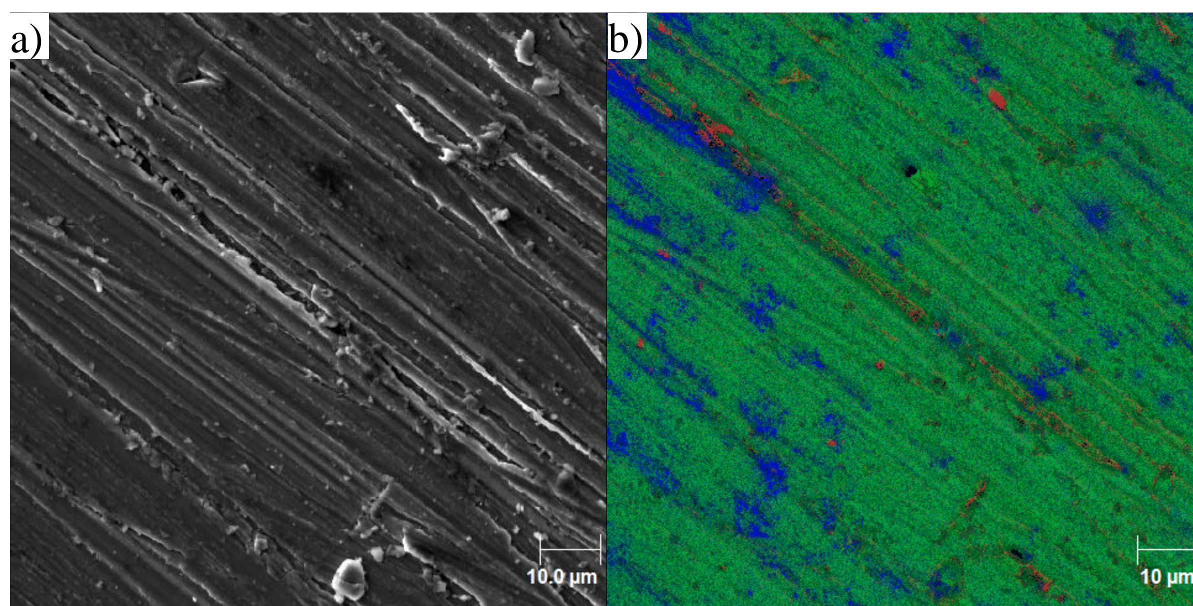

Figure 4.27 a) SEM image of a magnesium surface exposed to a PTMS plasma at 100W for 60 seconds. b) Overlayed elemental maps of magnesium (red), silicon (green) and carbon (blue)

This is further evidence that the plasma deposition process is strongly affected by surface morphology and is not a completely homogenous process. A noteworthy result present from this investigation is that despite an increase in film thickness (to the extent that signal from the magnesium substrate is no longer detected), there is still a strong carbon presence on the surface, separate to that included in silicon containing areas of the film. Some of this carbon are present in ‘rougher’ areas of the surface and (similar to how there are regions of magnesium that remain uncoated) were not removed during pre-treatment due to localised surface roughness. There are other areas of carbon however, that are not associated with such sites. These areas could potentially come from carbon deposited as part of the plasma process, with carbon originating from the PTMS molecule, or as contamination from atmospheric sources after the samples’ removal from the plasma deposition chamber. XPS results were not able to distinguish between such areas of carbon, so through elemental mapping with scanning Auger microscopy, further indirect evidence is found for the dissociation of the PTMS molecule within the plasma state.

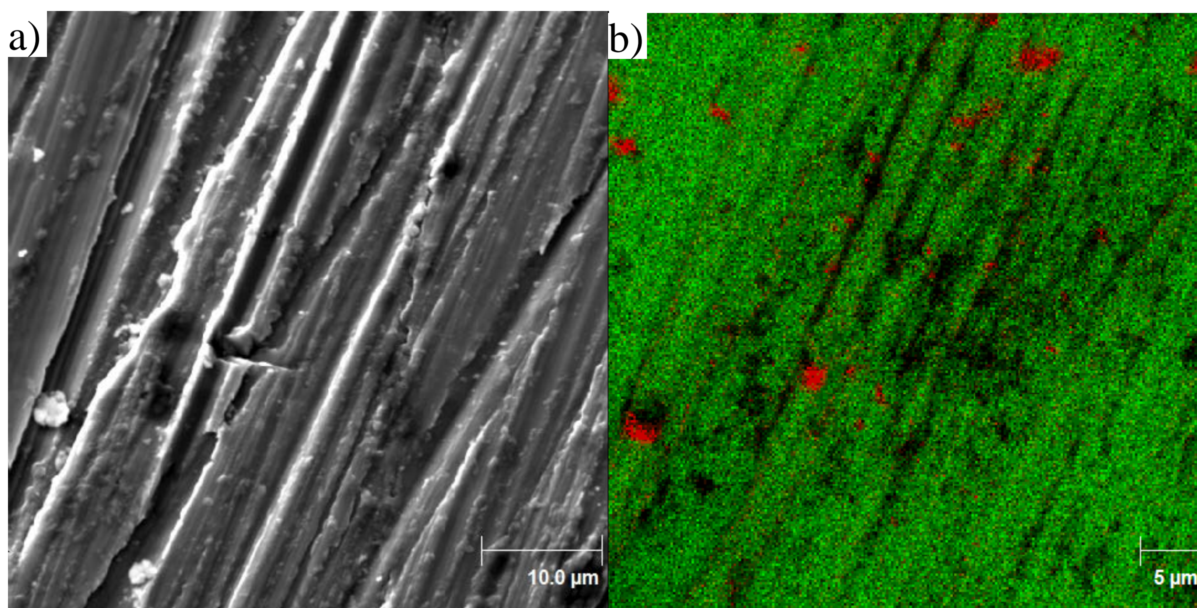

Figure 4.28: a) SEM image of a magnesium surface exposed to a PTMS plasma at 50W for 60 seconds. b) Overlayed elemental maps of magnesium (red) and silicon (green)

Another SEM/Elemental map combination in Figure 4.28 was obtained with a Field of View (FoV) of 50µm, half that seen previously. In addition, the carbon elemental map is not included (which now appears as black). This gives a better view of the location of magnesium signal on the surface. Upon close inspection, while the areas of magnesium do agree with features on the surface, they are not the ones that would necessarily be expected. The deeper 'scratches' appear to be filled with carbon (which is likely a remnant from abrasion with silicon carbide), rather than exposed magnesium while there are several locations where the magnesium is detectable that appear on smoother regions of the surface, which is not consistent with the previous explanations of shadowing preventing the coating of the surface. It could be that these areas of detectable magnesium are caused by the etching of the surface by the plasma (which would occur at a greater rate in more energetic plasma). Yet, adjacent to these regions, there is sufficient silicon to completely prevent magnesium being detected spectrally. The reason for this may be similar to the cause of the oscillations in the chemical dip coating. If silicon binds to some areas of carbon, or is otherwise weakly attached, then it could be vulnerable to displacement (or etching) by energetic ions in the plasma, whereas any highly cross-linked silicon/oxygen structures being formed would be resistant to such etching (as is the point of the coating). This may be an alternative explanation as to why, for the long plasma durations, the surface appears to homogenise – weakly attached species are selectively replaced by those that attach more strongly, which in the case of the PTMS plasma is a mixed silicon-oxygen-carbon layer.

The plot in Figure 4.29 shows a selection of the silicon depth profiles obtained from surfaces

exposed to PTMS plasma at a range of RF plasma powers. These results follow both the XPS and previous Auger data well. As power increases, there is a trend towards increasing film depth although compared to plasma treatments of a slightly longer duration as shown previously in Figures 4.19 and 4.20, the relationship between film depth and power is very different to that of exposure duration.

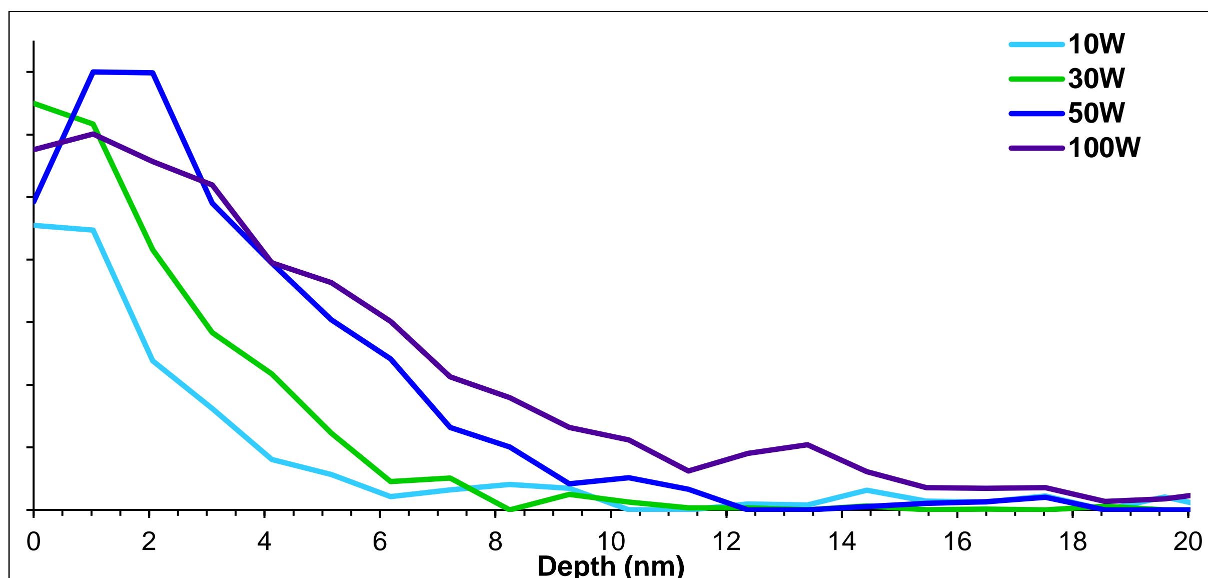

Figure 4.29: Depth profiles of the silicon KLL Auger transition for samples of magnesium oxide exposed for 60 seconds to PTMS plasma at a range of applied RF powers.

This is best expressed in Figure 4.30, which contains a plot of average values for film depth against the applied plasma power. As these values are all quite low, the relative uncertainty in the results is high. Despite this, is a trend with film depth increasing with power, although the relationship is best modelled logarithmically. This trend has many similarities to the result seen in the XPS data from Figure 4.20 in Section 4.4.1, implying that in this case, the value for coverage was indicative of the film depth.

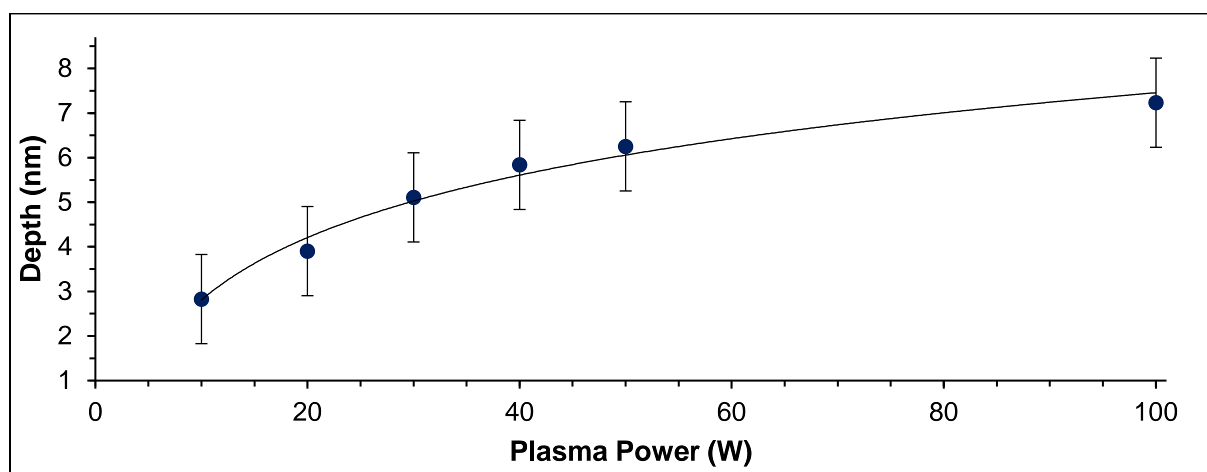

Figure 4.30 Plot of film depth vs applied plasma power. Error bars are given as the standard deviation. A natural logarithmic trend line has also been fitted, with an R^2 value of 0.9814.

4.5 **Stability of plasma deposited PTMS films**

The choice of PTMS as the organosilane precursor used in these experiments was explained previously, in Chapter 1. The key reason given there, was that PTMS has limited functionality, allowing film formation to be investigated in detail without the effects of functional groups to consider, making PTMS a good model for other organosilanes. However, this also means that PTMS is not particularly suited to industrial applications, so little attention has been given here to the effectiveness or longevity or PTMS plasma films. Nevertheless, a brief study was undertaken in order to investigate how the deposited films are attached to the magnesium substrates.

The basis of these experiments involved placing complete PTMS films in various solvents and ultrasonically agitating them in an attempt to remove the film. The plasma deposition conditions chosen were 20W of applied power a pressure of $1x10^{-3}$Torr for 1800 seconds, a treatment that has been demonstrated in the preceding chapter to form a complete film. The solvents chosen were pure acetone, pure ethanol and pure water. If the films are bonded to the magnesium surface through a metal-siloxane bond, then it is expected that the protic solvents, water and ethanol (those that possess a hydrogen atom bound to oxygen) will be able to more easily remove the film as occurs in the case of chemical dip coating.

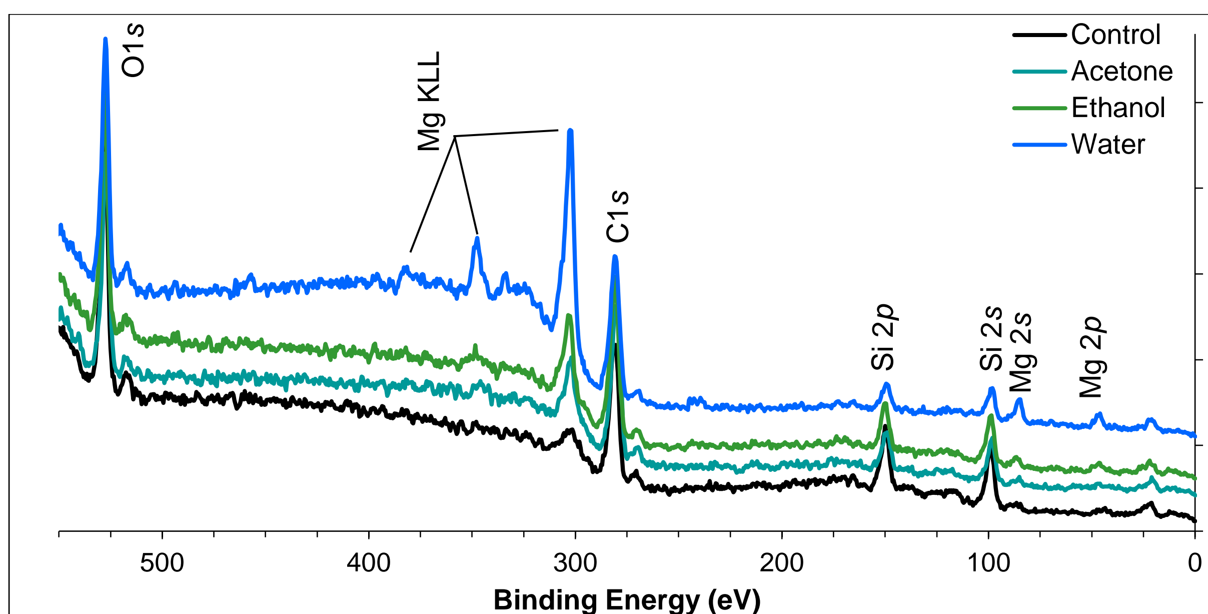

Figure 4.31 XPS spectra of PTMS plasma coated magnesium surfaces sonicated in various solvents for a duration of 5 minutes.

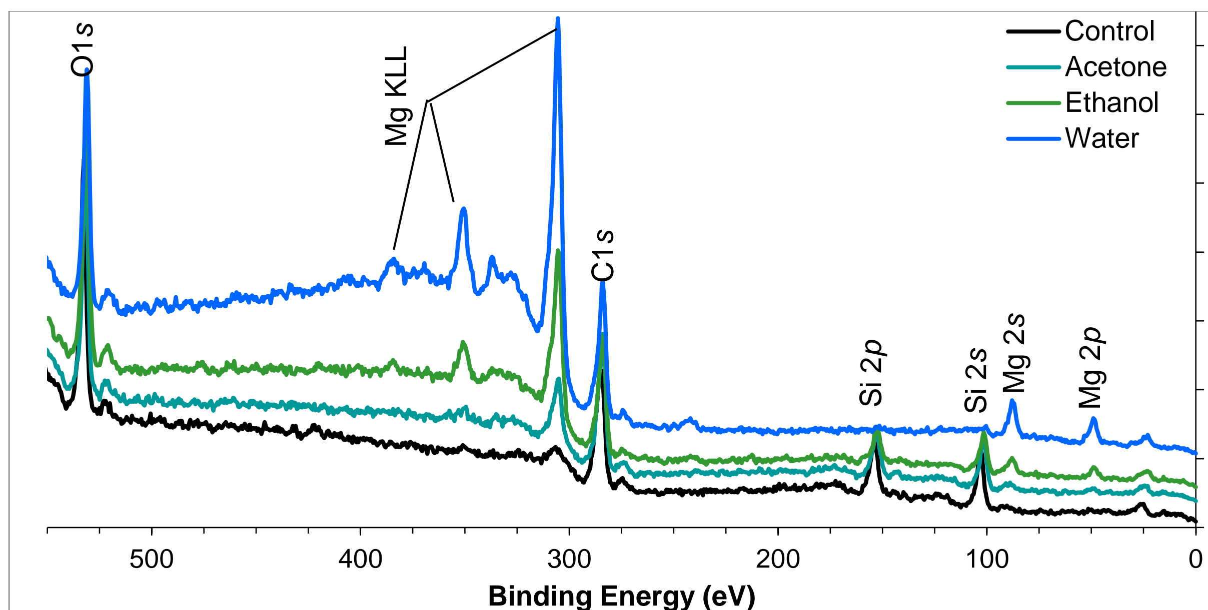

Figures 4.31 and 4.32 show the results of this attempted removal after a sonication period of 5 and 60 minutes respectively. After 5 minutes, it can be observed that the film sonicated in water has been removed to such a degree that magnesium is readily detected spectrally. The films sonicated in acetone and ethanol do not experience the same rate of film removal, implying that the mechanism of removal is a chemical process, rather than a mechanical one. This is supported by the data obtained after an hour of sonication. As seen in Figure 4.32, silicon can no longer be detected within the XPS spectrum of the sample sonicated in water, implying that the film has been completely removed. This is in contrast to the samples sonicated in ethanol and acetone, the latter of which is nearly indistinguishable from the control sample (that was not sonicated at all). Some magnesium signal is detectable in the spectrum associated with the sample sonicated in ethanol however, which implies that it is the proticity of the solvent that has led to the removal of the organosilane film. If the film was only loosely attached to the surface, then the mechanical action of the sonication alone could remove the film, so that only the films sonicated in the solvents that are able to hydrogen bond (and hence reverse siloxane linkages) were removed provides some useful, if indirect, evidence of the formation of metal-siloxane bonding. This has important implications for any usage of organosilane in industry, especially those that involve aqueous environments (such as for corrosion protection in marine environs or biomedical implants) as the ability for water to easily remove films could make the usage of organosilanes unviable.

4.6 **Summary**

Throughout this chapter, the process of creating organosilane films through the use of plasma enhanced chemical vapour deposition has been detailed. Beginning with a simple

steel chamber and copper coil antenna, a vacuum system and appropriate RF matching unit and was designed and constructed in order to produce plasma from both gaseous and liquid precursors. This chamber was used to successfully pre-treat and deposit films of PTMS onto pure magnesium surfaces, with no observable damage to the substrate itself. These films were characterised though a combination of XPS and scanning Auger spectromicroscopy, which were able to determine the coverage, composition and thickness of films created through variation to a range of experimental plasma conditions. By varying the duration of plasma exposure, the thickness of the film was controllable. Increasing the thickness of the deposited film also led to an increase in uniformity of the film composition. The composition of the film itself was significantly different to that of the precursor PTMS molecule, most notably with a significant reduction in the carbon to silicon ratio from 6:1 for PTMS, to approximately 2:1. Additionally, the oxygen to silicon ratio was reduced from 3:1 for PTMS to approximately 1.3:1. That both the carbon and oxygen content within the film is reduced compared to PTMS implies that individual molecules are decomposed, either in the plasma phase or through etching by reactive plasma species after attachment to the surface. Changing the amount of RF power applied to the PTMS plasma did not lead to a significant change in the chemical composition of the deposited film as measured with either XPS or Scanning Auger analysis. Greater film coverage was observed as power was increased along with a slight increase in film thickness as measured by depth profiling of the silicon KLL Auger peak. The plasma exposure duration chosen for these experiments was relatively short, and a key result of this work was that for the plasma duration chosen, although film coverage increased, a complete film was never formed, with magnesium detectable spectrally both in XPS and AES data, as well as through Scanning Auger Microscopy.

5 Chapter 5: Effect of Experimental Plasma Parameter Variation on PTMS Thin Film Composition and Structure

In the previous chapter, a relatively short duration (60 seconds) of exposure was used to investigate the effects of plasma power on the coverage of the deposited film. A consequence of this was that while changes in coverage were observed, a complete film was not able to be deposited. In addition, elemental mapping determined the existence of carbon contamination still present after the oxygen plasma pre-treatment. Due to short deposition time, a very thin layer was deposited, allowing this carbon material to be detectable in XPS measurements. How the composition of the deposited film changes with applied plasma was then skewed by the presence of this underlying material.

With increased deposition time, much thicker films more uniform in composition were produced. In order to properly study the effect of varying the applied plasma power on the composition and structure of the film, a much longer deposition time of one hour was used. The increased thickness of the deposited film should give more certainty that any results obtained with XPS are due to the deposited film, and not the underlying magnesium surface, and any remnant carbon contamination.

Another discovery in the previous chapter is the effect of the surface morphology on the structure of the film. The surface finish used in those experiments was created by abrading with 1200p silicon carbide paper. On the macro-scale, the surface produced by such a treatment was deemed suitable, however when examined more closely with both SEM and AFM, it was found that the microstructure of the surface was very rough, and elemental mapping with AES confirmed that the deposited film was affected by this surface roughness. Therefore, in addition to increasing the duration of the plasma, silicon carbide abraded magnesium surfaces were subsequently diamond polished using successive grades of diamond paste down to 1μm in order to reduce the effects of surface roughness on the deposited film.

5.1 Surface Morphology Analysis by AFM

5.1.1 Roughness of Magnesium Substrate

While not atomically flat, the surfaces produced upon polishing were much smoother than those used previously. Figure (5.1). A value for Root-Mean Squared roughness (R_q) was

calculated to be 11.5±1.97nm, from 10 separate locations across 2 different samples, all with a scan size of 10nm. This is compared to a RMS roughness of 92.8±59.4nm found for the previous, silicon carbide abraded samples.

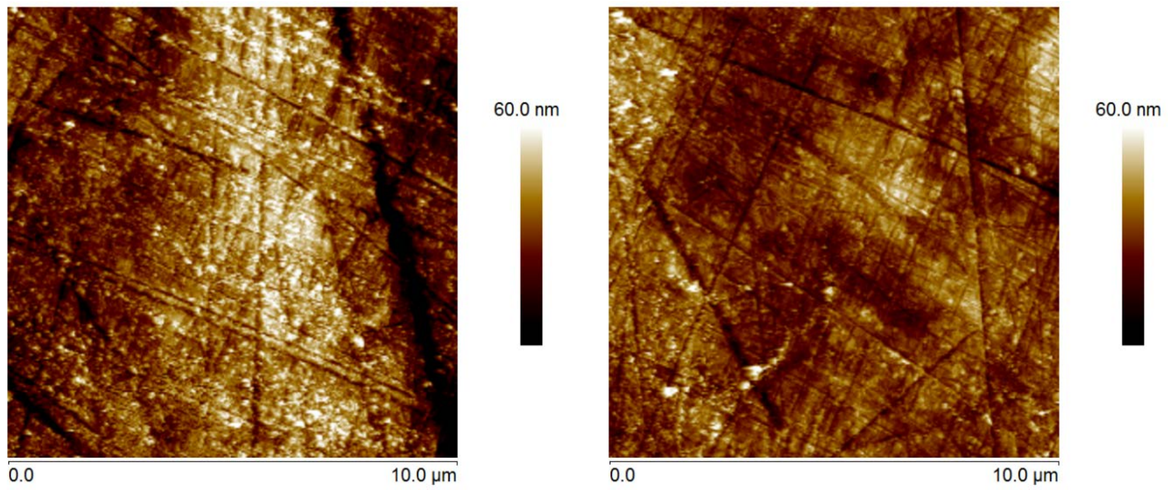

Figure 5.1: AFM images of diamond polished (1µm) magnesium surfaces

This reduced surface roughness should provide a better foundation for the analysis of the thin films produced.

5.1.2 Effect of PTMS film on Surface Roughness

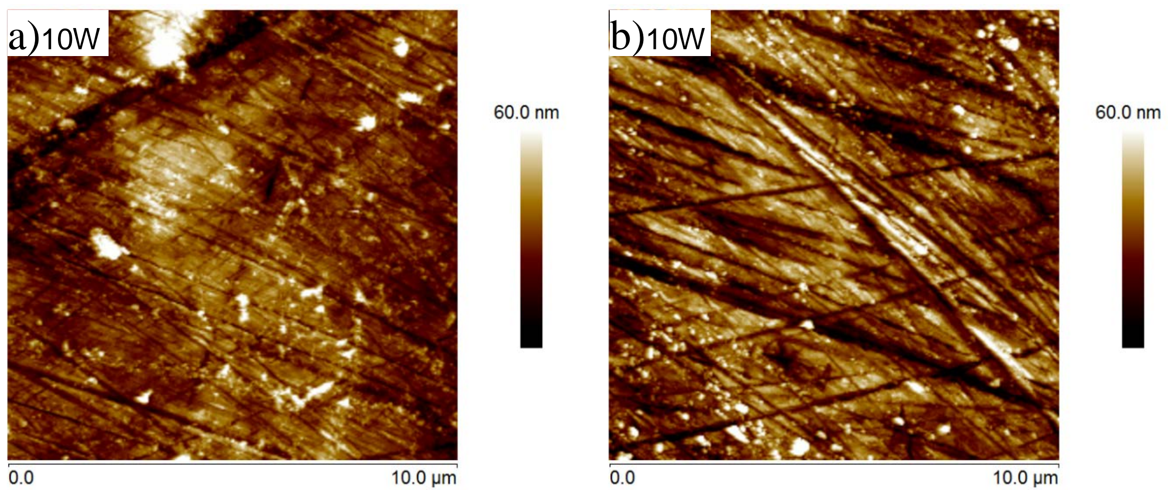

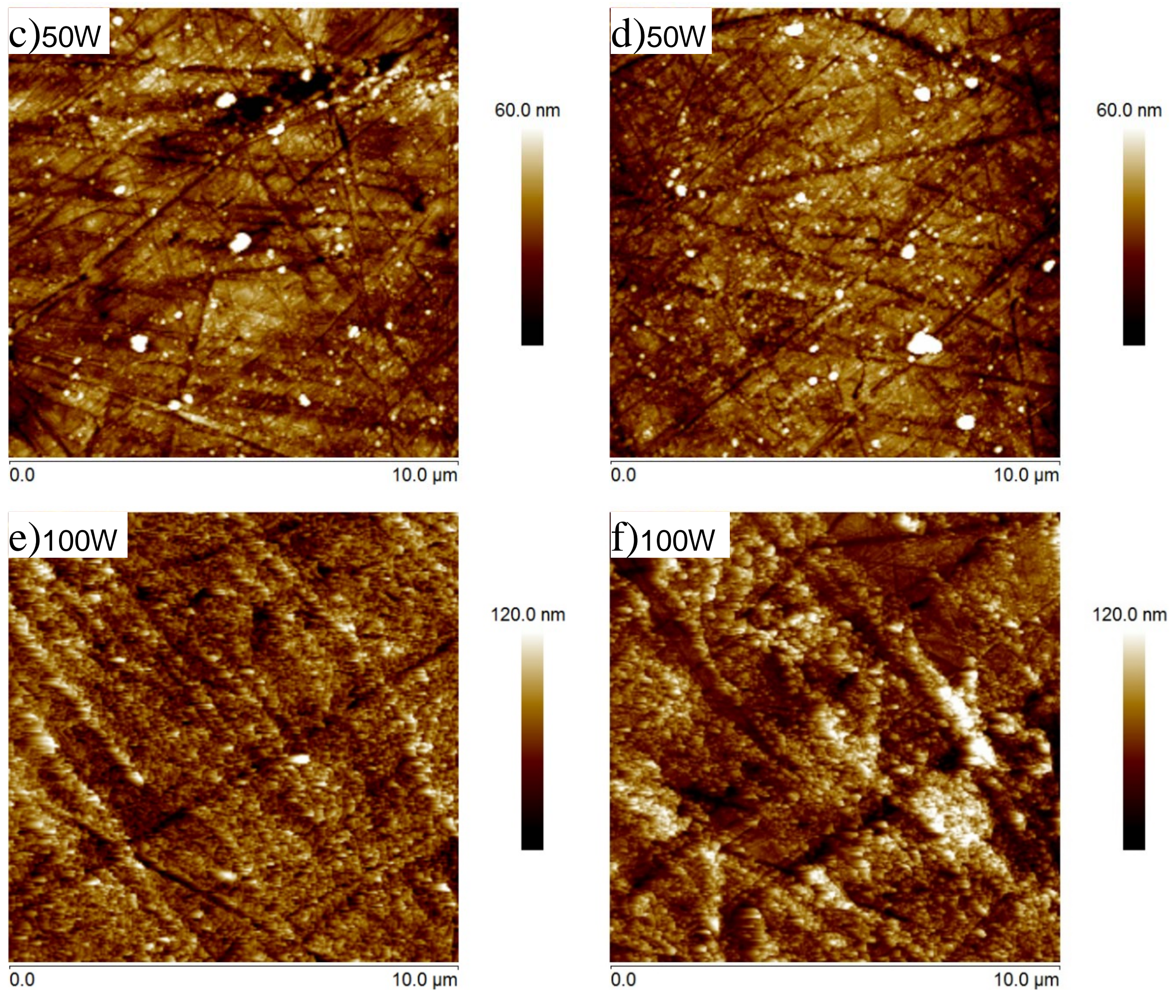

Figure 5.2: a-f) Representative AFM images of PTMS coated, diamond polished magnesium surfaces

Table 5.1 Average RMS roughness of PTMS coated, diamond polished magnesium surfaces.

Power	Average RMS Roughness (nm)
0W (No coating)	11.5±2.0
10W	11.8±2.9
50W	9.9±1.7
100W	17.2±3.4

Representative AFM images and calculated values for surface roughness are shown respectively in Figure 5.2 and Table 5.1. There is little difference either visually, or in the values for roughness between the samples coated at 10W and 50W in the samples imaged,

with all surfaces exhibiting the same features of the uncoated magnesium seen after the pre-treatment in Figure 5.1. This illustrates a key difference between plasma deposition methods, and chemical ones. Whereas a liquid chemical would “fill up” the scratches and troughs on the surface, in a plasma, only those species that both make contact and have sufficient energy will have the possibility of binding to the surface, and those that do attach have very limited mobility, especially compared to a liquid solution which is able to penetrate recessed areas of the substrate. A consequence of this is that it is difficult for plasma species to ‘fill’ such areas of a surface, as the binding plasma species can only reach the lower parts of these features through a relatively small angle of acceptance, whilst species approaching from a wider angle will be intercepted by the surrounding ‘higher’ areas of the substrate, and gives some indication as to why the roughness of the substrates is of such high importance for plasma deposition.

The average value for surface roughness for the sample coated with the 100W plasma is significantly greater than for the other plasma treatments. The cause of this increase in RMS roughness is apparent visually in Figures 5.2 e) and f). While the same general features caused by the polishing process are still visible, there is also a secondary group of rougher features at a smaller scale. It is most probable that this layer is the deposited PTMS film. Due to the power used, etching of the film by high energy species within the plasma leads to the observed surface features. Whether this etching is significant enough to prevent a full film being formed can be determined through analysis with both XPS and scanning Auger spectromicroscopy.

5.2 XPS Analysis of PTMS Films

5.2.1 Compositional Analysis

The XPS data seen in Figure 5.3 shows the average concentration of each element present in the deposited film, plotted against the plasma power used. This is a slightly different presentation of XPS data to previous chapters, but due to the longer deposition times and thus thickness of the deposited films, no magnesium signal is present in the acquired spectra. As the value for coverage (Γ) equals 1 in these cases it is not presented graphically in this section of the investigation as a measure of surface coverage for the deposited films.

In the data series, it does appear that there is a slight downward trend in silicon and oxygen percentage (and thus increasing carbon content), and a corresponding increase in carbon with power. The difference is slight though, with each of the vales within the standard error of the mean of each other, so there is no significant difference in the overall elemental composition of the film with increasing power.

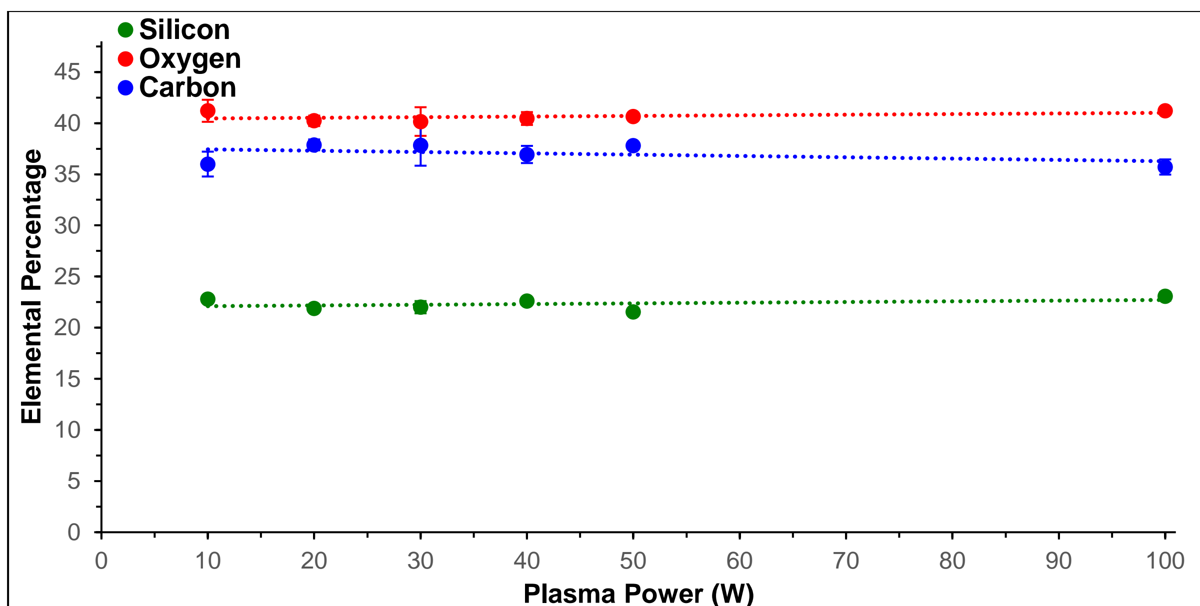

Figure 5.3 Variation of elemental composition with applied plasma power of PTMS films on magnesium

When this data was first collected, there were several anomalous values regarding elemental concentrations, which were of some concern. These values led to significant uncertainties in coverage for the 30W and 100W samples larger than that of the samples coated with other values for applied plasma power. The cause of this large variation appeared to be that the carbon concentration for an individual sample in each of these sets was much greater than all others. Each set of samples was exposed to the same plasma, so it is unlikely that this increased carbon content is a product of plasma conditions, and is more probably deposited onto the surface as a contaminant after the plasma process. The XPS analysis spot size for the SPECS apparatus used for these measurements is at least 2mm in diameter, so areas of localized contamination present within this analysis area will be detected spectrally, potentially leading to an exaggeration in the carbon content of the film. Therefore, the aberrant samples were removed from the calculation of mean elemental composition and standard deviations (leaving two samples for 30W and 100W each, rather than the three samples for each of the other powers). The resulting flat lines of best fit in Figure 5.3 for each element show almost no slope, which heavily implies that the composition of the plasma film does not vary with applied plasma power.

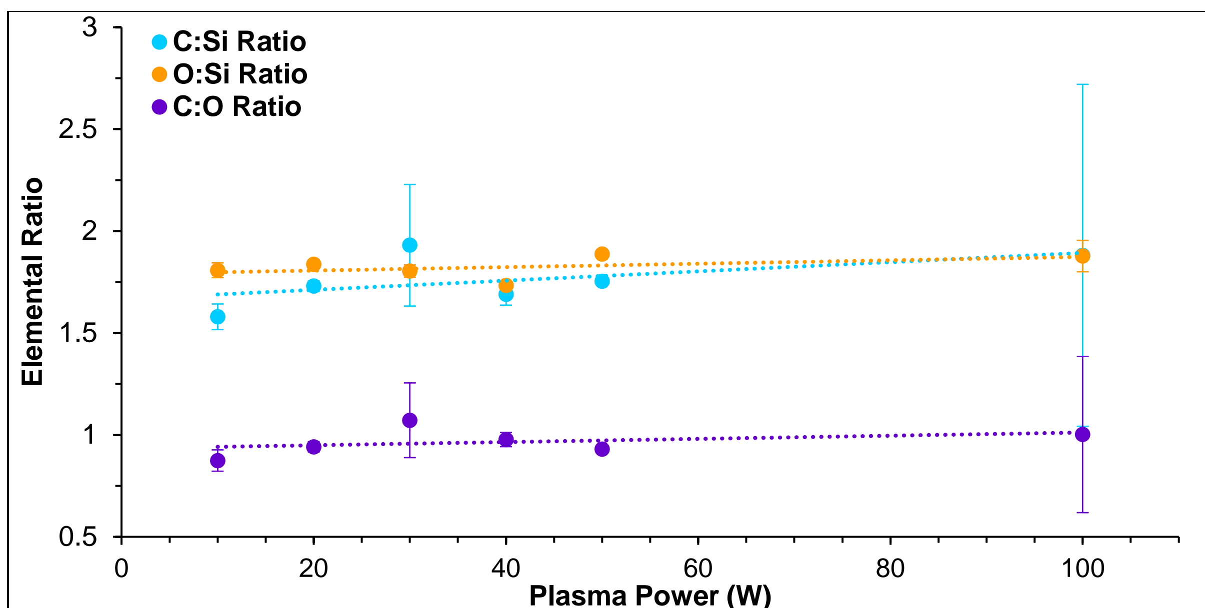

Figure 5.4: Ratios of elemental composition vs applied plasma power

By comparing elemental ratios, as in the previous chapter, further information about the composition of the film can be gained and more easily compared with previously obtained data. Presented in Figure 5.4 are the plots of the C:Si, O:Si and C:O ratios vs applied plasma power. The values for the C:Si ratio are, for the most part, between 1.5:1 and 1.8:1 (excluding those values for which excess carbon contamination is suspected). These values are slightly lower than those obtained in the previous chapter for a complete film (a value of approximately 2). Conversely, the O:Si ratio is increased compared to the results obtained for films previously deposited on rougher surfaces. Previously a value for this was approximately 1.3:1, whereas for the films deposited here, a value closer of approximately 1.9:1 is observed. This increase in relative oxygen content and corresponding decrease in carbon is attributed to the smoother surface produced by the diamond polishing process; decreasing the roughness of the samples reduces the areas that are able to harbour carbonaceous material that are not removable by the oxygen plasma cleaning process.

5.2.2 Analysis of Silicon Bonding Environment through High Resolution XPS

As useful as they are in determining the overall elemental composition of the deposited film, there is further information available through XPS analysis of individual elemental peaks with higher energy resolution. Previously, studies by Alexander et al. [149, 150] and Hillborg et al. [182] have shown how the Si2*p* photoelectron peak may be deconvoluted to determine the bonding environment of the silicon atom. Generally, as the 'oxygenation' of the silicon atom increased, the binding energy of Si2*p* electrons also increases. In those studies, the precursor material used for plasma deposition was 'HMDSO', the structure of which is

presented in Figure 5.5, compared to the structure of the PTMS molecule used in this work. The key difference in structure between the two molecules is that the silicon atom in PTMS has three oxygen and one carbon neighbouring atoms, in comparison with the inverse of three carbon and one oxygen present in HMDSO. These silicon environments will be referred to as $Si(-O)_3$ and $Si(-O)_1$, etc. Unless Si-O bonds are being broken in the plasma and replaced with Si-C bonds, which is an energetically unfavourable process, then the vast majority of silicon atoms in PTMS should still be in the $Si(-O)_3$ environment, with a binding energy of approximately 102.8eV [149]. It should also be noted that this peak energy was assumed by Alexander et al. to be at a binding energy equidistant between two known control samples, one of pure PDMS (with silicon entirely in the $Si(-O)_2$ state), and the other of pure silicon dioxide (entirely $Si(-O)_4$). A study by O'Hare et al. [183] called into question the fitting performed by Alexander and Hillborg, in that it did not include components which should arise due to the multiplet splitting of the Si2*p* photoelectron peak. Ignoring these peaks was stated as a deliberate choice within the manuscript by Alexander et al. to quote: "the information present in the spectra does not justify additional complexity". Conversely, O'Hare et al. fitted the Si2*p* spectrum of various silicon containing compounds with two separate peaks, one corresponding to Si2*p* 3/2 and one for Si2*p* 1/2. Similar to previous results, the binding energy of the silicon peak increased for silicon containing more bonds to oxygen, however, the shift in this peak was not linear as previously assumed. Conveniently, the difference between $Si(-O)_3$ and $Si(-O)_4$ was found to be approximately the same as assumed by Alexander et al. therefore, for the peak fitting performed here, both methods are equally valid. Therefore, due to the added complexity needed to fit with both Si2*p* 3/2 and 1/2 components only a single symmetrical peak will be used, as by the method prescribed by Alexander et al.

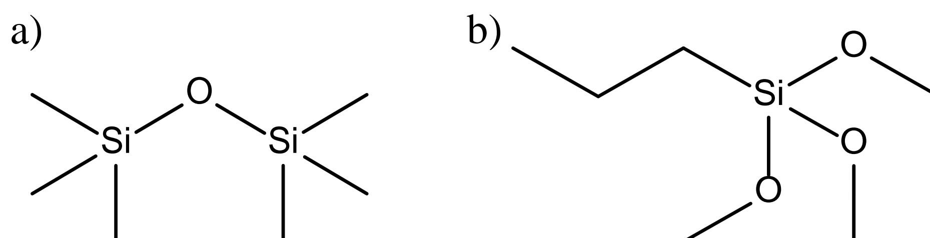

Figure 5.5 a) Structure of the molecule "HMDSO" b) Structure of the molecule "PTMS"

Presented in Figure 5.6 is an example of the Si2p peak, with fitting process applied, with two observed components. In order to achieve a fit that makes physical sense, some constraints were applied to the fitting process within CASA XPS. Firstly, a Gaussian:Lorentzian ratio of 4:6 for the fitted curves was chosen to match the one used by Alexander et al. [149], which was found to provide a very good match for the tails of the Si2*p* spectral peak. Peaks were

then added with a binding energy of 102.7eV which, according to the investigation by O'Hare et al, should be the location of silicon in the Si(-O)$_3$ environment. Several fitting iterations were performed, which resulted in an incomplete fit with the prescribed parameters, indicating that additional silicon environments were present. Therefore, a second peak was added to the high binding energy side of the existing curve at 103.5eV, the approximate position of silicon in the Si(-O)$_4$ environment as found by O'Hare et al. [149]. After several fitting iterations, the curves seen in Figure 5.6 were produced.

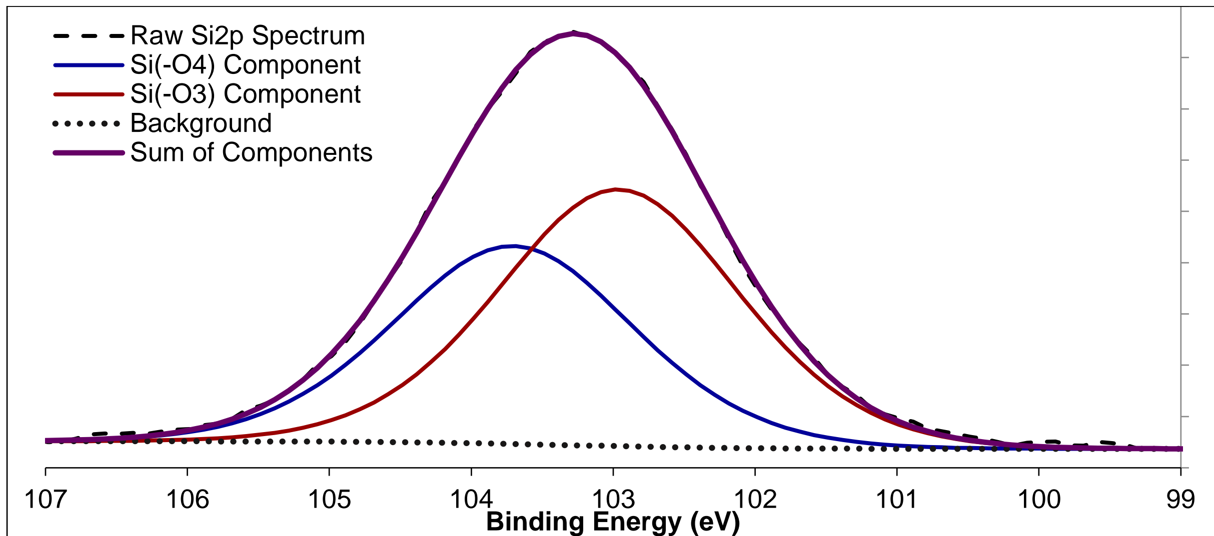

5.6 Example Deconvolution of the Si2*p* photoelectron peak. This spectrum is obtained from a PTMS film deposited at 10W

The data presented in Figure 5.7 is the result of collating the data from each of these peaks, with the percentage of the total Si2*p* peak area of each component is plotted separately. As only two components are fitted for the Si2*p* peak, they necessarily vary inversely with each other.

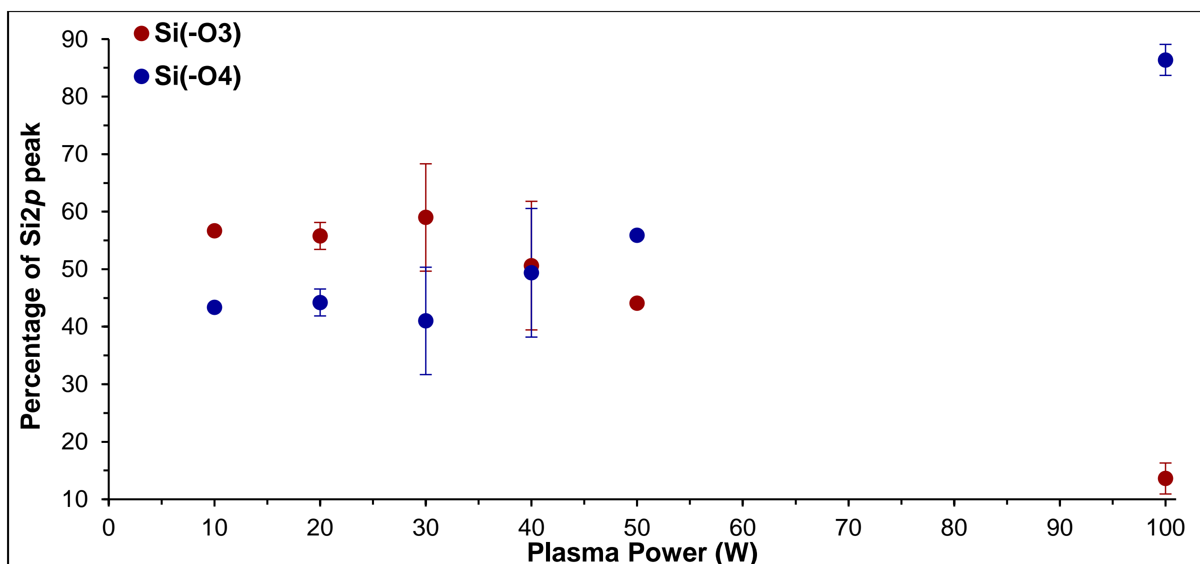

Figure 5.7 Plot of Si2*p* peak composition vs applied plasma power.

All of the prepared samples had a non zero amount of silicon in the Si(-O)$_4$ environment, which gives evidence for the Si-C bond being broken in the plasma state of the PTMS molecule, even for the lowest powers used here. This goes some way to describing the silicon to carbon ratio in the survey spectra, where the amount of carbon present within the film was significantly lower than that of a typical PTMS molecule. For plasma powers of approximately 40W and above there is a trend towards increasing Si(-O)$_4$ content, with films deposited from a 100W plasma having approximately 85% of their silicon atoms bonded to four oxygen atoms. This is direct evidence of the complete removal of the propyl chain of PTMS, as lower energy Si-C bonds are replaced with Si-O bonds. So, an increase in plasma power leads to an increase in the decomposition of the PTMS molecule, with an increased proportion of the weaker Si-C bonds breaking during the deposition process by the higher power plasma environment. This provides an available bonding site for any reactive oxygen species (either free or attached to PTMS molecules) to attach, forming a strong Si-O bond which is less likely to be broken within the plasma environment. However, when considering the overall composition of the film as determined by XPS survey spectra there is no significant change in the ratio of silicon to either oxygen or carbon as plasma power increases. So: while the bonding environment of silicon is changing as the power applied to the PTMS plasma increases, the amount of oxygen or carbon within the film is not. The implication here, is that at least some carbon is deposited onto the surface independently of the silicon 'core', or alternatively, PTMS is deposited in a more intact state and bombardment by high energy plasma species causes fragmentation through sputtering of the surface. Without being able to quantify the species present within the plasma, it is difficult to state with certainty the exact mechanism of deposition, however it is likely that both processes occur to some extent. In both cases, as the pressure of the PTMS vapour is

kept constant, an equilibrium is established between the flow of PTMS vapour into the chamber and evacuation of reaction by-products from the chamber by the pumping system. This equilibrium is what appears to dominate the composition of deposited films, rather than the power applied to the plasma system.

5.3 Scanning Auger SpectroMicroscopy Studies on PTMS Film Composition and Coverage

The AFM data shown previously in Section 5.1.1 has shown that there is a significant decrease in the surface roughness as a consequence of diamond polishing the samples. The surface finish is certainly not atomically flat, with some areas of the surface still possessing deeper features that were not removed through diamond polishing. Previous scanning Auger spectromicroscopy analysis of films deposited from PTMS plasma showed a strong variance in film composition across the magnesium substrate, which was well correlated with such physical surface features. Scratches in the magnesium surface caused by abrasion with silicon carbide paper made for regions where carbonaceous material was able to remain, despite pre-treatment processes. Therefore, similar regions present here could also contain areas of increased carbon which, due to the comparatively large analysis area of XPS, could cause the amount of carbon actually present in the film to be over represented. By using SEM in conjunction with scanning Auger spectromicroscopy it is possible to locate smooth areas of the surface, excluding areas of contamination, and thus accurately determine the composition. In addition, elemental mapping of these areas will give a good indication of film uniformity. Depth profiling the film should also give a good indication of how the plasma power affects the growth rate of the PTMS film, again without the dominant influence of surface roughness.

5.3.1 Film Uniformity

The elemental maps present in Figure 5.8 a) to l) show the coverage of silicon, oxygen and carbon combined into RGB images (where silicon is green, carbon is blue, and oxygen is red) for representative areas of the films deposited at each plasma power. As was expected for the duration of the plasma treatments used here (when compared to the 60 second treatments used to investigate the effects of plasma power in Chapter 4) the surfaces are, for the most part, uniform in composition, with a few exceptions. Several surfaces, most notably the overlays of the 10W and 50W surfaces show areas of carbon in high concentration which appear to the exclusion of both silicon and oxygen. In the case of the films deposited using a plasma power of 50W, carbon appears most strongly in locations that align well with surface features. However, for films deposited at other powers, these physical surface features observed in SEM imaging are also identifiable through changes in

intensity in all of the elemental maps, despite the decrease in surface roughness of the magnesium substrate. Some of these surface features are more easily identifiable (most notably in the 30W and 40W cases) than others, but it is clear that the deposited film is not completely uniform.

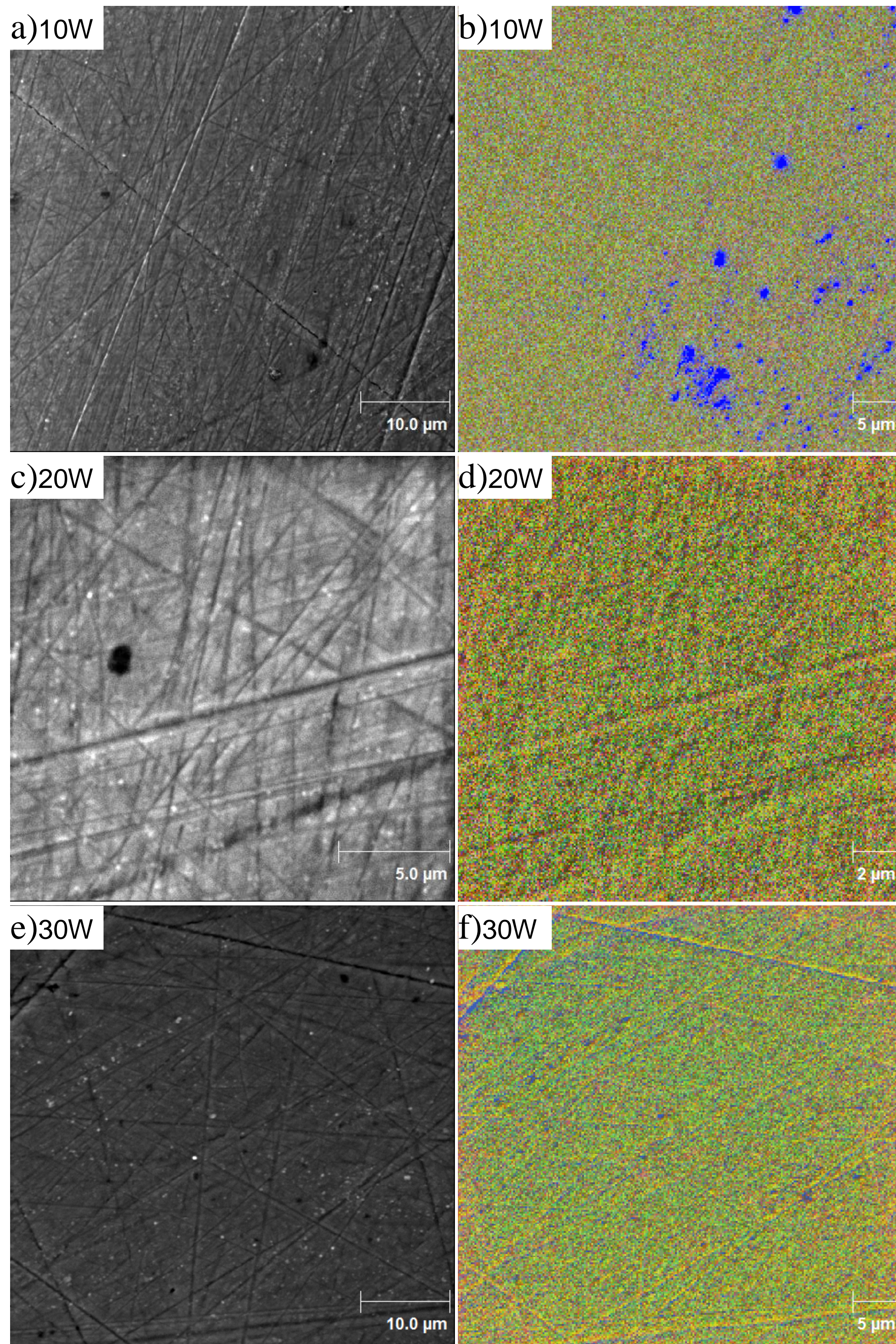

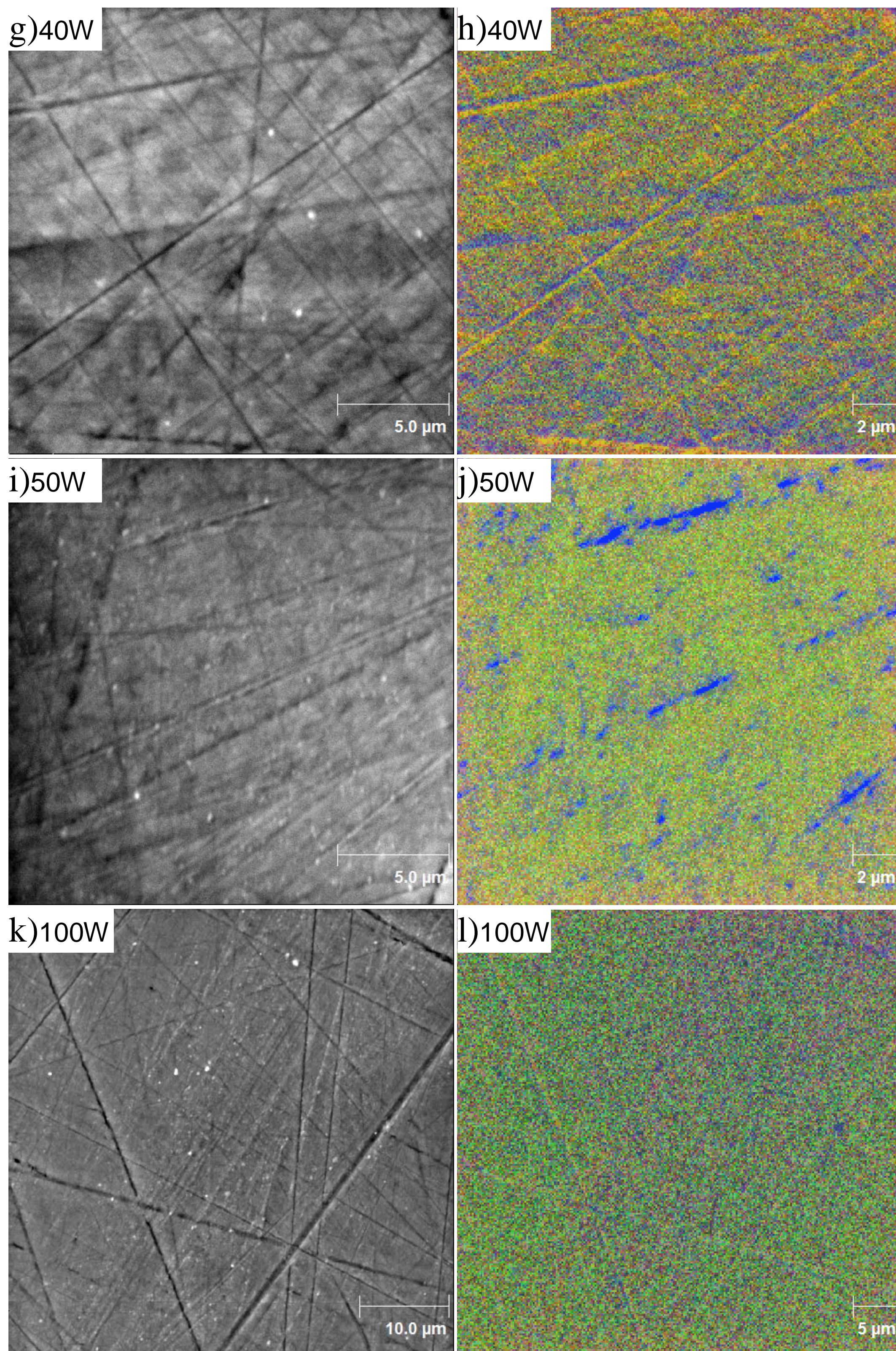

Figure 5.8: a-l) SEM images of magnesium surface after PTMS plasma deposition with an applied power of between 10W and 100W, along with accompanying overlayed elemental maps of silicon (green), oxygen (red) and carbon (blue).

Previously, the high roughness of the substrate was shown to have a significant effect on the

growth of the plasma film, and while analysis with AFM has shown that the surface roughness is considerably lessened by diamond polishing, similar features can be observed in the SEM images in Figure 5.8. From examination of the corresponding elemental maps, it appears that even small physical surface features influence the morphology of the final film. Of the constituent elements within the deposited films, carbon appears to be affected most strongly by the physical structure of the surface, with greater changes in spectral intensity than what occurs for silicon and oxygen. This is illustrated in Figure 5.9, which depicts five separate copies of the SEM image seen previously in Figure 5.8 h), which corresponds to the magnesium surface after plasma deposition using 40W applied RF power. Overlayed over each image, are copies of the corresponding Auger elemental map of carbon map with varying decreasing levels of transparency.

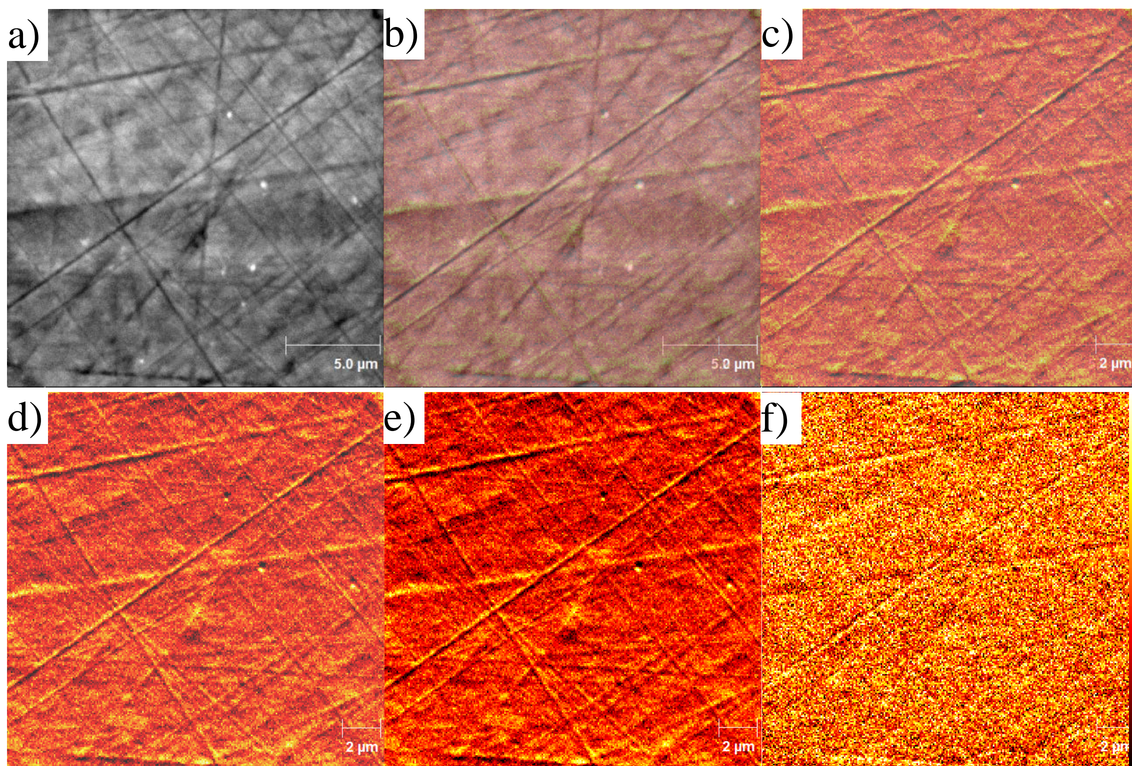

Figure 5.9: a) SEM Image of a magnesium surface coated by a PTMS plasma with an applied power of 40W. b)-e) Elemental map of carbon overlayed onto SEM image with decreasing transparency. f) Elemental map of silicon. The bar on the right hand side of the image gives an indication of the intensity scale for all presented maps. The "thermal" scale ranges from black at the lowest intensity to white at the highest.

There is a baseline concentration of carbon across the smoothest parts of the surface, with smaller areas of increased carbon concentration (where the map becomes more ‘yellow’), which do not appear ascribable to any particular features present in the SEM image. In contrast to this, the scratches in surface seen in the SEM image agree strongly with lines of differing carbon intensity in the elemental map. The ‘channel’ part of the scratch lines up

quite well with a decrease in carbon concentration, while adjacent to this is an area of high carbon concentration. A potential explanation for this behaviour is that there are fewer electrons being emitted from these areas (which is why as a direct measure of emitted secondary electrons, the SEM image appears darker at these locations). If this were the case, however, then other elemental maps would show the same features. By considering the silicon map in Figure 5.9 f) then as with the carbon map, the larger scratches can be observed through changes in silicon intensity. Unlike the carbon map, the concentration of silicon appears to be greater within the 'trough', and lesser alongside it, inverse to the carbon map. This implies that voids on the surface, while not 'filled' in the conventional sense (as AFM data in Section (5.1.2) still clearly shows that these features are depressions in the surface), do appear to contain a higher concentration of silicon containing material.

There are two key findings presented here from the elemental mapping performed. Firstly, it appears that the variations in plasma power used here do not appear to have a strong effect on the uniformity of the final film. This occurs despite changes in the bonding state of silicon between low and high powers found in XPS data. If regions of $Si(-O)_4$ were growing in a cross-linked network, then associated areas (even small ones) of increased oxygen concentration should be seen in elemental mapping. Such areas are not observed and in smoother areas of the magnesium surface the elemental composition remains very consistent between low and high power plasma-modified samples. In the less smooth areas of the surface however, there are variations in the composition which implies the physical morphology of the substrate plays a role. This behaviour leads to another key finding through elemental mapping. Despite a much smoother diamond polished surface, areas of non-uniformity in the form of scratches approximately 1μm in width still remain. These surface features are shallower than the ones produced by abrasion with 1200p silicon carbide paper, and the effect of the surface morphology is therefore lessened. Most notably, areas of deep carbon contamination are absent, implying that the morphology of the substrate itself has some influence over the final film.

5.3.2 AES Study of Film Composition

While the ability to see any variation in elemental composition across a surface is a significant advantage of Scanning Auger elemental mapping, using this information to perform further analysis in-situ is an even greater strength. By selecting areas identified by elemental mapping to be uniform in composition for more in depth analysis with AES, the effects of any surface contamination on the measured film composition can be reduced.

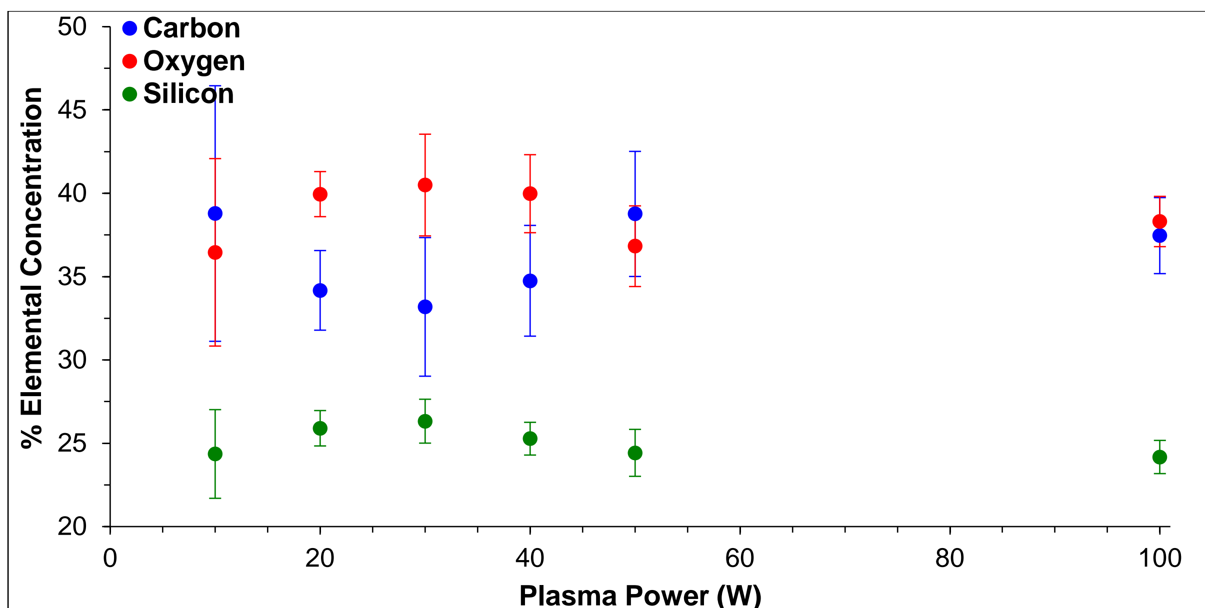

Figure 5.10: Percentage elemental composition of Plasma deposited PTMS films obtained from AES spectra vs applied plasma power

Upon comparing this data presented in Figure 5.10, to the XPS results in Figure 5.3, there is a discernible increase in variation between individual samples. In addition, the uncertainty in each sample is significantly higher than what was seen previously. This is most likely a consequence of taking measurements from a large number of smaller sites across each of the surfaces, rather than a single XPS measurement for each of the samples.

That such variation is seen does at first glance, imply that there are more significant changes in the film composition across the surface than was apparent through elemental mapping. However upon closer inspection, the concentration of carbon appears to vary inversely to that of both oxygen and silicon. This effect is highlighted in Figure 5.12, where the ratios of carbon, oxygen and silicon for films deposited at each plasma power are plotted.

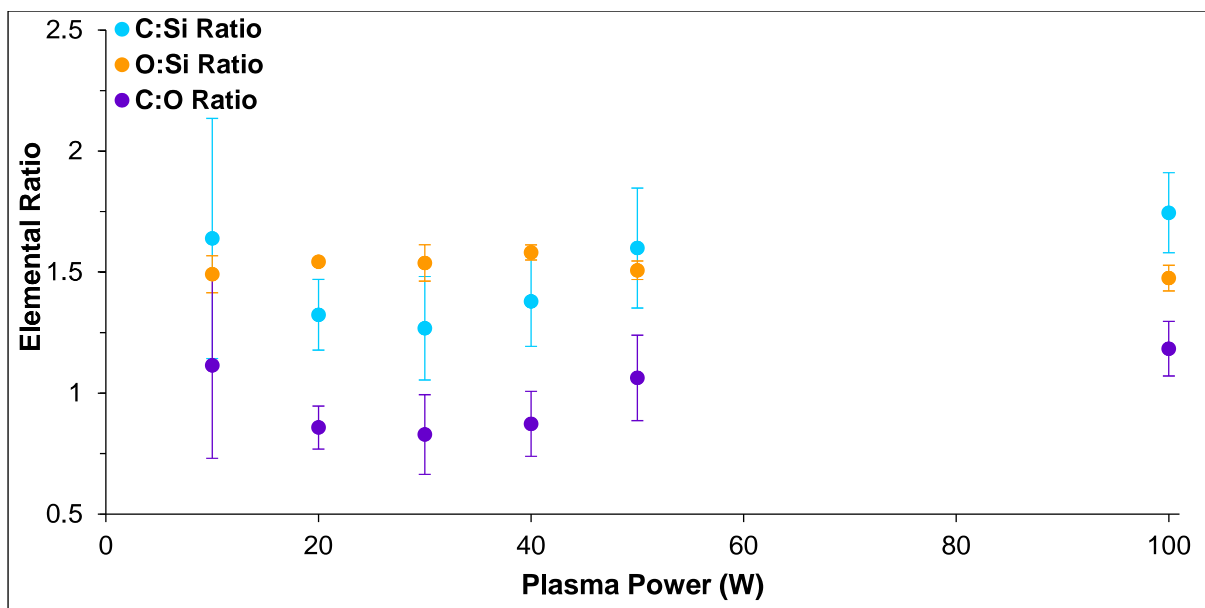

Figure 5.11: Elemental ratios of C:Si, O:Si, and C:O of films deposited from PTMS plasma vs applied plasma power, obtained from AES spectra.

Of particular note here are the C:Si and C:O ratios compared to O:Si. The former vary with changing plasma power while the latter remains relatively constant in addition to possessing much smaller uncertainty than the ratios involving carbon. The largest deviations between the ratios appear for the films deposited at 20W, 30W and 40W. It is possible that the cause of this variation is related to the plasma power. If individual species within the plasma have different deposition rates (assuming that the PTMS molecule is decomposed in the plasma phase), then it is possible that carbon containing species are deposited at a faster rate for the 'middle' powers. Yet, if this were the case then the why was such variation not observed in XPS data? An alternative explanation is that despite attempting to select areas of the surface that were representative the film, there is adventitious carbon present across all of the surfaces in varying concentrations. There was a necessity that samples were transferred between the vacuum chamber used for deposition and analytical apparatus through air, which could have resulted in additional interactions between molecular species present on the surface and the prevailing atmosphere. The exposure to a non-pristine atmosphere could therefore allow a very thin film of adventitious carbon to adsorb onto the surface. As can be observed (in blue) across the elemental maps in Figure 5.8, some areas of carbon appear relatively intense, and it was these areas which were avoided in order to guide the choice of AES analysis location. As carbon is a component of the film itself, then it is possible and likely that adventitious carbon is present as a surface film that is not easily distinguishable within elemental maps, or even spectrally. Through use of the argon ion gun present on the Scanning Auger Nanoprobe, and the depth profiling capability that it provides, this is able to be tested experimentally.

5.3.3 Depth Profiling Study of Plasma Deposited PTMS Films

5.3.3.1 Carbon as a surface contaminant

In Figure 5.12, the SEM image and elemental map previously presented in Figure 5.8 a) and b) are reproduced, with two separate regions highlighted. AES spectra obtained for each of these regions are displayed in Figure 5.12 c), colour coded to the appropriate locations.

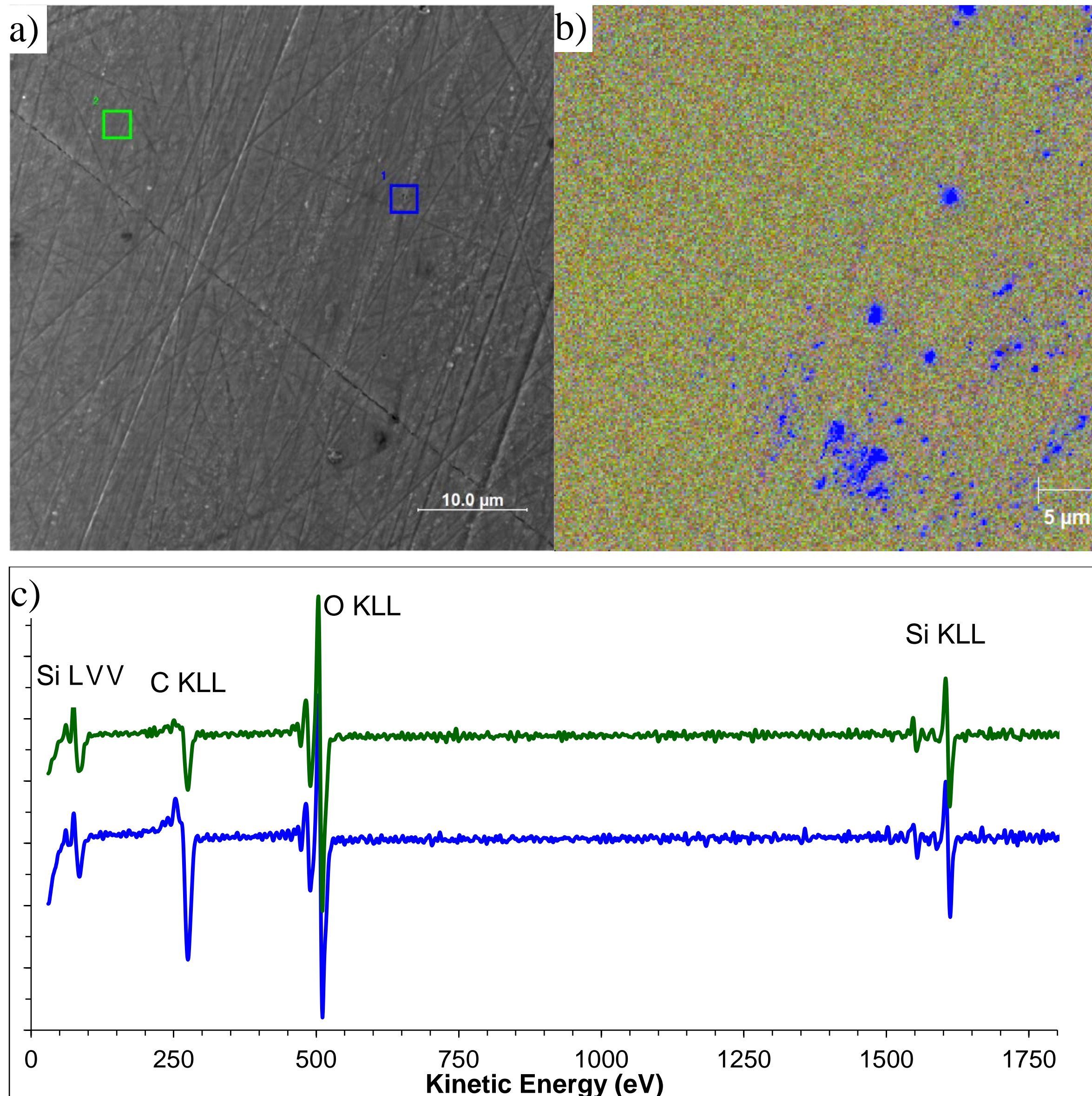

Figure 5.12 a) SEM image of a PTMS film deposited onto polished magnesium with an applied plasma power of 10W. b) AES spectra taken at the areas indicated.

When comparing the two spectra, it is apparent that the carbon concentration is much higher in spectrum 1 (in blue), as evident from the corresponding location within the elemental maps in Figure 5.12 b), where carbon dominates. In addition to this, the AES spectrum for this location also contains a significant silicon and oxygen presence, which is not shown

clearly in the elemental map. It was already stated that the elemental mapping technique used here is not quantitative, and is instead used to give a guide as to spatial differences in relative elemental concentrations, especially the overlayed maps. Instrumental limitations could also be a factor in the discrepancy. The AES spectra are created from the electron beam as it is rastered across the indicated analysis areas. As the areas chosen are limited to be squares, it is possible that there is some overlap of the analysis area, such that both carbon contamination and film are observed spectrally. In order to reduce this as a possibility, the analysis areas created were chosen to be smaller than might be intuitively necessary.

If the cause is not solely experimental, then there are several explanations for the increase in carbon concentration. Firstly, it could be that these features are created during the plasma deposition process as localised areas of film that are different in composition to that of the 'bulk'. It is far more likely however, that this carbon presence is only present as surface contaminant. So, similar to how signal from magnesium was still detectable through a thin organosilane surface film, that film is detectable spectrally underneath areas of carbon. This can be tested directly through the application of argon ion depth profiling. Presented in Figure 5.13 are the depth profiles for the analysis regions shown in Figure 5.12. With only a small amount of sputtering, the carbon signal in both areas decreases to a level that is consistent with each other, implying that carbon is present as a surface contaminant not only in the areas that it shows up clearly in elemental maps, but across the entire surface.

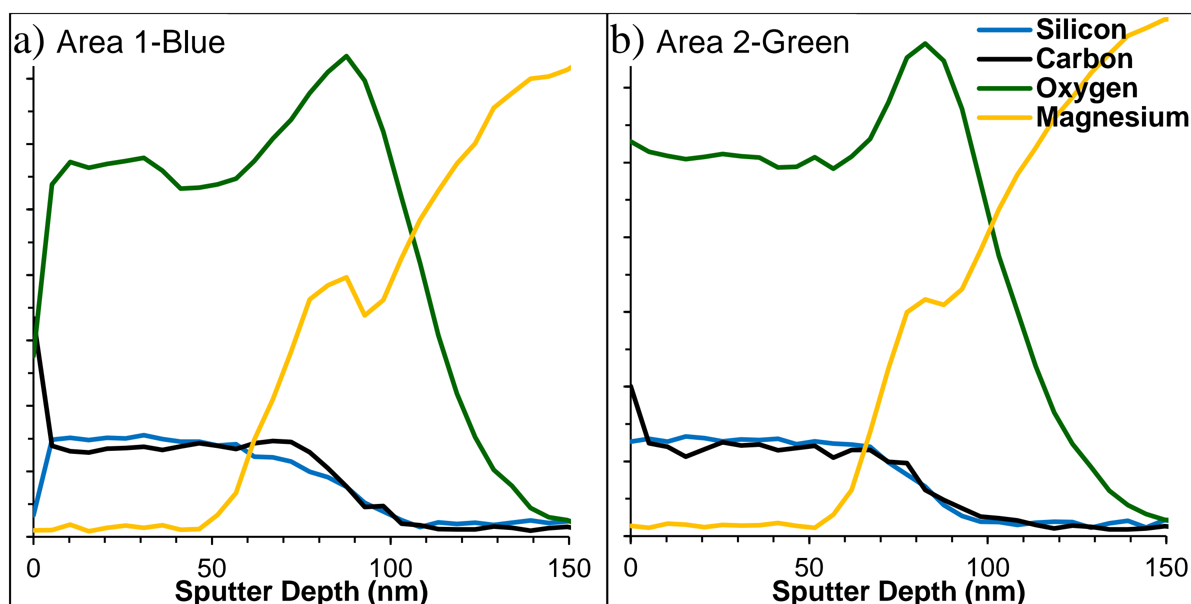

Figure 5.13 a) and b) Depth profiles of areas highlighted in Figure 5.12

5.3.3.2 Determination of Film Composition through Depth Profiling

As the depth profiles presented in the previous section are actually comprised of many individual spectra, further information may be extracted. Having established that carbon present as a surface contaminant then calculating the elemental concentration for the following region of the depth profile, a more precise result for film composition with depth can be determined.

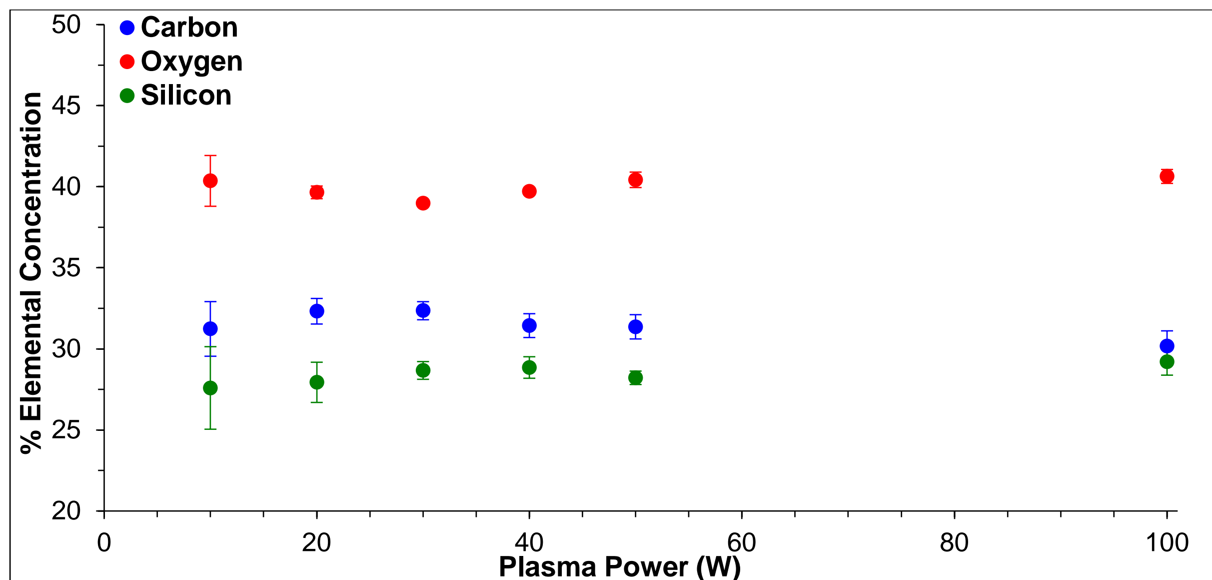

Figure 5.14: Percentage elemental compositions of films deposited from PTMS plasma vs applied plasma power as determined by AES and argon ion depth profiling

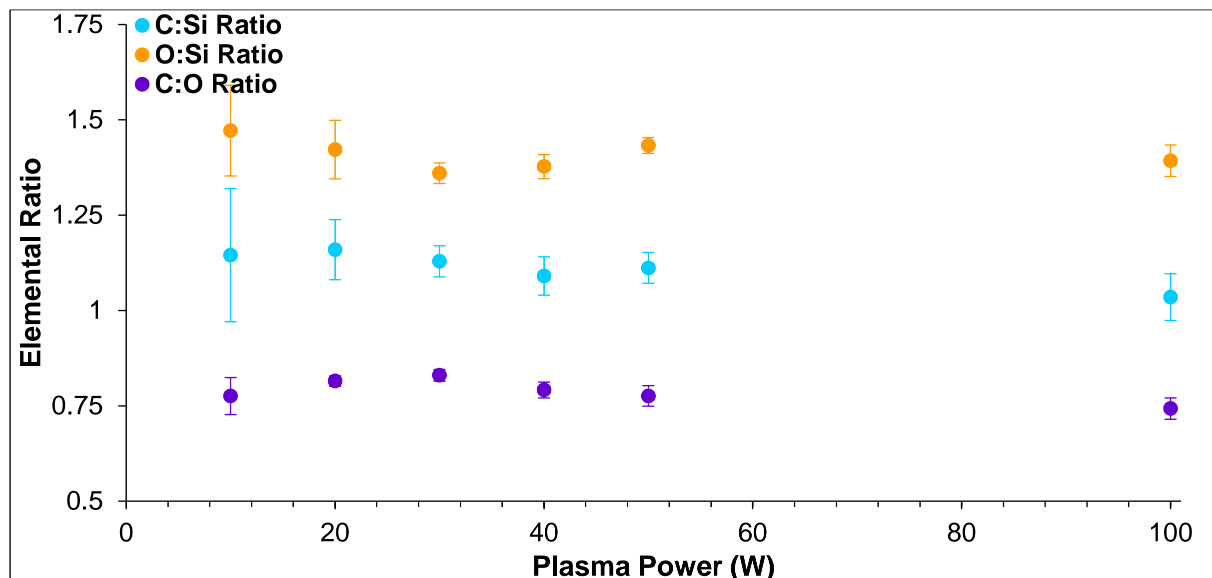

Figure 5.15: Elemental ratios of C:Si, O:Si and C:O for films deposited from PTMS plasma vs applied plasma power as determined by AES and argon ion depth profile.

There are several differences between the elemental compositions depicted in Figure 5.14 and previous XPS and AES results. Firstly, as adventitious carbon contamination has been

removed from the surface by the argon ion sputtering process, a lower concentration of carbon is observed here than for previous AES and XPS spectra. This consequently leads to an increase in the observed silicon and oxygen elemental concentrations. The removal of carbon also appears to have considerably reduced the variation in elemental concentration between films deposited at different plasma power which was seen in previous AES data, as well as reducing the overall uncertainty. Without this variation, the overall trend with increasing plasma power appears similar to that seen in XPS data in Section 5.2.1 namely, that despite the initial decrease in carbon content with sputtering there is no significant change in film composition with increasing plasma power. This reduced variation also applies to the elemental ratios, as depicted in Figure 5.15. As before, there is no significant trend for the elemental ratios with increasing power, although the ratios themselves have changed due to the removal of carbon from the surface. As would be expected, the values for C:Si and C:O are significantly affected. The mean of these values are approximately 1.1:1 and 0.8:1 respectively, compared to approximately 1.8:1 and 0.9:1 obtained from XPS data. Interestingly, the O:Si ratio is also decreased, from approximately 1.9:1 to 1.4:1, implying that oxygen was either present as a contaminant (possibly attached to carbon species), or present preferentially on the film surface. This 'surface' oxygen could also be a product of the plasma deposition process. It is possible that radical species present in the plasma environment are embedded in the plasma film. The 'dangling bonds' caused by the unpaired electrons in these immobilized radicals could react with oxygen present in the atmosphere upon exposure to air, resulting in an increased concentration of oxygen present on the surface. In all cases, the reduction in both carbon and oxygen compared to the original PTMS molecule is further evidence for its dissociation, even at the lowest applied plasma power of 10W. The reduction in carbon has a physical explanation - the bonds involving carbon are weaker than the silicon oxygen bond, so these are more likely to break within the plasma. It is not removed entirely however, but it is unknown whether or not carbon remains attached to the core of the PTMS molecule, or is co-deposited as a separate ionic species after decomposition in the plasma phase.

The reduction in oxygen, is more surprising, and has some implications for the structure of the film. For a film comprised entirely of silicon dioxide, a O:Si ratio of 2:1 would be expected, while in a completely cross-linked network of pure, hydrolysed PTMS, the value would be lower at 1.5:1. This does seem to imply that the deposited film is more similar to what would occur in the ideal hydrolysed case of a chemically deposited PTMS film than a silica-like film.

5.3.3.3 Determination of Film Thickness through Depth Profiling

In addition to providing elemental concentrations, argon ion depth profiling was used as a method for estimating film depth. The images presented in Figure 5.16 are example depth profiles of films deposited at three separate values for plasma power: 10W, 40W and 100W.

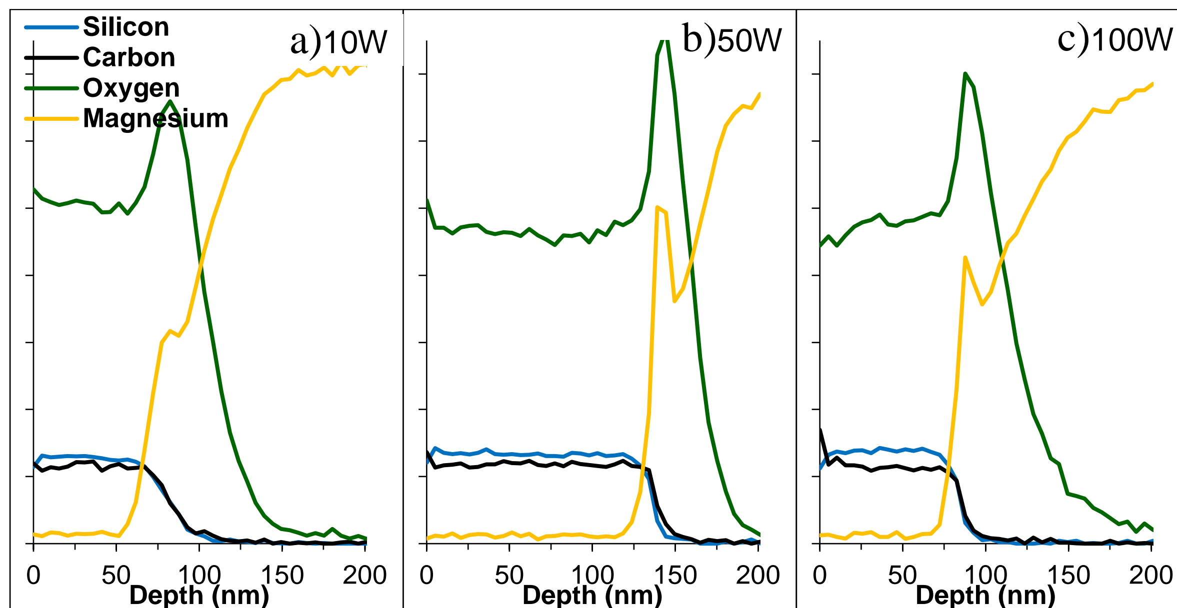

Figure 5.16 Depth profiles from multiple magnesium surfaces coated with PTMS plasma with an applied power of a) 10W, b) 50W and c) 100W

The important features of these profiles are that any carbon contamination present (as shown in the previous section) is immediately removed from the surface upon argon ion sputtering, implying that it is a very thin surface coating, likely adventitious carbon from atmospheric exposure. Once the outer carbon layer is removed the composition of the film stabilises with constant presence and thus ratios of silicon, carbon and oxygen. A decrease in both carbon and silicon concentrations corresponds to the emergence of signal associated with the magnesium substrate, along with an increase in oxygen, belonging to magnesium oxide present on the magnesium surface under the coating. With the removal of the oxide, no other elemental presence is detected. To maintain a non-ambiguous approach in determining the point at which the film is completely removed, the individual spectra making up the depth profile were examined. The sputter depth at which silicon signal was not resolvable above noise was then selected as the film depth. Two separate profiles containing multiple analysis regions were performed on each sample with the collated results plotted in Figure 5.17.

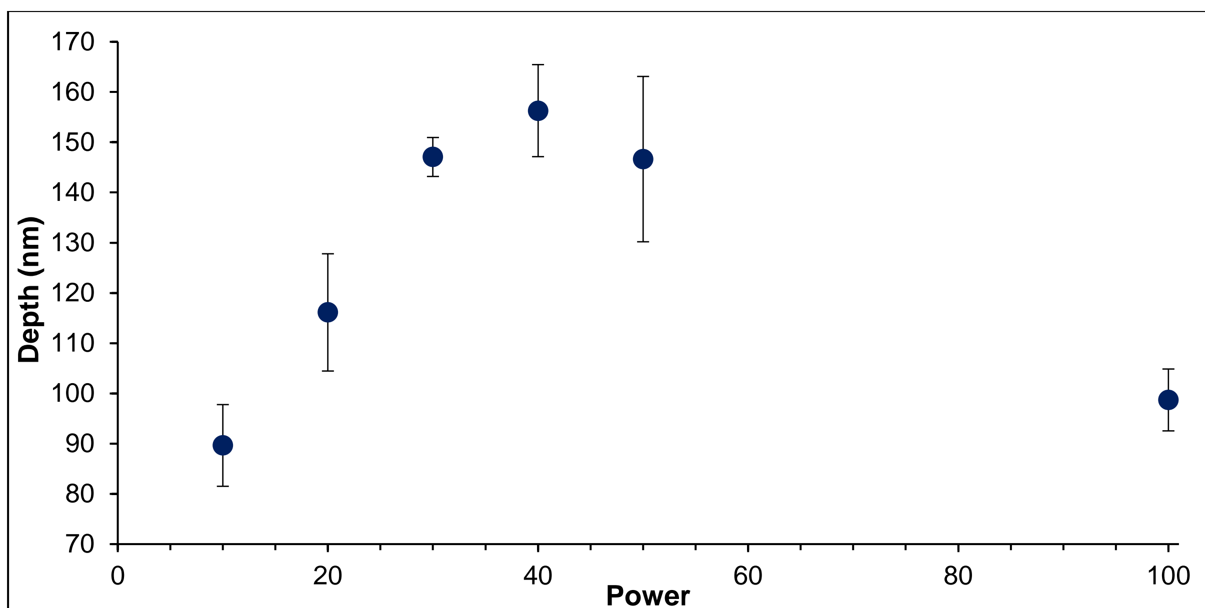

Figure 5.17 Average values for PTMS film depth with increasing applied plasma power.

The presented results show that from a depth of approximately 90nm deposited from a 10W PTMS plasma, the thickness of the film increases steadily to approximately 155nm deposited at 40W. As the power increases to 50W however, there is a slight decrease in measured film depth, a downward trend which continues with increasing power, with the films deposited at 100W only just above those deposited at 10W. This is somewhat contrary to the behaviour seen in Figure 4.29, in Section 4.4.2, where increased power corresponded with a thicker film. Therefore, to explain the behaviour seen in the plot above, plasma deposition must be considered as a function of both film deposition and etching. For plasma powers up to 40W the film deposition rate increases faster than the rate of etching, leading to an overall net rate of growth that results in an increase in film thickness. As the power increases past this point the rate of etching increases proportionately, reducing the overall deposition rate. In other words, material is still clearly being deposited, though the *net rate* at which it occurs decreases as the plasma power increases. The same range of applied plasma powers were used for film depositions presented in Chapter 4, and no such decrease in the rate of film growth was observed.

There are two significant changes in the experimental details between the two cases: the increased duration of the plasma, and the reduced roughness of the substrate. Either of these could have caused the discrepancy in film deposition behaviours, however the simplest explanation is the fact that the plasma deposition was carried out for an hour in as opposed to the considerably shorter 60 second deposition previously used. The rate of film deposition is likely affected by the surface energy of the surface presented to the plasma. If the oxygen plasma pre-treated magnesium surface is higher in surface energy, then when

exposed to the PTMS plasma, a film would form more rapidly. Increased plasma power thus providing additional energy to the deposition process for short time scales until the surface is completely coated. As the metallic areas of the sample are coated, the rate of continued deposition decreases, and increasing plasma power contributes relatively more to the etching process than to aiding in deposition. That is not to say that increased etching does not also occur at short time scales with increased power – evidence for the etching of the PTMS film during deposition was observed previously, with a magnesium presence detectable in elemental maps that are shown in Figures 4.26 and 4.27 that do not correspond to physical surface features.

5.4 **ATR-FTIR**

Fourier Transform Infra-Red Spectroscopy (FTIR) was used in conjunction with electron spectroscopy to further study the films deposited from PTMS plasma. FTIR directly probes chemical bonds present within the film, providing complimentary information to that obtained about the elemental composition by electron spectroscopy alone. The form of FTIR performed here attenuated total reflection (ATR) and is described in more detail in Section 2.2.2. The basic concept involves placing the surface to be analysed into contact with a high refractive index crystal which allows an interaction to take place between an evanescent wave that is generated upon the internal reflection of infrared radiation within the crystal and the sample itself. FTIR spectroscopy was attempted previously, however little to no signal was detected. This was primarily due to the roughness of the magnesium substrate - the area of contact between the film and the crystal was too low for a detectable level of signal to be obtained. In many cases, this is remedied by applying pressure to the sample on the crystal, leading to increased surface contact (depending on the compressibility of the material in question). As magnesium is a hard, stiff material, the applied pressure necessary to get this amount of contact would crack the crystal. Therefore, by decreasing the surface roughness through polishing the magnesium substrate, a greater area of the film surface can contact the ATR crystal, and thus a detectable amount of signal.

5.4.1 Comparison between PTMS precursor, and plasma deposition.

The first experiment performed with FTIR here is a comparison between the liquid PTMS precursor and the plasma deposited film. Example spectra for each are shown in Figures 5.18 a) and b), with important peaks labelled according to their location energies (in wavenumbers, cm^{-1}). The location of all observed peaks are presented in Table 5.1

There are several differences between the presented spectra for the pure PTMS and the plasma deposited sample. One such difference is the presence of a series of small

vibrations visible at approximately 2100cm^{-1} which are associated with the ATR crystal itself. Another difference is the broad feature seen between 3700cm^{-1} and 3400cm^{-1} in the plasma deposited film, but not the liquid PTMS. This peak is caused by the presence of water either in the deposited film, or adsorbed to the surface.

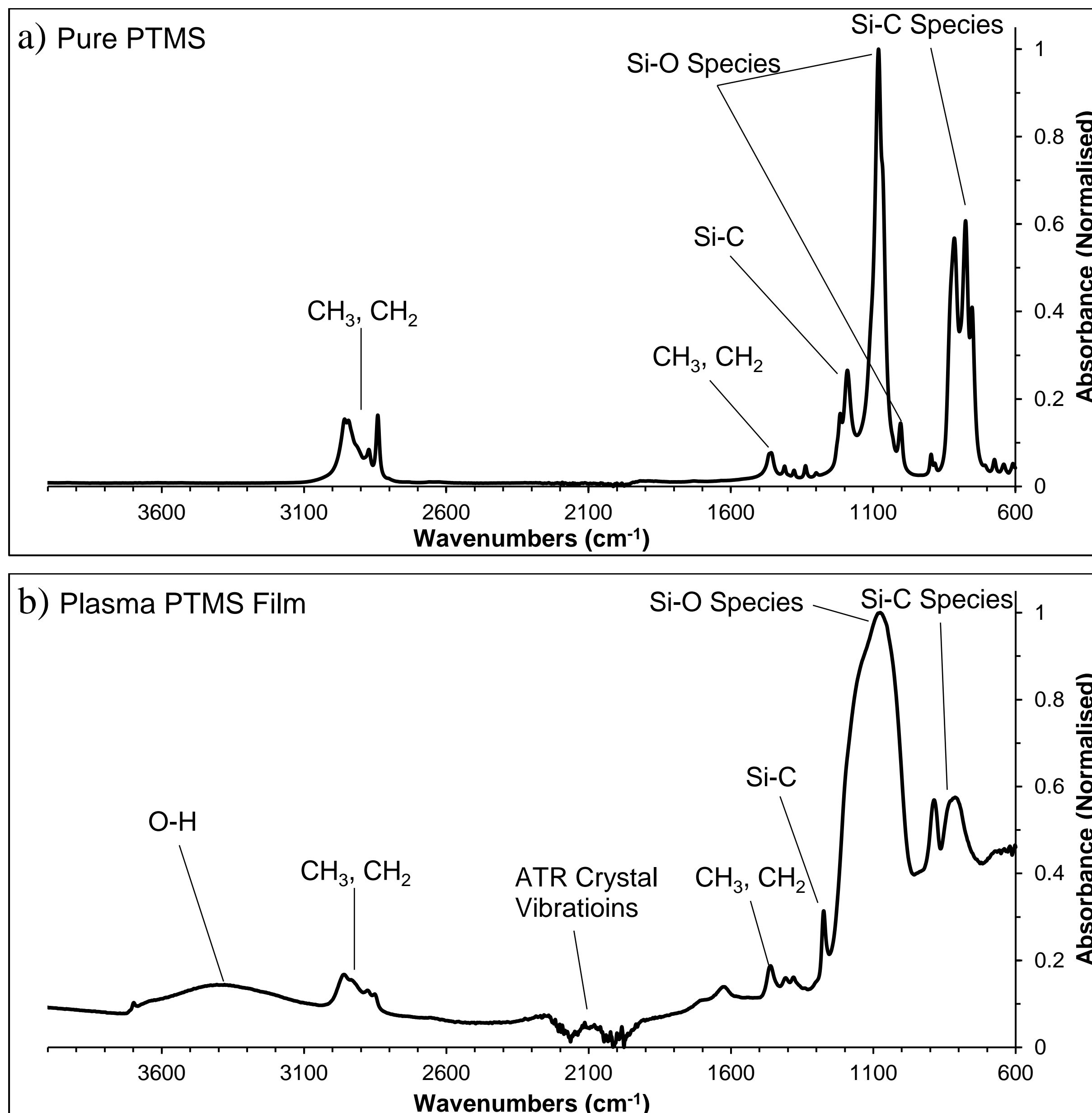

Figure 5.18: FTIR spectrum between 4000cm^{-1} and 600cm^{-1} of a) Pure liquid PTMS and b) A film deposited from PTMS plasma

The first major difference between the PTMS films themselves however, is the primary peak seen on all samples here, between the energies of 1200cm^{-1} and 1000cm^{-1}. This series of sharp absorbance peaks in the liquid PTMS, and broad feature on the plasma deposited film is associated with a range of silicon to oxygen bonds, including Si-O-Si bonds [82, 151, 184-

186]. As individual silicon/oxygen species condense into a cross-linked network, the Si-O-Si peak becomes visible. This is a much broader peak than that of the methoxy- groups, or other Si-O vibrations, and thus dominates that area of the spectrum as a single broad peak [151, 184, 187]. The existence of this peak is a key finding, as direct evidence of crosslinking between PTMS molecules during the plasma deposition.

Other differences between the spectra include the reduction of the vibrations associated with hydrogenated carbon species that is present in a band from 2960cm^{-1} to 2850cm^{-1}. From XPS and AES results, it is know that the carbon content of the film is reduced compared to that of the original PTMS molecule, the reduction in peaks associated with carbon-carbon bonding is expected. This is also supported by the reduction in intensity of similarly attributed peaks near 800cm^{-1}.

An unexpected finding in the spectra for plasma deposited films, is the presence of two peaks at 1705cm^{-1} and 1625 cm^{-1}, potentially associated with C=O and C=C bonds, neither of which are present in the pure PTMS spectra, but appear to be formed in the plasma environment. The presence of these peaks, in addition to the reduction in the previously mentioned adsorption peak related to hydrogenated carbon (between 2960cm^{-1} to 2850cm^{-1}) implies that hydrogen is being removed as a cross linked film is formed from fragmented PTMS molecules, and pumped out of the plasma reaction chamber. As was discussed in chapter 2, hydrogen cannot be detected with XPS or AES, so this is the first evidence of its role in film formation in this research. Within literature, the removal of hydrogen has been linked to increased density in plasma deposited films [188-190], so the role hydrogen plays in the deposition is something that should be investigated further when considering the final properties of a film for applications.

The peak that appears at approximately 1270cm^{-1} on the plasma deposited film sample IR spectrum has been assigned to the Si-CH_3 Bond, which is likely formed as the propyl chain of the PTMS molecule is dissociated, but is not present in the precursor molecule.

Table 5.1 FTIR peak assignments

Wavenumber (cm^{-1})	**Bond Assignment**	**Reference**
3700-3000	O-H	[184-186]
2980-2800	CH_3, CH_2	[35, 151, 184, 186]
2300-1900	Crystal Vibrations	
1735-1685	C=O (Carboxyl or aldehyde)	[35, 184]
1660-1590	C=C	[191]

1480-1370	Multiple Peaks associated with CH_3 and CH_2	[184, 191]
1360	(Si)-CH2-(Si) – Broad shoulder	[35]
1280-1260	Si-CH_3	[35, 151, 186, 191, 192]
1250-1170	Si-CH_2, Si-OCH_3	[191]
1200-1000	Si-O, Si-O-Si, Si-O-C	[82, 151, 184-186]
1020-1000	Si-CH_2	[151]
910-865	Hydrogen Bonded Si-OH	[82]
850-750	Multiple Peaks: Si-$(CH_3)_3$, Si-C, Si-OH, Si-$(CH_3)_2$, CH_3, Si-O-Si	[35, 151, 186, 191]
685-665	Si-C-R	[191]
650-600	Si-$(CH_3)_3$	[191]

5.4.2 Effect of Applied Plasma power on FTIR

Knowing the bonding that occurs within films deposited from a PTMS plasma, it is then possible to compare any variations that occur as the applied plasma power is changed. Plotted in Figure 5.19 are the overlayed FTIR spectra of samples coated at a range of applied plasma powers.

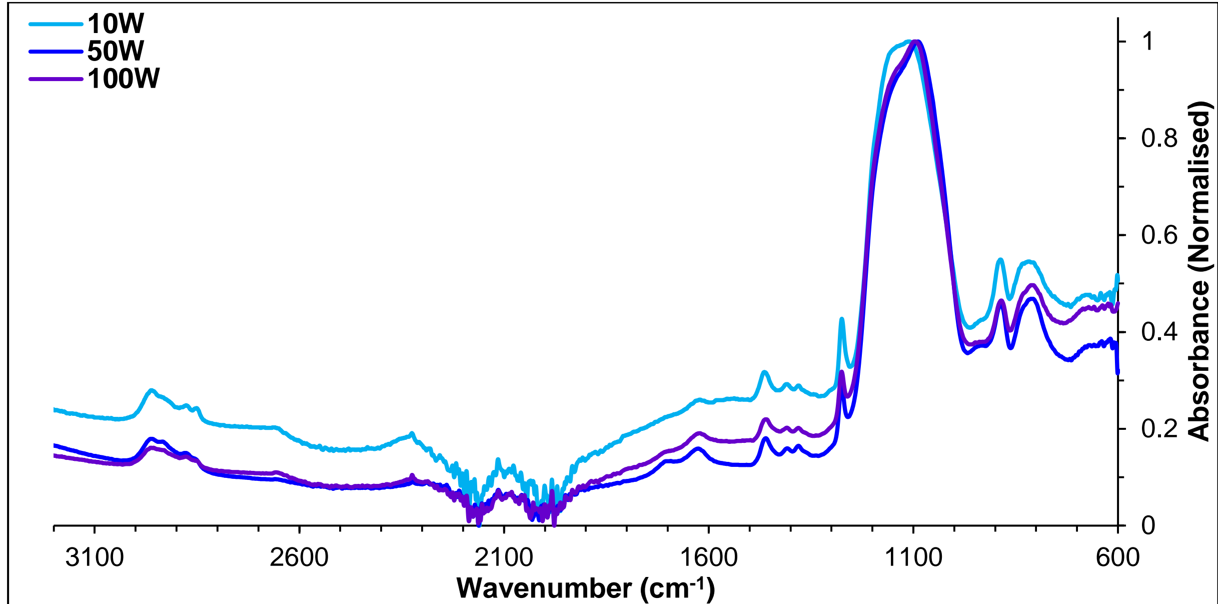

Figure 5.19: Overlayed FTIR spectra obtained for films deposited onto magnesium surfaces from PTMS plasma at applied powers of 10W, 50W and 100W.

As might be expected, given the lack of any significant change in the elemental ratios observed for XPS and AES data, there is likewise very little variation in the bonds present in the FTIR data as the plasma power is increased. There are a number of subtle changes

between these spectra however as the film depth varies with plasma power, such variations in absorbance (especially in regard to the intensity of individual peaks) are not likely a direct product of changes in plasma power. This reinforces the hypothesis that the energy present in the 10W plasma is enough to cause the majority of the dissociation undergone by the PTMS molecule within the plasma environment.

5.5 **Summary**

Small diameter diamond paste was used to produce a magnesium oxide surface of much lower roughness than that surfaces examined previously. Onto these smooth surfaces, silicon containing films were deposited, using pure PTMS vapour. The power of these treatments was varied, with their durations controlled to one hour, in order to study the effect of plasma power on the structure and thickness of the deposited film. The reduced roughness of the diamond polished magnesium surfaces allowed FTIR analysis to be undertaken. These measurements found evidence of carbon chain removal, as well as the presence of double bond formation, potentially increasing with plasma power. Of significant importance is the presence of a peak associated with cross-linked siloxane films, giving direct evidence of polymerisation taking place.

The removal of carbon species was supported by both XPS and AES results, which showed a significant decrease in carbon concentration to what would be expected from the pure PTMS molecule. The combination of argon ion sputtering with scanning Auger microscopy, allowed the accurate measurement of film elemental composition, without the presence of adventitious carbon contamination. The film composition was found to be approximately 32% carbon, 40% oxygen and 28% silicon, compared to 60%, 30% and 10% for pure PTMS a significant increase in silicon, primarily at the expense of carbon. This composition was found to be relatively invariable with increasing plasma power. Sputtering was also used to produce depth profiles for each plasma power. As opposed to the relationship found previously, where increasing plasma power led to increased coverage, film depth increased with power up to 40W, after which it decreased. The cause of this is thought to be a factor of two competing processes within the plasma environment: the deposition reactions that are occurring, and the etching of the surface by high energy plasma species.

Finally, high resolution XPS was used to investigate the chemical state of the silicon atoms within the deposited films. In pure PTMS, all silicon atoms are bonded to three oxygen atoms, whereas it was found that for films deposited at even the lowest investigated plasma power of 10W, a significant proportion of silicon (approximately 40%) was found to be attached to four oxygen atoms, implying the complete removal of the propyl chain. When

power was increased to 100W, this was found to be more pronounced with approximately 85% of silicon atoms in this more oxidised state.

6 Chapter 6: Modification of PTMS Plasma Films Through the Addition of Functional Gases

It has thus far been demonstrated that it is possible to deposit silicon containing films onto magnesium surfaces through the plasma decomposition of the molecule PTMS. Through manipulation of parameters such as exposure time and applied plasma power, film depth and bonding state of the silicon within the film was controllable.

The overall elemental composition of the films however, remained relatively constant with changes in both of the investigated plasma parameters. Previous studies into organosilane surfaces have chosen precursor molecules with particular chemistry as a method of influencing the elemental composition and thus properties of the deposited film.

PTMS was originally chosen for use as a precursor in this work as a model for other, functional organosilanes such as APS. One of the results obtained in previous chapters is that the elemental composition of the film resulting from the plasma deposition of PTMS is drastically different to that of the original chemical, with a reduction in both carbon and oxygen concentration. It has been shown in literature that increasing the carbon content of an organosilane film has beneficial impact on barrier properties [35, 147]. Indeed, the choice of HMDSO as a monomer in many of these studies was for just this reason. Conversely, other studies have used mixtures of organosilanes and oxygen to create silica-like films with an increased inorganic character for applications in the optics, electronics and telecommunications industries [193].

As previously indicated, one of the primary reasons for choosing PTMS to produce organosilane films is the similarity to APS, amino functionalised organosilane with several applications including as an adhesion promoter [115, 194, 195] and in sensors [196, 197]. Plasma deposition of APS has been achieved previously [184, 194-197] with similar plasma deposition systems. It is known that differences in geometry between plasma chambers can lead to significant differences between the plasma specie which are generated [157, 158, 198]. As it has been shown that PTMS is at least partially dissociated within the plasma chamber used here, even at low power it is unknown whether it is possible to deposit films of APS with the current experimental setup. Therefore, a different approach will be attempted.

In this chapter, all three of these different functionalities are investigated through the addition of appropriate gases to the plasma environment. Methane, as the simplest hydrocarbon, is chosen in an attempt to increase film carbon content. Both water vapour and oxygen are used to increase oxygen present within the plasma environment in order to produce a more

silica-like film. Finally nitrogen gas is combined with PTMS vapour in an attempt to provide amine functionality to deposited films.

With regard to the plasma parameters chosen for the following experiments; it is known that for films deposited at 100W there is a distinct increase in the amount of silicon atoms in the $Si(-O)_4$ environment compared to those deposited at lower powers. Therefore, films deposited at two separate plasma powers will be compared: 20W and 100W, where the former will be used as a representative for other low plasma powers (with more silicon present in the $Si(-O)_3$ environment). Again, a one hour plasma duration was selected due to it being established previously that under these conditions, a complete film is able to develop on the order of 100nm. One aspect of the plasma that was not able to remain consistent however, is the pressure. By adding other gases to the plasma then either the total pressure must increase or the partial pressure of PTMS must decrease, depending on what is to remain constant. For this investigation, it was decided that the partial pressure of PTMS would remain consistent with previous studies. Therefore, the total pressure in the plasma chamber for a 50:50 mixture of PTMS and another gas would be $2x10^{-3}$Torr. To ensure that any effects observed are not simply due to an increase in PTMS pressure, control experiments were conducted.

It was established in Section 5.3.3.2 that in order to obtain an accurate value for film composition, without the inclusion of surface contaminants, argon ion depth profiling in combination with Auger electron spectromicroscopy may be utilised. Table 6.1, contains such results for films deposited at 20W and 100W at a pressure of $1x10^{-3}$Torr, reproduced from Chapter 5, as well as films deposited for the same powers, but at twice the pressure: $2x10^{-3}$Torr. These results show that is no significant change in film composition with an increase in plasma pressure, meaning that the relative densities of species within the plasma does not change as the pressure increases.

Table 6.1: Comparison of elemental compositions of PTMS films deposited at two separate powers and pressures, obtained through AES depth profiling

Plasma Treatment	%O	%C	%Si	C:Si	O:Si	C:O
PTMS $1x10^{-3}$Torr 20W	39.7±0.4	32.3±0.8	27.9±1.2	1.2±0.08	1.4±0.08	0.8±0.05
PTMS $1x10^{-3}$Torr 100W	40.6±0.4	30.2±0.9	29.2±0.8	1.0±0.06	1.4±0.04	0.7±0.03
PTMS $2x10^{-3}$Torr 20W	40.8±3.2	31.6±2.5	27.6±0.7	1.1±0.06	1.5±0.15	0.8±0.13
PTMS $2x10^{-3}$Torr 100W	41.5±1.2	28.8±0.9	29.7±1.4	1.0±0.06	1.4±0.10	0.7±0.03

A comparison of film depth obtained through AES depth profiling is presented in Table 6.2.

The increase in PTMS pressure does appear to have had a slight impact on the thickness of the deposited film, however the variation seen between the two sets of data is still within one standard deviation. This is somewhat more surprising than the lack of change in composition, as supplying more material to the plasma (in the form of increased pressure) should increase the rate at which the film is deposited (as per most common kinetic models for adsorption of gases to surfaces. A plasma is not a regular gas however, and possess energetic species which are able to etch material from the surface, so increasing the pressure of plasma also increases the amount of etching that occurs, along with deposition, so the overall rate of film growth remains approximately constant.

Table 6.2 Film thickness obtained from depth profiling

Plasma Treatment	Film Depth (nm)
PTMS $1x10^{-3}$Torr 20W	136.1±11.7nm
PTMS $1x10^{-3}$Torr 100W	98.7±6.2nm
PTMS $2x10^{-3}$Torr 20W	129.7±5.4nm
PTMS $2x10^{-3}$Torr 100W	112.7±11.9nm

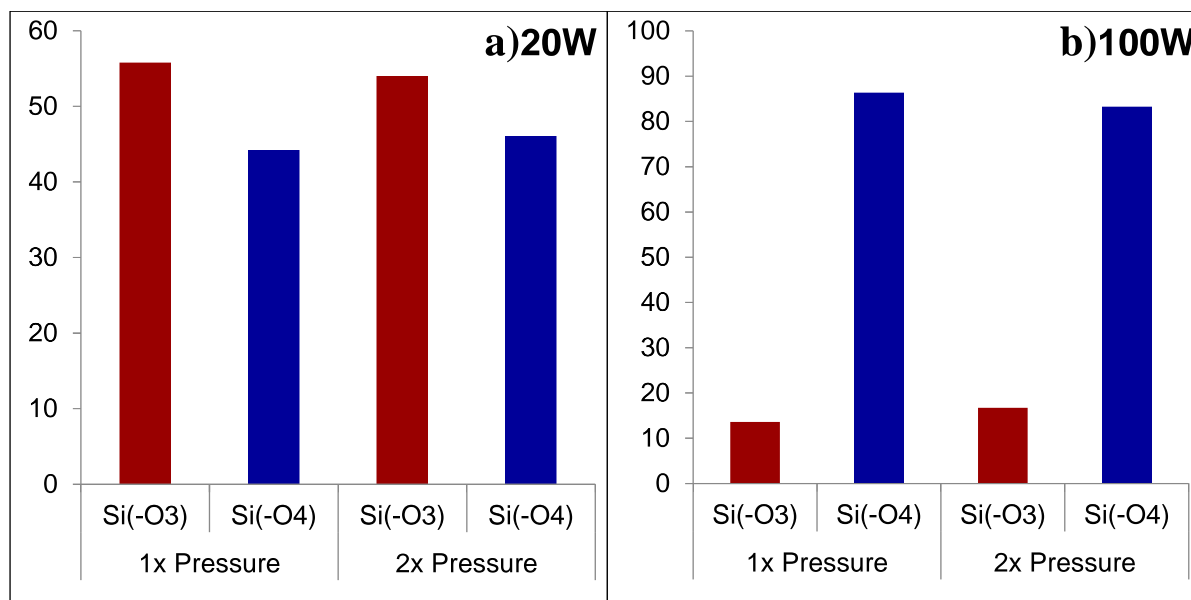

Figure 6.1 Comparison between silicon bonding environment present in PTMS films deposited at two separate pressures: $1x10^{-3}$Torr and $2x10^{-3}$Torr at a) 20W, and b) 100W

XPS is used to examine the bonding environments present within the film. It previously found that a lack of change in composition does not necessarily mean that the bonding environment is also static. As demonstrated by the XPS results in Figure 6.1 a) and b), there does not appear to be a significant change in the Si2*p* peak shape with an increase in PTMS pressure within the plasma. This establishes a baseline for films deposited at a higher

plasma pressure, thereby allowing it to be understood that any differences observed to the composition or depth of films deposited from mixtures of materials are caused by the addition of difference species to the plasma environment.

6.1 Modifying Elemental Composition of Plasma Deposited PTMS Films

6.1.1 Carbon content of PTMS films

The elemental composition of the films resulting from the deposition of a PTMS/methane mixture were characterised through AES depth profiling. Table 6.3 gives both elemental compositions and ratios obtained in this way, along with film depth. By comparing the films deposited from a mixture of methane and PTMS to those of PTMS alone it can be seen that for films deposited at 100W there is no significant difference in elemental composition with the addition of methane to the plasma environment. At a power of 20W however, there is a significant increase in carbon within the film and a consequent decrease of both oxygen and silicon. While the carbon to silicon ratio is increased to 1.6:1, this remains far lower than the original PTMS molecule.

Table 6.3 Composition of films deposited from a mixture of PTMS and Methane as determined by AES depth profiling.

Plasma Treatment	%O	%C	%Si	C:Si	O:Si	C:O	Film Depth (nm)
PTMS 20W	40.8±3.2	31.6±2.5	27.6±0.7	1.1±0.06	1.5±0.15	0.8±0.13	129.7±5.4
PTMS 100W	41.5±1.2	28.8±0.9	29.7±1.4	1.0±0.06	1.4±0.10	0.7±0.03	112.7±11.9
PTMS+CH_4 20W	37.9±0.6	37.7±1.0	24.4±0.5	1.6±0.07	1.6±0.03	1.0±0.04	120.6±3.0
PTMS+CH_4 100W	42.5±0.4	28.2±0.8	29.3±1.2	1.0±0.07	1.5±0.08	0.7±0.01	112.1±3.2

That adding a considerable quantity of carbonaceous material to the plasma does not lead to a corresponding increase in carbon within the film for a plasma power of 100W, but does for 20W is somewhat surprising. When considered in detail however, it supplies further evidence for previous suppositions about the film deposition mechanisms. In particular, the energy available within the plasma is in excess of what is necessary to break the bonds present in the PTMS molecule, and of importance here: those that involve carbon. The silicon and oxygen bonds present are of comparatively higher energy, thus are more resistant to attack by higher energy species within the plasma, resulting in an enhancement

of these materials within the deposited film. An increase in carbon within the plasma mixture may lead to more carbon containing bonds being formed, but due to their relatively lower energy they are also more likely to be broken during the deposition process, resulting in a similar film to that of the one deposited from pure PTMS. Therefore, at the lower plasma power of 20W, the reduced energy compared to 100W means that an increased proportion of bonds containing carbon are able to remain intact. In addition to determining the composition of deposited films, argon ion sputtering was also used to provide a measure of film depth. As with composition, the films deposited at a plasma power of 100W had the same depth as the control PTMS samples. The films deposited at 20W however, were found to be slightly shallower lying just outside the range of a single standard deviation of each other. A decrease in film depth could have several different causes. Firstly, the growth rate of the film could be affected by the presence of methane in the plasma either through a decrease in deposition, or an enhancement of etching. As the films deposited at 100W are similar in depth to the control case, it is therefore unlikely that the cause is solely the presence of methane within the plasma contributing to etching, as this effect would be enhanced at increased power, as found in Chapter 5, Section 5.3.3. A possibility that has yet to be considered is that the increase in carbon content makes the film more compact, or dense, however without more direct evidence this is pure speculation.

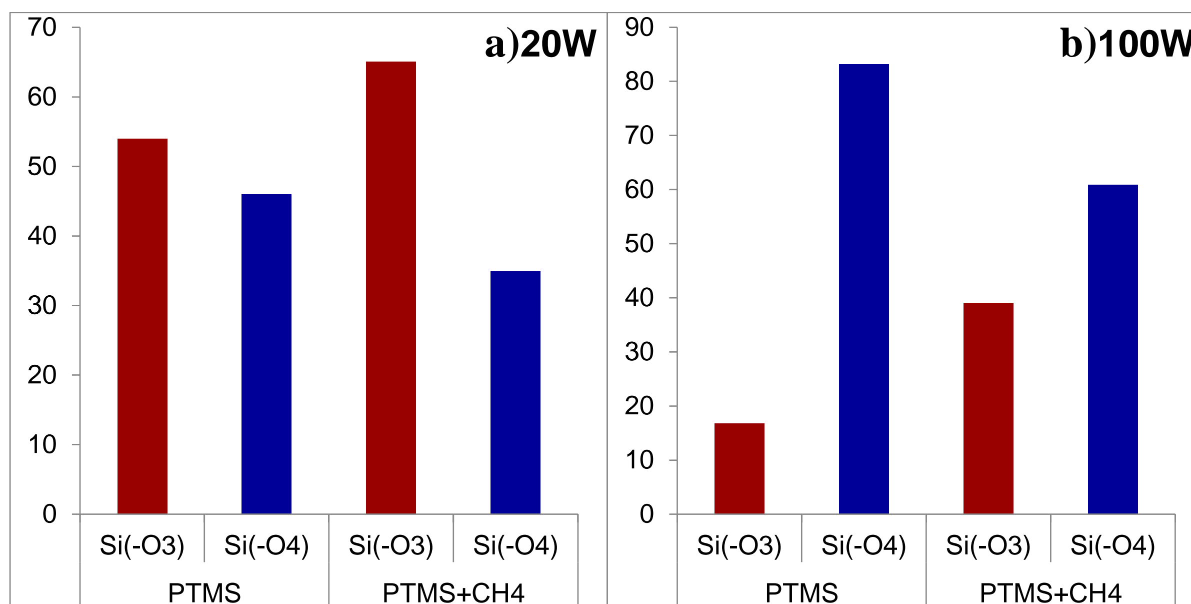

Figure 6.2: Comparison between silicon bonding environment present in films deposited from pure PTMS and a mixture of PTMS and CH_4 at a) 20W, and b) 100W

As in the previous section, the use of high resolution XPS allows information about the bonding state of silicon to be obtained. Figure 6.2 a) and b), compares the percentage concentrations of the silicon 2*p* photoelectron peak in either the $Si(-O)_3$ or $Si(-O)_4$ bonding

environment for films deposited from pure PTMS vapour and a mixture of PTMS and methane. Previously, it has been found that a lack of change in elemental composition does not necessarily mean that the bonding environment of silicon is equally static. Conversely it follows that an increase in carbon concentration within the film (as found for the films deposited from a mixture of PTMS and methane at 20W) will not necessitate an increase in the amount of silicon in the $Si(-O)_3$ environment. However, as can be observed in Figure 6.2 a) this does appear to be what has occurred. In addition, the “mixed” films deposited at 100W (which did not show a change in composition compared to pure PTMS) also show an increase in $Si(-O)_3$, albeit still lower than the 20W films. It was postulated in Section 5.2.2 that the increase in power leads to the decomposition of the comparatively weaker Si-C bond present within the PTMS molecule. It appears that while this remains the case, by adding methane to the plasma mixture the probability of a new silicon-carbon bond being formed is increased, leading to the observed changes in the Si2*p* peak.

6.1.2 Oxygen Content of PTMS Films

Two different gases were combined with PTMS in order to produce films that were more inorganic in nature: oxygen and water vapour. In Table 6.4, the elemental concentrations and ratios of films produced from each of these mixtures at two separate plasma powers are shown. The addition of oxygen to the plasma mixture through either pure O_2, or water vapour (H_2O) led to significant changes in observed film compositions compared to those deposited from PTMS alone. Most notable of these changes was the dramatic decrease in carbon within the film. The cause of this decrease is most likely the presence of additional oxygen species within the plasma that react with the carbon of PTMS, either in the plasma phase or with material present on the surface of the film as it is being deposited. These carbon/oxygen species are then pumped away rather than incorporated into the film. Of the two oxygen containing gases, films deposited from the mixture of PTMS and O_2 show less carbon than those of PTMS and H_2O by a significant margin. The simplest explanation for this is that more oxygen atoms are present in O_2 than H_2O and hence, once ionized in the plasma, are able to react with more carbon. Something that is more difficult to explain, is that increasing the plasma power leads to more carbon in the resultant films, which is counter to what was expected, and what is found for films deposited from a plasma of pure PTMS and indeed, a mixture of PTMS and methane. The presence of oxygen within the plasma must somehow change the rate at which carbon is deposited from the surface, however the mechanisms that would accomplish this are unknown and require further investigation.

Table 6.4 Composition of films deposited from a mixture of PTMS and either oxygen or water vapour as determined by AES depth profiling

Plasma Treatment	%O	%C	%Si	C:Si	O:Si	C:O	Film Depth (nm)
PTMS 20W	40.8±3.2	31.6±2.5	27.6±0.7	1.1±0.06	1.5±0.15	0.8±0.13	129.7±5.4
PTMS 100W	41.5±1.2	28.8±0.9	29.7±1.4	1.0±0.06	1.4±0.10	0.7±0.03	112.7±11.9
PTMS+O_2 20W	58.8±0.9	4.4±1.1	36.8±0.3	0.1±0.03	1.6±0.02	0.1±0.02	138.9±5.2
PTMS+O_2 100W	53.2±0.6	11.5±0.9	35.4±1.3	0.3±0.04	1.5±0.07	0.2±0.02	99.8±2.1
PTMS+H_2O 20W	51.5±0.8	15.3±1.5	33.2±0.9	0.5±0.06	1.6±0.03	0.3±0.03	62.7±1.1
PTMS+H_2O 100W	45.8±1.9	22.6±2.2	31.6±0.5	0.7±0.08	1.5±0.05	0.5±0.07	91.9±2.7

An additional surprising result is encountered when examining the thickness of the deposited films. The films deposited from a mixture of O_2 and PTMS were found to have a slightly different depth, but still within a single standard deviation of the control PTMS films. The PTMS/H_2O films however, were significantly different to what has been previously observed – films at both 20W and 100W are shallower than what has been seen previously and in addition, the films deposited at a lower power were thinner than those deposited at a higher power. It is possible that introducing hydrogen ions (from H_2O) leads to the reduction of oxygen already present in the PTMS molecule. Hydrogen plasma is used industrially to remove oxides from metal surfaces [199], so the presence of both oxygen and hydrogen in the plasma could explain the reduction in film depth, with hydrogen reducing oxygen and oxygen removing the carbon. However, as the oxygen to silicon ratio does not change significantly with either power or plasma composition so either silicon is also removed, or there is a different cause for the disparity in observed film depth. An alternative explanation is that the presence of hydrogen “caps off” active bond sites, thus reducing the chance of silicon containing species from binding to the surface and growing the film. At higher power, this effect could be lessened through the removal of terminal hydrogen atoms by higher energy species within the plasma, though without a means of measuring the hydrogen content of the film (with a technique such as Time of Flight Secondary Ion Mass Spectrometry), this is only speculation.

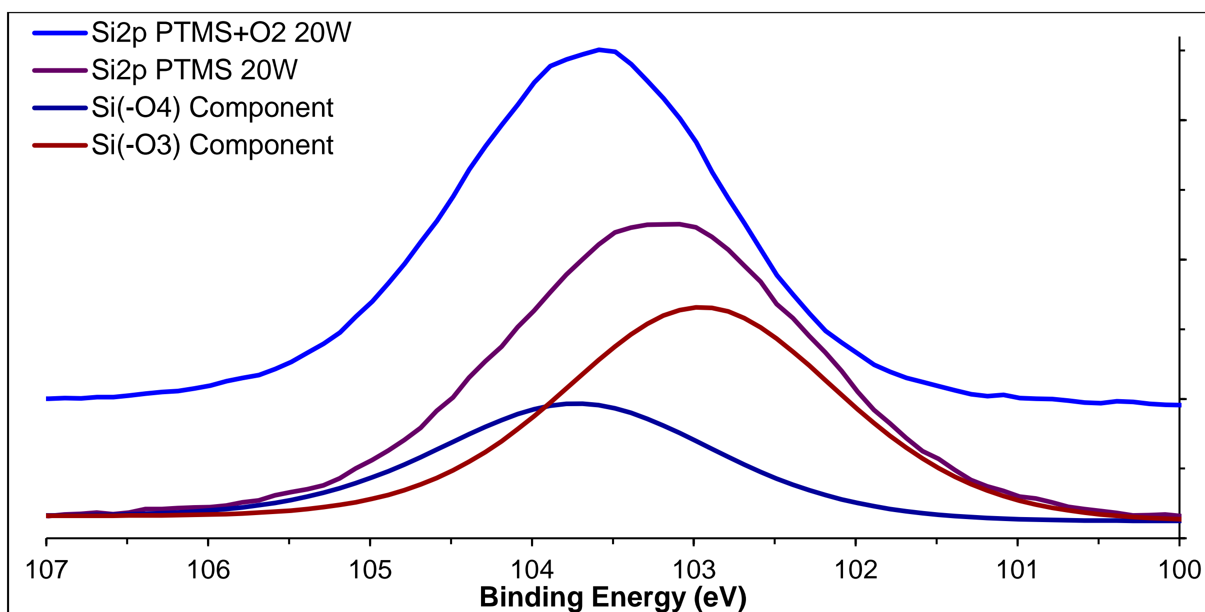

Figure 6.3 Comparison of Si2*p* photoelectron peak deposited at 20W from pure PTMS vapour and a mixture of PTMS and oxygen

With regard to the silicon to oxygen ratio, the O:Si value of 2:1 is what would be expected of a film of pure silicon dioxide, but as can be seen in Table 6.4, the ratio obtained for even the 20W O_2+PTMS film (with a near zero carbon concentration) is lower than this at approximately 1.6:1. Evidence of silicon dioxide can be found however, through examination of high resolution XPS results. As can be seen in Figure 6.3, an example Si2*p* photoelectron peak from a 20W PTMS+O_2 plasma film is shifted to a higher binding energy by approximately half an electron volt (to 103.6) compared to the film deposited at the same power from pure PTMS vapour. This discrepancy in peak location can be explained through the fitting of these peaks with individual Voight functions (as per the method described in Section 5.2.2). For the example peaks displayed in Figure 6.3, the functions fitted to the peak associated with the pure PTMS film are shown underneath the primary peak. The peak fitted for the Si(-O)$_4$ state is present at approximately 103.4 eV, near to that of the Si2*p* peak deposited from the mixture of PTMS and O_2. Both are within the range prescribed for Si(-O)$_4$ by O'Hare et al. [183]. In the case of the 'pure' PTMS film, a second peak component can be fitted at a lower binding energy (corresponding to silicon in the Si(-O)$_3$ environment) however, a second such component cannot be fitted successfully to the mixed PTMS+O_2 film, implying that the Si2*p* peak in those cases consists entirely of the Si(-O)$_4$ state. This implies that the film deposited is primarily silicon dioxide, a result that is duplicated for all other films deposited from a mixture of either oxygen or water vapour. This is surprising for the films deposited from PTMS and H_2O, as they contain a significant amount of carbon.

This implies that carbon within these films is either present independently, or present as a defect attached to oxygen within the film structure.

6.2 Nitrogen Functionalised PTMS Plasma Films

APS is a molecule identical in composition to PTMS, with the exception that the propyl chain is functionalised with a terminal amine group. This amine functionalisation gives films formed of APS applications as a coupling agent [95, 106, 115, 200]. Amine containing organosilanes have previously deposited through plasma polymerization [184], however they require the use of a 'bubbler' setup due to the lower vapour pressure of APS compared to PTMS and the consequent difficulty this adds to introducing it to a vacuum plasma chamber. As the cost of APS is also significantly greater than that of PTMS, a more cost effective way of producing amino-functionalised organosilane films is investigated here through the addition of nitrogen (N_2) into the PTMS vapour mixture.

Table 6.5 Composition of films deposited from a mixture of PTMS and nitrogen as determined by XPS.

Plasma Treatment	%O	%C	%Si	%N	C:Si	O:Si	C:O
PTMS 20W	40.0±1.1	39.0±1.2	21.0±0.8	--	1.9±0.03	1.9±0.11	1.0±0.01
PTMS 100W	40.2±2.2	38.5±3.9	21.3±1.5	--	1.8±0.08	1.9±0.05	1.0±0.03
PTMS+N_2 20W	40.1±1.4	39.3±3.5	19.8±2.0	0.8±0.5	2.0±0.04	2.0±0.05	1.0±0.08
PTMS+N_2 100W	40.6±2.8	38.1±2.3	19.8±2.5	1.5±0.4	1.9±0.06	2.1±0.04	0.9±0.11

The initial XPS results shown in Table 6.5 are promising, with nitrogen readily detectable on the surface, albeit with a low concentration. The film resulting from the 100W plasma treatment shows an increase in nitrogen content within the film. The nitrogen-nitrogen triple bond is one of the strongest known covalent bonds, so the addition of additional energy to the plasma system causes a larger proportion of the nitrogen molecules to separate into individual ionised species that are able to be incorporated chemically into the PTMS film.

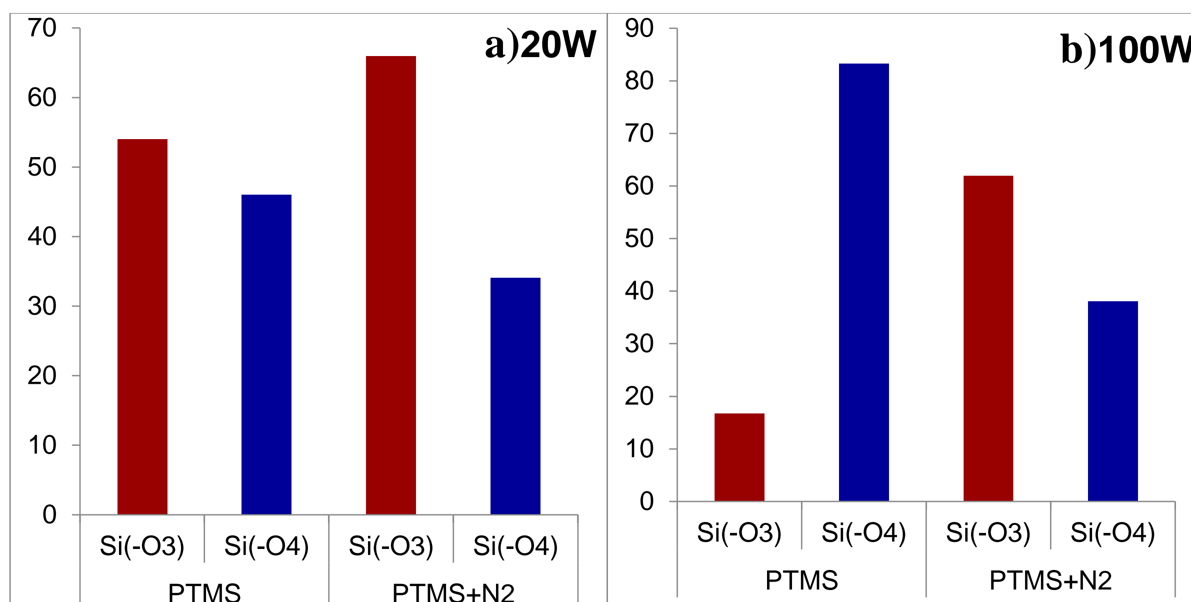

Figure 6.4 Comparison between silicon bonding environment present in films deposited from pure PTMS and a mixture of PTMS and N_2 at a) 20W, and b) 100W

The addition to nitrogen in such a small quantity does not have any perceivable change on the chemical states detected within the Si2*p* peak in high resolution XPS analysis. However, as can be seen in Figure 6.4, there is a distinct increase in the $Si(-O)_3$ environment for the films deposited with N2 compared to the pure PTMS films at both 20W and 100W. In addition, increasing plasma power does not result in a dramatic increase in the presence of $Si(-O)_4$ as it does for other depositions. There are several explanations as to how the addition of nitrogen to the plasma could elicit this behaviour during film formation. The most likely is that nitrogen radicals present in the plasma phase react with oxygen also present to form oxides of nitrogen which are pumped away. Less oxygen present and able to react with silicon species could allow a greater proportion of PTMS molecules possessing Si-C species to remain within the film. Another explanation is that silicon-nitrogen species are formed instead of Si-O bonds where the Si-C bond has broken and while no additional species are detected spectrally within the Si2*p* region of the XPS spectrum, this may be a product of the overall low concentration of nitrogen present within the film.

In order to determine how the nitrogen in the PTMS film was distributed, scanning Auger spectromicroscopy was used. However, nitrogen was not detected spectrally using AES, despite many spectra taken at a range of magnifications on both 20W and 100W samples. In addition, when depth profiling was performed in order to determine the composition of the deposited films, the spectral location of nitrogen was included in the analysis, in case the surface nitrogen detected in XPS had been somehow removed. However, nitrogen was unable to be detected at any point during the AES analysis procedure.

Table 6.5 Composition of films deposited from a mixture of PTMS and nitrogen as determined by AES depth profiling.

Plasma Treatment	%O	%C	%Si	C:Si	O:Si	C:O	Film Depth (nm)
PTMS 20W	40.8±3.2	31.6±2.5	27.6±0.7	1.1±0.06	1.5±0.15	0.8±0.13	129.7±5.4
PTMS 100W	41.5±1.2	28.8±0.9	29.7±1.4	1.0±0.06	1.4±0.10	0.7±0.03	112.7±11.9
PTMS+N_2 20W	39.1±1.3	31.3±0.8	29.5±0.9	1.1±0.04	1.3±0.08	0.8±0.04	120.1±5.0
PTMS+N_2 100W	38.9±0.7	31.2±2.1	29.9±1.5	1.1±0.13	1.3±0.05	0.8±0.07	103.1±4.2

That nitrogen was detected during XPS analysis but not AES is surprising. The cross section for Auger electron emission for lightweight elements such as nitrogen is greater than that of XPS, which should lead to greater nitrogen signal present on AES spectra; even though this would be accounted for through elemental sensitivity factors when determining composition. An assumption that has been made so far is that the nitrogen is chemically attached within the organosilane film. There is the possibility that the N_2 molecule, instead of being split by the plasma environment, is ionised and attracted to charged sites in the forming film. As the film grows, these nitrogen molecules are trapped within. As XPS was performed prior to AES analysis, it is possible that under vacuum conditions, or simply time, any trapped nitrogen is able to escape from the film and is therefore not detected in AES. A final possibility is that nitrogen is present in the film in isolated locations in higher concentrations, however the uniformity of the film makes identifying any such areas an exercise in pure chance.

6.3 **Summary**

The functionalisation of PTMS films through the addition of other chemical species during the plasma process was met with mixed success. The addition of oxygen to the plasma phase led to the deposition of a film with a composition close to that of silicon dioxide, a process commonly undertaken using precursors such as HMDSO and TEOS, but never performed before with PTMS. Through a similar mechanism, the addition of carbon to the PTMS film through methane did not meet with the same success. While there was an increase of silicon species in the $Si(-O)_3$ chemical state, the overall elemental composition did not change. In addition, the resultant films were of approximately the same thickness. The goal of producing an organosilane film with nitrogen functionality was not realised. Films containing nitrogen functionality were attempted to be produced through the addition of nitrogen gas to the plasma mixture and initial results from XPS were promising, with limited quantities of nitrogen were detected in XPS. However, nitrogen was not detected on the same samples with AES. Argon depth profiling showed that this lack of nitrogen was not due

to surface contamination or segregation. As this kind of study has not been previously performed using PTMS however, it is a solid foundation for future studies.

7 CHAPTER 7: CONCLUSIONS AND FUTURE WORK

7.1 Conclusions

The work presented as part of this dissertation has primarily been focussed on the deposition of organosilane films onto pure magnesium metal substrates. This was accomplished via two primary methods: wet chemical dip coating, and RF plasma deposition. Compositional and structural analysis of these films was accomplished through a range of analytical techniques, but primary among them were X-ray photoelectron spectroscopy and scanning Auger spectromicroscopy.

Initial investigations into the uptake of the organosilane PTMS onto magnesium were performed in order to determine if the adsorption behaviour is oscillatory, as it has been shown in literature for a range of other metals. These experiments revealed the inherent difficulty working with a substrate as reactive as magnesium, with the acetic acid catalyst used to hydrolyse PTMS etching the surface and causing considerable damage. Despite this damage, partial films were deposited and oscillatory uptake behaviour confirmed for PTMS deposition on magnesium surfaces, with a peak of uptake occurring at 30 seconds. Further analysis of the deposited films using scanning Auger spectromicroscopy provided further information about the structure of the film at various points during the chemical deposition process. This gave direct evidence for the island-like growth of PTMS films, with small regions of attached PTMS detectable through elemental mapping. These grew to a thin film covering a significant portion of the surface at the peak of the uptake oscillation before being removed in solution, leaving several larger areas of more well attached film before the magnesium is dissolved by the catalyst completely. A key finding here is that the grain boundaries of the magnesium substrate appear to play a role in the uptake of PTMS onto the surface. These boundaries appear to pose an inhibition to the spread of PTMS film across the surface, providing a location for the acetic acid to attack the underlying magnesium, undermining the film such that a barrier coating is not formed.

Due to the desire to produce a film from PTMS in a way that does not damage the magnesium substrate in such a dramatic way, alternative methods of deposition were considered. Plasma deposition was chosen as a means of creating an organosilane film from the pure PTMS monomer. The design, construction and testing of a plasma chamber for this purpose was therefore undertaken. The chamber is an RF, inductively coupled plasma system, utilizing an external planar coil antenna. Such a design allows the RF signal used to excite the source gases into a plasma through a quartz window, without being at risk of being itself coated, potentially affecting the transfer of energy between the RF source and

plasma.

Films were successfully deposited using this plasma apparatus. Compositional analysis of the surfaces resulting from plasma deposition at applied powers of 10W to 100W has shown that as power increases, so too does the coverage (Γ); asymptotically to a value of approximately 0.9, implying a near complete film. These results, obtained using XPS cannot distinguish a film that is incomplete, from one that is simply thinner than the escape depth of the photoelectrons that are produced. Hence elemental mapping of these surfaces was undertaken using scanning Auger spectromicroscopy, clearly showing that as power increases, the thickness of the film increases, but remains incomplete. This is confirmed using argon ion depth profiling which gave an estimate of film depth of between 2-8nm. The composition of these films, obtained from both XPS and AES analysis gives ratios of carbon, oxygen and silicon as approximately 2:1.3:1 (C:O:Si), showing a dramatic decrease in both carbon and oxygen from the original PTMS molecule (6:3:1, C:O:Si). The PTMS molecule then, must be undergoing decomposition either in the plasma phase and forming a film from constituent material or by bombardment by high energy material present in the plasma phase after attachment to the surface. As the films produced for this series of experiments were known to be incomplete, further studies were undertaken in order to investigate the effect plasma treatment duration had on the completeness and thickness of the produced film. Both forms of spectromicroscopy 'used' clearly show that as deposition time increases, a complete film is formed, with a linear deposition rate of approximately 100nm per hour at an applied plasma power of 20W. For those films where complete coverage was observed, a relatively constant film composition was obtained of 2:1.3:1 (C:O:Si). The slight decrease in oxygen content can be expected, as magnesium is present in the form of an oxide. Thus completely coating the substrate removes this source of oxygen from the spectra obtained from such a surface.

A key result obtained through elemental mapping of the deposited films was the effect of substrate morphology on the resultant films. The magnesium surfaces were prepared in a standardised way through abrasion with 1200p silicon carbide paper, resulting in an average surface roughness of approximately 90nm (with a large standard deviation of ~50nm), obtained from AFM analysis. In order to reduce any affects that surface morphology had on the deposition of the organosilane films. Successively finer grades of diamond paste, from 15μm to 1μm were used to produce a mirror finish magnesium surface. AFM was again used to measure the surface roughness of these surfaces, with a value of 11.5nm±1.97. A plasma duration of one hour was chosen for the deposition of films onto these surfaces, with the applied plasma power again varied between 10 and 100W. The deposited films for the most

part, had very little effect on the surface roughness, with the exception of films deposited at 100W. This increase in roughness was postulated to be a product of increased etching of the surface by higher energy species present in the plasma environment. Further evidence for this kind of etching was discovered after film thickness was analysed with argon ion depth profiling. Increasing plasma power led to an increase in film depth, from ~90nm at 10W, up to a peak of approximately 150nm at 40W. Above this power, film depth decreased to 100nm at 100W. This curve is thought to be a product of the competing etching and deposition processes that occur simultaneously during the plasma deposition. Increasing the plasma power increases the energy available within the system, activating species and allowing bonding to occur. However, other high energy species are formed which are able to bombard the surface and remove material. The optimal power for film growth is therefore one that minimizes the rate of etching, whilst still providing sufficient energy to allow the deposition of a film. This was found to be 40W for the combination of monomer, chamber and other experimental parameters investigated here.

The composition of these films was found to be relatively constant with changing power. It was however, slightly different than those films previously deposited onto a rougher magnesium surface. In particular, from XPS analysis a decrease in carbon content was found with a consequent increase in oxygen and silicon. The average elemental ratio of material present was 1.75:2:1. The difference between this and previous results was attributed to the removal of many sites present on a rougher surface that harboured carbonaceous material. These sites were visible on the surface through elemental mapping and corresponded well to channel-like features in the surface left as a remnant of the silicon carbide abrasion process. Elemental mapping of the diamond polished samples showed a marked decrease in the existence of such regions, as could be expected with a decrease in surface roughness. Despite this, areas of increased carbon concentration were still detectable, associated with the depressions and ridges on the surface. In order to determine the elemental composition of the films without the influence of surface contamination, depth profiling of selected areas of the film, without significant surface contamination was undertaken. Ratios obtained from depth profiles for the concentration of elements within the film were found to have a significant reduction in carbon to that of all previous measurements. The oxygen content of the interior of the film was also found to be lower than seen previously, with a C:O:Si ratio of 1.1:1.4:1. Such a significant decrease in both oxygen and carbon implies that the PTMS molecule is nearly completely dissociated, and the resulting film is quite dissimilar to that which could be obtained chemically from PTMS. Indeed, the composition of the deposited film seems to be quite close in composition to a silicon dioxide film containing carbon impurities.

To this end, the chemical state of silicon was analysed with high resolution XPS. In the PTMS molecule, all silicon present is bonded to 3 oxygen and 1 carbon atoms. The films deposited with even the lowest achievable power (10W), approximately 40% of the silicon was found bonded to 4 silicon atoms, increasing up to over 85% at 100W, despite no significant change in overall film composition.

An additional benefit of the smooth surface obtained from diamond polishing the magnesium substrates is that it allows the use of ATR-FTIR spectroscopy. Previously, the high roughness of the surfaces resulted in low levels of contact between the film and the ATR crystal, and therefore very low signal. Though films on the order of 100nm are still far thinner than would be ideal for this technique, sufficient signal was obtained for analysis. A significant reduction in carbon-carbon bonding species was observed from a reference spectra of the pure liquid PTMS, supporting electron spectroscopy results. Most importantly, individual silicon-oxygen peaks which are obtained for pure liquid PTMS are converted into a single, broad absorption which is well known to indicate the existence of a polymerized network of Si-O-Si species.

Plasma deposition is a versatile technique, and the chamber constructed possesses multiple input gas lines. Consequently, attempts were made to adjust the mixture of gases added to the plasma in order to influence the composition and thus final properties of the deposited films. Firstly, due to the significant decrease in carbon concentration from the original PTMS molecule, an additional source of carbon in the form of methane was included. The majority of the resultant films did not show any significant increase in carbon concentration compared to films deposited from pure PTMS, however a slight increase of the amount of silicon in the $Si(-O)_3$ bonding environment was observed. Through the addition of oxygen to the PTMS plasma mixture an attempt was made to produce silicon dioxide films. Both oxygen and water vapour were investigated for this purpose and had a significant impact on the deposited film through a reduction in carbon concentration. High resolution XPS spectra showed silicon present only in the $Si(-O)_4$ bonding environment implying the existence of a silicon dioxide film. In an attempt to produce films with nitrogen functionality, akin to APS, nitrogen gas was added to PTMS plasma. XPS showed the presence of a small amount of nitrogen on the surfaces, but this was unable to be corroborated through AES, including the use of depth profiling.

7.2 Recommendations for Future Work

The development of the plasma chamber used for the research presented in this work was a significant endeavour. The apparatus provides a rich ground for further experimental

research within the field of thin film deposition of organosilane materials. The high vacuum environment provides a clean environment, ideal for the coating of reactive or otherwise contaminant sensitive materials. The research undertaken here has provided a fundamental grounding in the capabilities and challenges in working with this apparatus, however, there is a broad range of further research possible.

The addition of functionalisation to organosilane films was briefly explored, but was far from comprehensive. By altering the composition of the plasma through both the choice of organosilane and any additional functional gases, it should be possible to tailor the composition of any deposited film. This could include the successive depositions of differing materials in order to create layered structures without the need to expose the material to the atmosphere, and all the contaminants that it contains. Another useful aspect of plasma deposition not fully explored here was the optimization of plasma pre-treatment. The interfacial layer between the substrate and any deposited film is vitally important for its growth and long term stability.

Another area of research only briefly investigated here was the effect of pre-treatments. In the future, research dedicated to the optimization of both the constituents and experimental plasma parameters of the pre-treatment process is necessary in order to provide the best possible foundation and interface to any deposited films.

This leads directly into possibly the most important area for future study: the effects that changes in the composition or silicon bonding environment have on the properties and attachment strength of the produced films, with particular regard to the long term stability of films. Due to the focus of this project on the proof of concept deposition parameters and elemental analysis of films, time was not available to examine the corrosion protection properties said films. As such, it remains a priority for future investigation. One particular aspect that would be interesting to examine is if a plasma deposited organosilane film provides a suitable pre-treatment for further chemical dip coating. Additionally, if the addition of a thin passivation layer prevents the rapid etching of pure magnesium, and subsequent undermining of chemically deposited films, then would oscillatory uptake still be seen on such a non-metallic surface?

8 REFERENCES

1. Kibel, M.H., *X-Ray Photoelectron Spectroscopy*, in *Surface Analysis Methods in Materials Science*, D.J.S. O'Connor, B. A.; Smart, R. S. C, Editor. 1992, Springer-Verlag Berlin Heidelberg: Berlin, Germany. p. 175-201.
2. Berger, R., et al., *The influence of alkali-degreasing on the chemical composition of hot-dip galvanized steel surfaces.* Surface and Interface Analysis, 2006. **38**(7): p. 1130-1138.
3. Lumley, R., ed. *Fundamentals of Aluminium Metallurgy, Production, Processing and Applications*. 1 ed. 2011, Woodhead Publishing: Abington Hall, Granta Park, Great Abington, Cambridge, UK.
4. Luo, A.A., *8 - Applications: aerospace, automotive and other structural applications of magnesium*, in *Fundamentals of Magnesium Alloy Metallurgy*, M.O. Pekguleryuz, K.U. Kainer, and A. Arslan Kaya, Editors. 2013, Woodhead Publishing. p. 266-316.
5. Mordike, B.L. and T. Ebert, *Magnesium: Properties — applications — potential.* Materials Science and Engineering: A, 2001. **302**(1): p. 37-45.
6. Lindström, R., et al., *Corrosion of magnesium in humid air.* Corrosion Science, 2004. **46**(5): p. 1141-1158.
7. Gray, J.E. and B. Luan, *Protective coatings on magnesium and its alloys -- a critical review.* Journal of Alloys and Compounds, 2002. **336**(1-2): p. 88-113.
8. Angelini, E., et al., *Electrochemical impedance spectroscopy evaluation of the corrosion behaviour of Mg alloy coated with PECVD organosilicon thin film.* Progress in Organic Coatings, 2003. **46**(2): p. 107-111.
9. Neupane, M.P., et al., *Surface characterization and corrosion behavior of silanized magnesium coated with graphene for biomedical application.* Materials Chemistry and Physics, 2015. **163**: p. 229-235.
10. Asmussen, R.M., et al., *Tracking the corrosion of magnesium sand cast AM50 alloy in chloride environments.* Corrosion Science, 2013. **75**: p. 114-122.
11. Abbas, G., Z. Liu, and P. Skeldon, *Corrosion behaviour of laser-melted magnesium alloys.* Applied Surface Science, 2005. **247**(1–4): p. 347-353.
12. Pinto, R., et al., *A two-step surface treatment, combining anodisation and silanisation, for improved corrosion protection of the Mg alloy WE54.* Progress in Organic Coatings, 2010. **69**(2): p. 143-149.
13. Zhao, M., et al., *A chromium-free conversion coating of magnesium alloy by a phosphate–permanganate solution.* Surface and Coatings Technology, 2006. **200**(18–19): p. 5407-5412.
14. Khramov, A.N., et al., *Sol–gel coatings with phosphonate functionalities for surface modification of magnesium alloys.* Thin Solid Films, 2006. **514**(1–2): p. 174-181.
15. Eliezer, D., E. Aghion, and F.H. Froes, *Magnesium Science, Technology and Applications.* Advanced Performance Materials, 1998. **5**(3): p. 201-212.
16. Supplit, R., T. Koch, and U. Schubert, *Evaluation of the anti-corrosive effect of acid pickling and sol–gel coating on magnesium AZ31 alloy.* Corrosion Science, 2007. **49**(7): p. 3015-3023.
17. Fournier, V., P. Marcus, and I. Olefjord, *Oxidation of magnesium.* Surface and Interface Analysis, 2002. **34**(1): p. 494-497.
18. Pardo, A., et al., *Corrosion behaviour of magnesium/aluminium alloys in 3.5 wt.% NaCl.* Corrosion Science, 2008. **50**(3): p. 823-834.
19. Ballerini, G., et al., *About some corrosion mechanisms of AZ91D magnesium alloy.* Corrosion Science, 2005. **47**(9): p. 2173-2184.
20. Zhang, J., et al., *Effect of composition on the microstructure and mechanical properties of Mg–Zn–Al alloys.* Materials Science and Engineering: A, 2007. **456**(1–2): p. 43-51.
21. Polmear, I.J., *Recent Developments in Light Alloys.* Materials Transactions, JIM,

1996. **37**(1): p. 12-31.
22. Shih, T.-S., J.-B. Liu, and P.-S. Wei, *Oxide films on magnesium and magnesium alloys.* Materials Chemistry and Physics, 2007. **104**(2-3): p. 497-504.
23. Kojima, Y., *Platform Science and Technology for Advanced Magnesium Alloys.* Mater. Sci. Forum, 2000. **350-351**: p. 3-17.
24. Denkena, B. and A. Lucas, *Biocompatible Magnesium Alloys as Absorbable Implant Materials – Adjusted Surface and Subsurface Properties by Machining Processes.* CIRP Annals - Manufacturing Technology, 2007. **56**(1): p. 113-116.
25. Kuwahara, H., Al-Abdullat, Y., Ohta, M., Tsutsumi, S., Ikeuchi, K., Mazaki, N., & Aizawa, T. *Surface reaction of magnesium in Hank's solutions*. in *Proceedings of the 1st Nagaoka International Workshop on Magnesium Platform Science and Technology 2000*. 2000. Nagaoka, Jpn: Materials Science Forum.
26. Seiler, H.G.S., H.; Sigel, A. , ed. *Handbook on toxicity of inorganic compounds*. Vol. 24. 1988, Marcel Dekker: New York, United States.
27. Saris, N.-E.L., et al., *Magnesium: An update on physiological, clinical and analytical aspects.* Clinica Chimica Acta, 2000. **294**(1–2): p. 1-26.
28. Witte, F., et al., *In vivo corrosion of four magnesium alloys and the associated bone response.* Biomaterials, 2005. **26**(17): p. 3557-3563.
29. Song, G. and S. Song, *A Possible Biodegradable Magnesium Implant Material.* Advanced Engineering Materials, 2007. **9**(4): p. 298-302.
30. Heublein, B., et al., *Biocorrosion of magnesium alloys: a new principle in cardiovascular implant technology?* Heart, 2003. **89**(6): p. 651-656.
31. Song, G., *Control of biodegradation of biocompatable magnesium alloys.* Corrosion Science, 2007. **49**(4): p. 1696-1701.
32. Atrens, A., et al., *Review of Recent Developments in the Field of Magnesium Corrosion.* Advanced Engineering Materials, 2015. **17**(4): p. 400-453.
33. Ed, M., *Absorbable metal in bone surgery: A further report on the use of magnesium alloys.* Journal of the American Medical Association, 1938. **111**(27): p. 2464-2467.
34. Vormann, J., *Magnesium: nutrition and metabolism.* Molecular Aspects of Medicine, 2003. **24**(1–3): p. 27-37.
35. Ko, Y.-M., et al., *Plasma deposition of a silicone-like layer for the corrosion protection of magnesium.* Progress in Organic Coatings, 2013. **76**(12): p. 1827-1832.
36. Levesque, J., et al., *Materials and properties for coronary stents: coronary stents must have excellent mechanical properties to provide strength to artery walls.* Advanced Materials & Processes, 2004. **162**: p. 45+.
37. Polini, W. and L. Sorrentino, *Improving the wettability of 2024 aluminium alloy by means of cold plasma treatment.* Applied Surface Science, 2003. **214**(1–4): p. 232-242.
38. Schmitt, G., et al., *Global Needs for Knowledge Dissemination, Research and Development in Materials Deteriation and Corrosion Control*. 2009, World Corrosion Organisation: New York.
39. McIntyre, N.S. and C. Chen, *Role of impurities on Mg surfaces under ambient exposure conditions.* Corrosion Science, 1998. **40**(10): p. 1697-1709.
40. Do, T., et al., *The oxidation kinetics of Mg and Al surfaces studied by AES and XPS.* Surface Science, 1997. **387**(1-3): p. 192-198.
41. Fuggle, J.C., et al., *X-ray photoelectron studies of the reaction of clean metals (Mg, Al, Cr, Mn) with oxygen and water vapour.* Surface Science, 1975. **49**(1): p. 61-76.
42. Chen, C., et al., *Measurement of oxide film growth on Mg and Al surfaces over extended periods using XPS.* Surface Science, 1997. **382**(1-3): p. L652-L657.
43. Alexander, M.R., G.E. Thompson, and G. Beamson, *Characterization of the oxide/hydroxide surface of aluminium using x-ray photoelectron spectroscopy: a procedure for curve fitting the O 1s core level.* Surface and Interface Analysis, 2000. **29**(7): p. 468-477.
44. Yao, H.B., Y. Li, and A.T.S. Wee, *An XPS investigation of the oxidation/corrosion of melt-spun Mg.* Applied Surface Science, 2000. **158**(1-2): p. 112-119.

45. Snijders, P.C., L.P.H. Jeurgens, and W.G. Sloof, *Structure of thin aluminium-oxide films determined from valence band spectra measured using XPS.* Surface Science, 2002. **496**(1-2): p. 97-109.
46. Frerichs, M., et al., *Corrosion of aluminium components studied with MIES, UPS and XPS.* Applied Surface Science, 2005. **252**(1): p. 108-112.
47. Splinter, S.J., et al., *An AES and XPS study of the initial oxidation of polycrystalline magnesium with water vapour at room temperature.* Surface Science, 1993. **292**(1-2): p. 130-144.
48. Strohmeier, B.R., *An ESCA method for determining the oxide thickness on aluminum alloys.* Surface and Interface Analysis, 1990. **15**(1): p. 51-56.
49. Kuroda, Y., et al., *Interaction of water with the surface of magnesium oxide.* Journal of the Chemical Society, Faraday Transactions 1: Physical Chemistry in Condensed Phases, 1988. **84**(7).
50. Cabrera, N. and N.F. Mott, *Theory of the oxidation of metals.* Reports on Progress in Physics, 1949. **12**(1): p. 163.
51. Moffitt, C.E., D.M. Wieliczka, and H.K. Yasuda, *An XPS study of the elemental enrichment on aluminum alloy surfaces from chemical cleaning.* Surface and Coatings Technology, 2001. **137**(2-3): p. 188-196.
52. Ghali, E., W. Dietzel, and K.-U. Kainer, *General and localized corrosion of magnesium alloys: A critical review.* Journal of Materials Engineering and Performance, 2004. **13**(1): p. 7-23.
53. Pourbaix, M. and J. Burbank, *Atlas D-Equilibres Electrochimiques*, in *Journal of The Electrochemical Society*. 1964, ECS. p. 14C-15C.
54. Winzer, N., et al., *A Critical Review of the Stress Corrosion Cracking (SCC) of Magnesium Alloys.* Advanced Engineering Materials, 2005. **7**(8): p. 659-693.
55. Montemor, M.F. and M.G.S. Ferreira, *Electrochemical study of modified bis-[triethoxysilylpropyl] tetrasulfide silane films applied on the AZ31 Mg alloy.* Electrochimica Acta, 2007. **52**(27): p. 7486-7495.
56. Song, G.L. and A. Atrens, *Corrosion Mechanisms of Magnesium Alloys.* Advanced Engineering Materials, 1999. **1**(1): p. 11-33.
57. Thomas, S., et al., *Corrosion mechanism and hydrogen evolution on Mg.* Current Opinion in Solid State and Materials Science, 2015. **19**(2): p. 85-94.
58. Song, G. and A. Atrens, *Understanding Magnesium Corrosion—A Framework for Improved Alloy Performance.* Advanced Engineering Materials, 2003. **5**(12): p. 837-858.
59. Song, G., A. Atrens, and M. Dargusch, *Influence of microstructure on the corrosion of diecast AZ91D.* Corrosion Science, 1998. **41**(2): p. 249-273.
60. Comittee, A.H., ed. *ASM Handbook, Vol. 10: Materials Characterization*. Vol. 10. 1992, American Society for Metals: Metals Park, Ohio. 761.
61. Lunder, O., et al., *The Role of Mg17Al12 Phase in the Corrosion of Mg Alloy AZ91*. Vol. 45. 1989: NACE. 741-748.
62. Kaesel, V., et al., *Approach to Control the Corrosion of Magnesium by Alloying*, in *Magnesium*. 2005, Wiley-VCH Verlag GmbH & Co. KGaA. p. 534-539.
63. Fontenier, G., R. Freschard, and M. Mourot, *Study of the corrosionin vitro andin vivo of magnesium anodes involved in an implantable bioelectric battery.* Medical and biological engineering, 1975. **13**(5): p. 683-689.
64. McCord, J.F. and I. Blum, *Prevention of bone loss for edentulous patients.* Eur J Prosthodont Restor Dent, 2003. **11**(2): p. 71-4.
65. Song, G., *Recent Progress in Corrosion and Protection of Magnesium Alloys.* Advanced Engineering Materials, 2005. **7**(7): p. 563-586.
66. Birbilis, N., et al., *Evidence for enhanced catalytic activity of magnesium arising from anodic dissolution.* Electrochimica Acta, 2014. **132**: p. 277-283.
67. Pourbaix, M., *Atlas of electrochemical equilibria in aqueous solutions*. 1974: National Association of Corrosion Engineers. 644.
68. Song, G. and A. Atrens, *Recent Insights into the Mechanism of Magnesium*

Corrosion and Research Suggestions. Advanced Engineering Materials, 2007. **9**(3): p. 177-183.

69. Tylecote, R.F., *A History of Metallurgy*. 1992, Maney Publishing for the Institute of Materials: London.
70. Cramer, S.D.C., Bernard S. Jr., ed. *ASM Handbook 13A: Corrosion: Fundamentals, Testing, and Protection*. 2003, ASM International: Materials Park,Ohio. 1135.
71. Song, G., et al., *Corrosion behaviour of AZ21, AZ501 and AZ91 in sodium chloride.* Corrosion Science, 1998. **40**(10): p. 1769-1791.
72. Song, G., A.L. Bowles, and D.H. StJohn, *Corrosion resistance of aged die cast magnesium alloy AZ91D.* Materials Science and Engineering: A, 2004. **366**(1): p. 74-86.
73. Lunder, O., et al., *The Role of Mg17Al12 Phase in the Corrosion of Mg Alloy AZ91.* CORROSION, 1989. **45**(9): p. 741-748.
74. Danaie, M., et al., *The role of aluminum distribution on the local corrosion resistance of the microstructure in a sand-cast AM50 alloy.* Corrosion Science, 2013. **77**: p. 151-163.
75. Mathieu, S., et al., *A corrosion study of the main constituent phases of AZ91 magnesium alloys.* Corrosion Science, 2003. **45**(12): p. 2741-2755.
76. Makar, G.L. and J. Kruger, *Corrosion of magnesium.* International Materials Reviews, 1993. **38**(3): p. 138-153.
77. Choi, H.Y. and W.J. Kim, *Development of the highly corrosion resistant AZ31 magnesium alloy by the addition of a trace amount of Ti.* Journal of Alloys and Compounds, 2016. **664**: p. 25-37.
78. Song, G. and D. StJohn, *Corrosion performance of magnesium alloys MEZ and AZ91.* International Journal of Cast Metals Research, 2000. **12**(6): p. 327-334.
79. Shi, Z., G. Song, and A. Atrens, *Corrosion resistance of anodised single-phase Mg alloys.* Surface and Coatings Technology, 2006. **201**(1–2): p. 492-503.
80. Cao, F., et al., *Corrosion behaviour in salt spray and in 3.5% NaCl solution saturated with Mg(OH)2 of as-cast and solution heat-treated binary Mg–X alloys: X = Mn, Sn, Ca, Zn, Al, Zr, Si, Sr.* Corrosion Science, 2013. **76**: p. 60-97.
81. Li, H., et al., *An in situ XPS study of oxygen plasma cleaning of aluminum surfaces.* Surface and Coatings Technology, 1997. **92**(3): p. 171-177.
82. van Ooij, W.J., et al., *Corrosion Protection Properties of Organofunctional Silanes--An Overview.* Tsinghua Science & Technology, 2005. **10**(6): p. 639-664.
83. Maeda, S., *Surface chemistry of galvanized steel sheets relevant to adhesion performance.* Progress in Organic Coatings, 1996. **28**(4): p. 227-238.
84. Hughes, A.E., R.J. Taylor, and B.R.W. Hinton, *Chromate Conversion Coatings on 2024 Al Alloy.* Surface and Interface Analysis, 1997. **25**(4): p. 223-234.
85. Machle, W. and F. Gregorius, *Cancer of the respiratory system in the United States chromate-producing industry.* Public Health Rep, 1948. **63**: p. 1114-1127.
86. Mancuso, T.F. and W.C. Hueper, *Occupational cancer and other health hazards in a chromate plant: a medical appraisal. I. Lung cancers in chromate workers.* Industrial medicine & surgery, 1951. **20**(8): p. 358-363.
87. Child, T.F. and W.J. van Ooij, *Application of Silane Technology to Prevent Corrosion of Metals and Improve Paint Adhesion.* Transactions of the IMF, 1999. **77**(2): p. 64-70.
88. Plueddemann, E.p., *Silane Coupling Agents*. 2nd ed. 1990, New York: Plenum Press.
89. Osterholtz, F.D. and E.R. Pohl, *Kinetics of the hydrolysis and condensation of organofunctional alkoxysilanes: a review.* Journal of Adhesion Science and Technology, 1992. **6**(1): p. 127-149.
90. Arkles, B., et al., *Factors contributing to the stability of alkoxysilanes in aqueous solution.* Journal of Adhesion Science and Technology, 1992. **6**(1): p. 193-206.
91. Montemor, M.F. and M.G.S. Ferreira, *Analytical and microscopic characterisation of modified bis-[triethoxysilylpropyl] tetrasulphide silane films on magnesium AZ31*

substrates. Progress in Organic Coatings, 2007. **60**(3): p. 228-237.
92. Leung, Y.L., et al., *XPS studies of interfaces between γ-glycidoxypropyltrimethoxysilane and aluminum surfaces.* Applied Surface Science, 1992. **59**(1): p. 23-29.
93. Fang, J., et al., *A characterization of the <i>β</i>-glycidoxypropyltrimethoxysilane and aluminium interface by SIMS and XPS.* Journal of Materials Science Letters, 1997. **16**(20): p. 1675-1676.
94. Abel, M.-L., et al., *Evidence of specific interaction between γ-glycidoxypropyltrimethoxysilane and oxidized aluminium using high-mass resolution ToF-SIMS†.* Surface and Interface Analysis, 2000. **29**(2): p. 115-125.
95. Abel, M.L. and J. Watts, *Influence of temperature on aminosilane thin films deposited on aluminium substrates: A study by surface analysis.* Journal of Adhesion, 2008. **84**(10): p. 849-873.
96. Leung, Y.L., et al., *X-ray photoelectron spectroscopic studies with a bias-potential method for studying silane-aluminium interfaces.* Journal of Materials Science Letters, 1993. **12**(11): p. 844-846.
97. Quinton, J., L. Thomsen, and P. Dastoor, *Adsorption of organosilanes on iron and aluminium oxide surfaces.* Surface and Interface Analysis, 1997. **25**(12): p. 931-936.
98. Quinton, J., P. Dastoor, and W. Allison, *PTMS on iron and aluminium oxide surfaces: a study of damped adsorption kinetics.* Surface Science, 1998. **402–404**(0): p. 66-70.
99. Quinton, J.S. and P.C. Dastoor, *Characterizing the bonding mechanisms at silane-metal interfaces: A model system.* Journal of Materials Science Letters, 1999. **18**(22): p. 1833-1835.
100. Quinton, J.S. and P.C. Dastoor, *The effect of experimental conditions on the oscillatory adsorption of propyltrimethoxysilane on aluminium oxide surfaces.* Applied Surface Science, 1999. **152**(3–4): p. 131-137.
101. Quinton, J.S. and P.C. Dastoor, *Influence of surface electrokinetics on organosilane adsorption.* Surface and Interface Analysis, 1999. **28**(1): p. 12-15.
102. Quinton, J.S. and P.C. Dastoor, *Modelling the observed oscillations in the adsorption kinetics of propyltrimethoxysilane on iron and aluminium oxide surfaces.* Surface and Interface Analysis, 2000. **30**(1): p. 25-28.
103. Quinton, J.S. and P.C. Dastoor, *Oscillatory adsorption: a first-principles linear kinetic model.* Surface and Interface Analysis, 2001. **32**(1): p. 57-61.
104. Quinton, J.S. and P.C. Dastoor, *Conformational dynamics of γ-APS on the iron oxide surface: an adsorption kinetic study using XPS and ToF-SIMS.* Surface and Interface Analysis, 2000. **30**(1): p. 21-24.
105. Watts, B., et al., *Understanding the Conformational Dynamics of Organosilanes: γ-APS on Zinc Oxide Surfaces.* Langmuir, 2002. **18**(1): p. 148-154.
106. Thomsen, L., B. Watts, and P.C. Dastoor, *A NEXAFS orientation study of γ-aminopropyltriethoxysilane on zinc oxide surfaces.* Surface and Interface Analysis, 2006. **38**(7): p. 1139-1145.
107. Yang, L., et al., *Study on the adsorption behavior of γ-GPS on low carbon steel surfaces using RA-IR, EIS and AFM.* Applied Surface Science, 2011. **257**(23): p. 9895-9903.
108. Houssiau, L. and P. Bertrand, *ToF–SIMS study of organosilane self-assembly on aluminum surfaces.* Applied Surface Science, 2001. **175–176**(0): p. 351-356.
109. Thomsen, L., et al., *Adsorption and orientation kinetics of self-assembled films of octadecyltrimethoxysilane on aluminium oxide surfaces.* Surface and Interface Analysis, 2005. **37**(5): p. 472-477.
110. Moses, P.R., et al., *X-ray photoelectron spectroscopy of alkylaminesilanes bound to metal oxide electrodes.* Analytical Chemistry, 1978. **50**(4): p. 576-585.
111. Dillingham, R.G. and F.J. Boerio, *Interphase Composition in Aluminum/Epoxy Adhesive Joints.* The Journal of Adhesion, 1987. **24**(2-4): p. 315-335.
112. van Ooij, W.J. and A. Sabata, *Characterization of films of organofunctional silanes by ToF-SIMS. Part II. Films of γ-APS, AEAPS and FPS on cold-rolled steel and cold-*

rolled zinc substrates. Surface and Interface Analysis, 1993. **20**(5): p. 475-484.
113. Fowkes, F.M., et al., *Acid-base properties of glass surfaces.* Journal of Non-Crystalline Solids, 1990. **120**(1): p. 47-60.
114. Boerio, F.J.D., R.G., *Hydrothermal Stability of Titanium/Epoxy Adhesive Joints*, in *Adhesive Joints: Formation, Characteristics and Testing.*, K.L. Mittal, Editor. 1984, Springer US: New York. p. 541-553.
115. Horner, M.R., F.J. Boerio, and H.M. Clearfield, *An XPS investigation of the adsorption of aminosilanes onto metal substrates.* Journal of Adhesion Science and Technology, 1992. **6**(1): p. 1-22.
116. Subramanian, V. and W.J.v. Ooij, *Effect of the Amine Functional Group on Corrosion Rate of Iron Coated with Films of Organofunctional Silanes.* CORROSION, 1998. **54**(3): p. 204-215.
117. Susac, D., X. Sun, and K.A.R. Mitchell, *Adsorption of BTSE and γ-APS organosilanes on different microstructural regions of 2024-T3 aluminum alloy.* Applied Surface Science, 2003. **207**(1-4): p. 40-50.
118. Kim, J., et al., *Pre-treatments applied to oxidized aluminum surfaces to modify the interfacial bonding with bis-1,2-(triethoxysilyl)ethane (BTSE): Part II. Anodized 7075-T6 Al alloy.* Applied Surface Science, 2005. **252**(5): p. 1305-1312.
119. Teo, M., et al., *Pre-treatments applied to oxidized aluminum surfaces to modify the interfacial bonding with bis-1,2-(triethoxysilyl)ethane (BTSE): Part I. High-purity Al with native oxide.* Applied Surface Science, 2005. **252**(5): p. 1293-1304.
120. Franquet, A., H. Terryn, and J. Vereecken, *Study of the effect of different aluminium surface pretreatments on the deposition of thin non-functional silane coatings.* Surface and Interface Analysis, 2004. **36**(8): p. 681-684.
121. Franquet, A., et al., *Study of the interaction of hydrolysed silane solutions with pre-treated aluminium substrates.* Surface and Interface Analysis, 2006. **38**(4): p. 172-175.
122. Song, J. and W.J. Van Ooij, *Bonding and corrosion protection mechanisms of γ-APS and BTSE silane films on aluminum substrates.* Journal of Adhesion Science and Technology, 2003. **17**(16): p. 2191-2221.
123. Liu, X., et al., *Biofunctionalized anti-corrosive silane coatings for magnesium alloys.* Acta Biomaterialia, 2013. **9**(10): p. 8671-8677.
124. Meadows Telly, A. and L. Bhatt Deepak, *Clinical Aspects of Platelet Inhibitors and Thrombus Formation.* Circulation Research, 2007. **100**(9): p. 1261-1275.
125. Bajat, J.B., et al., *Corrosion protection of aluminium pretreated by vinyltriethoxysilane in sodium chloride solution.* Corrosion Science, 2010. **52**(3): p. 1060-1069.
126. De Graeve, I., et al., *Silane coating of metal substrates: Complementary use of electrochemical, optical and thermal analysis for the evaluation of film properties.* Progress in Organic Coatings, 2007. **59**(3): p. 224-229.
127. Chico, B., et al., *Electrochemical impedance spectroscopy study of the effect of curing time on the early barrier properties of silane systems applied on steel substrates.* Progress in Organic Coatings, 2007. **60**(1): p. 45-53.
128. Zhu, D. and W.J. van Ooij, *Corrosion protection of metals by water-based silane mixtures of bis-[trimethoxysilylpropyl]amine and vinyltriacetoxysilane.* Progress in Organic Coatings, 2004. **49**(1): p. 42-53.
129. De Graeve, I., et al., *Silane solution stability and film morphology of water-based bis-1,2-(triethoxysilyl)ethane for thin-film deposition on aluminium.* Progress in Organic Coatings, 2008. **63**(1): p. 38-42.
130. Merche, D., N. Vandencasteele, and F. Reniers, *Atmospheric plasmas for thin film deposition: A critical review.* Thin Solid Films, 2012. **520**(13): p. 4219-4236.
131. Langmuir, I., *Oscillations in Ionized Gases.* Proceedings of the National Academy of Sciences of the United States of America, 1928. **14**(8): p. 627-637.
132. Chen, F.F., *Introduction to Plasma Physics and Controlled Fusion.* Vol. 1. 1984, New York: Plenum Press.
133. Swift, J.D. and M.J.R. Schwar, *Electrical probes for plasma diagnostics.* 1969,

London; New York: Iliffe Books; American Elsevier.
134. Lieberman, M.A. and A.J. Lichtenberg, *Principles of Plasma Discharges and Materials Processing. Second Edition.* 2005, New Jersey: John Wiley & Sons.
135. Shoda, K. and S. Takeda, *Transmission Electron Microscopy Study on the Surface Properties of CNTs and Fullerites Exposed to CF4 Plasma.* MRS Proceedings, 2011. **1018**.
136. Merlino, R.L., *Understanding Langmuir probe current-voltage characteristics.* American Journal of Physics, 2007. **75**(12): p. 1078-1085.
137. Michelmore, A., et al., *Where physics meets chemistry: Thin film deposition from reactive plasmas.* Frontiers of Chemical Science and Engineering, 2016. **10**(4): p. 441-458.
138. Yasuda, H. and T. Hsu, *Some aspects of plasma polymerization investigated by pulsed R.F. discharge.* Journal of Polymer Science: Polymer Chemistry Edition, 1977. **15**(1): p. 81-97.
139. Yasuda, H. and T. Hirotsu, *Critical evaluation of conditions of plasma polymerization.* Journal of Polymer Science: Polymer Chemistry Edition, 1978. **16**(4): p. 743-759.
140. Yasuda, H., *Plasma polymerization for protective coatings and composite membranes.* Journal of Membrane Science, 1984. **18**: p. 273-284.
141. Walkiewicz-Pietrzykowska, A., J. Cotrino, and A.R. González-Elipe, *Deposition of Thin Films of SiOxCyH in a Surfatron Microwave Plasma Reactor with Hexamethyldisiloxane as Precursor.* Chemical Vapor Deposition, 2005. **11**(6-7): p. 317-323.
142. Bogart, K.H.A., et al., *Plasma enhanced chemical vapor deposition of SiO2 using novel alkoxysilane precursors.* Journal of Vacuum Science & Technology A: Vacuum, Surfaces, and Films, 1995. **13**(2): p. 476-480.
143. van Ooij, W.J., D. Surman, and H.K. Yasuda, *Plasma-polymerized coatings of trimethylsilane deposited on cold-rolled steel substrates Part 2. Effect of deposition conditions on corrosion performance.* Progress in Organic Coatings, 1995. **25**(4): p. 319-337.
144. Sabata, A., W.J. van Ooij, and H.K. Yasuda, *Plasma-polymerized films of trimethylsilane deposited on cold-rolled steel substrates. Part 1. Characterization by XPS, AES and TOF-SIMS.* Surface and Interface Analysis, 1993. **20**(10): p. 845-859.
145. Yasuda, H.K., et al., *Corrosion protection of cold-rolled steel by low temperature plasma interface engineering II. Effects of oxides on corrosion performance of E-coated steels.* Progress in Organic Coatings, 1996. **30**(1-2): p. 31-38.
146. Lin, T.J., et al., *Plasma treatment of automotive steel for corrosion protection - a dry energetic process for coatings.* Progress in Organic Coatings, 1997. **31**(4): p. 351-361.
147. Zajíčková, L., et al., *Deposition of protective coatings in rf organosilicon discharges.* Plasma Sources Science and Technology, 2007. **16**(1): p. S123.
148. Angelini, E., et al., *Surface analysis of PECVD organosilicon films for corrosion protection of steel substrates.* Surface and Interface Analysis, 2002. **34**(1): p. 155-159.
149. Alexander, M.R., et al., *A study of HMDSO/O2 plasma deposits using a high-sensitivity and -energy resolution XPS instrument: curve fitting of the Si 2p core level.* Applied Surface Science, 1999. **137**(1–4): p. 179-183.
150. Alexander, M.R., et al., *An X-ray photoelectron spectroscopic investigation into the chemical structure of deposits formed from hexamethyldisiloxane/ oxygen plasmas.* Journal of Materials Science, 1996. **31**(7): p. 1879-1885.
151. Batan, A., et al., *Comparison between wet deposition and plasma deposition of silane coatings on aluminium.* Progress in Organic Coatings, 2010. **69**(2): p. 126-132.
152. Batan, A., et al., *Evidence of covalent bond formation at the silane-metal interface during plasma polymerization of bis-1,2-(triethoxysilyl)ethane (BTSE) on aluminium.* Chemical Physics Letters, 2010. **493**(1-3): p. 107-112.
153. Michelmore, A., et al., *Nanoscale deposition of chemically functionalised films via*

plasma polymerisation. RSC Advances, 2013. **3**(33): p. 13540-13557.
154. Elodie, L., et al., *Plasma Polymerization of APTES to Elaborate Nitrogen Containing Organosilicon Thin Films: Influence of Process Parameters and Discussion About the Growing Mechanisms.* Plasma Processes and Polymers, 2013. **10**(3): p. 250-261.
155. Garzia Trulli, M., et al., *Deposition of aminosilane coatings on porous Al2O3 microspheres by means of dielectric barrier discharges.* Plasma Processes and Polymers, 2017. **14**(9): p. 1600211.
156. Cech, V., J. Zemek, and V. Perina, *Chemistry of Plasma-Polymerized Vinyltriethoxysilane Controlled by Deposition Conditions.* Plasma Processes and Polymers, 2008. **5**(8): p. 745-752.
157. Yasuda, H.K., *Some Important Aspects of Plasma Polymerization.* Plasma Processes and Polymers, 2005. **2**(4): p. 293-304.
158. Lin, Y. and H. Yasuda, *Effect of plasma polymer deposition methods on copper corrosion protection.* Journal of Applied Polymer Science, 1996. **60**(4): p. 543-555.
159. Chen, R.T., et al., *New Insights into the Substrate–Plasma Polymer Interface.* The Journal of Physical Chemistry B, 2011. **115**(20): p. 6495-6502.
160. Vasilev, K., et al., *Early Stages of Growth of Plasma Polymer Coatings Deposited from Nitrogen- and Oxygen-Containing Monomers.* Plasma Processes and Polymers, 2010. **7**(9-10): p. 824-835.
161. Vasilev, K., et al., *Substrate influence on the initial growth phase of plasma-deposited polymer films.* Chemical Communications, 2009(24): p. 3600-3602.
162. Michelmore, A., et al., *Surface Morphology in the Early Stages of Plasma Polymer Film Growth from Amine-Containing Monomers.* Plasma Processes and Polymers, 2011. **8**(5): p. 367-372.
163. Meitner, L., *Über die Entstehung der β-Strahl-Spektren radioaktiver Substanzen.* Zeitschrift für Physik, 1922. **9**(1): p. 131-144.
164. Hardouin Duparc, O., *Pierre Auger – Lise Meitner: Comparative contributions to the Auger effect.* International Journal of Materials Research, 2009. **100**(9): p. 1162-1166.
165. Lander, J.J., *Auger Peaks in the Energy Spectra of Secondary Electrons from Various Materials.* Physical Review, 1953. **91**(6): p. 1382-1387.
166. Harris, L.A., *Analysis of Materials by Electron-Excited Auger Electrons.* Journal of Applied Physics, 1968. **39**(3): p. 1419-1427.
167. Harris, L.A., *Some Observations of Surface Segregation by Auger Electron Emission.* Journal of Applied Physics, 1968. **39**(3): p. 1428-1431.
168. Weber, R.E. and W.T. Peria, *Use of LEED Apparatus for the Detection and Identification of Surface Contaminants.* Journal of Applied Physics, 1967. **38**(11): p. 4355-4358.
169. Hofmann, S., *Auger- and X-Ray Photoelectron Spectroscopy in Materials Science*

A User-Oriented Guide. 1 ed. Springer Series in Surface Science, ed. G.L. Ertl, H; Mills, D. L. . 2013, Heidelberg, Germany: Springer-Verlag Berlin Heidelberg. XX, 528.
170. Weissmann, R. and K. Müller, *Auger electron spectroscopy - a local probe for solid surfaces.* Surface Science Reports, 1981. **1**(5): p. 251-309.
171. Hubin, A. and H. Terryn, *Chapter 6 X-ray photoelectron and Auger electron spectroscopy*, in *Non-destructive Micro Analysis of Cultural Heritage Materials*, K.G. Janssens, R. Van, Editor. 2004, Elsevier. p. 277-312.
172. Lipson, S.G.S.G., H.H. Lipson, and D.S.D.S. Tannhauser, *Optical physics*. 3rd ed ed. 1995: Cambridge University Press.
173. Goldstein, J.I.N., D.E.; Michael, J.R.; Ritchie, N.W.M.; Scott, J.H.J.; Joy, D.C., *Scanning electron microscopy and x-ray microanalysis*. 2018, New York, NY, USA: Springer.
174. Seah, M.P. and W.A. Dench, *Quantitative electron spectroscopy of surfaces: A standard data base for electron inelastic mean free paths in solids.* Surface and

Interface Analysis, 1979. **1**(1): p. 2-11.
175. **Seah, M.P.**, *Electron and ion energy analysis*, in *Methods of surface analysis : techniques and applications*, J. Walls, Editor. 1990, Cambridge University Press: Cambridge, UK. p. 57-86.
176. Riviere, J.C., *Instrumentation*, in *Practical surface analysis Vol. 1 (AES and XPS)*, D.D. Briggs and M.P. Seah, Editors. 1990, John Wiley & Sons: Chinchester, West Sussex, UK.
177. Stuart, B.H., *Infrared Spectroscopy: Fundamentals and Applications*. Analytical Techniques in the Sciences (AnTs), ed. D.J. Ando. 2004, Chichester, West Sussex, England: John Wiley & Sons.
178. Stuart, B.B.H., D.J.D.J. Ando, and ACOL, *Modern infrared spectroscopy*. 1996: Published on behalf of ACOL (University of Greenwich) by Wiley.
179. Cheung, F.M.H., et al., *Rotation of Coulomb crystals in a magnetized inductively coupled complex plasma.* IEEE Transactions on Plasma Science, 2003. **31**(1): p. 112-118.
180. Prior, N.J., L.W. Mitchell, and A.A. Samarian, *Determination of charge on vertically aligned particles in a complex plasma using laser excitations.* Journal of Physics D: Applied Physics, 2003. **36**(11): p. 1249.
181. Huheey, J.E., *Inorganic chemistry : principles of structure and reactivity*. 4th ed. ed, ed. E.A. Keiter and R.L. Keiter. 1993, New York, NY: New York, NY : HarperCollins College Publishers.
182. Hillborg, H., et al., *Crosslinked polydimethylsiloxane exposed to oxygen plasma studied by neutron reflectometry and other surface specific techniques.* Polymer, 2000. **41**(18): p. 6851-6863.
183. O'Hare, L.-A., B. Parbhoo, and S.R. Leadley, *Development of a methodology for XPS curve-fitting of the Si 2p core level of siloxane materials.* Surface and Interface Analysis, 2004. **36**(10): p. 1427-1434.
184. Lecoq, E., et al., *Plasma Polymerization of APTES to Elaborate Nitrogen Containing Organosilicon Thin Films: Influence of Process Parameters and Discussion About the Growing Mechanisms.* Plasma Processes and Polymers, 2013. **10**(3): p. 250-261.
185. Gu, X.N., et al., *Degradation, hemolysis, and cytotoxicity of silane coatings on biodegradable magnesium alloy.* Materials Letters, 2017. **193**: p. 266-269.
186. Liu, C.-N., et al., *Combined in situ FTIR-spectroscopic and electrochemical analysis of nanopores in ultra-thin SiO x -like plasma polymer barrier films.* Journal of Physics D: Applied Physics, 2013. **46**(8): p. 084015.
187. Kurth, D.G. and T. Bein, *Thin Films of (3-Aminopropyl)triethoxysilane on Aluminum Oxide and Gold Substrates.* Langmuir, 1995. **11**(8): p. 3061-3067.
188. Schwarz-Selinger, T., A.v. Keudell, and W. Jacob, *Plasma chemical vapor deposition of hydrocarbon films: The influence of hydrocarbon source gas on the film properties.* Journal of Applied Physics, 1999. **86**(7): p. 3988-3996.
189. Blanchard, N.E., et al., *Densification and Hydration of HMDSO Plasma Polymers.* Plasma Processes and Polymers, 2015. **12**(1): p. 32-41.
190. Hegemann, D., *4.09 - Plasma Polymer Deposition and Coatings on Polymers*, in *Comprehensive Materials Processing*, S. Hashmi, et al., Editors. 2014, Elsevier: Oxford. p. 201-228.
191. Socrates, G., *Infrared and Raman Characteristic Group Frequencies Tables and Charts*. Third Edition ed. 2004, West Sussex, England: John Wiley & Sons Ltd.
192. Creatore, M., et al., *RF plasma deposition of SiO2-like films: plasma phase diagnostics and gas barrier film properties optimisation.* Surface and Coatings Technology, 2001. **142-144**: p. 163-168.
193. Barreca, D., et al., *Low-Temperature PECVD of Transparent SiOxCyHz Thin Films.* Chemical Vapor Deposition, 2007. **13**(5): p. 205-210.
194. Borges, J.N., et al., *Functionalization of Copper Surfaces by Plasma Treatments to Improve Adhesion of Epoxy Resins.* Plasma Processes and Polymers, 2009. **6**(1): p. S490-S495.

195. Borris, J., et al., *Investigations into Composition and Structure of DBD-Deposited Amino Group Containing Polymer Layers.* Plasma Processes and Polymers, 2007. **4**(1): p. S482-486.
196. Gandhiraman, R.P., et al., *Deposition of chemically reactive and repellent sites on biosensor chips for reduced non-specific binding.* Colloids and Surfaces B: Biointerfaces, 2010. **79**(1): p. 270-275.
197. Volcke, C., et al., *Plasma functionalization of AFM tips for measurement of chemical interactions.* Journal of Colloid and Interface Science, 2010. **348**(2): p. 322-328.
198. Hegemann, D., et al., *Deposition of Functional Plasma Polymers Influenced by Reactor Geometry in Capacitively Coupled Discharges.* Plasma Processes and Polymers, 2016. **13**(2): p. 279-286.
199. Sabat, K.C., et al., *Reduction of Oxide Minerals by Hydrogen Plasma: An Overview.* Plasma Chemistry and Plasma Processing, 2014. **34**(1): p. 1-23.
200. Plueddemann, E., *Aqueous Solutions of Silane Coupling Agents*, in *Silane Coupling Agents*. 1991, Springer US. p. 55-78.